TiO$_2$-based Photoelectrocatalysis Technology for Degradation and Detection of Organics in Wastewater

Meng Zu

B. Sc., M. Eng.

School of Environment and Science

Gold Coast Campus, Griffith University

Submitted in fulfillment of the requirements of the degree of Doctor of Philosophy

April 2021

ABSTRACT

With industrialization rapidly progressing in recent decades, great amounts of refractory organic pollutants are found in water bodies, which severely jeopardizes ecosystem health. Monitoring the organic compounds in water bodies and removing organic pollutants from wastewater is essential for ameliorating threats to aquatic life and human health. Photocatalytic (PC) and photoelectrocatalytic (PEC) degradation and detection of organic pollutants in wastewater are promising strategies for fulfilling these goals sustainably, since PC and PEC technologies can take advantage of solar energy, which is one of the most abundant energy sources on earth. Titanium dioxide (TiO_2) is a commonly used photocatalyst due to its appropriate band position, high chemical stability, low cost, and nontoxicity. However, pristine TiO_2 photocatalysts can only be stimulated by UV irradiation because the band gap of pristine TiO_2 is higher than 3.0 eV, which seriously impedes its development with low-cost and environmentally friendly solar energy. There are several efficient strategies to overcome these disadvantages of pristine TiO_2, such as morphology modification, bandgap engineering, and applying co-catalysts with the host photocatalysts. Herein, this thesis aims to utilize different strategies to enhance the photocatalytic performance of TiO_2-based photocatalysts under visible light irradiation and apply those modified photocatalysts to degradation and detection of organics in wastewater.

In the first study, a photoelectrochemical Chemical Oxygen Demand (COD) sensor based on a linear photocurrent-concentration analytical principle was designed for the on-site determination of COD. A high-performance anatase-branch@hydrogenated rutile-nanorod TiO_2 (AB@H-RTNR) photoelectrode was fabricated. The as-prepared photoanodes successfully achieved sensitive determination of COD with a detection limit of 0.2 ppm (S/N = 3), an RSD% of 1.5 %, a wide linear detection range of 1.25−576 ppm, and an average recovery rate fluctuating between 100% ± 4% for artificial wastewater sample analyses. The satisfying results of this work suggest that

AB@H-RTNR can serve as a promising photocatalyst for fast and accurate detection of organic compounds in water bodies.

In addition to detecting COD in water bodies, the degradation of refractory organic compounds in water is also crucial for healthy ecosystems. Highly efficient, low-cost, and portable wastewater treatment and purification solutions are urgently needed for aqueous pollution removal. Herein, in the second study, we coupled a TiO_2-based PC system with a persulphate (PS) oxidation system into a portable advanced oxidation device for rapid and deep degradation of organic contaminants in wastewater. Using hydrogenation, we fabricated hydrogenated anatase branched-rutile TiO_2 nanorod (H-AB@RTNR) photocatalysts that enable PC degradation to occur under visible light to improve the utilization of solar energy. A degradation rate of 100% and a reaction rate constant of 0.0221 min^{-1} for degrading 1 L Rhodamine B (20 mg L^{-1}) was achieved in 120 min in a specially designed thin-layer cell under visible light irradiation. These encouraging results suggest that the H-AB@RTNR photocatalysts/PS synergistic degradation system could be an alternative approach for the efficient degradation of organic pollutants in wastewater.

Motivated by the result of the PC/PS synergistic degradation system, we further employed a PC/chlorination system for synergistic degradation of antibiotics. In the third study, we demonstrated the use of visible light (>420 nm) to produce •HO and •ClO through the assistance of photocatalysts (TiO_2/WO_3 nanofibers) and free chlorine (HOCl/ClO$^-$). The introduction of visible-light-driven photocatalysts can significantly boost the yield of active radicals, which favors the degradation of antibiotics in water bodies. The synergistic PC/chlorination degradation system obtained a pseudo-first-order degradation rate constant of a model antibiotic, tetracycline hydrochloride, of 21.438 min^{-1}, which is 3.66 and 86.57 times higher than that in the pure TiO_2/WO_3 photocatalysis and traditional chlorination processes, respectively. The stability test exhibits that the performance decline is negligible after multiple

use cycles. The results of this study suggest that PC/chlorine degradation is a feasible, low-cost, and environmental-friendly strategy for antibiotics removal under visible irradiation.

Another approach to improve the degradation efficiency of TiO_2-based photocatalysts is using co-catalysts to assist the host photocatalysts. In the fourth study, we fabricated noble-metal free co-catalysts, i.e., N-doped carbon wrapped FeNi nanoparticles (FeNi@NGC), via a pyrolysis method. Hydrogenated TiO_2 (H-TiO_2) was synthesized as the host photocatalysts and coupled with as-prepared FeNi@NGC to obtain superior PC activity in the degradation of tetracycline hydrochloride (TC-HCl), a model antibiotic. The FeNi@NGC/H-TiO_2 system achieved a degradation rate of 100% within 120 min on degrading 100 mL 20 mg L^{-1} TC-HCl under visible light irradiation (λ>420 nm). The degradation rate constant of the FeNi@NGC/H-TiO_2 system reached 23.18 min^{-1}, which was 33.99, 26.98, and 2.23 times compared to that of TiO_2, FeNi@NGC/TiO_2, and H-TiO_2 system. The favorable performance of the FeNi@NGC/H-TiO_2 system can be ascribed to two reasons: the secondary electron transfer in the FeNi intermetallic compounds that facilitates the photo-induced charge separation in photocatalysts; and the enhanced visible light absorption ability resulted from the N-doped graphitized carbon shell. Moreover, the oxygen vacancies brought by the hydrogenation process also improves the visible light absorbance of the photocatalysts, which favors the degradation performance. This study suggests that coupling FeNi@NGC co-catalyst with H-TiO_2 is a promising strategy for improving the photocatalytic degradation performance on antibiotics.

In summary, the strategies presented in this thesis show that the morphology and electronic properties of TiO_2 can be manipulated to resolve the problems of poor visible light absorption and the large recombination rate of photogenerated charge carriers.Moreover, the degradation performances of organic compounds show that applying a synergistic system with TiO_2-based materials is promising in the removal of refractory organics in the wastewater. The
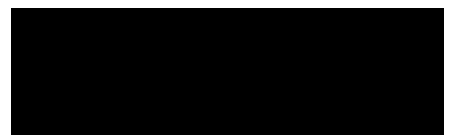
strategies utilized in the thesis (i.e., morphology manipulation, bandgap engineering, and applying co-catalysts) can be utilized in other members of the semiconductors family (such as SnO_2, $BiVO_4$, $SrTiO_3$) for developing more sustainable and low-cost approaches and techniques to improve human and aquatic ecosystem health.

STATEMENT OF ORIGINALITY

This work has not previously been submitted for a degree or diploma in any university.

To the best of my knowledge and belief, the thesis contains no material previously

published or written by another person except where due reference is made in the thesis

itself.

Signature of Candidate

15th April 2021

TABLE OF CONTENTS

ACKNOWLEDGEMENTS

The writing and completion of this thesis would not be possible without the help and support of many notable people throughout my Ph.D. study.

Firstly, I wish to sincerely thank my principal supervisor, Prof. Shanqing Zhang, for giving me the opportunity to join his research group here in Australia. His brilliant ideas, continuous encouragement, and professional advice accompanied me throughout my whole Ph.D. He brought the best out of me every day; his genius research insight and suggestions gave me inspiration and encouragement for further achievements in this research field. Without his support, many difficulties would notbe solved, and several academic achievements would not be possible. My sincere thanks also go to my external supervisor, Prof. Shengsen Zhang, and associate supervisor Dr. Porun Liu. Their helpful discussions and patience always helped me make progress during my Ph.D. study.

My sincere appreciation goes to Dr. Yazhou Wang and Dr. Michael Ling for their tutelage and guidance in the lab. They taught me the basics of electrochemistry and characterization methods. I extend my gratitude to all team membersof the Shanqing Zhang group: Mr. Hao Chen, Mr. Zhong Su, Mr. Meng Li, Mr. Luke Hencz, Mr. Shangshu Qian, Mr. Yuhui Tian, Ms. Zhenzhen Wu, Ms. Yubai Zhang, and Ms. Ding Yuan for their continuous support during my Ph.D. research. They have made my research journey full of fun and enjoyment.

Many thanks to all the staff and colleagues in ENV, EFRI, ESC, and CCEE, especially Dr. Lei Zhang, Dr. Yuhai Dou, Dr. Sean Lowe, Dr. Mohammad Al-Mamun,Dr. Yun Wang, and Prof. Huijun Zhao. I also want to thank the secretaries in CCEE and ESC, Ms. Christina Perry and Ms. Michelle Ryan, respectively, for their assistance during the past 3.5 years. Moreover, I want to thank the Australian Government and Griffith University for offering me the GUIPRS and GUPRS scholarships and other funding to support my research and living

expenses.

Finally, my most profound appreciation goes to my family for their encouragement and support during my Ph.D. study over the years.

ACRONYMS

AB@RTNR	Anatase-branch @ rutile TiO_2 nanorods
AB@H-RTNR	Anatase-branch @ hydrogenated rutile TiO_2 nanorods
AOP	Advanced oxidation process
AOS	Average oxidation state
COD	Chemical oxygen demand
COS	Carbon oxidation state
CV	Cyclic voltammetry
DOS	Density of states
e^-	Photogenerated electrons
EIS	Electrochemical impedance spectroscopy
EPR	Electron paramagnetic resonance
eV	Electron volt
FC	Free chlorine
FeNi@NGC	FeNi intermetallic compounds wrapped with N-doped graphitized carbon
FL	Fluorescence
FTIR	Fourier Transform infrared spectroscopy
FTO	Fluorine-doped tin oxide
GO	Graphene oxide
h^+	Photogenerated holes
HRTEM	High-resolution transmission electron microscopy
H-AB@RTNR	Hydrogenated anatase-branch @ rutile TiO_2 nanorods
H-RTNR	Hydrogenated rutile TiO_2 nanorods
H-TiO_2	Hydrogenated titanium dioxide
ICDD	International Centre for Diffraction Data

IPCE	Incident photo-to-current conversion efficiency
JCPDS	Joint committee on powder diffraction standards
LC/MS	Liquid chromatography/mass spectrometry
LED	Light-emitting diode
M-S	Mott-Schottky
NHE	Normal Hydrogen Electrode
PC	Photocatalytic
PEC	Photoelectrocatalytic
PS	Persulphate
R_s	Electrolyte resistance
R_{ct}	Charge-transfer resistance
RhB	Rhodamine B
RHE	Reversible hydrogen electrode
RSD	Relative standard deviation
RTNR	Rutile TiO_2 nanorods
SEM	Scanning electron microscopy
SHE	Standard Hydrogen Electrode
TC-HCl	Tetracycline- hydrochloride
TEM	Transmission electron microscopy
TOC	Total organic carbon
XRD	X-ray diffraction spectroscopy
XPS	X-ray photoelectron spectroscopy

PUBLICATIONS

Acknowledgment of papers included in this thesis

Section 9.1 of the Griffith University Code for the Responsible Conduct of Research ("Criteria for Authorship"), in accordance with Section 5 of the Australian Code for the Responsible Conduct of Research, states:

> To be named as an author, a researcher must have made a substantial scholarly contribution to the creative or scholarly work that constitutes the research output, and be able to take public responsibility for at least that part of the work they contributed. Attribution of authorship depends to some extent on the discipline and publisher policies, but in all cases, authorship must be based on substantial contributions in a combination of one or more of:
>
> - Conception and design of the research project
> - Analysis and interpretation of research data
> - Drafting or making significant parts of the creative or scholarly work or critically revising it so as to contribute significantly to the final output.

Section 9.3 of the Griffith University Code ("Responsibilities of Researchers"), in accordance with Section 5 of the Australian Code, states:

> Researchers are expected to:
> - Offer authorship to all people, including research trainees, who meet the criteria for authorship listed above, but only those people.
> - Accept or decline offers of authorship promptly in writing.
> - Include in the list of authors only those who have accepted authorship
> - Appoint one author to be the executive author to record authorship and manage correspondence about the work with the publisher and other interested parties.
> - Acknowledge all those who have contributed to the research, facilities or materials but who do not qualify as authors, such as research assistants, technical staff, and advisors on cultural or community knowledge. Obtain written consent to name individuals.

Chapter Publications

This thesis consists of three published papers from Chapters 2, 3, and 4, one submitted manuscript (Chapter 5), and one drafted manuscript (Chapter 6), which are co-authored with other researchers. My contribution to each co-authored paper is outlined at the front of the relevant chapter.

(Note: IF: Impact Factor 2019)

Chapter 2:

M. Zu, X. Zhou, S. Zhang, S. Qian, D. Li, S. Liu, S. Zhang, Sustainable engineering of TiO$_2$-based advanced oxidation technologies: From photocatalyst to application devices, *Journal of Materials Science & Technology*, 78, 202-222.

https://doi.org/10.1016/j.jmst.2020.10.061. (IF: 6.155) (2021)

Chapter 3:

M. Zu, M. Zheng, S. Zhang, C. Xing, M. Zhou, H. Liu, S. Zhang, Designing robust anatase-branch@hydrogenated-rutile-nanorod TiO$_2$ as accurate and sensitive photoelectrochemical sensors, *Sensors and Actuators B: Chemical*, 321, 128504.

https://doi.org/10.1016/j.snb.2020.128504. (IF: 7.100) (2020).

Chapter 4:

M. Zu, S. Zhang, C. Liu, C. Xing, D. Li, P. Liu, S. Zhang, Portable wastewater treatment system based on synergetic photocatalytic and persulphate degradation under visible light. *SCIENCE CHINA Materials*, 1-12

https://doi.org/10.1007/s40843-020-1599-2 (IF: 6.098) (2021)

Chapter 5:

M. Zu, S. Zhang, C. Liu, C. Xing, D. Li, P. Liu, S. Zhang, Efficient removal of antibiotics via a synergetic process combining visible-light-driven TiO$_2$/WO$_3$ nanofibers photocatalysis and

chlorination, ***Chemical Engineering Journal***, In review. (IF: 10.652)

Chapter 6:

M. Zu, S. Zhang, C. Liu, C. Xing, D. Li, P. Liu, S. Zhang, N-doped carbon wrapped FeNi nanoparticles co-catalysts for the photodegradation of antibiotics under visible-light irradiation, ***ACS Sustainable Chemistry & Engineering***, To be submitted. (IF: 7.632)

Appropriate acknowledgments of those who contributed to the research but did notqualify as authors are included in each paper.
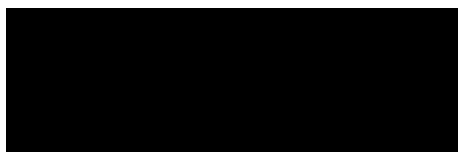
Meng Zu
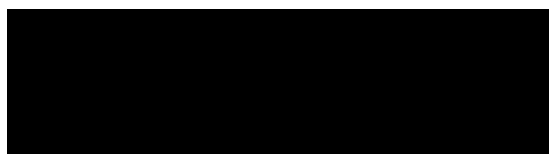
Supervisor: Prof. Shanqing Zhang

Additional Relevant Publications

In addition to the published works that formed the research chapters of this thesis, several other co-authored publications were relevant but did not form part of the thesis itself.

1. Y. Wang, **<u>M. Zu</u>**, X. Zhou, H. Lin, F. Peng, S. Zhang. (2020). Designing efficient TiO_2-based photoelectrocatalysis systems for chemical engineering and sensing. ***Chemical Engineering Journal***, 381, 122605.

2. M. Zhou, T. Li, **<u>M. Zu</u>**, S. Zhang, Y. Liu, H. Zhao. (2021). Membrane-based colorimetric flow-injection system for online free chlorine monitoring in drinking water. ***Sensors and Actuators B: Chemical***, 327, 128905.

3. R. Wang, **<u>M. Zu</u>**, S. Yang, S. Zhang, W. Zhou, Z. Mai, S. Zhang. (2018). Visible-light-driven photoelectrochemical determination of Cu^{2+} based on CdS sensitized hydrogenated TiO_2 nanorod arrays. ***Sensors and Actuators B: Chemical***, 270, 270-276.

4. R. Wang, J. Yan, **<u>M. Zu</u>**, S. Yang, X. Cai, Q. Gao, S. Zhang. (2018). Facile synthesis of interlocking $g-C_3N_4$/CdS photoanode for stable photoelectrochemical hydrogen production. ***Electrochimica Acta***, 279, 74-83.

5. Y. Wang, **<u>M. Zu</u>**, S. Li, T. Butburee, L. Wang, F. Peng, S. Zhang. (2017). Dual modification of TiO_2 nanorods for selective photoelectrochemical detection of organic compounds. ***Sensors and Actuators B: Chemical***, 250, 307-314.

CHAPTER 1
INTRODUCTION

1.1 SIGNIFICANCE OF THE PROJECT

Pollution in water bodies, caused by the discharge of inadequately treated industrial and municipal wastewater into rivers and oceans, has aroused more and more concerns for all countries worldwide.[1] Majority of municipal and industrial wastewater contains organic pollutants in varying combinations and concentrations.[2] Hence the assessment and monitoring of chemical oxygen demand (COD) and degradation of refractory organics in water bodies are urgently required.[3,4] In recent decades, photocatalytic (PC) and photoelectrocatalytic (PEC) techniques for detecting COD and degradation of organic compounds have been reported as superior alternative methods to overcome the drawbacks of the current methods. The core component in the PC and PEC is the photocatalyst, which absorbs light energy and converts it into electrical or chemical power to activate the target reaction, i.e., producing the photo-excited electrons and holes to drive various types of PC and PEC reactions. The photoelectrochemical properties that affect the performance of photocatalysts are chemical and mechanical stability, nanostructure, energy band position, bandgap energy, electron mobility, and the lifetime of the charge carriers. A variety of semiconductors, including TiO_2, ZnO, WO_3, $BiVO_4$, and CdS, have been studied and developed for PC application.[5-8] Among various photocatalysts, TiO_2 is regarded as the most efficient and environmental-friendly photocatalyst due to its photolytic stability, high photocatalytic efficiency, zero toxicity, and affordable cost.[9-11] However, the pristine TiO_2 photocatalysts can only be stimulated by UV light for their broad bandgap, which is higher than 3.0 eV. Therefore, strategies to improve the visible light absorption of TiO_2-based photocatalysts are urgently needed.

To overcome the hindrances existing in pristine TiO_2 and exploit them in the application of degradation and detection of organic pollutants, I successfully designed a series of TiO_2-based photocatalysts (i.e., AB@H-RTNR, H-AB@RTNR, TiO_2/WO_3 nanofibers) which extend the light absorption range to visible light region, so that the TiO_2-based photocatalysts can take

advantage of solar energy. Moreover, to enhance PC degradation performance on refractory organic compounds, I adopted other AOP techniques and designed several synergistic degradation systems (i.e., PC/PS degradation system, PC/chlorination degradation system) and therefore address the issue. Furthermore, I also fabricate an efficient co-catalyst (FeNi@NGC) to boost the degradation performance on TC-HCl by H-TiO$_2$. These results exhibit the promising potential of TiO$_2$-based photocatalysts in developing sustainable, low-cost, efficient, and easily implementable techniques in the degradation and detection of organic compounds in wastewater.

1.2 RESEARCH OBJECTIVES

The central point of this thesis is to study controllable modification strategies (including cell design, morphology fabrication, bang gap engineering, and potential bias on TiO$_2$ photoelectrodes) to improve the efficiency of detection and degradation of organic compounds, bridging fundamental research and practical applications. More specifically, the objectives are:

- The cell design aims to boost the mass transport at the TiO$_2$ and bulk solution interface, minimize photon energy loss in the reaction media, and maximize the light intensity at the TiO$_2$ surface.

- The morphology fabrication can enhance the light absorption efficiency, charge transport to the catalyst surface and subsequently improve the PEC efficiency by fabricating different TiO$_2$ nanostructures.

- The bandgap engineering is to modify the photocatalyst's electronic structure or combine the bandgap of a different phase of TiO$_2$ and facilitate the harvest of the photons of different wavelengths, especially the visible and infrared regions of solar light.

- The control of electrochemical bias to achieve effective separation of photoelectron

and photo hole and allow synergetic oxidation of organics.

1.3 THESIS OUTLINE

The first aim of this project is to design and synthesize high-efficiency TiO$_2$-based photocatalysts via several rational strategies mentioned previously. The second aim is to apply those photocatalysts in the degradation and detection of organic compounds and evaluate the PC and PEC performance of the as-prepared materials. More specifically, the research objectives for each thesis chapter are to:

1) Highlight the significance of the project, summarize the research objectives and major contributions to the research of TiO$_2$-based PC technology (Chapter 1)

2) Provide a comprehensive review of sustainable engineering of TiO$_2$-based advanced oxidation technologies (Chapter 2)

3) Demonstrate the design and application of anatase-branch@hydrogenated-rutile-nanorod TiO$_2$ as accurate and sensitive photoelectrochemical sensors and compare the performance with pristine TiO$_2$ (Chapter 3).

4) Design a portable wastewater treatment system based on synergetic photocatalytic and persulphate degradation under visible light (Chapter 4).

5) Compare the performance of a PC/chlorination system with a traditional chlorination system and a regular PC system using the TiO$_2$/WO$_3$ nanofibers as photocatalysts under visible light irradiation (Chapter 5).

6) Exhibit the fabrication of FeNi intermetallic compound nanoparticles wrapped with N-doped graphitized carbon (FeNi@NGC) co-catalysts, assisting efficient TC-HCl PC degradation by hydrogenated TiO$_2$ nanorods (Chapter 6).

1.4 REFERENCES

1. Wu S, Hu H, Lin Y, Zhang J, Hu YH. Visible light photocatalytic degradation of tetracycline over TiO_2. *Chemical Engineering Journal*. 2020 Feb 15;382:122842.

2. Hu X, Hu X, Peng Q, Zhou L, Tan X, Jiang L, Tang C, Wang H, Liu S, Wang Y, Ning Z. Mechanisms underlying the photocatalytic degradation pathway of ciprofloxacin with heterogeneous TiO_2. *Chemical Engineering Journal*. 2020 Jan 15;380:122366.

3. Onkani SP, Diagboya PN, Mtunzi FM, Klink MJ, Olu-Owolabi BI, Pakade V. Comparative study of the photocatalytic degradation of 2–chlorophenol under UV irradiation using pristine and Ag-doped species of TiO_2, ZnO and ZnS photocatalysts. *Journal of Environmental Management*. 2020 Apr 15;260:110145.

4. Wang X, Sun M, Murugananthan M, Zhang Y, Zhang L. Electrochemically self-doped WO_3/TiO_2 nanotubes for photocatalytic degradation of volatile organic compounds. *Applied Catalysis B: Environmental*. 2020 Jan 1;260:118205.

5. Jahdi M, Mishra SB, Nxumalo EN, Mhlanga SD, Mishra AK. Smart pathways for the photocatalytic degradation of sulfamethoxazole drug using F-Pd co-doped TiO_2 nanocomposites. *Applied Catalysis B: Environmental*. 2020 Jun 15;267:118716.

6. Wang Y, Zhu C, Zuo G, Guo Y, Xiao W, Dai Y, Kong J, Xu X, Zhou Y, Xie A, Sun C. 0D/2D Co_3O_4/TiO_2 Z-Scheme heterojunction for boosted photocatalytic degradation and mechanism investigation. *Applied Catalysis B: Environmental*. 2020 Dec 5;278:119298.

7. Ariza-Tarazona MC, Villarreal-Chiu JF, Hernández-López JM, De la Rosa JR, Barbieri V, Siligardi C, Cedillo-González EI. Microplastic pollution reduction by a carbon and nitrogen-doped TiO_2: Effect of pH and temperature in the photocatalytic degradation process. *Journal of Hazardous Materials*. 2020 Aug 5;395:122632.

8. Sriramoju JB, Muniyappa M, Marilingaiah NR, Sabbanahalli C, Shetty M, Mudike R, Chitrabanu CP, Shivaramu PD, Nagaraju G, Rangappa KS, Kumar A. Carbon-based

TiO$_2$-x heterostructure nanocomposites for enhanced photocatalytic degradation of dye molecules. *Ceramics International*. 2021 Apr 1;47(7):10314-21.

9. Zheng H, Meng X, Chen J, Que M, Wang W, Liu X, Yang L, Zhao Y. In situ phase evolution of TiO$_2$/Ti$_3$C$_2$Tx heterojunction for enhancing adsorption and photocatalytic degradation. *Applied Surface Science*. 2021 Apr 15;545:149031.

10. Wu S, Li X, Tian Y, Lin Y, Hu YH. Excellent photocatalytic degradation of tetracycline over black anatase-TiO$_2$ under visible light. *Chemical Engineering Journal*. 2021;406:126747.

11. Tang KY, Chen JX, Legaspi ED, Owh C, Lin M, Tee IS, Kai D, Loh XJ, Li Z, Regulacio MD, Ye E. Gold-decorated TiO$_2$ nanofibrous hybrid for improved solar-driven photocatalytic pollutant degradation. *Chemosphere*. 2021 Feb 1;265:129114.

CHAPTER 2

Sustainable engineering of TiO$_2$-based advanced oxidation technologies: From photocatalyst to application devices

2.1 INTRODUCTORY REMARKS

This chapter includes one review article published in *Journal of Materials Science & Technology*, 2021, 78, 202-222.

Article 1 is a review of titanium dioxide (TiO_2)-based PC and PEC sustainable technologies for advanced oxidation applications. In the review, I present a comprehensive and insightful overview of the state-of-the-art techniques in the rational strategies for improving the performance of TiO_2-based photocatalysts and summarize their applications. I categorized the strategies into two aspects: photocatalysts engineering and device engineering. The former consists of morphology fabrication, bandgap engineering, and co-catalysts; the latter includes irradiation source design, reactor structure design, and potential bias assistance. Moreover, I review the existing and emerging applications of those modified photocatalytic systems, such as sensing, wastewater treatment, and water splitting. Finally, I propose prospective future development of TiO_2-based PC and PEC technology from the lab-scale to large-scale facilities.

2.2 STATEMENT OF CONTRIBUTION

This chapter includes a co-authored paper. The bibliographic details of the co-authored paper, including all authors, are:

Meng Zu, Xiaosong Zhou, Shengsen Zhang, Shangshu Qian, Dongsheng Li, Xianhu Liu, Shanqing Zhang

Sustainable engineering of TiO$_2$-based advanced oxidation technologies: From photocatalyst to application devices

Journal of Materials Science & Technology, 2021, 78, 202-222.

My contribution to the papers involved:

Literature review, collection, and organization of information, data, and references; Preparation of manuscript.

(Signed)_____(Date) <u>15-04-2021</u>

Name of Student: Meng Zu

(Countersigned)_____(Date) <u>15-04-2021</u>

Corresponding author of paper: Shanqing Zhang

(Countersigned)_____(Date) <u>15-04-2021</u>

Supervisor: Shanqing Zhang

2.3 Article 1

Due to copyright restrictions, the published version of this journal article is not available here. Please view the published version online at:

https://doi.org/10.1016/j.jmst.2020.10.061

Sustainable engineering of TiO₂-based advanced oxidation technologies: From photocatalyst to application devices

Meng Zu [a,b], Xiaosong Zhou [a,*], Shengsen Zhang [c], Shangshu Qian [b], Dong-Sheng Li [d], Xianhu Liu [e], Shanqing Zhang [b,*]

[a] College of Chemistry and Chemical Engineering, Lingnan Normal University, Zhanjiang, Guangdong, 524048, China
[b] Centre for Clean Environment and Energy and Griffith School of Environment, Griffith University, Gold Coast, QLD, 4222, Australia
[c] College of Materials and Energy, South China Agricultural University, Guangzhou, 510643, China
[d] College of Materials and Chemical Engineering, Key Laboratory of Inorganic Nonmetallic Crystalline and Energy Conversion Materials, China Three Gorges University, Yichang, 443002, China
[e] Key Laboratory of Materials Processing and Mold (Zhengzhou University), Ministry of Education, Zhengzhou, 450002, China

ARTICLE INFO

ABSTRACT

In recent years, photocatalysis (PC) and photoelectrocatalysis (PEC) technologies have shown great promise as low-cost, environmentally friendly, and sustainable strategies in addressing the issues of energy shortages and environmental pollution, which has become a research hotspot. Titanium dioxide (TiO₂)-based PC and PEC are the most promising sustainable technologies for advanced oxidation applications. Due to its inherent characteristics, including high oxidation ability, low price, and stability, TiO₂ photocatalyst has been widely studied and used in different scales for numerous decades. For practical applications in these areas, the engineering of the photocatalysts and the design of the PC and PEC devices must be both environmentally and economically sustainable. On the one hand, for the engineering of the photocatalysts, the photocatalyst shall be able to deliver the following characteristics, including large specific surface area, high absorption of light, rapid and low-cost separation and regeneration, and high stability. On the other hand, the design of the PC and PEC devices shall facilitate high in energy utilization and catalytic efficiency, and low in building and operational cost. This work covers the reaction mechanism of TiO₂-based PC and PEC technologies, sustainable design, and preparation of TiO₂ photocatalysts as well as sustainable design in PC and PEC devices for wastewater treatment, sensing, and water splitting. Finally, we provide some critical perspectives on the future development of TiO₂-based PC and PEC technology.

© 2020 Published by Elsevier Ltd on behalf of The editorial office of Journal of Materials Science & Technology.

1. Introduction

As the industrialization process accelerates, energy and environmental issues arose at the same time. Nowadays, fossil fuels, such as natural gas, coal, and oil, are still the world's primary sources of energy. Some fossil fuels are projected to be consumed in the 21 st century, with the ongoing growth of industrialization. Furthermore, the use of fossil fuels also causes significant environmental pollution. In recent years, more and more severe air pollution and water contamination have put human life and health at immediate risk [1]. Therefore, sustainable responses to these questions are

urgently demanded. In 1972, Fujishima and Honda found that TiO₂ electrodes would decompose hydrogen under sunlight in aquatic products [2]. Since then, TiO₂-based photocatalytic (PC) and photoelectrocatalytic (PEC) technologies, which can directly convert solar energy into easily stored hydrogen without pollutants emissions, has drawn widespread attention because of their sustainable features.

Enormous efforts have been made recently for optimizing the sustainability of PC and PEC technology [3]. The sustainable engineering of PC and PEC technologies can be categorized into two parts: environmentally sustainable and economically sustainable. For improving environmental sustainability, the photocatalysts and device design should meet the requirements of high utilization of solar energy and large specific surface area. For enhancing economic sustainability, the cost of synthesizing photocatalysts,

---

* Corresponding authors.
  E-mail addresses: zxs801213@163.com (X. Zhou), s.zhang@griffith.edu.au (S. Zhang).

11

building and operating devices need to be reduced. Therefore, in order to advance the sustainability of PC and PEC technologies both environmentally and economically, the optimizing methods can be concluded in two directions: photocatalysts engineering and device engineering. Firstly, the critical component in the sustainable PC and PEC technology is the photocatalyst, which absorbs light energy and transforms it into electrical or chemical power to cause the target reaction, i.e., to generate the photo-excited electrons and holes to drive different types of oxidation and reduction reaction. The determining factors of the performance of photocatalysts include chemical and mechanical stability, nanostructure, semiconductor properties such as the location and band-gap of the energy band, electron mobility, and lifetime of charge carriers. Great deals of semiconductors were studied and developed for PC and PEC use, including TiO_2, ZnO [4,5], WO_3 [6,7], Fe_2O_3 [8,9], $BiVO_4$ [10,11], CdS [12,13], and CdSe [14]. TiO_2 has been the most widely used photocatalyst among all semiconductors because of several merits. Firstly, TiO_2 is the most versatile semiconductor that has been applied in various fields, including photocatalytic wastewater treatment [15,16], sensing [17], hydrogen production [18,19], reduction of CO_2 [20,21], disinfection [22,23], and air purification [24,25].

Moreover, the superior physical and chemical stability bestows TiO_2 robust performance in PC and PEC applications [26,27]. Most importantly, TiO_2 is the most economically friendly photocatalyst due to the simplicity in preparation and low cost [28,29]. Based on these advantages mentioned above, TiO_2 is an ideal photocatalyst for the sustainable application of PC and PEC technologies. Nonetheless, some inherent disadvantages, e.g., limited light absorption range (only UV absorbance) and poor charge separation efficiency, significantly restrict sustainable PC and PEC applications. Comprehensive work on PC and PEC technologies are broadened the possible spectrum of TiO_2-based photocatalyst applications [30–32].

Device engineering is another critical factor in improving the sustainability of PC and PEC technologies. Enormous effort has been devoted to the development of TiO_2-based photocatalysts incorporated into various PC and PEC devices for different applications. However, PC and PEC technologies are still in the laboratory stage, and many hindrances impede the practical application of these technologies [33]. The objective of efficient reactor design research and development is to scale laboratory-scale processes to industrially practical applications. Realistically, the scaling up of photocatalytic reactors is a complicated process with many factors that need to be considered in order to produce a technically and economically efficient practical application. Such considerations include the composition of the optical system, the transfer of pollutant mass, reaction kinetics, and specific features for different applications. The selection of irradiation source and design of an active optical system for PC and PEC application is especially important because the illumination initiates the PC and PEC process and maintain them.

Researchers have published many excellent comments with the continuous advancement of PC and PEC technology. For example, Wang et al. [33] reviewed the latest designing of efficient PEC applications. Zhou et al. [34] summarized the all-solid-state Z-type photocatalyst system, including the configuration, structure, optimization, and application of the Z-type photocatalyst system. Fajrina et al. [35] gave the latest developments and challenges of strategies to improve photocatalytic water splitting. Most recent reviews focus only on one or more aspects of the photocatalyst. A full description of the sustainable engineering of TiO_2-based photocatalyst design, from materials and devices to applications, has yet to be found. To help researchers understand more practical information about sustainable engineering of PC and PEC technologies, we have summarised some popular methods of TiO_2-based PC and
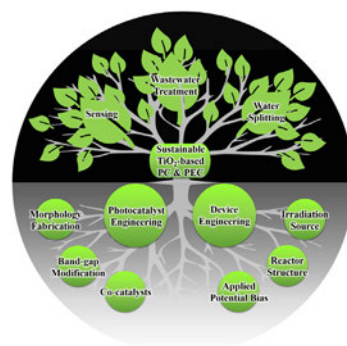

Fig. 1. Sustainable engineering of TiO2-based PC and PEC technologies: photocatalyst engineering (morphology fabrication, band-gap engineering, and co-catalysts) and device engineering (irradiation source, reactor structure, and applied potential bias), which are utilized for applications for wastewater treatment, sensing, and water splitting.
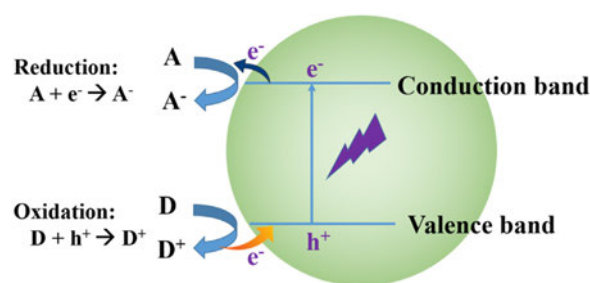

Fig. 2. Electron-hole generation and separation by the electron acceptor (A) and the electron donor (D) under illumination in n-type semiconductor TiO2 in a PC process.

PEC modification to improve efficiency and sustainability, including photocatalyst engineering (morphology fabrication, band-gap engineering and co-catalysts) and device engineering (irradiation source, reactor structure and applied potential bias) (Fig. 1). A series of advances in PC and PEC technologies are being reviewed to encourage researchers' understanding of the latest research trends in photocatalyst based on TiO_2. Besides, this study also summarized the progress of the industrialization device of PC and PEC technologies. In the end, the future perspectives of the TiO_2-based composites used in PC and PEC applications were displayed.

2. Reaction mechanism and influencing factors

2.1. PC reaction mechanism

The PC reaction occurs when the illumination activates the photocatalyst (e.g., TiO_2) and creates photo-excited charging carriers, i.e., electrons and holes. The energy-band model of semiconductors will generally view these processes at the TiO_2 photocatalyst (see Fig. 2). When the process of photoexcitation is activated under proper illumination with the energy higher than the bandgap energy of semiconductors, the electron in the valence band (VB) will be excited and transferred to the conduction band (CB), leaving a photo-generated hole in the VB as seen in Eq. (1):

$$TiO_2 \underset{recombination}{\overset{h\nu}{\rightleftarrows}} TiO_2(e^-_{CB}) + TiO_2(h^+_{VB}) \tag{1}$$
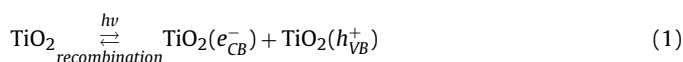
While at the same time, the recombination of the photogenerated electrons (e^-) and holes (h^+) happens as well, resulting in unnecessary heat and decreasing the PC and PEC efficiency.

TiO_2 is a typical n-type semiconductor [36]. TiO_2 naturally exists in three different forms; anatase, rutile, and brookite, where titanium (Ti^{4+}) atoms are coordinated with six oxygen (O^{2-}) atoms,
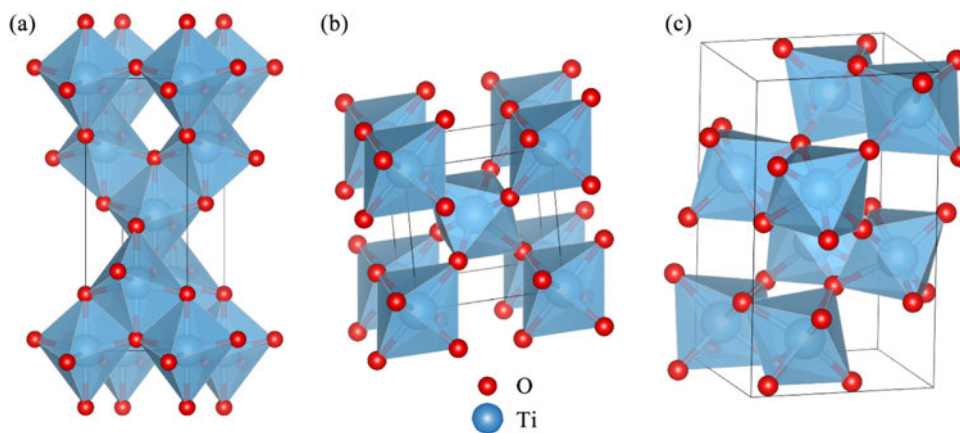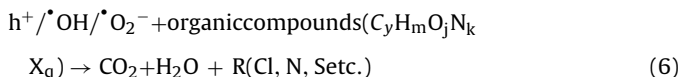
12

Fig. 3. Crystalline structures of titanium dioxide (a) anatase, (b) rutile, and (c) brookite.

forming TiO$_6$ octahedrons (see Fig. 3). The number of shared edges per TiO$_6$ octahedron for rutile and the manner of the connections determine the crystal structure, surface structure, and electronic structure of TiO$_2$. This structure, in turn, affects bulk diffusion, surface transfer capability, and redox potentials of photo-induced charge carriers. The occupancy of the d band in transition metal oxides is the main factor for the valence band energy [37]. Due to empty d bands, the valence band energy levels in TiO$_2$ are strongly dictated by the O 2p levels. Subsequently, TiO$_2$ possesses a shallow valence band and large bandgap (3.2 eV for anatase, 3.03 eV for rutile, and ~3.2 eV for brookite) [38]. The broad band-gap means that TiO$_2$ is only able to use the UV region of solar light. In other words, the direct utilization of solar light in the visible light region is theoretically not possible for pure TiO$_2$.

2.2. PEC reaction mechanism

To further improve PC efficiency, the potential bias is applied in the PC process, leading to numerous PEC applications. The application of the electric field on the charge carriers can effectively force the separation of the charge carriers, suppress the recombination reaction, and consequently increase PC performance. To incorporate a PC process into a PEC process, the photoactive semiconductors usually are immobilized onto a conductive substrate, i.e., the fabrication of a photoelectrode. Under proper conditions, such as suitable light irradiation and potential bias, the photoelectrode can carry out a sequence of oxidation reactions and reductions in the PEC cells in an aqueous solution, as shown in Eqs. (2)–(6):

$$4h^+ + 2H_2O \rightarrow O_2 + 4H^+ \tag{2}$$

$$2e^- + 2H^+ \rightarrow H_2 \tag{3}$$

$$e^- + O_2 \rightarrow \bullet O_2^- \tag{4}$$

$$h^+ + OH^- \rightarrow \bullet OH \tag{5}$$

$$h^+/{}^\bullet OH/{}^\bullet O_2{}^- + organic compounds (C_yH_mO_jN_k$$
$$X_q) \rightarrow CO_2 + H_2O + R(Cl, N, S etc.) \tag{6}$$

Where X is a halogen atom, and the y, m, j, k, and q represent the stoichiometric ratio of elements in the organic compounds. The relay or the combination of these reactions leads to different applications. In particular, the reduction and oxidation reactions at PEC cathodes and anodes form the basis of hydrogen production, oxygen production, and photodegradation of organic compounds. Thermodynamically, to allow PEC water splitting to occur, the photo-excited electron at E$_{CB}$ levels needs to obtain energy to

reduce the H$^+$ ions to H$_2$, and the photo-induced holes at E$_{VB}$ levels can oxidize H$_2$O to form O$_2$ at the same time as shown in Eqs. (2) and (3). In the photodegradation of organic compounds, the generated electron needs to have enough energy to react with the dissolved oxygen molecules to form the oxygen peroxide radicals ($\bullet O_2^-$, Eq. (4)), while the holes (h$^+$) react with OH$^-$ to generate hydroxyl radicals (${}^\bullet$OH, Eq. (5)). The generation of hydroxyl radicals (${}^\bullet$OH), oxygen peroxide radicals ($\bullet O_2^-$) and photo hole (h$^+$) can oxidize a wide range of organic compounds due to its reliable oxidant power (Eq. (6)). The applied potential between the photocatalytic anode and counter cathode can significantly increase the separation rates of the photoinduced electron-hole pairs and promote the efficiency of various PEC devices [39]. In PEC water splitting, the PEC system allows the spatial separation of gas production at different chambers, i.e., the collection of hydrogen at the cathode and oxygen at the anode.

2.3. Rational strategies for sustainable engineering of PC and PEC

Many attempts have been made in the last decade to improve PC and PEC sustainability using various methods. The working direction can be divided into two pathways: photocatalyst engineering and device engineering. In order to meet the demand for sustainability, photocatalysts are generally designed to possess a bigger specific surface area and utilize solar energy as much as possible. Naturally, photocatalyst engineering may conclude three different strategies: morphology fabrication, bandgap modification, and adding co-catalysts. The morphology fabrication method of TiO$_2$ includes constructing different dimensions of TiO$_2$ photocatalysts and controlling TiO$_2$ to expose specific crystalline facets [40–42]. This method is used to improve the charge transportation speed in photocatalysts and broaden the range of light absorption spectrum of photocatalysts, which enables the technology can fully utilize solar energy. The bandgap engineering is always applied in improving the photocatalysts light-harvesting of a broad spectrum of light, especially solar irradiation [43–45]. This method is usually accomplished by combining semiconductors of deferent bandgaps and modifying the electronic state of photocatalysts, such as heterostructure and doping. The cocatalyst can also facilitate the separation of photogenerated electrons and holes by offering trapping sites for the charge carriers [46–48], which enhances the quantum efficiency of the photocatalyst. Adding co-catalyst into the system could improve the stability of photocatalysts by consuming photogenerated holes.

For device engineering, sustainable demand is fulfilled by reducing the cost of building and operating. Moreover, the maximized utilization of solar energy should also be considered for improving

13

the sustainability of PC and PEC devices. Typically, there are two optimizing directions of the PC and PEC cell design. On the one hand, the devices are designed to facilitate the mass transport between photocatalysts and the aqueous solution [49,50]. On the other hand, cell design is also required to be capable of reducing the loss of photon energy in the reaction media and thus to increase the light intensity reaching on photocatalysts surface [51,52]. Another rational strategy for device engineering is applying potential bias into the system [53–55]. Applying potential bias can effectively facilitate the separation of photogenerated electron/hole pairs, which enables them to react with organic compounds in solution synergistically.

3. Photocatalyst engineering

3.1. Morphology fabrication

TiO_2-based photocatalysts are generally fabricated with nanostructured morphologies to maintain high efficiency in PC and PEC devices. The nanostructured TiO_2 photocatalysts facilitate the separation of photoelectrons and holes via shortening diffusion distance and maximize light absorption via light scattering and consequently improve the PC efficiency [56–58]. Many factors have significant influences on the PC performance of TiO_2 electrodes, including the size, specific surface area, pore-volume, crystalline phase, and exposed surface facets. Various morphologies of nanostructured TiO_2 electrodes have been studied to optimize the PC performance of photocatalyst. The zero, one, two, and three-dimensional (0D, 1D, 2D, and 3D) nanostructures of TiO_2 have different properties due to their sizes, shapes, and light absorption efficiency.

As the photocatalyst, the film of nanoparticles may provide a wide specific area and sufficient irradiation path length to facilitate light harvest and reduce the length of charging diffusion. Nevertheless, the nanoparticles are separated and not connected, which obstructs the transfer of photo-charge to the conductive substrate through inter-particles. Instead of guiding the PC reaction, this method increases the recombination rate of charge carriers at the inter-particle boundary. For single-crystalline nanostructures, the 1D structures, i.e., nanorod, nanorod arrays, or nanotube arrays, may provide a direct route along the longitudinal direction and shorten the diffusion duration of the charge. The 2D nanofilms can provide a large surface area of highly efficient facets, as well as shorten the length of charge diffusion. The 3D ordered nanostructures have specific properties for improving PC performance [33].

3.1.1. TiO₂ nanorods-based nanostructure

The 1D TiO_2 nanostructures (e.g., nanorod arrays [59,60], branched nanorods [61,62], and nanotube arrays [63,64]) show superior PC performance due to the fast electron transport to back-contact via 1D direct pathways (Fig. 4). This property leads to improved charge separation when compared with the particulate electrode [65]. The nanorod/nanowire structures synthesized by various methods, such as hydrothermal [66–68], template [69], electrospinning [70], CVD [71], and PVD [72]. These are typical synthesis methods for 1D structures TiO_2 photocatalysts, which are widely used in PC devices. However, the TiO_2 nanoparticle electrodes still have larger surface areas to absorb light irradiation. In order to address this problem, one possible solution is to design the branched TiO_2 nanorod electrodes. Cho et al. [65] studied the comparison of TiO_2 nanoparticles, nanorods, and branched-nanorods. The research indicated that the branched arrays had better charge transport and light absorption properties than TiO_2 nanoparticle films and larger surface areas for more efficient carrier collec-

tion. These ultrathin branched TiO_2 nanorods were very active in the light harvest, and transporting charge carries with enhanced surface-to-volume ratios. To further improve PC performance, various nanostructures have been designed and synthesized based on TiO_2 nanorods [61,73]. The TiO_2 nanorods@nanobowls arrays synthesized by Wang et al. took the advantages of nanorods and 3D nanobowls. This TiO_2 nanorods@nanobowls array photocatalyst, made of rutile TiO_2 nanorods grown on the inner surface of arrayed anatase TiO_2 nanobowls, was designed and successfully fabricated for high efficient water splitting [61]. The nano-structure of nanobowls had a superior light-scattering ability, which considerably increased the light-harvesting of the photocatalyst. Also, the TiO_2 nanorods are almost radially aligned on the inner surface of the TiO_2 nanobowls, providing increased photoanode/electrolyte contact area offering fast hole transportation pathways. The TiO_2 nanorods@nanobowls nanostructures increased light scattering ability, had a faster transfer of photogenerated holes, and facilitated charge separation to improve PC efficiency.

3.1.2. TiO₂ nanotubes-based nanostructure

The TiO_2 nanotubes are also attractive as photocatalysts for PC devices due to their aligned porosity, crystallinity, and self-orientated nanotubular morphology (Fig. 5). These characteristics subsequently result in a highly ordered TiO_2 nanotube array morphology [78]. The TiO_2 nanotubes shorten carrier diffusion paths significantly along their walls to minimize the loss of charge carriers. The most common methods for synthesizing TiO_2 nanotubes are template [79–81], hydrothermal [82,83], and anodic self-organization approaches [84,85]. Electrochemical anodization of Ti foil is a powerful and simple tool to synthesize the TiO_2 nanotubes in many reports [86–88], and it has been widely applied in various PC applications [89]. Anodization is typically conducted in an electrolyte containing hydrogen fluoride (HF)-based aqueous solution. Following the anodization process with a constant voltage between the Ti electrode and counter electrode, TiO_2 nanotube arrays are formed on the foil surface and have straight channels against the foil. The size of the tubular channel could be controlled by the anodization potential [90]. Besides, hierarchical TiO_2 nanostructures with two or more different pore-size layers can also be constructed by multi-step electrochemical anodization [91]. Also, the vertically aligned titanate nanotubes could directly grow on a Ti foil substrate via a vapour phase hydrothermal method with the ammonia vapour in the reactors [92]. The growth of TiO_2 nanotubes is related to two steps mechanism: the formation and the rolling up of nanosheets to form nanotubes. The superior performance of these TiO_2 nanotube arrays photocatalysts can be attributed to characteristics of the morphology, which could increase the density of photogenerated electron carriers and improve the transportation and separation of electron-hole pairs.

3.1.3. Porous TiO₂ films

Porous TiO_2 films are used in numerous PC devices because the porous structure allows excellent accessibility to the reaction sites in combination with the interconnected network [94–97]. However, the high photoelectron-hole recombination rate at grain boundaries in the nanocrystalline TiO_2 films could reduce the PC performance [98–100]. To fulfill the advantages of the porous structure, Crossland et al. [101] reported a micron-sized porous anatase single crystals synthesized by the bottom-up seeded template method. They found that the porous anatase single crystals significantly reduced the grain boundaries and maintained a maximum porous structure surface area [101]. Combining the remarkable electron mobility in a single crystal TiO_2 and large surface area of porous structured TiO_2, mesoporous single crys-
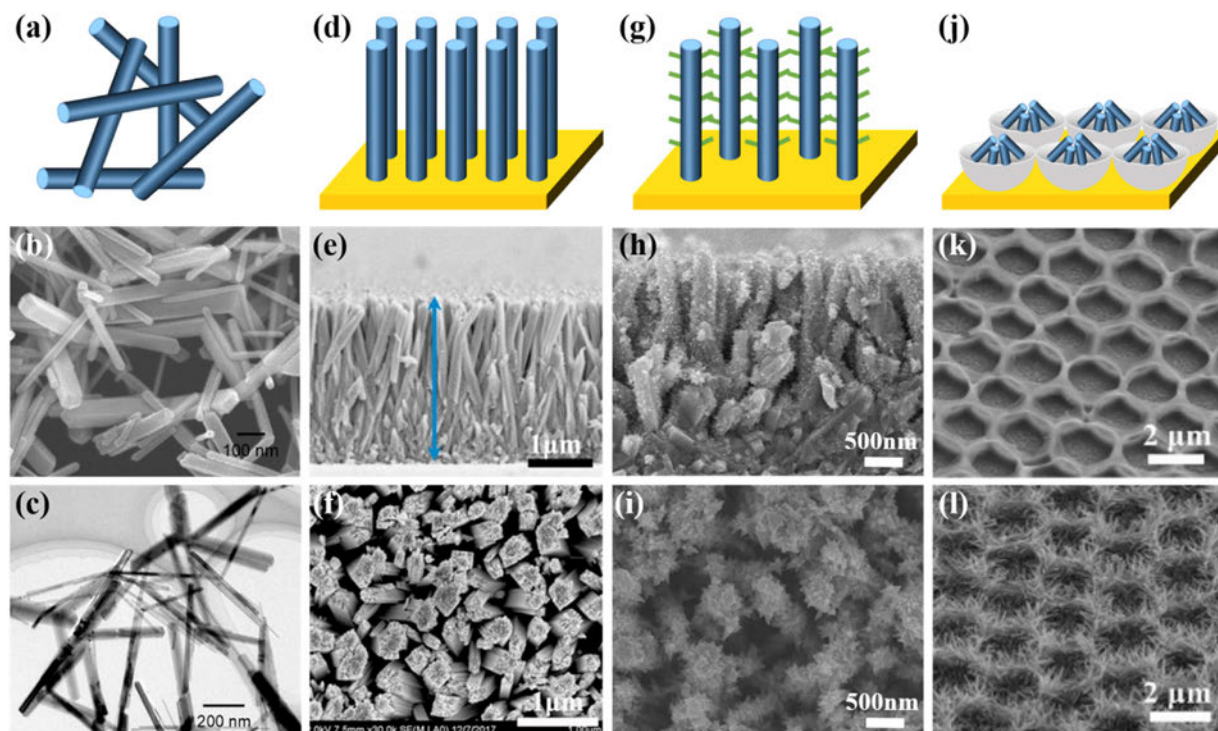
Fig. 4. Schematic description and corresponding SEM/TEM images of (a-c) TiO_2 nanorods, (d-f) TiO_2 nanorod arrays, (g-i) branched TiO_2 nanorod arrays and (j-l) TiO_2 nanorod@nanobowls. (e,h) represent the cross-sectional view, (b,f,i,l) represents the top view. (k) SEM images of TiO_2 nanobowls. (Derived from Ref. [74–77]).
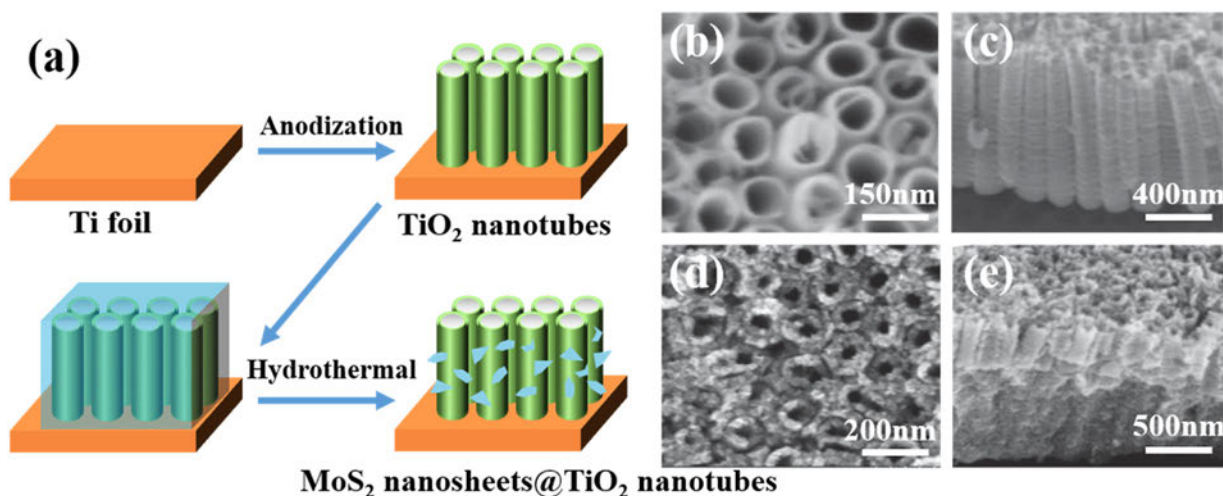

Fig. 5. (a) Schematic illustration of the preparation process of TiO_2 nanotubes and MoS_2 nanosheets@TiO_2 nanotubes. The top view and the cross-sectional view of the SEM images of (b,c) TiO_2 nanotubes and (d,e) MoS_2 nanosheets@TiO_2 nanotubes. (Derived from Ref. [93]).

tals of rutile TiO_2 demonstrated the enhancement of PC activities [102–104]. Porous structured TiO_2 films can also offer a way to develop unique functionalities, such as photonic effects, in controllable interactions with light. Zhang et al. [105] designed a bi-layer structure photocatalyst constructed by fabricating a porous TiO_2 layer through a template-assisted sol-gel process on a TiO_2 nanorod array layer (see Fig. 6). By alternating the characteristic pore size, the porous TiO_2 layer could induce a slow photon effect at the red edge of the photonic bandgap, which was purposely tuned to enhance localized surface plasmon resonance of Au nanoparticles leading to the generation of more hot electrons.

3.2. Band-gap modification

3.2.1. Heterostructure

An efficient technique to improve the PC and PEC sustainability of TiO_2 is to pair the photocatalyst with a semiconductor to create a heterostructure with a smaller band-gap [106–108]. The enhancement of PC activities through a heterostructured semiconductor can be due to two reasons. Firstly, the heterojunction can impede the recombination of photogenerated electrons and holes because the oxidation reaction and reduction reaction happen separately at two different places on the photocatalyst. Secondly, the coupling semiconductor can expand the light absorption range by coupling suitable structures. There are three different forms of heterostructures based on the mechanisms of charge carriers
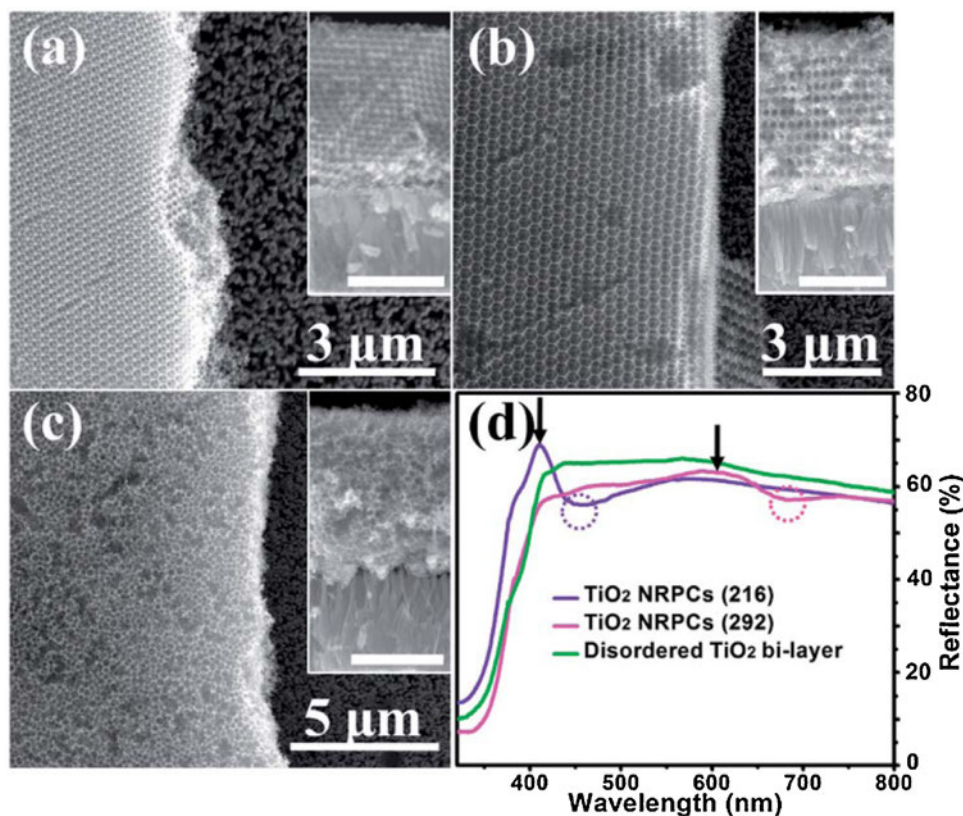
Fig. 6. Top view and a corresponding cross-sectional view (inserted) SEM images of different pore sizes of (a) TiO_2 nanorod photonic crystals (216), (b) TiO_2 nanorod photonic crystals (292), and (c) disordered TiO_2 bi-layer. (d) UV–vis diffused reflectance spectra of the three TiO_2 films on the FTO substrate. Scale bars of all inserts in (a), (b), and (c) are 2 mm [105].
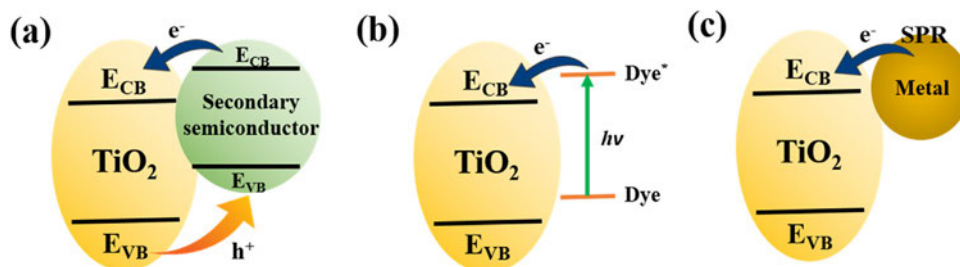

Fig. 7. Schematic picture of heterostructures of (a) conventional charge-carrier transfer, (b) dye-sensitized transfer, and (c) SPR metal transfer for TiO_2-based photocatalyst.

Table 1
The TiO_2–based PC/PEC application with different heterostructure formation.

Photocatalyst	Heterostructure formation	PC/PEC application	Performance	Ref.
Ag_3PO_4/TiO_2	conventional	MO degradation, visible light ($\lambda > 500$ nm)	MO degradation rate: 95.5 % after 60min	[136]
porous $ZrO_2@TiO_2$	conventional	HER, UV light	H_2 evolution rate: 39.7 mmol/h/g	[137]
$TiO_2/ZnFe_2O_4$	Z-scheme	N_2 photofixation, visible light	ammonia generation rate: 1.48 μmol/L/min	[138]
TiO_2/CdS	Z-scheme	HER, UV light	H_2 evolution rate: 51.4 μmol/h	[139]
E-$TiO_2/Au/TiO_2$	SPR	HER, visible light	H_2 evolution rate: 26.25 μmol/h/g	[140]
Ag-loaded TiO_2 nanotube arrays	SPR	CO_2 reduction, visible light	CH_4 production rate: 48 mmol/h/m^2	[141]

movement, conventional charge-carrier transfer, dye-sensitized transfer, and Surface plasmonic Resonance (SPR) plasmonic metal transfer (Fig. 7). Table 1 shows the TiO2–based PC/PEC application with different heterostructure formation.

Heterostructures based on conventional load-carrier transfers and plasmonic metal coupling were more commonly explored of these mechanisms. Photoelectrons and photoholes can be moved easily from one semiconductor with a higher minimum E_{CB} (lower maximum E_{VB}) to another with a lower minimum E_{CB} (higher max-

imum E_{VB}) in conventional charge-carrier transfer mechanisms (Fig. 7a). It reduces the possibility of electrons and holes to recombine by maintaining processes of reduction and oxidation in various areas. The mixed-phase photocatalysts of anatase/rutile TiO_2 show better PC output as compared to the single-phase TiO_2. Experimental studies demonstrated that the mechanism of enhancement was because the anatase E_{CB} was ∼0.2 eV above that of rutile. This results in the rapid transfer of photo-generated electrons from anatase to rutile, and holes from rutile to anatase [109]. There are

16

several studies in the literature support this conclusion [110,111]. A theoretical and experimental study indicated that the electron affinity of anatase is higher than that of rutile, and therefore the photo-generated electrons flew from rutile to anatase with a band alignment of ~0.4 eV [112]. Although the mechanisms of charge transfer between anatase and rutile TiO_2 are controversial in the literature [110–113], it is commonly agreed that PC performance at mixed anatase/rutile phases is significantly enhanced via the augmented charge separation efficiency at the heterojunction.

The band structure alignment at interfaces in traditional heterostructured photocatalysts is also crucial in extracting photo-generated electrons and transporting them to the conducting substrates. It is generally established that the transfer of electrons to TiO_2 from the coupled semiconductors with higher E_{CB} (such as CdS [114,115], C_3N_4 [116,117], CdSe [118,119]) leads to fast charge separation. The most commonly used second semiconductor to modify the TiO_2 photocatalyst for PC applications is the CdS. Coupling CdS with TiO_2 broadens the light absorption range of visible light and improves the separation rate of photogenerated charge carriers [120,121]. In the past few years, researches on this system have become more popular, mainly due to the exponentially rapid development of CdS quantum dots (QDs) and nanosized TiO_2 with varied morphologies. For example, Wang et al. prepared CdS QDs on the vertically aligned TiO_2 nanorods photocatalyst to form a type II heterojunction and investigated its PC properties [122]. The photocatalysts had a photocurrent density of 5.778 mA/cm^2 at a potential of 0 V versus Ag/AgCl, which has an IPCE (Incident Photon to Converted Electron) of about 20 % in the visible light region from 400 to 500 nm. An et al. [123] investigated the influence of intrinsic defects on the interfacial charge transfer between TiO_2 and $BiVO_4$ to form defect-mediated heterostructured photocatalysts. The defects in TiO_2, such as Ti^{3+} and oxygen vacancies, were formed by foreign $BiVO_4$ nuclei on the surface of TiO_2. The experimental results and theoretical calculation demonstrated that the photo-generated electrons in the conduction band of $BiVO_4$ could be transferred to the TiO_2 surface in the presence of oxygen vacancies. The electrons are localized at the TiO_2 defective sites and undergo secondary excitation and transfer to the conductor substrate.

In the dye-sensitized TiO_2 photocatalyst, the dye, as a sensitizer, takes over the role of absorbing and converting visible light energy into chemical energy (see Fig. 7b). To date, most studies of dye-sensitized photoanodes have employed [Ru(bpy)$_3$]$^{2+}$ derivatives or high potential porphyrins, which have been extensively studied in dye-sensitized solar cells (DSSC) [124–126]. Because the excited state redox potential of dyes is comparatively lower than that of oxidizing water, dye-sensitized TiO_2 is considered a promising photoanode for PC water splitting. Youngblood et al. [127,128] demonstrated the dye-sensitized PC cell for water splitting, which employed heteroleptic ruthenium dye as the sensitizer and IrO_2 as the co-catalyst on the TiO_2 photoanode. This PC cell can split water into hydrogen and oxygen under visible light with a small bias potential but has low quantum efficiency due to slow electron transfer. Li et al. [129] designed a dye-sensitized tandem PC cell for water splitting without applied bias potential (see Fig. 8). The cell is comprised of an organic dye (4-(diphenylamino) phenyl-cyanoacrylic acid), sensitized mesoporous TiO_2 photoanode, and another organic dye (4-(Bis-[4-[5-(2,2-dicyano-vinyl)-thiophene-2-yl]-phenyl]-amino)-benzoic acid) sensitized nanostructured NiO photocathode. The tandem PC cell can split water by visible light with IPCE of 25 % at 380 nm under neutral pH conditions without bias. However, the stability and electron back transfer from TiO_2 to dye are unsatisfying and require the development of photosensitizers with better stability and a more suitable band position.

Noble metals can be used to broaden the light absorption range of TiO_2. The most effective and widely used noble metals are

Pt, Au, Ag, and Pd. All these four noble metals can be used as co-catalysts to assist and enhance TiO_2-based PC and PEC performance, while Au and Ag possess a unique mechanism responsible for such an action, which is the SPR effect. SPR is known as the resonance energy generated when the incident light photon frequency matches the frequency of the conductive electrons confined to the metal nanoparticles' surface volume (Fig. 7c). Two main processes are involved in a typical plasmonic enhancement of photocatalysis under visible illumination, charge transfer, and local electric field enhancement. In the charge transfer process, the plasmon resonance excites electrons in the deposited metal particles; these electrons are then transferred to the conduction band of the adjacent TiO_2 [130,131]. The irradiated metal nanoparticles can generate intense local electric fields near the surface of the nanoparticles based on this SPR effect. This local plasmonic hot spots region on deposited nanoparticles can induce an increased generation rate (up to 1000 x) of electron-hole pairs in TiO_2 [132]. Pu et al. [133] prepared the photocatalyst by depositing Au nanoparticles (NPs), Au nanorods (NRs), and a mixture of Au NPs and NRs on the surface of TiO_2 nanowire arrays to investigate the SPR effect of the different shapes of decorated Au. The finite difference time domain (FDTD) simulation outcomes indicated that the increased electric-field intensity at decorated- Au NPs and NRs result in the improvement of PC performance of Au NPs and NRs decorated-TiO_2 photocatalysts. This study supported the idea that the electrical field amplification effect causes photoactivity enhancement in the visible region for Au nanostructure-decorated TiO_2 samples. Zhan et al. [134] reported that the PC performance of the Au embedded in the TiO_2 (Au-in-TiO_2) electrode was superior to that of the Au sitting on the TiO_2 (Au-on-TiO_2) electrode. This phenomenon indicated that the intense local electric field in the proximate semiconductor surrounding plasmonic nanoparticles helps to generate electron − hole pairs. In recent studies examining the dominant enhancement mechanisms in different plasmonic configurations, Au nanoparticles and Al_2O_3 were coated on the anodic TiO_2 nanotubes with different deposition orders (see Fig. 9a) [135]. The FDTD results indicated that the proposed near-field electromagnetic enhancement mechanism hardly contributed to the PC performance because of the thin Al_2O_3 spacer layer (see Fig. 9b). Therefore, the plasmon resonance energy transfer in the presence of a thin non-conductive spacer is predominantly governed by SPR-mediated hot-electron injection rather than near-field electromagnetic enhancement.

3.2.2. Doping

Considering the band gap of pristine TiO_2 is higher than 3.0 eV, as shown in Fig. 10a, pristine TiO_2-based photocatalytic reaction can only be stimulated by UV irradiation, which makes up less than 0.5 % of total solar radiation [142]. Doping can modify the electronic band structure of TiO_2 by introducing foreign atoms into the pristine crystal lattice. The resulting improvement in light-harvesting bestows TiO_2 the ability to harness more visible light and extend the PC application to the visible light range [143–145]. The main functions of doping modification for engineering the band-gap can be concluded into two parts. Firstly, additional local states are inserted to shorten the band-gap and therefore allow the absorption of longer wavelength light and the generation of photoelectron-hole pairs (see Fig. 10b). Secondly, the band-gap narrowing can be achieved by the shift of the E_{CB} band edge to a lower band edge and the shift of E_{VB} to a higher band edge (see Fig. 10c). Since N-doped TiO_2 ($TiO_{2-x}N_x$) revealed band gap narrowing and visible photoactivity, the doping of TiO_2 has been intensively investigated with metal substances and non-metal substances [146]. Table 2 exhibits the performance of TiO2-based PC/PEC applications using different doping elements.
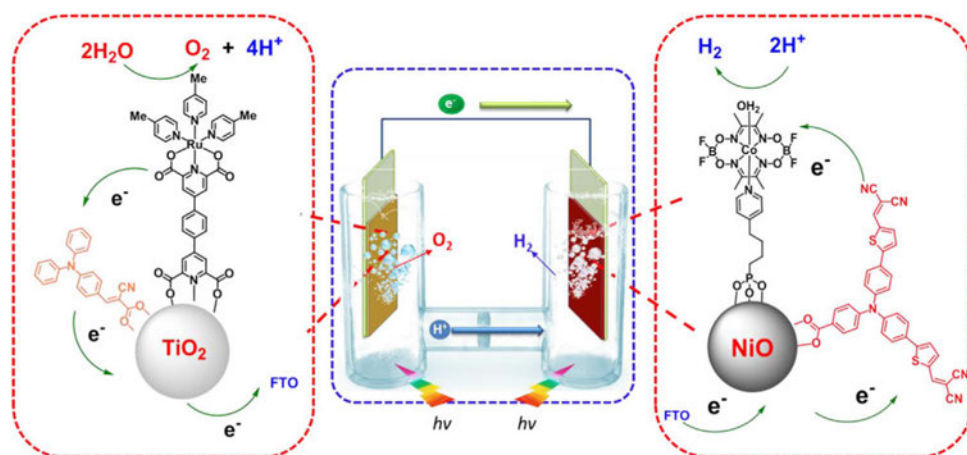
Fig. 8. Scheme of self-driven dye-sensitized tandem PC cell for water splitting [129].
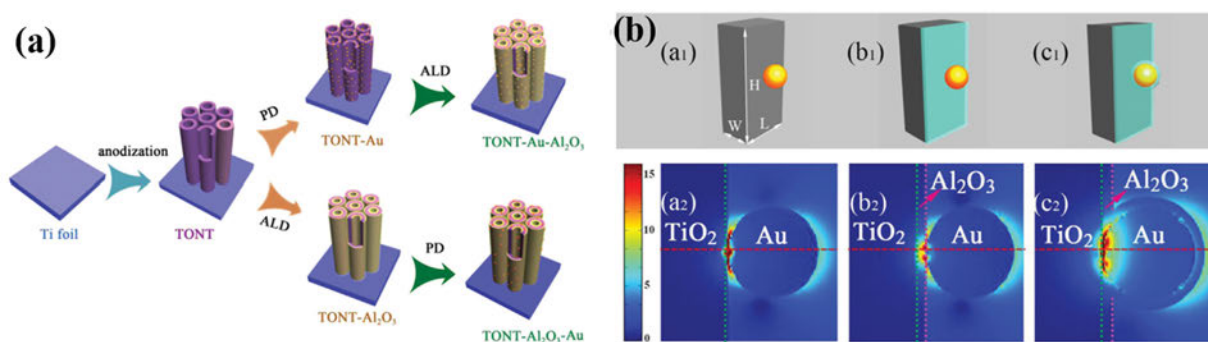

Fig. 9. Schematic procedure for fabricating the five different samples: (a) TiO_2 nanotubes, TiO_2 nanotubes-Al_2O_3, TiO_2 nanotubes-Au, TiO_2 nanotubes-Au-Al_2O_3, and TiO_2 nanotubes-Al_2O_3-Au; (b) the simplified schematic structures of (a1) TiO_2 nanotubes-Au, (b1) TiO_2 nanotubes-Al_2O_3-Au, and (c1) TiO_2 nanotubes-Au-Al_2O_3 and (a2–c2) the finite difference time domain (FDTD) simulation of the corresponding spatial distribution of electric field density ($|E|$) on the *y*-plane for the three structures under 570 nm incident light irradiation [135].
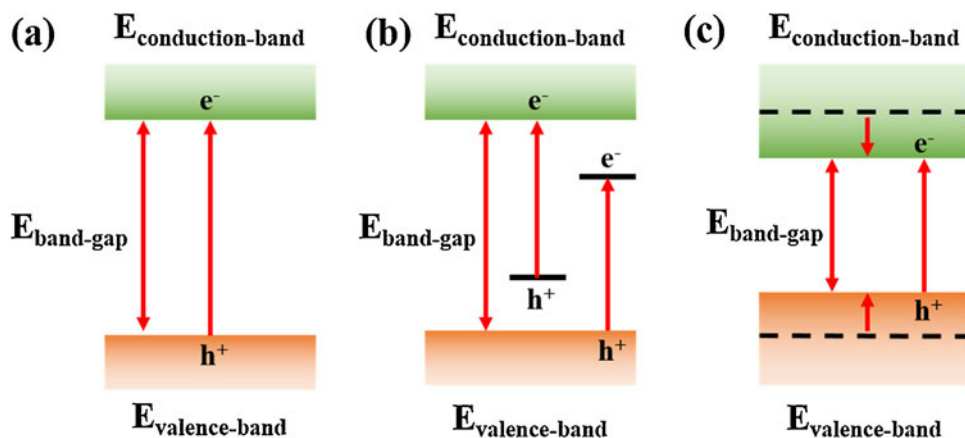

Fig. 10. Scheme for a possible influence of electronic band structure at doped TiO_2; (a) standard band-gap in pristine TiO_2, (b) insertion of local states within the band-gap in a doped TiO_2, (c) band-gap narrowing in a doped TiO_2.

3.2.2.1. Metal doping. Since the E_{CB}'s minimum TiO_2 incorporates Ti *d* states, it can be noticed that metals are promising doping elements for Ti to reduce the energy levels of *d* states to close the distance between bands. Decreasing the TiO_2 band-gap energy and thus expanding the spectrum of light absorption make it more convenient for water treatment and hydrogen generation. Large amounts of metals (such as Fe [147,148], Zn [149–151], Mn [152,153], Ni [154–156]) have been investigated because of its unique d electronic property [157,158].

Earlier theoretical studies analyzed the electronic structures of TiO_2 doped with 3d transition metals (V, Cr, Mn, Fe, Co, and Ni) by ab initio band calculations based on the density functional theory (DFT) using the full potential linearized-augmented-plane-wave method [159]. The metal doping of TiO_2 induced a redshift in the bandgap transition or the appearance of new visible light absorption. Based on the density of states (DOS) of doped TiO_2 (see Fig. 11a), the 3d metal doping created an occupied level in the band-gap or VB. Consequently, the dopant t_{2g} level in the

18

Table 2
The TiO_2–based PC/PEC application with different doping elements.

| Photocatalyst	Doping elements	PC/PEC application	Performance	Ref.
Pt-TiO_2	metal	HER, near-UV light	H_2 evolution rate: 0.116 μmol/h/cm^3	[194]
Fe-TiO_2	metal	MB degradation, visible light	MB degradation rate: 75 % after 90 min	[195]
Cu-TiO_2	metal	antimicrobial, visible light	E-coli degradation rate: 99.9999% after 30 min	[196]
N-TiO_2	non-metal	MO degradation, visible light	MO degradation rate: 65 % after 60 min	[197]
S-TiO_2	non-metal	Acetaldehyde degradation, visible light	Acetaldehyde degradation rate: 75 % after 300 min	[198]
black C-TiO_2	non-metal	MB degradation, UV and visible light	MB degradation rate: 97 % after 120 min under UV light; 74 % after 120 min under visible light	[45]
Pd-H-TiO_2 nanofibers	self-doping & metal	HER, UV light	H_2 evolution rate: 17 mmol/h/g under UV-A irradiation; ~25.6 mmol/h/g under UV-B irradiation	[199]
H-TiO_2/MoS_2	self-doping	HER, visible light	H_2 evolution rate: 1840 mmol/h/m^2	[200]
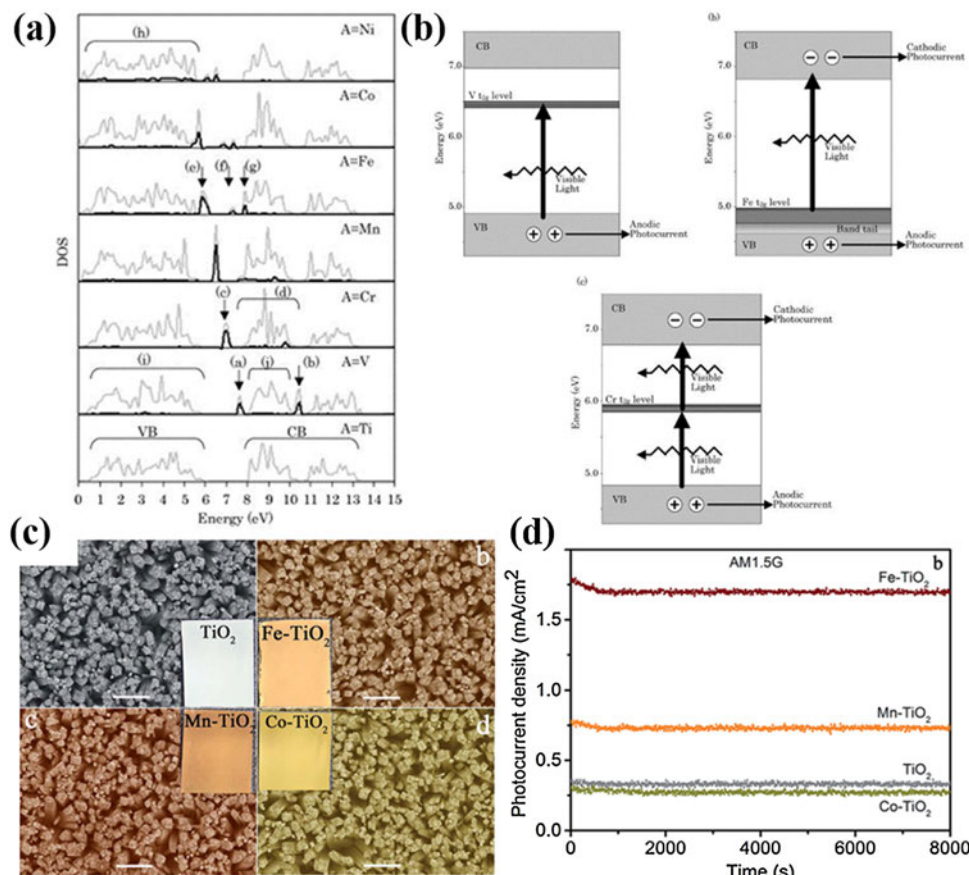
Fig. 11. (a) The DOS calculation results of the metal-doped TiO_2 ($Ti_{1-x}A_xO_2$: A=V, Cr, Mn, Fe, Co, or Ni). Gray solid lines: total DOS; solid black lines: dopant's DOS; (b) scheme of the electronic band structure of doped TiO_2 from DOS results [159]; (c) SEM images of i. TiO_2, ii. Fe–TiO_2, iii. Mn–TiO_2 and ix. Co-TiO_2 nanorod arrays on FTO substrates. Inserts are the corresponding digital pictures, respectively. All scale bars represent 1 mm. Photocurrent densities vs. time of the Fe-doped TiO_2, Mn-doped TiO_2, Co-doped TiO_2, and TiO_2 nanorods measured at 0.5 V vs. RHE under 100 mW cm^{-2} solar illumination; (d) photocurrent density profile of as-prepared photocatalysts [160].

band-gap has been identified as a vital role in the visible light responses of TiO_2. Photoexcitation occurs for the V$^-$, Cr$^-$, Mn$^-$ and Fe-doped TiO_2 via the t_{2g} level of the dopant (see Fig. 11b). Recently, Wang et al. reported a significant improvement of the PC water splitting activity under visible light irradiation based on Fe$^-$, Co$^-$ and Mn-doped TiO_2 nanorod array photocatalysts [160]. All absorption of metal-doped TiO_2 revealed noticeable redshifts (see Fig. 11c), which contributes to the significant enhancement of PC performance. The photocurrent profiles showed that Fe doping is the most effective route to enhance the photoactivity of TiO_2 (Fig. 11d).

Rare-earth metals with lanthanide-doped TiO_2 nanotubes have been investigated and reported by Nie et al. [161]. The doped nanotube arrays showed a significant enhancement in their

PC properties compared with undoped nanotubes. The maximum photo-conversion efficiency was 0.598 %, which was twice that of the undoped one (0.257 %) under the same supporting electrolyte solution. PC degradation of p-nitrophenol (PNP) was used to investigate the PC activities of the as-prepared electrode. The La-doped TiO_2 nanotube array electrode showed much higher degradation efficiencies (99.33 %) than the undoped TiO_2 nanotube array electrode (70.16 %) under the same conditions.

3.2.2.2. Non-metal doping. Non-metal doping is similar to the metal doping of TiO_2. In recent years, non-metals (N, F, S, C, P) have been applied in doping TiO_2 for enhanced visible-light photocatalytic performance [158,162–165]. The non-metal dop-

ing commonly involves a band-gap narrowing and a corresponding redshift of light-harvesting by tuning the E_{VB} in TiO_2. Asahi et al. [146] investigated the N-doped TiO_2 photocatalyst used for hydrogen generation with a total conversion efficiency of 11 % at 0.3 V bias potential under visible light [166]. The N-doped TiO_2 can also be prepared via wet chemistry by treating the TiO_2 with a guanidine carbonate aqueous solution [167,168]. After calcinating for one hour at a high temperature, it was found that the N-doped TiO_2 displayed a noticeable shift of absorption edge towards the visible light region compared to the undoped TiO_2 nanotubes. Horikawa et al. [169] also obtained similar results for their as-synthesized N-doped TiO_2 leading to improved PC performance. Similar results for N-doped TiO_2 have also been reported by Abdelhaleem et al. [170], Yan et al. [171], and Chen et al. [172].

Following the breakthrough mentioned above of N-doping TiO_2 catalysts, non-metal doping has been intensively investigated in TiO_2 photocatalysts. Doping TiO_2 with carbon is a well-investigated doping mechanism. It is essentially the same as nitrogen doping, but using carbon as a replacement. Another widely used element for doping TiO_2 is sulfur. While sulfur is abundant and exchanges with oxygen, instead of sitting in between the lattice structure, it has shown evidence of improved light absorption of TiO_2.

3.2.2.3. Self-doping. In TiO_2, the role of concomitant intrinsic point defects, such as oxygen defects, Ti defects, Ti^{3+}, and Ti^{4+} interstitials) can be considered as doping elements. Therefore, these defects could affect the electronic structure of TiO_2, resulting in visible light absorption [173,174]. In 2004, Sekiya et al. [175]. systematically investigated the effects of calcination conditions (under oxygen or hydrogen atmosphere) on the reversible color-transformation of single-crystal anatase TiO_2 from colorless, pale blue, dark blue, dark green to yellow. The optical absorption spectra showed an additional shoulder absorption band in the visible-light range and a tail absorption band in the near-infrared and infrared region, indicating that the color-changes of TiO_2 are due to oxygen vacancy.

In 2011, Chen et al. [176] successfully synthesized the "black TiO_2", which is also known as reduced TiO_2 or hydrogenated TiO_2 (H-TiO_2), at 20 bar hydrogen atmosphere. The hydrogenated photocatalysts can absorb the visible and near-infrared irradiation, which is attributed to the surface disordered layer model. The main mechanism of the phenomenon is that on-lattice disorder in hydrogenated TiO_2 nanocrystals upshifts the valence band edge. The "black TiO_2" can more efficiently absorb solar light to improve the performance of photocatalytic water splitting. Because of the high solar energy absorption and enhanced PC activity of H-TiO_2, enormous efforts have been made in this photocatalyst [177–179]. Different strategies were investigated and developed in synthesizing H-TiO_2 photocatalysts, such as high-pressure hydrogen treatment [143,180], H_2-N_2 treatment [181], H_2-Ar treatment [182,183], plasma treatment [184,185], $NaBH_4$ reduction [186], and electrochemical reduction-anodization [187]. The H-TiO_2 were widely utilized in different variations of PC and PEC applications, including water splitting, CO_2 reduction, and degradation of organics [188–190]. Wang et al. [191] fabricated the H-TiO_2 rutile nanowires and anatase nanotubes for PEC water splitting. The IPCE analysis exhibited that the optimized STH efficiency for H-TiO_2 was 1.1 % under a standard AM 1.5 G solar spectrum. Wang et al. [192] developed the porous black TiO_2 film for the reduction of CO_2. Due to the existence of defect states (Ti^{3+} and oxygen vacancies) in black TiO_2, the production of CO and CH_4 were hundred times higher as compared to Degussa P25. Lin et al. [193] investigated a series of non-metal incorporated black TiO_2 for the photodegradation of methyl orange and H_2 generation. The superior performance of this photocatalysts was attributed to the

unique electronic band gap structure of Ti 3d states originated from hydrogen plasmonic treatment and chemical reduction process.

3.3. Co-catalysts

Coupling with semiconductor photocatalyst and the formation of a co-catalyst is very useful in improving the hydrogen evolution rate from water splitting by PC devices, in which the reduction reaction sites (e.g., H_2 evolution sites) are on the cathodes, while the oxidation reaction sites (e.g., O_2 evolution sites) are on the anode. At TiO_2, the water oxidation by the photo-generated holes is kinetically inefficient, and therefore the slow water oxidation rate aggravates a large number of holes on the TiO_2 surface leading to significant recombination (see Eq. 1). The presence of oxygen evolution catalysts (OECs) as co-catalysts on photoanodes can enhance PC efficiency and reduce the reaction energy barrier resulting in a negative shift of onset potential [201,202].

To date, the most widely used co-catalysts usually possess metals with variable valence states, such as iridium oxide, ruthenium oxide, cobalt phosphate, and cobalt oxide [203]. One of the most popular water oxidation catalysts is the cobalt-phosphate (Co-Pi) catalyst, invented by Nocera et al. in 2008 [204,205]. It has been rapidly applied to enhance the PC performance of semiconductor photocatalysts, such as TiO_2, Fe_2O_3, ZnO, and $BiVO_4$, due to its abundant reserves, self-healing features and functionality under benign conditions [204,205]. Ai et al. demonstrated that Co-Pi modified TiO_2 electrodes resulted in a generally enhanced photocurrent near the flat band potential region and a 2.3x photo-conversion efficiency improvement compared to pristine TiO_2 in the neutral electrolyte [206]. It was suggested that the mechanism responsible involved the Co-Pi catalyst facilitating the pathway of oxygen production and inducing band bending to decrease the charge recombination.

Recently, Sambur et al. [207] used single-molecule fluorescence microscopy to nanometre-scale map the surface PC reaction of photo-generated electrons and holes on a single TiO_2 nanorod. The measurement observation and following analysis revealed that ḧotspotsön the TiO_2 surface were the most important sites for both water oxidation reactions and unwanted charge-carrier recombinations. To investigate the OEC behaviour, they selectively deposited the cobalt-borate (Co-Bi) co-catalyst on high- or low-active sites based on the photocurrent results. Unexpectedly, the results indicated that the Co-Bi deposited on low-active sites enhanced PC water oxidation more significantly compared to the high-active sites. This conclusion could pave the way for maximizing PC efficiency via OEC deposition on TiO_2, as the excess OEC material on the surface can hinder light absorption [208]. Overall, co-catalysts are very promising for the energy conversion of solar light when addressing the technical problems and high-cost issues in up-scaled production.

4. Device engineering

In a traditional PC or PEC system, particularly slurry systems, the performance of the PC system is compromised by a significant loss of light energy in aqueous solution and a slower transfer of mass, which significantly restricts the sustainability of PC and PEC technologies. Such problems need to be resolved in the structure and design of the PC or PEC system. The design of the cell is to combine all components with improving the performance of the PC or PEC system. Well-designed PC or PEC devices may facilitate photocatalytic efficiency by suppressing energy loss by light irradiation and enabling mass transfer in aqueous electrolytes. Therein, the

cell design can be discussed from three aspects: irradiation source, reactor structure, and applied potential bias.

4.1. Irradiation source

Generally, mercury light, halogen lamp, and xenon lamps are widely utilized in the PEC devices. Mercury lamps can produce UV-light with a significant amount of heat through the electric arc and vaporized mercury. The applied mercury lamp generally produces a line spectrum at 365 nm (UV-A) and 250 nm (UV-C), which can be effectively absorbed in TiO$_2$ photocatalyst. It works with good energy efficiency and excellent stability. However, it requires a constant-voltage source and an electric ballast to limit the current through it and a cooling system to reduce the produced heat. The halogen lamp is a promising irradiation source for PC, which could produce a continuous spectrum of illumination from UV (300 nm) to the infrared region (2500 nm), and this incandescent lamp is often applied as visible light sources in PC devices. The xenon lamp can also emit a reasonably continuous spectrum from UV to the infrared range (e.g., 300–2500 nm) with high light intensity. In many cases, the xenon lamp is ideal for simulations of solar light with proper filters (air mass 1.5 G).

For practical application (i.e., large-scale application), it is attractive in using solar irradiations to minimize energy usage and operating cost. Unfortunately, the solar irradiation is unstable and highly depended on the weather and climate. The TiO$_2$ photocatalysts can only utilize UV irradiation, which only possesses c.a. 4% of solar light [209,210]. Although the solar energy will emerge as an alternative cost-effective light source, the artificial UV light with high light intensity is more competitive than the solar light, mainly employed on PC degradation and PC sensors.

However, the volume of the tube-type light source is relatively large, so that it cannot meet the requirements of various PEC devices. The UV light-emitting diode (LED) has been introduced as a promising alternative light source due to its high flexibility in configuration. Since the UV-LEDs are easily adjustable, they are usually used in the thin-layer PC cells for irradiation [211]. Besides, another advantage of UV-LEDs is that they generate lesser heat than traditional UV lamps during PC reaction, which minimizes the influence of temperature on the PC experiment and prevents the waste of massive unnecessary heat generation [212]. Furthermore, the stable monochromatic property of UV-LEDs enables them are suitable in PC sensing applications [66]. Considering the price of UV-LED continuously dropping [213], it is predictable that UV-LEDs are not confined in a lab-scale PC application, some UV-LED-based products such as LED array [214] and LED panel [215] are also promising irradiation sources for scaling up PC devices.

4.2. Reactor structure

4.2.1. PC system

Various types of TiO$_2$ PC devices have been designed, ranging from different shapes (simple batch, continuous flow cell, thin-layer, and cylindrical cells), difference scales (e.g., from lab scale to pilot scale), and different electrochemical systems (from two-electrode system to three-electrode system). PC batch cell reactor is most often used to evaluate and characterize the performance of photocatalysts in degrading organic compounds, being simple and low cost. However, this PC batch cells are incapable of processing pollutants in a large scale owing to the non-continuous operation and low efficiency that results from strong light absorption by aqueous solution and insufficient mass transfer of the organic pollutants. As shown in Fig. 12, three strategies, including back-illumination, thin layer, and cylindrical PC cells, are proposed to address these problems [216]. However, for the back-illumination shown in Fig. 12a, a significant amount of light, especially UV

light, are absorbed by the glass substrate, the conducting substrate such as Indium doped tin oxide (ITO) and Florine doped tin oxide (FTO) and TiO$_2$ layer, causing the light energy loses before the light reaches the surfaces of the electrodes. Therefore, the other two designs, i.e., the thin-layer (Fig. 12b) and cylindrical PC reactors (Fig. 12c), are the most often adopted in real practice.

Firstly, for the thin-layer PC reactor, the decreased thickness of the liquid layer could reduce the light losses and increase the mass transfer to improve the PC degradation rate and PC efficiency. Based on Beer's Law, the light energy can be absorbed in aqueous solution (Eq. (8)).

$$A = \varepsilon bc \tag{8}$$

Where A is the absorbance; ε is the molar absorptivity; b represents the path length of light traveling through the sample, and c is the concentration of the solution. Therefore, light energy loss can be effectively suppressed by decreasing the length of light transfer in the solution.

Secondly, mass transfer is another main hindrance for the practical application of PC devices. The reactor design for high efficient PC performance should focus on increasing the mass transfer efficiency. In order to achieve this goal, the surface area of photocatalysts and surface to volume ratio is always considered in designing PC reactor [66]. Since most large-scale poser light sources, such as mercury lamp and xenon lamp, are made in a shape of tubular, cylindrical reactors are designed for full utilization of illumination. The light source is designed to be in the middle of a cylindrical PC reactor (Fig. 12c). The central illumination lamp in cylindrical PC devices leads to full utilization of light irradiation from every direction [217,218].

Backside illumination of immobilized photocatalysts is another effective method in improving the light energy absorption of semiconductor [219,220]. In the backside illumination system, the incident irradiation and aqueous solution occur on the different sides of the photocatalysts film. In this way, the incident irradiation can reach the photocatalysts' back surface without being absorbed by fluid flow, which is majorly applied in treating wastewater with high turbidity [221]. Despite the advantages of the backside illumination system for lab-scaled experiments, several flaws impede its potential in scaling up. Firstly, the photocatalysts have to be immobilized to the transparent substrate, such as FTO and ITO glasses. Since the incident irradiation passes through the transparent substrate, the light transmittance of substrates needs to be high enough to minimize the light loss in them, which increases the build cost of the PC and PEC reactor. Moreover, for some immobilized TiO$_2$ nanostructure, such as TiO$_2$ nanorod arrays and nanotube arrays, the bottom part of photocatalysts connected to the surface of the substrate is usually aggregated to each other because of the crystal grown mechanism. In this way, the backside-illuminated light will be blocked by the aggregated bottom film and cannot be fully utilized by the upper part of the photocatalysts, which reduces the efficiency of PC and PEC performance.

4.2.2. PEC system

A working PEC device consists of light irradiation sources, electrodes, proper containers, and a circulating electrolyte system. Therefore, PEC cell design is to optimize all components to maximize the efficiency of the PEC devices. Specifically, the efficiency of light harvest, mass transfer, and cell structure can be enhanced via cell design.

Based on Beer's Law, in consideration of PEC cells' structure, reducing energy loss can also be delivered by decreasing the path length of light irradiation in the electrolyte, which is similar to the PC system [222]. In the standard designs, the shape of the PEC cell is decided by the irradiation source. For practical application (i.e., large-scale application), it is attractive in using the solar irradia-
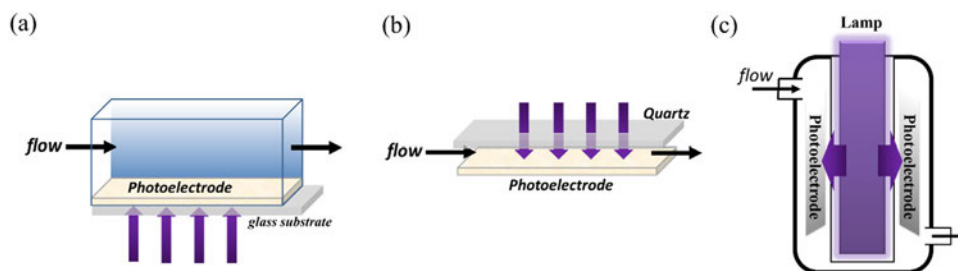
Fig. 12. The design of electrode back-illumination (a), thin-layer (b), and cylindrical PC reactors (c) to address light absorption from aqueous solution and slow mass transport problems in PC degradation.

tions to minimize energy usage and operating cost, resulting in the bed reactor for sufficiently receiving the collimated light. Unfortunately, the solar irradiation is unstable and highly depended on the weather and climate. As a stable illumination light source, the artificial lamp irradiation (tubular shape) is also applied in many cases to achieve proper performance regardless of several drawbacks, e.g., high cost, inconvenience in operating, and unnecessary heat produced by illumination [223,224]. Applying the lamp as an irradiation source, the cylindrical PEC reactors are commonly used with annular parallel electrodes placed around the lamp.

Compared with the conventional photocatalytic system, the immobilized photoelectrode in PEC cells allows the continued use of the photocatalyst, eliminating the catalyst post-separation problem. However, it is well-known that mass transfer is another main hindrance for practical application for PEC devices, which is need to increase reaction surface or increase the surface to volume ration in the cell design. Indeed, in the PEC reactors, the photocatalytic reaction can occur heterogeneously. The reactants must be transported to the photoelectrode surface at first, and then be reacted there as a result of products owing to the photogenerated electrons and holes [66,225–227]. Therefore, the development of practical applications is required to consider the mass transfer coefficient's value and study the hydrodynamic conditions.

4.3. Applied potential bias

An efficient method to improve PC performance is applying the potential bias into the PC system. The applied potential bias could adequately capture the photogenerated electrons from the conduction band of photocatalysts and facilitate the separation of photoinduced electron-hole pairs [228]. Though high potential bias could facilitate the separation rate of photogenerated electrons and holes, the overloaded potential bias could also impede the Solar-to-hydrogen (STH) efficiency. In the PEC treatment of highly polluted wastewater and degradation of landfill leachate, the applied potential bias is much higher (e.g., 20 V) than other applications in order to facilitate the mineralization rate of resistant organics. Zhou et al. proved that increasing the applied potential from 5 V to 20 V could result in an improvement of landfill leachate degradation rate [229].

Great deals of PC and PEC devices were developed and used in the laboratory and pilot-scale research; however, only a few can be practically applied for practical industrialization. The main hindrance of PC and PEC devices scaling up is the difficulties in achieving less energy loss of uniformly distributed irradiation and high-specific photocatalyst surface area.

5. Sustainable design in PC and PEC application devices

5.1. Wastewater treatment

Organic contamination is a big environmental problem contributing to the unhealthy environment [230–232]. The processing of pollutants leads to a vast volume of toxic chemicals being released into waterways and the atmosphere over the past few decades. The TiO$_2$-based PC devices have been intensively studied as an effective alternative for pollution degradation. Besides the modification strategies of TiO$_2$ photocatalysts to enhance the performance of PC pollution degradation (see Table 3), the design of the PC cell could play critical roles in PC performance.

As mentioned before, the thin-layer PC system is a promising strategy to maximize the efficiency of pollution degradation. Gan et al. [227,242] developed a thin layer PC device for the degradation of organic pollutants utilizing mesoporous TiO$_2$ film photoelectrodes (Fig. 13a). The ultraviolet light-emitting diodes (UV-LEDs) array was applied as an irradiation source. There were several advantages of applying UV-LED as an irradiation source. Firstly, UV-LED is known as "cold light" which generates a small amount of heat and beneficial to room or cold temperature operation. Secondly, the shape of UV-LED is quite adjustable, which exhibits flexibility in applying for different shapes of devices. Moreover, the lifetime and stability of UV-LED are considerably better than other conventional light sources. The exit of the cell was equipped with a PeCOD cell, where the degradation efficiency was monitoring online [227]. Jia's group [243,244] designed a rotating disk thin layer PEC reactor by mounting a rotating TiO$_2$/Ti disk photoelectrode in the bulk reactor. The disk electrode was half-immersed into the aqueous sample solution. When the disk started rotating, the aqueous solution will be carried by the disk to the upper half, where the thickness of the aqueous solution can be negligible. With a rotating speed of 90 rpm, the sample on the upper-half disk surface was continuously refreshed, and the mass transportation of the sample was significantly improved. The rotating disk PEC reactor combines a thin layer cell on the upper-half and traditional bulk cell on the lower-half, which achieved a degradation rate of 57 % and 41 % for Rhodamine B and TOC in 1 h, respectively. Wang et al. recently developed and published the study of microfluidic PC-reactors for water purification [245]. (Fig. 13b) The reactor has a planar reaction chamber ($10 \times 10 \times 0.1$ mm^3). The system was recycled more than 200 times and showed superior stability and long lifetime. This microfluidic PC reactor exhibited numerous advantages with the small quantities of fluids used, including the large specific surface area, small light loss in aqueous solution, and rapid reaction.

Another strategy for improving PC efficiency on water treatment is using cylindrical reactors. Horikoshi et al. [217] designed a cylindrical PC reactor by linking six TiO$_2$ photocatalysts together, surrounding the middle lamp to achieve maximized light utilization. The benzene degradation rate was approximately 35 % in one hour. Palmisano et al. [218] followed this process and used six TiO$_2$/graphite rods as electrodes surrounding the middle light source. The degradation rate of 4- nitrophenol was achieved by 70 % in 6.5 h. Pablos et al. [246] invented a cylindrical reactor for methanol degradation. The upsized cylinder reactor achieved uniform photocurrent density, which is comparable to the small size

22

Table 3
The TiO$_2$–based electrodes for sustainable PC and PEC water treatment.

| Photocatalyst	Irradiation source	Pollutants degradation	Time for degradation of 50 % pollutants (/min)	Ref.
Pt(Au,Ag)/TiO$_2$	6 × 6 W fluorescent lamps (λmax = 365 nm)	MO	70	[233]
Mesoporous TiO$_2$	15W 365 nm UV lamp	Rhodamine B	100	[234]
TiO$_2$@C	Sunlight	Rhodamine B	2	[235]
Y-TiO$_2$ film	30 W UV lamp	MO and Cr(VI) ions	130	[236]
BiOI/TiO$_2$ NBAs	Visible light 150 mW cm^{-2}	Methyl orange	3.5	[237]
TiO$_2$/rGO	15W UV-C lamp	Rhodamine B	60	[238]
MnFe2O4@rGO@TiO$_2$	Solar simulator (1000 W/m^2)	Ofloxacin	50	[16]
Nano TiO$_2$ meshes	30 W low-pressure Hg vapor UV-C lamp emitting at 254 nm	Real water sample	50	[239]
Graphene/Cu$_2$O /TiO$_2$ mesh	Solar light 150 W Xe lamp	Bisphenol A	25	[240]
Au/TiO$_2$ NTAs	Visible light 350 W Xe lamp	Methyl orange	230	[241]
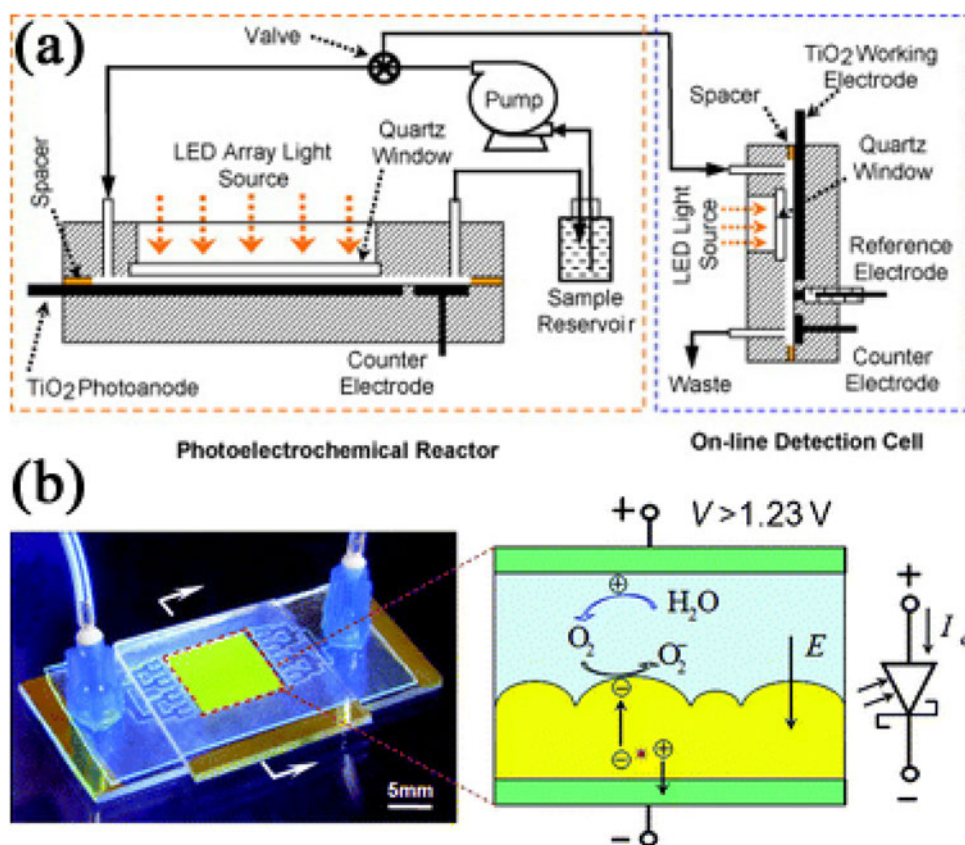
Fig. 13. (a) Schematic design of the PC reactor incorporated with an economically friendly UV-LED array and a PeCOD detector, (b) the image of the microfluidic thin-layer PC system with low building and operating cost. [242,245].
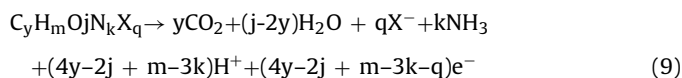
reactor, showing its promising potential in scaling up for industrialized water treatment.

5.2. PEC sensing

The PEC sensing approach was considered for many analytical applications, with advantages such as low price, simple operation, short reaction time, and high sensitivity. There are several advantages of using light illumination instead of electrochemical stimulation for sense because the light irradiation provides plain background for higher sensitivity and lower detection limits. The working mechanism of PEC sensing is converting the target molecules' chemical property into electrical signals by light irradiation, in which way the interaction between target and photocurrent can be interpreted and recorded for further use. Typically, PEC sensing can be categorized into two parts: Chemical Oxygen Demand (COD) sensor and biosensor.

5.2.1. COD sensor

Determining water quality is widely acknowledged as the monitoring of different pollutants in water bodies, in which the total concentration of various chemicals is detected as a whole. PEC sensors can exhaustively degrade the organic compounds in aqueous solutions due to the superior oxidation power of the TiO$_2$ photoanode. TiO$_2$ electrode is capable of indiscriminately detecting organic compounds. In this way, the sensor can fully oxidize all organic compounds in water solution under irradiation and produce feedback photocurrent. These PEC sensors employ a general equation which can be summarized as follows (Eq. (9)):

$$C_yH_mOjN_kX_q \rightarrow yCO_2 + (j\text{-}2y)H_2O + qX^- + kNH_3$$

$$+ (4y\text{-}2j + m\text{-}3k)H^+ + (4y\text{-}2j + m\text{-}3k\text{-}q)e^- \quad (9)$$

where X is a halogen atom, and the $y, m, j, k,$ and q represent the stoichiometric ratio of elements in the organic compounds. Therefore, the oxidation number ($n = 4y\text{-}2j + m\text{-}3k\text{-}q$) can reflect the
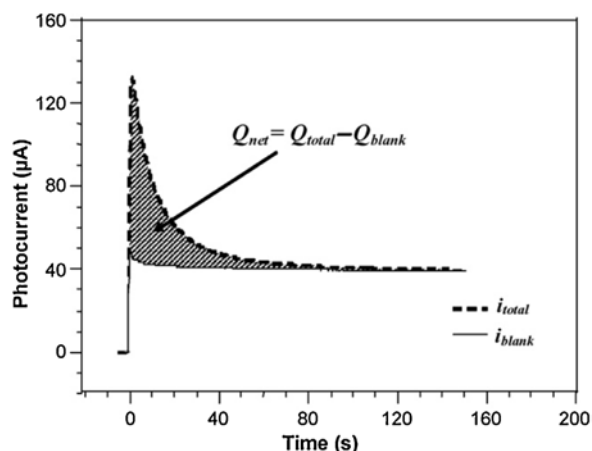
Fig. 14. Photocurrent profile of a blank solution and a sample after injecting organic compounds in a PEC thin-layer cell [247].

number of electrons captured in this process. The mineralization reaction has been used to determine the COD using two analysis modes, thin-layer PEC cell or PEC probe.

The first photoelectrochemical thin-layer cell was designed and developed by Zhang et al. in 2004 for COD sensing [247–249]. There are two modes for this thin-layer cell design. First is the static flow mode for exhaustive oxidation of organic matters. The second one is the continuous flow mode for partial oxidation [250]. When inputting irradiation into the thin-layer PEC sensor, a constant photocurrent (i_{blank}) will be obtained, which corresponds to the PEC oxidation of water. After injecting the sample containing organics through the thin layer cell, the photocurrent will increase and reach a platform. The photocurrent of this platform is denoted as i_{sample}, which consists of two parts: the oxidation of water (i_{blank}) and the oxidation of organics (i_{net}). In this way, the photocurrent (i_{net}), which represents the oxidation of organic matters can be calculated as (Eq. (10)):

$$i_{net} = i_{sample} - i_{blank} \tag{10}$$

As it is shown in Fig. 14, the charge value of blank photocurrent (Q_{blank}) and total photocurrent (Q_{total}) can, therefore, be calculated by integrating the photocurrents(Eq. (11)):

$$Q = \int i \, dt = nFVC \tag{11}$$

where i represents the photocurrent, n, F, V, and C represents the oxidation number, Faraday constant, reactor cell volume, and molar concentration of the injected sample, respectively. Consequently, the net charge value Q_{net}, which represents the oxidation of organic matters, can be calculated by Eq. (12):

$$Q_{net} = Q_{total} - Q_{blank} \tag{12}$$

When one oxygen molecule is evolved in reaction, four electrons will be transferred from anode to cathode. Subsequently, the charge value Q can be easily converted to the oxygen demand of the sample (Eq. (13)):

$$COD \ (mg \ L^{-1} \ O_2) = \frac{Q}{4FV} \times 32,000 \tag{13}$$

According to Eq. (13), the net charge value is proportional to the COD value, which is well explained and illustrated in the literature [248]. This proportional relationship proves that TiO$_2$ photoelectrodes are capable of being applied in COD sensing.

According to this analytical principle, the PeCOD method can directly interpret the COD into a photocurrent signal without further calibration. Zhang et al. [251] achieved an analytical, linear

range of 0−360 ppm COD with a practical detection limit of 0.2 ppm COD for COD sensing with the PeCOD method, which proved that the PeCOD method is fast and as accurate as the conventional COD testing methods. Zhou et al. [252,253] fabricated highly organized arrays of TiO$_2$ nanotubes as COD sensors under UV illumination, applying the exhaustive oxidation model. The high photocatalytic activity of the nanotubes is attributed to the efficient separation of photo-generated electrons and holes and enables COD determination with a more extensive dynamic working range of 0−700 mg L^{-1} and a detection limit of 1 mg L^{-1}.

Zhang et al. [228] developed a PEC portable probe for fast detecting of COD values. The nanostructured anatase–rutile mixed-phase TiO$_2$ were used as photoelectrodes, which can indiscriminately oxidize the whole spectrum of organic matter with its superior photocatalytic activities due to enhanced photoelectron-hole separation [110,112,254,255]. In order to apply this design for onsite use, the sensor used a UV-LED as a light source and a portable USB microelectrochemical station powered and controlled by a laptop computer for data processing. The analytical principle of this sensor is similar to the thin-layer PC cell, while the net photocurrent i_{net}, which is obtained from the oxidation of organic matters, is the parameter needed for representing COD values. A practical detection limit of 0.2 mg/l of O$_2$ and a linear range of 0–120 mg/L of O$_2$ was achieved using this design. Following a similar approach, TiO$_2$ nanotube electrodes were successfully fabricated into PC COD sensors via the anodization of a titanium sheet [256]. The TiO$_2$ nanotube electrode was subjected to a hydrogenation process to achieve higher PC performance, due to the reduced bandgap and oxygen vacancies. The intrinsic electrochemical resistance of the TiO$_2$ nanotube was decreased, and the hydrogen treated TiO$_2$ nanotube was significantly enhanced, including having a larger detection region. Peng et al. developed a COD sensor in a thin-layer PC cell with visible light (> 400 nm) as the light source by using hydrogen treated TiO$_2$ nanorod arrays [66]. The hydrogenated TiO$_2$ nanorod arrays achieved visible-light-driven PC activity and provided a relatively wide dynamic working range of 0–288 mg/L after assembly into the COD sensor. Zu et al. [76] designed a high-performance anatase-branch@hydrogenated rutile-nanorod TiO$_2$ (AB@H-RTNR) photoelectrode for COD sensing. The new design (Fig. 15) overcame the drawbacks of the COD sensor based on the photocurrent-concentration analytic principle, and this PEC sensor achieved a detection limit of 0.2 ppm (S/N = 3), an RSD% of 1.5 %, a broad linear detection range of 1.25−576 ppm. The average recovery rate fluctuates between 100 % ± 4% for artificial wastewater sample COD analyses.

5.2.2. Biosensor

A biosensor is an analytical sensing device used to analyze biomaterial samples by converting their biological analytical parameters into electrical signals. Great deals of methods for bioanalysis have been investigated and developed recently, such as electrochemical [257], optical [258], and piezoelectric [259]. Among all these bioanalysis technologies, the PEC biosensor is considered to be a sustainable method because it is economically friendly, easy to assemble, and high sensitive [260]. The PEC biosensor monitors the signal resulting from the interactions between various recognition components and analytes via photocurrent/voltage based on photoelectrodes [261–263]. Specifically, the photocurrent can be directly established (enhanced or impaired) by the target molecules, the biorecognition itself, or competition between the recognition and analyte [264,265]. However, the TiO$_2$ photoelectrodes can only be used in biosensors triggered by UV light, which will damage the biological properties of target biomaterials. Hence, large amounts of efforts have been put in modifying TiO$_2$ based photoelectrode for visible-light-driven biosensors, such as quantum dot modification [266,267], doping
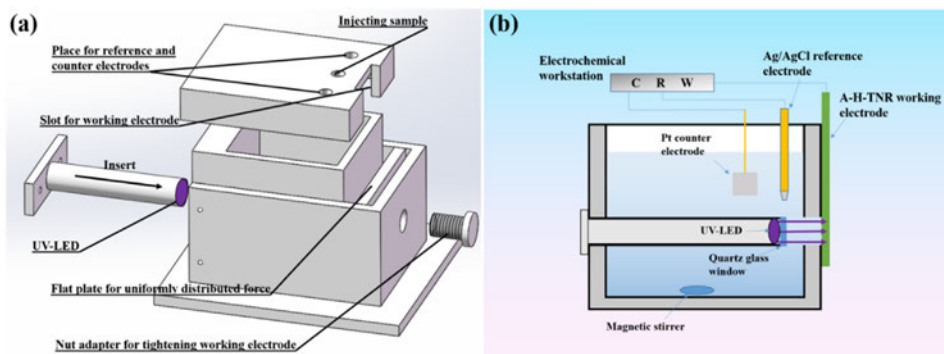
Fig. 15. (a) General view of three-electrode PEC bulk cell; (b) Schematic diagram of PEC bulk cell. [76].
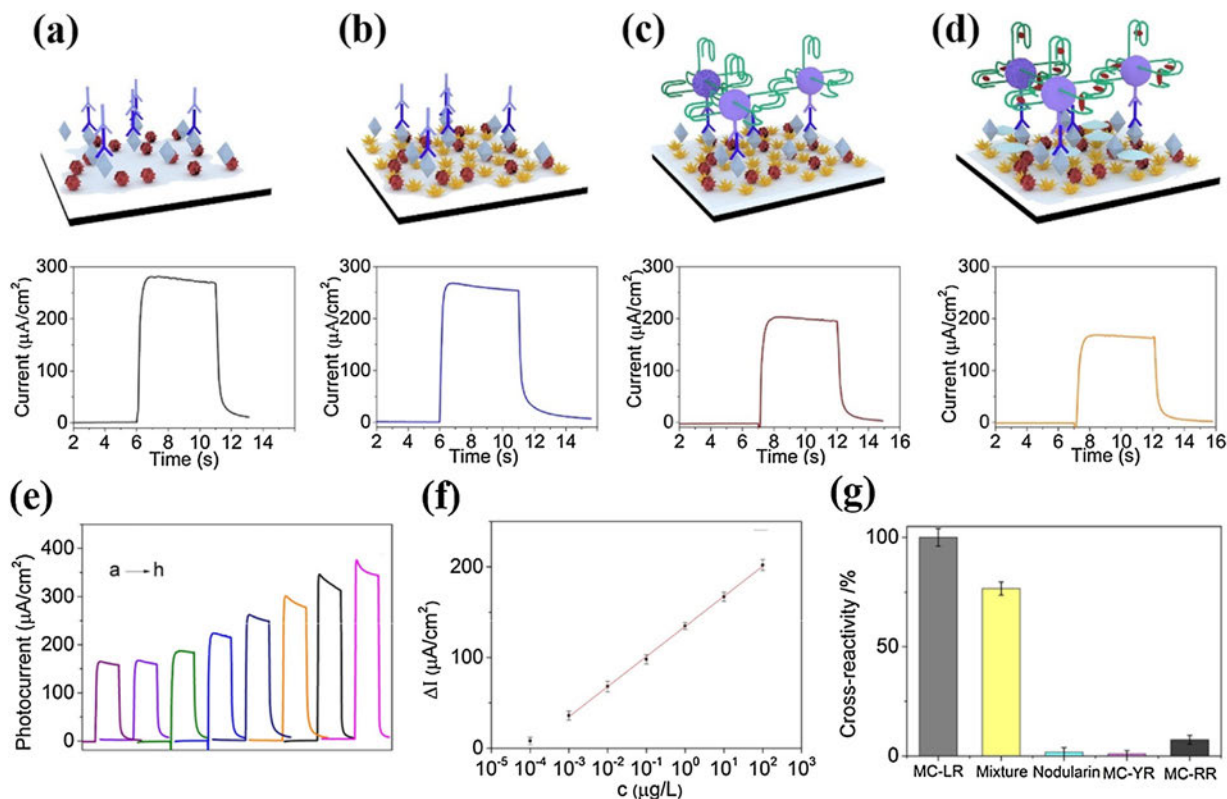

Fig. 16. The photocurrent for different biosensors (a) PDA platform-Ab2 label, (b) the Au nanoclusters/PDA platform-Ab2 label, (c) the Au nanoclusters/PDA platform-Ab2-SiO2@G-quadruplex label, and (d) the Au nanoclusters/PDA platform-Ab2-SiO2@G-quadruplex-hemin label under the condition of 4-CN and H_2O_2. (e) The photocurrent of biosensor with different concentrations of MC-LR, (f) the calibration curve, (g) the interference of other chemical compounds. (Derived from Ref. [276]or).

[268,269], the formation of heterojunction [270,271], and designing Z-scheme composites [272,273]. Zhao et al. [274] designed and synthesized a 3D $TiO_2@Cu_2O@Ni$ foam heterojunction photoelectrode for PEC enzymatic detection. With the synergetic effect of the GOx catalytic system, the signal of the biosensor was significantly amplified and exhibited a superior sensitive and selective response to glucose. The $TiO_2@Cu_2O@Ni$ heterojunction system demonstrated advanced performance because of the successful formation of a bifunctional protective layer and ideal matrix for immobilizing protein. Xue et al. [275] designed a quantum dots-based PEC biosensor for liposomal. The nanoporous TiO_2 nanotubes photoelectrodes can capture the released CdS quantum dots and therefore display superior sensitivity in the immunoassay of cardiac markers troponin I. Aori et al. [276] developed a PEC biosensor for detecting microcystin-LR (MC-LR) using CdS/branched-TiO_2 as photoelectrode. Au nanoclusters were used to amplifying the sig-

nals and enhancing PEC activity because of its surface effect. A detection range of 0.001–100 µg/L and a detection limit of 0.7 ng/l were successfully achieved (Fig. 16).

5.3. Water splitting

Hydrogen gas has been investigated for use as the future's clean and renewable energy source, ultimately leading to rapid development in hydrogen fuel cells. Today, large-scale production of hydrogen mainly relies on steam reforming of methane (SRM). This technology, however, involves the emission of greenhouse gases (such as CO_2 and NO_2). {Du, 2014 #62;Du, 2014 #62}Solar water splitting using PC devices is a promising alternative technology for hydrogen production. In PC devices, the semiconductor (as the photocatalyst) generates an electron/hole pair (e^-/h^+), which can drive water splitting. The oxidation of water to oxygen occurs at the

Table 4
Modified TiO_2 photocatalysts for sustainable water splitting.

Photocatalysts	Light intensity	Modification method	Electrolyte	Photocurrent Density	Hydrogen Production Rate ($mmol/h/cm^2$)	Ref.
TiO_2 NTAs	UV light 70 mW/cm^2	–	1 M KOH	112 μA/cm^2	7.1	[281]
H/TiO$_2$ NWs	UV light 100 mW/cm^2	doping	1 M NaOH	2.7 mA/cm^2	5.6	[191]
Pt/TiO$_2$ NTAs	UV light 30 mW/cm^2	co-catalysis	0.1 M Na$_2$SO$_4$ and 1 M ethylene glycol	45.7 μA/cm^2	135	[282]
Pd/TiO$_2$ NTAs	Solar light 320 mW/cm^2	co-catalysis	2 M Na$_2$CO$_3$ and 0.5 M ethylene glycol	26.8 mA/cm^2	592	[283]
Cu/TiO$_2$ NTAs	Visible light 300 W Xe lamp	co-catalysis	5% ethylene glycol	0.193 mA/cm^2	0.003	[284]
Cu$_2$O/TiO$_2$ NTAs	Visible light 300 W Xe lamp	heterostructure	5% ethylene glycol (pH = 7.40)	1 mA/cm^2	0.003	[285]
Graphite/ TiO$_2$ NWs	Solar light 150 mW/cm^2	heterostructure	30 % methanol	20 μA/cm^2	4.87	[286]
CdS/TiO$_2$ NR/NTA	Solar light 320 mW/cm^2	heterostructure	0.25 M Na$_2$S and 0.35 M Na$_2$SO$_3$	2.41 mA/cm^2	24.74	[287]
SrTiO$_3$/TiO$_2$ NWA	Solar light 320 mW/cm^2	heterostructure	0.5 M KOH and 0.5 M ethylene glycol	1.91 mA/cm^2	314.9	[288]
TiO$_2$@BiVO$_4$ NRAs	Solar light 100 mW/cm^2	heterostructure	0.1 M Na$_2$SO$_3$ (pH = 7.0)	1.3 mA/cm^2	16.4	[289]
Graphene/CdS/TiO$_2$ NTA	Solar light 300 mW/cm^2	multi-modification	0.1 M Na$_2$S and 0.1 M Na$_2$SO$_3$	–	10	[290]
CdS,CdSe/TiO$_2$ NRA	Solar light 100 mW/cm^2	multi-modification	10 % ethylene glycol and 0.1 M Na$_2$S	0.5 mA/cm^2	457	[291]

TiO_2 photocatalyst (usually as photoanode), while photoelectrons produce the hydrogen at the cathode (with platinum or p-type photocatalyst as a cathode). A techno-economic analysis suggested that PC methods will be able to substitute for conventional technology if the solar to hydrogen (STH) efficiency of a PC cell could be boosted to 15 % and the cost reduced to less than US$200 m^{-2} [277]. The standard definition for STH representing device operations under one-sun (Air Mass 1.5 Global G173 standard, AM 1.5 G) operations can be expressed as:

$$STH = [\frac{|j_{sc}(mA\,cm^{-2})| \times 1.23V \times \eta_F}{P_{total}(mW\,cm^{-2})}]_{AM\,1.5G} \quad (7)$$

In which, the j_{sc} is short-circuit photocurrent density normalized against the illuminated electrode area, 1.23 V is the thermodynamic water splitting potential, P_{total} is the total integrated power input density and η_F is Faradaic efficiency for hydrogen evolution. The photocurrent is zero voltage in the external circuit in the absence of any sacrificial electron donors or

acceptors. The theoretical STH efficiency ($\sim$2.2 %) of TiO_2 is limited by the large bandgap to absorb a sufficient fraction of the available solar spectrum [278]. Further experiments have revealed that the achieved STH efficiency of TiO_2 is well below the maximum theoretical efficiency. Therefore, enormous efforts were made toward narrowing the bandgap of TiO_2, which could enhance the TiO_2 theoretical efficiency as well as minimizing the recombination of photoelectron-holes. Most modification strategies mentioned in the previous section have been applied to TiO_2 photocatalysts to improve the PC hydrogen production rate (shown in Table 4).

There is a consensus that developing new nanomaterial photocatalysts is critical for PC water-splitting devices. As a result, few studies have investigated the full cell. Monguzzi et al. [279] developed a photocatalytic water splitting (PCWS) cell coupled to a broadband light upconverter that is capable of catching sub-bandgap photons and injecting this additional energy into the photocatalyst by effective light upconversion (UCA-WS device) (Fig. 17). The enhanced water division behavior was also correlated
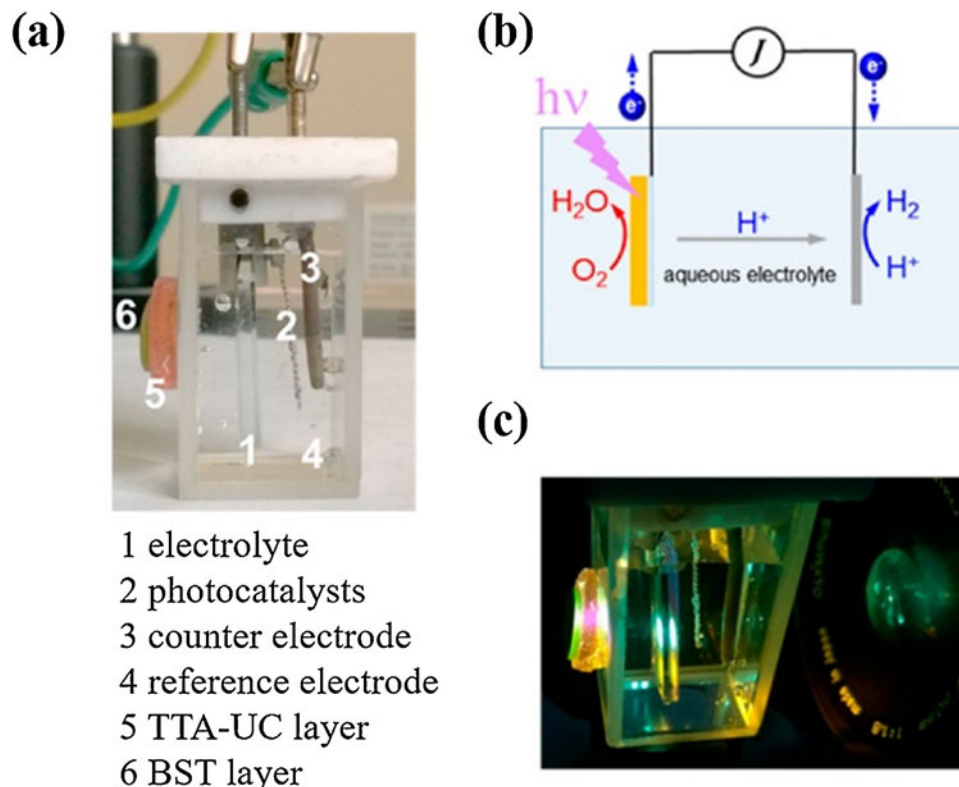

1 electrolyte
2 photocatalysts
3 counter electrode
4 reference electrode
5 TTA-UC layer
6 BST layer

Fig. 17. (a) Photo of UCA-WS device; (b) schematic diagram of UCA-ES device; (c) image of a UCA-WS prototype under white-light illumination. (Derived from Ref. [279]).
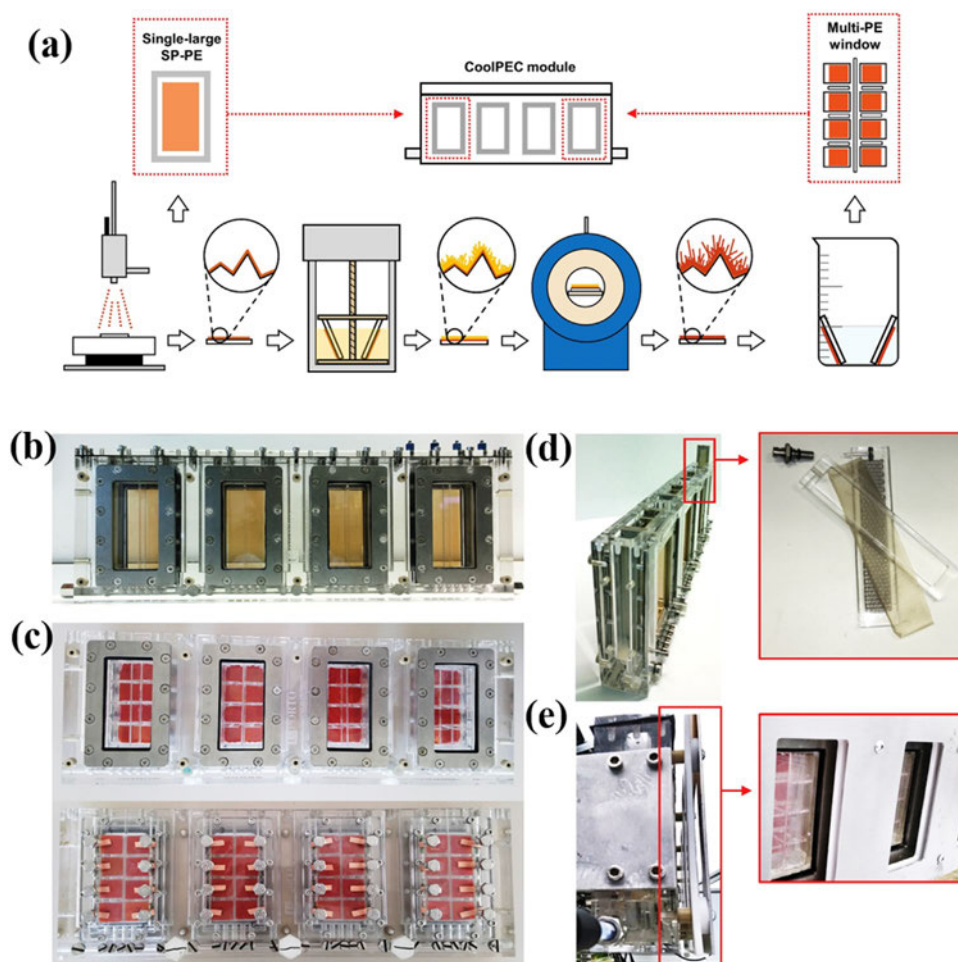
Fig. 18. (a) The preparation procedure of photoelectrodes and assemble process in the PEC-PV device; (b) front view of the module; (c) top view and bottom view of the module assembled with four multi-PE windows; (d) detailed view of the counter-electrode support; (e) detailed view of the double-layer reflective shield (PTFE-aluminium). (Derived from Ref. [280]).

with solar irradiance. This result was achieved by the creation of a multi-layer optical system that utilizes a highly effective sensitized conversion method in rubber polymers, improved by a fluorescent nanocrystal/polymer composite. Furthermore, the use of solid-state converting materials was not influenced by the existence of oxygen in solution, proving it is promising for water-related applications. This technique can not only enhance the ability of a wide range of photocatalysts utilizing solar energy, and it can also support the development of optimized up-conversion optical devices actively.

António et al. [280] designed a 200 cm^2 photoelectrocatalytic-photovoltaic (PEC-PV) modular device, which is functional under sunlight. The module was assembled by four 50 cm^2 PEC cells in a modular array. The nanostructured photoelectrodes were settled parallel in each cell, resulting in the optimized utilization of solar energy (Fig. 18). The device was tested and functioned in a continuous flow mode with electrolyte recirculation. Four 50 cm^2 multi-PE windows were used to reach higher STH conversion efficiencies under solar irradiation. Besides, it could also provide a better understanding of how those parameters, such as charge transfer, charge separation, and collection efficiency, influence the water splitting performance of the device under sunlight. The total H$_2$ production of 72 mg in 13.5 h was also achieved, which is comparatively reasonable compared to other water-splitting devices.

6. Conclusion and future outlook

In conclusion, the TiO$_2$-based PC and PEC technologies have been making progress for real applications in the past few decades. They have achieved significant advances in theoretical mechanism research and a large variety of practical application outcomes, due to the inherent advantages of TiO$_2$, such as strong oxidizing ability, convenient synthesis process, no secondary contamination emission, and its wide applications in the wastewater treatment, sensing, and water-splitting. However, the sustainability of TiO$_2$-based photocatalysts and practical devices could be further improved for these applications. In order to overcome the hindrances of improving sustainability for TiO$_2$-based PC and PEC technologies, such as low specific areas, low utilization of solar energy and high price in operating devices, and realize the practical applications, several strategies are studied and developed, such as material modification, material structure engineering, and device design.

The goal of TiO$_2$ material modification and material structure engineering can be inferred in two ways. Firstly, morphology design can directly facilitate the separation of photogenerated charge carriers and increase the efficiency of photochemical reactions. Secondly, the doping and heterostructure design modification of the electronic structure may increase the range of light absorption and impede the recombination of photogenerated electrons and holes. While the modification methods mentioned above can

effectively promote the efficiency of TiO$_2$ photocatalysts, there is also an increase in the instability and cost of synthesizing, which is not economically sustainable.

Because the specifications and requirements of PC and PEC reactors for different applications vary considerably, the device design often plays a crucial role in further advancing the sustainable industrialization of TiO$_2$-based PC and PEC technologies. However, the path to scaling up lab-scale PC devices lies in many hurdles. The most crucial factor is that, due to the simultaneous interaction of several parameters, such as irradiation, temperature, pressure, and applied potential, the energy demand for up-scaled PC devices is orders of magnitude higher than that of lab-scale PC devices.

Finally, we provide some critical perspectives on the future development of TiO$_2$-based PC and PEC technology. Considering the current state of PC and PEC technologies, it is far away from meeting the demand for successful and sustainable industrialization. There are several disadvantages of photocatalysts and device design at this stage, such as low utilization of solar energy, high cost in synthesizing photocatalyst, high cost in building and operating up-scaled devices. In the future, in order to further advance the sustainability of TiO$_2$-based photocatalysts, new photocatalysts and novel materials are highly anticipated, particularly for a visible light application, which is high-efficiency and economically friendly in synthesizing. The device design of TiO$_2$-based PC and PEC applications still need to be further optimized, especially in reducing the cost of building and operating when scaling up. In this way, the strategies mentioned above can be used as a guide for developing sustainability in practical application and industrialization of TiO$_2$-based PC and PEC technology both environmentally and economically.

Declaration of Competing Interest

The authors report no declarations of interest.

Acknowledgments

References

[1] Z. Wei, Q. Van Le, W. Peng, Y. Yang, H. Yang, H. Gu, S.S. Lam, C. Sonne,J. Hazard. Mater. (2020), 123658.
[2] A. Fujishima, K. Honda, Nature 238 (1972) 37–38.
[3] H. Wu, H.L. Tan, C.Y. Toe, J. Scott, L. Wang, R. Amal, Y.H. Ng,Adv. Mater. 32 (2020), 1904717.
[4] D. Ma, Z. Wang, J.-W. Shi, Y. Zou, Y. Lv, X. Ji, Z. Li, Y. Cheng, L. Wang, J. Mater. Chem. A 8 (2020) 11031–11042.
[5] X. Liu, C. Chen,Mater. Lett. 261 (2020), 127127.
[6] M. Kang, J. Liang, F. Wang, X. Chen, Y. Lu, J. Zhang,Mater. Res. Bull. 121 (2020), 110614.
[7] X. Wang, M. Sun, M. Murugananthan, Y. Zhang, L. Zhang,Appl. Catal. B 260 (2020), 118205.
[8] H. Zhu, Z. Chen, Y. Hu, L. Gong, D. Li, Z. Li,J. Hazard. Mater. 389 (2020), 122119.
[9] C. Hitam, A. Jalil,J. Environ. Manage. 258 (2020), 110050.
[10] J. Wang, C. Liu, S. Yang, X. Lin, W. Shi,J. Phys. Chem. Solids 136 (2020), 109164.
[11] S. Tang, Z. Wang, D. Yuan, Y. Zhang, J. Qi, Y. Rao, G. Lu, B. Li, K. Wang, K. Yin, Int. J. Electrochem. Sci. 15 (2020) 2470–2480.
[12] F. Li, J. Yang, J. Gao, Y. Liu, Y. Gong, Int. J. Hydrogen Energy 45 (2020) 1969–1980.
[13] Y. Hu, X. Hao, Z. Cui, J. Zhou, S. Chu, Y. Wang, Z. Zou,Appl. Catal. B 260 (2020), 118131.
[14] E.H. Edwards, A.A. Fertig, K.P. McClelland, M.T. Meidenbauer, S. Chakraborty, T.D. Krauss, K.L. Bren, E.M. Matson, Chem. Commun. (2020).
[15] M. Yu, J. Wang, L. Tang, C. Feng, H. Liu, H. Zhang, B. Peng, Z. Chen, Q. Xie,Water Res. (2020), 115673.
[16] M.S. Abdel-Wahed, A.S. El-Kalliny, M.I. Badawy, M.S. Attia, T.A. Gad-Allah,Chem. Eng. J. 382 (2020), 122936.
[17] X. Ge, P. Zhou, Q. Zhang, Z. Xia, S. Chen, P. Gao, Z. Zhang, L. Gu, S. Guo, Angew. Chemie 132 (2020) 238–242.
[18] T. Takata, J. Jiang, Y. Sakata, M. Nakabayashi, N. Shibata, V. Nandal, K. Seki, T. Hisatomi, K. Domen, Nature 581 (2020) 411–414.
[19] S. Zhang, G. Cheng, L. Guo, N. Wang, B. Tan, S. Jin, Angew. Chemie 132 (2020) 6063–6070.
[20] S. Ji, Y. Qu, T. Wang, Y. Chen, G. Wang, X. Li, J. Dong, Q. Chen, W. Zhang, Z. Zhang, Angew. Chemie (2020).
[21] Y. Zhang, B. Xia, J. Ran, K. Davey, S.Z. Qiao,Adv. Energy Mater. 10 (2020), 1903879.
[22] H. Liu, S. Ma, L. Shao, H. Liu, Q. Gao, B. Li, H. Fu, S. Fu, H. Ye, F. Zhao, Appl. Catal. B 261 (2020) 118201.
[23] A. Habibi-Yangjeh, S. Asadzadeh-Khaneghah, S. Feizpoor, A. Rouhi, J. Colloid Interface Sci. (2020).
[24] X. Zou, C. Yuan, Y. Dong, H. Ge, J. Ke, Y. Cui,Chem. Eng. J. 379 (2020) 122380.
[25] A.H. Mamaghani, F. Haghighat, C.-S. Lee,Appl. Catal. B 269 (2020), 118735.
[26] W. Hu, J. Huang, X. Zhang, S. Zhao, L. Pei, C. Zhang, Y. Liu, Z. Wang,Appl. Surf. Sci. 507 (2020), 145168.
[27] H. Li, Q. Gao, G. Wang, B. Han, K. Xia, C. Zhou,Chem. Eng. J. 392 (2020), 123819.
[28] Z. Shayegan, C.-S. Lee, F. Haghighat, Chem. Eng. J. 334 (2018) 2408–2439.
[29] S.G. Ullattil, S.B. Narendranath, S.C. Pillai, P. Periyat, Chem. Eng. J. 343 (2018) 708–736.
[30] Z. Xiu, M. Guo, T. Zhao, K. Pan, Z. Xing, Z. Li, W. Zhou,Chem. Eng. J. 382 (2020), 123011.
[31] A. Habibi-Yangjeh, S. Feizpoor, D. Seifzadeh, S. Ghosh,Sep. Purif. Technol. 238 (2020), 116404.
[32] C. Wang, Y. Zhao, H. Xu, Y. Li, Y. Wei, J. Liu, Z. Zhao,Appl. Catal. B 263 (2020), 118314.
[33] Y. Wang, M. Zu, X. Zhou, H. Lin, F. Peng, S. Zhang,Chem. Eng. J. 381 (2020), 122605.
[34] P. Zhou, J. Yu, M. Jaroniec, Adv. Mater. 26 (2014) 4920–4935.
[35] N. Fajrina, M. Tahir, Int. J. Hydrogen Energy 44 (2019) 540–577.
[36] M. Pelaez, N.T. Nolan, S.C. Pillai, M.K. Seery, P. Falaras, A.G. Kontos, P.S.M. Dunlop, J.W.J. Hamilton, J.A. Byrne, K. O'Shea, M.H. Entezari, D.D. Dionysiou, Appl Cata B: Environ 125 (2012) 331–349.
[37] P. Cox, The Surface Science of Metal Oxides, Cambridge university press, 1996.
[38] S.B.K. Moorthy, Thin Film Structures in Energy Applications, Springer, 2015.
[39] M. Gao, L. Zhu, W.L. Ong, J. Wang, G.W. Ho, Cat. Sci. Tec. 5 (2015) 4703–4726.
[40] K. Wang, B. Liu, J. Li, X. Liu, Y. Zhou, X. Zhang, X. Bi, X. Jiang, J. Mater. Sci. Technol. 35 (2019) 615–622.
[41] M.-J. Chang, W.-N. Cui, J. Liu, K. Wang, H.-L. Du, L. Qiu, S.-M. Fan, Z.-M. Luo, J. Mater. Sci. Technol. 36 (2020) 97–105.
[42] X. Sui, X. Li, T. Ni, F. Lin, G. Li, J. Mater. Sci. (2020) 1–16.
[43] H. Shindume L, Z. Zhao, N. Wang, H. Liu, A. Umar, J. Zhang, T. Wu, Z. Guo, J. Nanosci. Nanotechnol. 19 (2019) 839–849.
[44] J. Huang, J. Shen, S. Li, J Cai, S. Wang, Y. Lu, J. He, C.J. Carmalt, I.P. Parkin, Y. Lai, J. Mater. Sci. Technol. 39 (2020) 28–38.
[45] S. Varnagiris, A. Medvids, M. Lelis, D. Milcius, A. Antuzevics,J. Photochem. Photobiol. A: Chem. 382 (2019), 111941.
[46] H. Gong, Q. Liu, C. Huang, Int. J. Hydrogen Energy 44 (2019) 4821–4831.
[47] T. Su, Z.D. Hood, M. Naguib, L. Bai, S. Luo, C.M. Rouleau, I.N. Ivanov, H. Ji, Z. Qin, Z. Wu, Acs Appl. Energy Mater. 2 (2019) 4640–4651.
[48] S. Hejazi, S. Mohajernia, B. Osuagwu, G. Zoppellaro, P. Andryskova, O. Tomanec, S. Kment, R. Zbořil, P. Schmuki,Adv. Mater. 32 (2020), 1908505.
[49] X. Du, Y. Wu, Y. Kou, J. Mu, Z. Yang, X. Hu, F. Teng,J. Alloys. Compd. 810 (2019) 151917.
[50] S. Haffad, K.K. Kiprono, Surf. Sci. 686 (2019) 10–16.
[51] J. Dong, J. Huang, A. Wang, G.V. Biesold-McGee, X. Zhang, S. Gao, S. Wang, Y. Lai, Z. Lin, Nano Energy 71 (2020) 104579.
[52] H. Maleki, V. Bertola, Acs Appl. Nano Mater. 2 (2019) 7237–7244.
[53] Y. Fu, C.-L. Dong, W. Zhou, Y.-R. Lu, Y.-C. Huang, Y. Liu, P. Guo, L. Zhao, W.-C. Chou, S. Shen,Appl. Catal. B 260 (2020), 118206.
[54] M. Zhang, J. Wang, Y. Wang, J. Zhang, X. Han, Y. Chen, Y. Wang, Z. Karim, W. Hu, Y. Deng, J. Mater. Sci. Technol. (2020).
[55] X. Mei, J. Bai, S. Chen, M. Zhou, P. Jiang, C. Zhou, F. Fang, Y. Zhang, J. Li, M. Long, Environ. Sci. Technol. (2020).
[56] J. Li, N. Wu, Cat. Sci. Tec. 5 (2015) 1360–1384.
[57] X. Yue, J. Xiang, J. Chen, H. Li, Y. Qiu, X. Yu, J. Mater. Sci. Technol. 47 (2020) 223–230.
[58] C. Wang, W. Chen, D. Yuan, S. Qian, D. Cai, J. Jiang, S. Zhang,Nano Energy 69 (2020), 104453.
[59] Y. Li, R. Wang, H. Li, X. Wei, J. Feng, K. Liu, Y. Dang, A. Zhou, J. Phys. Chem C 119 (2015) 20283–20292.
[60] C. Ebenhoch, J. Kalb, J. Lim, T. Seewald, C. Scheu, L. Schmidt-Mende, ACS Appl. Mater. Interfaces 12 (2020) 23363–23369.
[61] W. Wang, J. Dong, X. Ye, Y. Li, Y. Ma, L. Qi, Small 12 (2016) 1469–1478.
[62] Z. Pan, Y. Qiu, J. Yang, M. Liu, L. Zhou, Y. Xu, L. Sheng, X. Zhao, Y. Zhang, J Mater Chem A 3 (2015) 4004–4009.
[63] J. Zhang, Z. Pang, Q. Sun, X. Chen, Y. Zhu, M. Li, J. Wang, H. Qiu, X. Li, Y. Li,J. Alloys. Compd. 820 (2020), 153128.
[64] S. Wang, Z. Zhang, W. Huo, K. Zhu, X. Zhang, X. Zhou, F. Fang, Z. Xie, J. Jiang,J. Hazard. Mater. (2020), 123016.

28

[65] I.S. Cho, Z. Chen, A.J. Forman, D.R. Kim, P.M. Rao, T.F. Jaramillo, X. Zheng, Nano Lett. 11 (2011) 4978–4984.

[66] X. Wang, S. Zhang, H. Wang, H. Yu, H. Wang, S. Zhang, F. Peng, RSC Adv. 5 (2015) 76315–76320.

[67] Y. Duan, P.A. Grah, F. Cai, Z. Yuan, J. Alloys. Compd. 803 (2019) 456–465.

[68] A. Morlando, J. McNamara, Y. Rehman, V. Sencadas, P.J. Barker, K. Konstantinov, J. Mater. Sci. 55 (2020) 8095–8108.

[69] T. Sreethawong, S. Laehsalee, S. Chavadej, Catal. Commun. 10 (2009) 538–543.

[70] D. Regonini, A.C. Teloeken, A.K. Alves, F.A. Berutti, K. Gajda-Schrantz, C.P. Bergmann, T. Graule, F. Clemens, ACS Appl. Mater. Interfaces 5 (2013) 11747–11755.

[71] M.S. Nasir, G. Yang, I. Ayub, S. Wang, W. Yan, Appl. Catal. B (2020), 118900.

[72] J. Zhang, G. Xiao, F.-X. Xiao, B. Liu, Mater. Chem. Front. 1 (2017) 231–250.

[73] Y. Yu, X. Yin, A. Kvit, X. Wang, Nano Lett. 14 (2014) 2528–2535.

[74] Y. Yamazaki, M. Fujitsuka, S. Yamazaki, Acs Appl. Nano Mater. 2 (2019) 5890–5899.

[75] Y. Wang, M. Zhang, J. Li, H. Yang, J. Gao, G. He, Z. Sun, Appl. Surf. Sci. 476 (2019) 84–93.

[76] M. Zu, M. Zheng, S. Zhang, C. Xing, M. Zhou, H. Liu, X. Zhou, S. Zhang, Sens. Actuators B Chem. (2020), 128504.

[77] W. Wang, J. Dong, X. Ye, Y. Li, Y. Ma, L. Qi, Small 12 (2016) 1469–1478.

[78] J.-H. Yun, A.J. Mozer, P. Wagner, D.L. Offier, R. Amal, Y.H. Ng, Sustain. Mater. Technol. 24 (2020), e00165.

[79] J. Wang, Y. Zeng, L. Wan, J. Zhao, J. Yang, J. Hu, F. Miao, W. Zhan, R. Chen, F. Liang, Appl. Surf. Sci. 509 (2020), 145301.

[80] G. He, J. Zhang, Y. Hu, Z. Bai, C. Wei, Appl. Catal. B 250 (2019) 301–312.

[81] L. Cheng, Y. Li, Y. Liu, J. Wang, R. Chen, H. Ni, Mater. Lett. 256 (2019), 126602.

[82] F. Cai, X. Chen, L. Qiu, L. Jiang, S. Ma, Q. Zhang, Y. Zhao, J. Alloys. Compd. 808 (2019), 151770.

[83] Q. Wang, Z. Liu, S. Zhang, Y. Cui, S. Gao, Y. Wang, Sep. Purif. Technol. 211 (2019) 866–872.

[84] T. Gakhar, A. Hazra, J. Electron. Mater. 48 (2019) 5342–5347.

[85] H. Fraoucene, V.A. Sugiawati, D. Hatem, M.S. Belkaid, F. Vacandio, M. Eyraud, M. Pasquinelli, T. Djenizian, Front. Chem. 7 (2019) 66.

[86] U.F. Gunputh, H. Le, R.D. Handy, C. Tredwin, Mater. Sci. Eng. C 91 (2018) 638–644.

[87] S. Ozkan, A. Mazare, P. Schmuki, Electrochim. Acta 268 (2018) 435–447.

[88] R.A. Ocampo, F.E. Echeverría, Appl. Surf. Sci. 469 (2019) 994–1006.

[89] Q. Zheng, B. Zhou, J. Bai, L. Li, Z. Jin, J. Zhang, J. Li, Y. Liu, W. Cai, X. Zhu, Adv. Mater. 20 (2008) 1044–1049.

[90] A. El Ruby Mohamed, S. Rohani, Synth. Lect. Energy Environ. Technol. Sci. Soc. 4 (2011) 1065–1086.

[91] Z. Zhang, L. Zhang, M.N. Hedhili, H. Zhang, P. Wang, Nano Lett. 13 (2012) 14–20.

[92] P. Liu, H. Zhang, H. Liu, Y. Wang, X. Yao, G. Zhu, S. Zhang, H. Zhao, J. Am. Chem. Soc. 133 (2011) 19032–19035.

[93] J. Zhou, M. Guo, L. Wang, Y. Ding, Z. Zhang, Y. Tang, C. Liu, S. Luo, Chem. Eng. J. 366 (2019) 163–171.

[94] N. Wei, H. Cui, C. Wang, G. Zhang, Q. Song, W. Sun, X. Song, M. Sun, J. Tian, J. Am. Ceram. Soc. 100 (2017) 1339–1349.

[95] Y. Chen, A. Li, Q. Li, X. Hou, L.-N. Wang, Z.-H. Huang, J. Mater. Sci. Technol. 34 (2018) 955–960.

[96] T. Butburee, Y. Bai, H. Wang, H. Chen, Z. Wang, G. Liu, J. Zou, P. Khemthong, G.Q.M. Lu, L. Wang, Adv. Mater. 30 (2018), 1705666.

[97] H.-J. Chen, Y.-L. Yang, M. Hong, J.-G. Chen, G.-Q. Suo, X.-J. Hou, L. Feng, Z.-G. Chen, Sustain. Mater. Technol. 21 (2019), e00105.

[98] J.E. Kroeze, T.J. Savenije, J.M. Warman, J. Am. Chem. Soc. 126 (2004) 7608–7618.

[99] Y. Wu, Y. Jiang, J. Shi, L. Gu, Y. Yu, Small 13 (2017), 1700129.

[100] F. Feng, C. Li, J. Jian, X. Qiao, H. Wang, L. Jia, Chem. Eng. J. 368 (2019) 959–967.

[101] E.J.W. Crossland, N. Noel, V. Sivaram, T. Leijtens, J.A. Alexander-Webber, H.J. Snaith, Nature 495 (2013) 215–219.

[102] N. Kanjana, W. Maiaugree, P. Poolcharuansin, P. Laokul, J. Mater. Sci. Technol. (2020).

[103] M.W. Kadi, R.M. Mohamed, A.A. Ismail, Ceram. Int. 46 (2020) 8819–8826.

[104] H. Li, S. Wu, Z.D. Hood, J. Sun, B. Hu, C. Liang, S. Yang, Y. Xu, B. Jiang, Appl. Surf. Sci. 513 (2020), 145723.

[105] X. Zhang, Y. Liu, S.-T. Lee, S. Yang, Z. Kang, Synth. Lect. Energy Environ. Technol. Sci. Soc. 7 (2014) 1409–1419.

[106] H.L. Tan, F.F. Abdi, Y.H. Ng, Chem. Soc. Rev. 48 (2019) 1255–1271.

[107] H. Park, Y. Park, W. Kim, W. Choi, Journal Of Photochemistry And Photobiology C-Photochemistry Reviews 15 (2013) 1–20.

[108] Y. Huang, Z. Guo, H. Liu, S. Zhang, P. Wang, J. Lu, Y. Tong, Adv. Funct. Mater. 29 (2019), 1903490.

[109] L. Kavan, M. Grätzel, S.E. Gilbert, C. Klemenz, H.J. Scheel, J. Am. Chem. Soc. 118 (1996) 6716–6723.

[110] T. Kawahara, Y. Konishi, H. Tada, N. Tohge, J. Nishii, S. Ito, Angew Chem 114 (2002) 2935–2937.

[111] T. Miyagi, M. Kamei, T. Mitsuhashi, T. Ishigaki, A. Yamazaki, Chem. Phys. Lett. 390 (2004) 399–402.

[112] D.O. Scanlon, C.W. Dunnill, J. Buckeridge, S.A. Shevlin, A.J. Logsdail, S.M. Woodley, C.R.A. Catlow, M.J. Powell, R.G. Palgrave, I.P. Parkin, G.W. Watson, T.W. Keal, P. Sherwood, A. Walsh, A.A. Sokol, Nat. Mater. 12 (2013) 798–801.

[113] J. Hu, S. Zhang, Y. Cao, H. Wang, H. Yu, F. Peng, ACS Sustain. Chem. Eng. 6 (2018) 10823–10832.

[114] T. Al-Fahdi, F. Al Marzouqi, A.T. Kuvarega, B.B. Mamba, S.M. Al Kindy, Y. Kim, R. Selvaraj, J. Photochem. Photobiol. A: Chem. 374 (2019) 75–83.

[115] Z. Wang, Y. Chen, L. Zhang, B. Cheng, J. Yu, J. Fan, J. Mater. Sci. Technol. (2020).

[116] Y. Sheng, Z. Wei, H. Miao, W. Yao, H. Li, Y. Zhu, Chem. Eng. J. 370 (2019) 287–294.

[117] A. Kumar, M. Khan, J. He, I.M. Lo, Appl. Catal. B (2020), 118898.

[118] Y. Wang, F. Zhang, M. Yang, Z. Wang, Y. Ren, J. Cui, Y. Zhao, J. Du, K. Li, W. Wang, Microporous Mesoporous Mater. 284 (2019) 403–409.

[119] V.N. Rao, S. Pitchaimuthu, P. Ravi, M. Sathish, H. Han, S.M. Venkatakrishnan, ChemCatChem (2020).

[120] Y. Qin, H. Li, J. Lu, F. Meng, C. Ma, Y. Yan, M. Meng, Chem. Eng. J. 384 (2020), 123275.

[121] X. Luo, Y. Ke, L. Yu, Y. Wang, K.P. Homewood, X. Chen, Y. Gao, Appl. Surf. Sci. (2020), 145970.

[122] H. Wang, Y. Bai, H. Zhang, Z. Zhang, J. Li, L. Guo, J. Phys. Chem. C 114 (2010) 16451–16455.

[123] X.Q. An, T. Li, B. Wen, J.W. Tang, Z.Y. Hu, L.M. Liu, J.H. Qu, C.P. Huang, H.J. Liu, Adv. Energy Mater. 6 (2016) 1614–6840.

[124] M. Pastore, F. De Angelis, J. Am. Chem. Soc. 137 (2015) 5798–5809.

[125] V. Leandri, P. Liu, A. Sadollahkhani, M. Safdari, L. Kloo, J.M. Gardner, ChemPhysChem 20 (2019) 618–626.

[126] S. Putthikorn, T. Tran-Duc, N. Thamwattana, J.M. Hill, D. Baowan, Mathematics 8 (2020) 841.

[127] W.J. Youngblood, S.-H.A. Lee, Y. Kobayashi, E.A. Hernandez-Pagan, P.G. Hoertz, T.A. Moore, A.L. Moore, D. Gust, T.E. Mallouk, J. Am. Chem. Soc. 131 (2009) 926–927.

[128] W.J. Youngblood, S.-H.A. Lee, K. Maeda, T.E. Mallouk, Accounts Chem Res 42 (2009) 1966–1973.

[129] F. Li, K. Fan, B. Xu, E. Gabrielsson, Q. Daniel, L. Li, L. Sun, J. Am. Chem. Soc. 137 (2015) 9153–9159.

[130] V. Kumaravel, S. Mathew, J. Bartlett, S.C. Pillai, Appl. Catal. B 244 (2019) 1021–1064.

[131] N.S. Ibrahim, W.L. Leaw, D. Mohamad, S.H. Alias, H. Nur, Int. J. Hydrogen Energy (2020).

[132] P. Ribao, J. Corredor, M.J. Rivero, I. Ortiz, J. Hazard. Mater. 372 (2019) 45–51.

[133] Y.-C. Pu, G. Wang, K.-D. Chang, Y. Ling, Y.-K. Lin, B.C. Fitzmorris, C.-M. Liu, X. Lu, Y. Tong, J.Z. Zhang, Y.-J. Hsu, Y. Li, Nano Lett. 13 (2013) 3817–3823.

[134] Z. Zhan, J. An, H. Zhang, R.V. Hansen, L. Zheng, ACS Appl. Mater. Interfaces 6 (2014) 1139–1144.

[135] Z. Xu, Y.Y. Lin, M. Yin, H.F. Zhang, C.W. Cheng, L.F. Lu, X.Z. Xue, H.J. Fan, X.Y. Chen, D.D. Li, Adv. Mater. Sci. Eng. Int. J. 2 (2015), 1500169.

[136] H. Liu, D. Li, X. Yang, H. Li, Mater. Technol. 34 (2019) 192–203.

[137] F. Li, Y. Jiao, J. Liu, Q. Li, C. Guo, C. Tian, B. Jiang, J. Colloid Interface Sci. 561 (2020) 568–575.

[138] X. Rong, H. Chen, J. Rong, X. Zhang, J. Wei, S. Liu, X. Zhou, J. Xu, F. Qiu, Z. Wu, Chem. Eng. J. 371 (2019) 286–293.

[139] A. Meng, B. Zhu, B. Zhong, L. Zhang, B. Cheng, Appl. Surf. Sci. 422 (2017) 518–527.

[140] X. Yu, X. Jin, X. Chen, A. Wang, J. Zhang, J. Zhang, Z. Zhao, M. Gao, L. Razzari, H. Liu, ACS Nano (2020).

[141] J. Low, S. Qiu, D. Xu, C. Jiang, B. Cheng, Appl. Surf. Sci. 434 (2018) 423–432.

[142] Y. Wang, F. Wang, Y. Sang, H. Liu, Adv. Energy Mater. 7 (2017), 1700473.

[143] X. Chen, L. Liu, Y.Y. Peter, S.S. Mao, Science 331 (2011) 746–750.

[144] D.P. Opra, S.V. Gnedenkov, S.L. Sinebryukhov, E.I. Voit, A.A. Sokolov, E.B. Modin, A.B. Podgorbunsky, Y.V. Sushkov, V.V. Zheleznov, J. Mater. Sci. Technol. 33 (2017) 527–534.

[145] K. Zou, G. Dong, J. Liu, B. Xu, D. Wang, J. Mater. Sci. Technol. 35 (2019) 483–490.

[146] R. Asahi, T. Morikawa, T. Ohwaki, K. Aoki, Y. Taga, Science 293 (2001) 269–271.

[147] M. Valero-Romero, J. Santaclara, L. Oar-Arteta, L. Van Koppen, D. Osadchii, J. Gascon, F. Kapteijn, Chem. Eng. J. 360 (2019) 75–88.

[148] H. Wang, N. Zhang, G. Cheng, H. Guo, Z. Shen, L. Yang, Y. Zhao, A. Alsaedi, T. Hayat, X. Wang, Appl. Surf. Sci. 505 (2020), 144640.

[149] P. Singla, M. Sharma, O.P. Pandey, K. Singh, Appl Phys A 116 (2014) 371–378.

[150] X. Liu, Z. Wu, Y. Zhang, C. Tsamis, Appl. Surf. Sci. 471 (2019) 28–35.

[151] E. Bayan, T. Lupeiko, L. Pustovaya, M. Volkova, V. Butova, A. Guda, J. Alloys. Compd. 822 (2020), 153662.

[152] V. Binas, V. Stefanopoulos, G. Kiriakidis, P. Papagiannakopoulos, J. Mater. 5 (2019) 56–65.

[153] B. Bharati, N. Mishra, A. Sinha, C. Rath, Mater. Res. Bull. 123 (2020), 110710.

[154] B. Gao, T. Wang, X. Fan, H. Gong, H. Guo, W. Xia, Y. Feng, X. Huang, J. He, Inorg. Chem. Front. 4 (2017) 898–906.

[155] M. Shaban, A.M. Ahmed, N. Shehata, M.A. Betiha, A.M. Rabie, J. Colloid Interface Sci. 555 (2019) 31–41.

[156] R. Darvishi Cheshmeh Soltani, M. Safari, R. Rezaee, A. Maleki, R. Ghanbari, Y. Zandsalimi, Int. J. Environ. Anal. Chem. (2020) 1–13.

[157] Y. Wang, R. Zhang, J. Li, L. Li, S. Lin, Nanoscale Res. Lett. 9 (2014) 1–8.

[158] P.S. Basavarajappa, S.B. Patil, N. Ganganagappa, K.R. Reddy, A.V. Raghu, C.V. Reddy, Int. J. Hydrogen Energy 45 (2020) 7764–7778.

[159] T. Umebayashi, T. Yamaki, H. Itoh, K. Asai, J. Phys. Chem. Solids 63 (2002) 1909–1920.

[160] C. Wang, Z. Chen, H. Jin, C. Cao, J. Li, Z. Mi, J. Mater. Chem. A Mater. Energy Sustain. 2 (2014) 17820–17827.

[161] J. Nie, Y. Mo, B. Zheng, H. Yuan, D. Xiao, Electrochim. Acta 90 (2013) 589–596.

29

[162] M.M. Momeni, Y. Ghayeb, Z. Ghonchegi, J. Solid State Electrochem. 19 (2015) 1359–1366.

[163] R. Xie, D. Lei, Y. Zhan, B. Liu, C.H.A. Tsang, Y. Zeng, K. Li, D.Y. Leung, H. Huang,Chem. Eng. J. 386 (2020), 121025.

[164] X. Han, L. An, Y. Hu, Y. Li, C. Hou, H. Wang, Q. Zhang,Appl. Catal. B 265 (2020), 118539.

[165] Z. Zhang, C. Zhao, Y. Duan, C. Wang, Z. Zhao, H. Wang, Y. Gao,Appl. Surf. Sci. 527 (2020), 146693.

[166] S.U.M. Khan, M. Al-Shahry, W.B. Ingler, Science 297 (2002) 2243–2245.

[167] J. Geng, D. Yang, J. Zhu, D. Chen, Z. Jiang, Mater. Res. Bull. 44 (2009) 146–150.

[168] S. Abu Bakar, C. Ribeiro, J. Photochem.Photobiol. C-Photochem. Rev. 27 (2016) 1–29.

[169] T. Horikawa, M. Katoh, T. Tomida, Microporous Mesoporous Mater. 110 (2008) 397–404.

[170] A. Abdelhaleem, W. Chu, X. Liang, Appl. Catal. B 244 (2019) 823–835.

[171] B. Yan, D. Liu, X. Feng, M. Shao, Y. Zhang,Adv. Funct. Mater. (2020), 2003007.

[172] X. Chen, P.-A. Glans, X. Qiu, S. Dayal, W.D. Jennings, K.E. Smith, C. Burda, J. Guo, J. Electron Spectros. Relat. Phenomena 162 (2008) 67–73.

[173] W. Fang, M. Xing, J. Zhang, J. Photochem. Photobiol. C Photochem. Rev. 32 (2017) 21–39.

[174] Z. Su, J. Liu, M. Li, Y. Zhu, S. Qian, M. Weng, J. Zheng, Y. Zhong, F. Pan, S. Zhang, Electrochem. Energy Rev. (2020) 1–58.

[175] T. Sekiya, T. Yagisawa, N. Kamiya, D. Das Mulmi, S. Kurita, Y. Murakami, T. Kodaira, J Phys Soc Jpn 73 (2004) 703–710.

[176] X. Chen, L. Liu, P.Y. Yu, S.S. Mao, Science 331 (2011) 746–750.

[177] J. Lim, Y. Yang, M.R. Hoffmann, Environ. Sci. Technol. 53 (2019) 6972–6980.

[178] F.-Y. Fu, I. Shown, C.-S. Li, P. Raghunath, T.-Y. Lin, T. Billo, H.-L. Wu, C.-I. Wu, P.-W. Chung, M.-C. Lin, ACS Appl. Mater. Interfaces 11 (2019) 25186–25194.

[179] Y. Chen, H. Yin, F. Li, J. Zhou, L. Wang, J. Wang, S. Ai,Chem. Eng. J. (2020), 124707.

[180] K. Zhang, W. Zhou, X. Zhang, Y. Qu, L. Wang, W. Hu, K. Pan, M. Li, Y. Xie, B. Jiang, RSC Adv. 6 (2016) 50506–50512.

[181] L. Han, Z. Ma, Z. Luo, G. Liu, J. Ma, X. An, RSC Adv. 6 (2016) 6643–6650.

[182] C.-F. Li, X. Guo, Q.-H. Shang, X. Yan, C. Ren, W.-Z. Lang, Y.-J. Guo, Ind. Eng. Chem. Res. 59 (2020) 4377–4387.

[183] A. Sinhamahapatra, J.-P. Jeon, J.-S. Yu, Energy Environ. Sci. 8 (2015) 3539–3544.

[184] H.-R. An, S.Y. Park, J.Y. Huh, H. Kim, Y.-C. Lee, Y.B. Lee, Y.C. Hong, H.U. Lee, Appl. Catal. B 211 (2017) 126–136.

[185] H.-R. An, Y.C. Hong, H. Kim, J.Y. Huh, E.C. Park, S.Y. Park, Y. Jeong, J.-I. Park, J.-P. Kim, Y.-C. Lee, J. Hazard. Mater. 358 (2018) 222–233.

[186] D. Ariyanti, L. Mills, J. Dong, Y. Yao, W. Gao, Mater. Chem. Phys. 199 (2017) 571–576.

[187] S. Bagheri, N.M. Julkapli, Int. J. Hydrogen Energy 41 (2016) 14652–14664.

[188] B. Wang, S. Shen, S.S. Mao, J. Mater. 3 (2017) 96–111.

[189] L. Shen, Z. Xing, J. Zou, Z. Li, X. Wu, Y. Zhang, Q. Zhu, S. Yang, W. Zhou, Sci. Rep. 7 (2017) 41978.

[190] M. Ge, C. Cao, J. Huang, S. Li, Z. Chen, K.-Q. Zhang, S. Al-Deyab, Y. Lai, J. Mater. Chem. A 4 (2016) 6772–6801.

[191] G. Wang, H. Wang, Y. Ling, Y. Tang, X. Yang, R.C. Fitzmorris, C. Wang, J.Z. Zhang, Y. Li, Nano Lett. 11 (2011) 3026–3033.

[192] W. Qingli, Z. Zhaoguo, C. Xudong, H. Zhengfeng, D. Peimei, C. Yi, Z. Xiwen, J. Co2 Util. 12 (2015) 7–11.

[193] T. Lin, C. Yang, Z. Wang, H. Yin, X. Lü, F. Huang, J. Lin, X. Xie, M. Jiang, Energy Environ. Sci. 7 (2014) 967–972.

[194] J.F. Guayaquil-Sosa, B. Serrano-Rosales, P.J. Valadés-Pelayo, H. de Lasa, Appl. Catal. B 211 (2017) 337–348.

[195] T. Ali, P. Tripathi, A. Azam, W. Raza, A.S. Ahmed, A. Ahmed, M. Muneer,Mater. Res. Express 4 (2017), 015022.

[196] S. Mathew, P. Ganguly, S. Rhatigan, V. Kumaravel, C. Byrne, S.J. Hinder, J. Bartlett, M. Nolan, S.C. Pillai, Appl. Sci. 8 (2018) 2067.

[197] J.T. Park, D.J. Kim, D.H. Kim, J.H. Kim, Mater. Lett. 202 (2017) 66–69.

[198] T. Boningari, S.N.R. Inturi, M. Suidan, P.G. Smirniotis, Chem. Eng. J. 339 (2018) 249–258.

[199] M.-C. Wu, W.-K. Huang, T.-H. Lin, Y.-J. Lu, Appl. Surf. Sci. 469 (2019) 34–43.

[200] J. Hu, Y. Li, S. Zhang, Q. Zhang, Y. Liu, J. Zuo, Q. Li, F. Peng, Int. J. Hydrogen Energy 44 (2019) 31008–31019.

[201] J. Yang, D. Wang, H. Han, C. Li, Accounts Chem Res 46 (2013) 1900–1909.

[202] P. Yilmaz, A.M. Lacerda, I. Larrosa, S. Dunn, Electrochim. Acta 231 (2017) 641–649.

[203] J. Park, J.W. Lee, B.U. Ye, S.H. Chun, S.H. Joo, H. Park, H. Lee, H.Y. Jeong, M.H. Kim, J.M. Baik, Sci. Rep. 5 (2015) 11933.

[204] M.W. Kanan, D.G. Nocera, Science 321 (2008) 1072–1075.

[205] M.W. Kanan, Y. Surendranath, D.G. Nocera, Chem. Soc. Rev. 38 (2009) 109–114.

[206] G. Ai, R. Mo, H. Li, J. Zhong, Nanoscale 7 (2015) 6722–6728.

[207] J.B. Sambur, T.-Y. Chen, E. Choudhary, G. Chen, E.J. Nissen, E.M. Thomas, N. Zou, P. Chen, Nature 530 (2016) 77–80.

[208] G.M. Carroll, D.K. Zhong, D.R. Gamelin, Synth. Lect. Energy Environ. Technol. Sci. Soc. 8 (2015) 577–584.

[209] Z. Jia, L. La, W. Zhang, S. Liang, B. Jiang, S. Xie, D. Habibi, L. Zhang, J. Mater. Sci. Technol. 33 (2017) 856–863.

[210] C. Li, W. Yang, Q. Li, J. Mater. Sci. Technol. 34 (2018) 969–975.

[211] K. Natarajan, T.S. Natarajan, H.C. Bajaj, R.J. Tayade, Chem. Eng. J. 178 (2011) 40–49.

[212] T.S. Natarajan, K. Natarajan, H.C. Bajaj, R.J. Tayade, Ind. Eng. Chem. Res. 50 (2011) 7753–7762.

[213] B. Liu, B. Chen, B. Zhang, X. Song, G. Zeng, K. Lee,J. Hazard. Mater. (2020), 123456.

[214] C. Casado, R. Timmers, A. Sergejevs, C. Clarke, D. Allsopp, C. Bowen, R. Van Grieken, J. Marugán, Chem. Eng. J. 327 (2017) 1043–1055.

[215] H. Xiong, S. Dong, J. Zhang, D. Zhou, B.E. Rittmann, Water Res. 136 (2018) 75–83.

[216] H. Tada, M. Tanaka, Langmuir 13 (1997) 360–364.

[217] S. Horikoshi, Y. Satou, H. Hidaka, N. Serpone, J. Photochem. Photobiol. A: Chem. 146 (2001) 109–119.

[218] G. Palmisano, V. Loddo, H.H.E. Nazer, S. Yurdakal, V. Augugliaro, R. Ciriminna, M. Pagliaro, Chem. Eng. J. 155 (2009) 339–346.

[219] M.G. Nielsen, S.-I. In, P.C.K. Vesborg, T. Pedersen, K.P. Almtoft, I.H. Andersen, O. Hansen, I. Chorkendorff, J. Catal. 289 (2012) 62–72.

[220] A. Visan, D. Rafieian, W. Ogieglo, R.G.H. Lammertink, Appl. Catal. B 150-151 (2014) 93–100.

[221] N. Padoin, C. Soares, Chem. Eng. J. 310 (2017) 381–388.

[222] S. Zhang, W. Wen, D. Jiang, H. Zhao, R. John, G.J. Wilson, G.D. Will, J. Photochem. Photobiol. A: Chem. 179 (2006) 305–313.

[223] X. Meng, Z. Zhang, X. Li, J. Photochem. Photobiol. C Photochem. Rev. 24 (2015) 83–101.

[224] G. Palmisano, V. Loddo, H.H.E. Nazer, S. Yurdakal, V. Augugliaro, R. Ciriminna, M. Pagliaro, Chem. Eng. J. 155 (2009) 339–346.

[225] Y. Xu, D. Zhong, J. Jia, K. Li, J. Li, X. Quan, Chem. Eng. J. 225 (2013) 138–143.

[226] W.Y. Gan, H. Zhao, R. Amal, Appl. Catal. A Gen. 354 (2009) 8–16.

[227] W.Y. Gan, D. Friedmann, R. Amal, S. Zhang, K. Chiang, H. Zhao, Chem. Eng. J. 158 (2010) 482–488.

[228] S. Zhang, L. Li, H. Zhao, Environ. Sci. Technol. 43 (2009) 7810–7815.

[229] X. Zhou, Y. Zheng, J. Zhou, S. Zhou, J. Nanomater. 2015 (2015) 7.

[230] M. Harada, Crit. Rev. Toxicol. 25 (1995) 1–24.

[231] A.H. Smith, E.O. Lingas, M. Rahman, B World Health Organ 78 (2000) 1093–1103.

[232] S. Garcia-Segura, E. Brillas, J. Photochem. Photobiol. C Photochem. Rev. 31 (2017) 1–35.

[233] M. Scarisoreanu, A.G. Ilie, E. Goncearenco, A.M. Banici, I.P. Morjan, E. Dutu, E. Tanasa, I. Fort, M. Stan, C.N. Mihailescu, C. Fleaca,Appl. Surf. Sci. 509 (2020), 145217.

[234] G. Huang, X. Liu, S. Shi, S. Li, Z. Xiao, W. Zhen, S. Liu, P.K. Wong, Chinese J. Catal. 41 (2020) 50–61.

[235] S. Kment, H. Kmentova, Z. Hubicka, J. Olejnicek, M. Cada, J. Krysa, Res Chem Intermediat 41 (2015) 9343–9355.

[236] Q. Zhang, Y. Fu, Y. Wu, Y.-N. Zhang, T. Zuo, ACS Sustain. Chem. Eng. 4 (2016) 1794–1803.

[237] Q. Teng, X. Zhou, B. Jin, J. Luo, X. Xu, H. Guan, W. Wang, F. Yang, RSC Adv. 6 (2016) 36881–36887.

[238] G. Byzynski, D.P. Volanti, C. Ribeiro, V.R. Mastelaro, E. Longo, J. Mater. Sci. Mater. Electron. 29 (2018) 17022–17037.

[239] S. Murgolo, S. Franz, H. Arab, M. Bestetti, E. Falletta, G. Mascolo,Water Res. 164 (2019), 114920.

[240] L. Yang, Z. Li, H. Jiang, W. Jiang, R. Su, S. Luo, Y. Luo, Appl Cata B: Environ 183 (2016) 75–85.

[241] L. Wu, F. Li, Y. Xu, J.W. Zhang, D. Zhang, G. Li, H. Li, Appl Cata B: Environ 164 (2015) 217–224.

[242] W.Y. Gan, H. Zhao, R. Amal, App Catal A: Gen 354 (2009) 8–16.

[243] Y. Xu, Y. He, X. Cao, D. Zhong, J. Jia, Environ. Sci. Technol. 42 (2008) 2612–2617.

[244] Y. Xu, Y. He, J. Jia, D. Zhong, Y. Wang, Environ. Sci. Technol. 43 (2009) 6289–6294.

[245] N. Wang, X. Zhang, B. Chen, W. Song, N.Y. Chan, H.L.W. Chan, Lab Chip 12 (2012) 3983–3990.

[246] C. Pablos, J. Marugán, R. van Grieken, C. Adán, A. Riquelme, J. Palma, Electrochim. Acta 130 (2014) 261–270.

[247] S. Zhang, H. Zhao, D. Jiang, R. John, Anal. Chim. Acta 514 (2004) 89–97.

[248] H. Zhao, D. Jiang, S. Zhang, K. Catterall, R. John, Anal. Chem. 76 (2004) 155–160.

[249] L. Li, S. Zhang, G. Li, H. Zhao, Anal. Chim. Acta 754 (2012) 47–53.

[250] L. Li, S. Zhang, H. Zhao, J. Electroanal. Chem. Lausanne (Lausanne) 656 (2011) 211–217.

[251] S. Zhang, L. Li, H. Zhao, G. Li, Sens. Actuators B Chem. 141 (2009) 634–640.

[252] X. Li, W. Yin, J. Li, J. Bai, K. Huang, J. Li, B. Zhou, Water Environ. Res. 86 (2014) 532–539.

[253] J. Zhang, B. Zhou, Q. Zheng, J. Li, J. Bai, Y. Liu, W. Cai, Water Res. 43 (2009) 1986–1992.

[254] D.C. Hurum, K.A. Gray, T. Rajh, M.C. Thurnauer, J. Phys. Chem. B 109 (2005) 977–980.

[255] D.C. Hurum, A.G. Agrios, K.A. Gray, T. Rajh, M.C. Thurnauer, J. Phys. Chem. B 107 (2003) 4545–4549.

[256] S. Li, J. Qiu, M. Ling, F. Peng, B. Wood, S. Zhang, ACS Appl. Mater. Interfaces 5 (2013) 11129–11135.

[257] S. Taniselass, M.M. Arshad, S.C. Gopinath, Biosens. Bioelectron. 130 (2019) 276–292.

[258] P. Steglich, M. Hülsemann, B. Dietzel, A. Mai, Molecules 24 (2019) 519.

[259] M.T. Chorsi, E.J. Curry, H.T. Chorsi, R. Das, J. Baroody, P.K. Purohit, H. Ilies, T.D. Nguyen,Adv. Mater. 31 (2019), 1802084.

[260] Q. Zhou, D. Tang,Trac Trends Anal. Chem. 124 (2020), 115814.

[261] W. Tu, Y. Dong, J. Lei, H. Ju, Anal. Chem. 82 (2010) 8711–8716.
[262] A. Devadoss, A. Kuragano, C. Terashima, P. Sudhagar, K. Nakata, T. Kondo, M. Yuasa, A. Fujishima, J. Mater. Chem. B Mater. Biol. Med. 4 (2016) 220–228.
[263] W.-W. Zhao, J.-J. Xu, H.-Y. Chen, Chem. Soc. Rev. 44 (2015) 729–741.
[264] R. Gill, M. Zayats, I. Willner, Angew. Chemie Int. Ed. English 47 (2008) 7602–7625.
[265] J. Tang, J. Li, P. Da, Y. Wang, G. Zheng, Chem. Eur. J. 21 (2015) 11288–11299.
[266] Y. Chen, Y. Zhou, H. Yin, F. Li, H. Li, R. Guo, Y. Han, S. Ai,Sens. Actuators B Chem. 307 (2020), 127633.
[267] P. Wang, L. Cao, Y. Chen, Y. Wu, J. Di, Acs Appl. Nano Mater. 2 (2019) 2204–2211.
[268] R. Atchudan, N. Muthuchamy, T.N.J.I. Edison, S. Perumal, R. Vinodh, K.H. Park, Y.R. Lee, Biosens. Bioelectron. 126 (2019) 160–169.
[269] W. Cheng, Z. Zheng, J. Yang, M. Chen, Q. Yao, Y. Chen, W. Gao, Electrochim. Acta 296 (2019) 627–636.
[270] C. Sui, F. Li, H. Wu, H. Yin, S. Zhang, G.I. Waterhouse, J. Wang, L. Zhu, S. Ai,Biosens. Bioelectron. 142 (2019), 111516.
[271] M. Wang, H. Yin, Y. Zhou, C. Sui, Y. Wang, X. Meng, G.I. Waterhouse, S. Ai, Biosens. Bioelectron. 128 (2019) 137–143.
[272] R. Zeng, Z. Luo, L. Su, L. Zhang, D. Tang, R. Niessner, D. Knopp, Anal. Chem. 91 (2019) 2447–2454.
[273] L. Meng, K. Xiao, X. Zhang, C. Du, J. Chen,Sens. Actuators B Chem. 305 (2020), 127480.
[274] Y.-C. Zhu, Y.-L. Liu, Y.-T. Xu, Y.-F. Ruan, G.-C. Fan, W.-W. Zhao, J.-J. Xu, H.-Y. Chen, ACS Appl. Mater. Interfaces 11 (2019) 25702–25707.
[275] T.-Y. Xue, L.-P. Mei, Y.-T. Xu, Y.-L. Liu, G.-C. Fan, H.-Y. Li, D. Ye, W.-W. Zhao, Anal. Chem. 91 (2019) 3795–3799.
[276] A. Qileng, Y. Cai, J. Wei, H. Lei, W. Liu, S. Zhang, Y. Liu, Sens. Actuators B Chem. 254 (2018) 727–735.
[277] B.A. Pinaud, J.D. Benck, L.C. Seitz, A.J. Forman, Z. Chen, T.G. Deutsch, B.D. James, K.N. Baum, G.N. Baum, S. Ardo, H. Wang, E. Miller, T.F. Jaramillo, Synth. Lect. Energy Environ. Technol. Sci. Soc. 6 (2013) 1983–2002.
[278] Z. Li, W. Luo, M. Zhang, J. Feng, Z. Zou, Synth. Lect. Energy Environ. Technol. Sci. Soc. 6 (2013) 347–370.
[279] A. Monguzzi, A. Oertel, D. Braga, A. Riedinger, D.K. Kim, P.N. Knüsel, A. Bianchi, M. Mauri, R. Simonutti, D.J. Norris, ACS Appl. Mater. Interfaces 9 (2017) 40180–40186.
[280] A. Vilanova, P. Dias, J. Azevedo, M. Wullenkord, C. Spenke, T. Lopes, A. Mendes,J. Power Sources 454 (2020), 227890.
[281] Y. Li, H. Yu, W. Song, G. Li, B. Yi, Z. Shao, Int J Hydrogen Energ 36 (2011) 14374–14380.
[282] L. Zhang, N. Pan, S. Lin, Int J Hydrogen Energ 39 (2014) 13474–13480.
[283] M. Ye, J. Gong, Y. Lai, C. Lin, Z. Lin, J. Am. Chem. Soc. 134 (2012) 15720–15723.
[284] S. Zhang, B. Peng, S. Yang, H. Wang, H. Yu, Y. Fang, F. Peng, Int J Hydrogen Energ 40 (2015) 303–310.
[285] S. Zhang, B. Peng, S. Yang, Y. Fang, F. Peng, Int J Hydrogen Energ 38 (2013) 13866–13871.
[286] X. Yu, X. Han, Z. Zhao, J. Zhang, W. Guo, C. Pan, A. Li, H. Liu, Z.L. Wang, Nano Energy 11 (2015) 19–27.
[287] X. Li, W. Teng, Q. Zhao, L. Wang, J. Nanopart. Res. 13 (2011) 6813–6820.
[288] Z. Wu, Y. Su, J. Yu, W. Xiao, L. Sun, C. Lin, Int J Hydrogen Energ 40 (2015) 9704–9712.
[289] X. Zhang, B. Zhang, K. Cao, J. Brillet, J. Chen, M. Wang, Y. Shen, J. Mater. Chem. A 3 (2015) 21630–21636.
[290] Y. Yu, J. Ren, M. Meng, Int J Hydrogen Energ 38 (2013) 12266–12272.
[291] H. Wang, W. Zhu, B. Chong, K. Qin, Int J Hydrogen Energ 39 (2014) 90–99.

31

CHAPTER 3

Designing robust anatase-branch@hydrogenated-rutile-nanorod TiO$_2$ as accurate and sensitive photoelectrochemical sensors

3.1 INTRODUCTORY REMARKS

The findings in this chapter were published in an article in ***Sensors and Actuators B: Chemical,*** 2020, 321, 128504.

This chapter reports a photoelectrochemical COD sensor based on the linear photocurrent-concentration analytical principle using high-performance anatase-branch@hydrogenated rutile-nanorod TiO$_2$ (AB@H-RTNR) as the photoelectrode. The as-prepared photoanodes successfully achieved sensitive determination of COD with a detection limit of 0.2 ppm (S/N = 3), an RSD% of 1.5%, a wide linear detection range of 1.25−576 ppm, and an average recovery rate fluctuating between 100% ± 4% for artificial wastewater sample analyses. Such performances are outstanding in comparison with the standard COD method. Furthermore, the AB@H-RTNR photoelectrode has a long lifetime, e.g., each electrode is capable of ca. 3000 measurements. This work suggests that the as-prepared AB@H-RTNR has overcome the barriers for practical application and final commercialization of this photocurrent-based PeCOD technology.

3.2 STATEMENT OF CONTRIBUTION

This chapter includes a co-authored paper. The bibliographic details of the co-authored paper, including all authors, are:

<u>Meng Zu</u>, Mengting Zheng, Shengsen Zhang, Chao Xing, Ming Zhou, Hu Liu, Xiaosong Zhou, Shanqing Zhang.

Designing robust anatase-branch@hydrogenated-rutile-nanorod TiO_2 as accurate and sensitive photoelectrochemical sensors

Sensors and Actuators B: Chemical, 2020, 321, 128504.

My contribution to the paper involved:

Initial concept, experimental design, and implementation; Collection and analysis of data; Preparation of manuscript.

(Signed)＿＿＿＿＿＿＿＿＿＿＿＿＿＿＿＿＿(Date) 15-04-2021

Name of Student: Meng Zu

(Countersigned)＿＿＿＿＿＿＿＿＿＿＿＿＿(Date) 15-04-2021

Corresponding author of paper: Shanqing Zhang

(Countersigned)＿＿＿＿＿＿＿＿＿＿＿＿＿(Date) 15-04-2021

Supervisor: Shanqing Zhang

3.3 Article 2

Due to copyright restrictions, the published version of this journal article is not available here. Please view the published version online at:

https://doi.org/10.1016/j.snb.2020.128504.

Designing robust anatase-branch@hydrogenated-rutile-nanorod TiO$_2$ as accurate and sensitive photoelectrochemical sensors

Meng Zu[a], Mengting Zheng[a], Shengsen Zhang[b,*], Chao Xing[a], Ming Zhou[a], Hu Liu[c], Xiaosong Zhou[a], Shanqing Zhang[a,*]

[a] Centre for Clean Environment and Energy and Griffith School of Environment, Griffith University, Gold Coast, QLD 4222, Australia
[b] College of Materials and Energy, South China Agricultural University, Guangzhou 510643, Guangdong, China
[c] Key Laboratory of Materials Processing and Mold (Zhengzhou University), Ministry of Education, Zhengzhou University, Zhengzhou, China
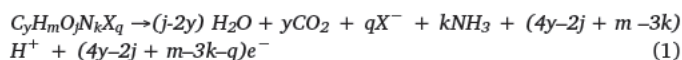
ABSTRACT

It is of great significance to design a simple, robust, rapid, and sensitive method for detecting chemical oxygen demand (COD) in wastewater. A photoelectrochemical COD sensor based on linear photocurrent-concentration analytical principle has attracted tremendous attention in the on-site determination of COD. However, insufficient accuracy, linear range, and short lifetime have been the major challenges impeding the commercialization of this analytical method for COD testing. To overcome these challenges, a high-performance anatase-branch@hydrogenated rutile-nanorod TiO$_2$ (AB@H-RTNR) photoelectrode is fabricated. The as-prepared photoanodes successfully achieved sensitive determination of COD with a detection limit of 0.2 ppm (S/N = 3), an RSD% of 1.5 %, a wide linear detection range of 1.25−576 ppm and an average recovery rate fluctuating between 100 % ± 4 % for artificial wastewater sample analyses. Such performances are outstanding in comparison with the standard COD method. Furthermore, the AB@H-RTNR photoelectrode has a long lifetime, e.g., each electrode is capable of ca. 3000 measurements. The favorable performance of AB@H-RTNR can be attributed to the adoption of the *in-situ* growth method of TiO$_2$ nanostructure and the oxygen vacancies in crystal lattice generated by the hydrogenation process. The result suggests that the as-prepared AB@H-RTNR has overcome the barriers for practical application and final commercialization of this photocurrent-based PeCOD technology.

1. Introduction

Organic pollution in water bodies has aroused more and more concerns all over the world [1]. Chemical Oxygen Demand (COD) is an important parameter that reflects the amount of aggregative organic compounds in water [2]. Monitoring COD in wastewater is of importance to the health of aquatic environment. Traditionally, potassium permanganate or potassium dichromate are used for COD determination because of their strong oxidizing ability to digest organic matters in solution [1]. Nevertheless, those traditional methods exhibit several disadvantages such as time-consuming and highly toxic reagents [3]. In recent decades, several novel methods of COD determination have been put forward and used, such as rapid catalysis, colorimetry and photoelectrochemical method [4–6]. The photoelectrochemical method for detecting COD, i.e., PeCOD, has received great attention because it can rapidly oxidize the organic compounds in wastewater indiscriminately without consuming chemical reagents and electrochemically quantify the exhaustive degradation of organic matters [7–12].

So far, the modes of PeCOD sensors can be mainly classified into two types: the first one is charge-based analysis resulted from exhaustive PEC degradation of organic matters (see Eq. (1)) in a thin-layer-cell [5].

$$C_yH_mO_jN_kX_q \rightarrow (j\text{-}2y)\ H_2O + yCO_2 + qX^- + kNH_3 + (4y\text{–}2j + m\text{ –}3k)\ H^+ + (4y\text{–}2j + m\text{–}3k\text{–}q)e^- \qquad (1)$$

where X represents a halogen atom and the coefficients y, m, j, k, and q stand for the stoichiometric ratio of elements in the organic compounds. However, this method needs a high-cost, sophisticated, and bubble-free thin-layer cell. It also exhibits short linear range and relatively long analytical time for complete oxidation of organics in samples with high COD. In order to address these issues, we proposed an alternative and simpler analytical method, i.e., the photocurrent-based COD measurement based on diffusion-controlled rapid oxidation kinetics in a bulk cell [6].

To achieve the high accuracy of the photocurrent-based COD

---

measurement, we must assure the oxidation reaction of organic compounds ($C_yH_mO_jN_kX_q$) follow Eq. (1). According to the postulates of this photocurrent-based method, organic compounds in sample solution need to be fully mineralized to CO_2 and H_2O so that the net photocurrent could precisely represent the number of electrons transferred from donors to acceptors. However, this postulate is difficult to be achieved in practical experiments if the photocatalysts do not possess sufficient photocatalytic activity. In this way, achieving more photocatalytic activity of photocatalysts makes the experimental results closer to the theoretical ones. The previous photocurrent-based PeCOD method exhibited insufficient photocatalytic activity indicated by its comparatively lower linear range and short lifetime. This is a hugely challenging task for the complete oxidation of a high concentration of organic compounds, which demands a particularly high photocatalytic activity of the photocatalysts electrode. Many metal oxide photocatalysts have been used recently for efficient photocatalytic and photoelectrocatalytic applications, such as Cu_2O [13,14], ZnO [15], SiO_2 [16], etc. Among all the photocatalysts, TiO_2 is most widely used mainly in photocatalytic COD measurement due to its strong chemical stability, high photocatalytic efficiency, zero toxicity and affordable cost [7–12]. With the TiO_2 nanoparticles photoelectrode, the proposed PeCOD probe realized a linear detection range of 0–120 mg/L with a detection limit of 0.2 mg/L [6]. In further practical trials and commercialization of this photocurrent-based PeCOD probe, insufficient accuracy for a large number of measurements, narrow linear range, and short lifetime due to its insufficient photocatalytic activity and the instability of the TiO_2 nanoparticles coated electrode are the only barriers for large-scale application of this method.

Compared with the TiO_2 nanoparticle coated electrodes [6], highly ordered one-dimensional (1-D) monocrystalline rutile TiO_2 nanorod arrays in-situ grown on FTO has excellent mechanical strength and good photocatalytic activity [17–22]. To further improve the photocatalytic activity of 1-D TiO_2 nanorods, many efforts have been devoted to further morphology manipulation, such as adding nanoparticles [23], nanobranches [22] and nanosheets [24] onto the surface of TiO_2 nanorods. These efforts have improved the surface-to-volume ratio of photocatalysts, thus making better use of illumination [25–27]. Moreover, the hydrogenation process is also known as an efficient method for improving photocatalytic activity because it could bring in the disordered layer on the surface of TiO_2 that contains abundant oxygen vacancies and Ti^{3+} [28–30]. As the oxygen vacancies provide a large number of sites for photogenerated electrons to occupy, the recombination rate of photogenerated electron-hole pairs could be significantly reduced during light irradiation. As a result, more holes are allowed to participate in photocatalytic oxidation of organic compounds [31].

Herein, an anatase-branched/hydrogenated rutile-nanorod TiO_2 photoelectrode with hydrogenated interface (AB@H-RTNR) was prepared and synthesized via a hydrothermal reaction and a subsequent hydrogenation process. The average photocurrent density of the AB@H-RTNR is up to 1.79 mA/cm², which is 1.42 times and 3.7 times higher than that of the AB@RTNR and pure RTNR electrode acquired under 6.6 mW/cm² of UV light at +0.3 V, respectively. Notably, the photoelectrode showed excellent stability and reusability. The role of hydrogenated heterophase interfaces in PEC degradation and determination of organics was systematically investigated. The hydrogenation process brings in a large number of oxygen vacancies that enhance the absorption of irradiation and impede the recombination of photogenerated electron-hole pairs. Considering the in-situ growth method of TiO_2 heterophase structure and oxygen vacancies generated by the hydrogenation process, this AB@H-RTNR photoelectrode can facilitate the indiscriminate oxidation of organic compounds as described in Eq. (1) and achieve sensitive detection of COD in a much wider liner range with for a long lifetime.

2. Experimental

2.1. Preparation of materials

Rutile nanorods (RTNRs) were prepared on a Fluorine-doped tin oxide (FTO) glass slide according to a previously reported hydrothermal method [32]. Briefly, 20 mL deionized water was mixed with 20 mL hydrochloric acid (36.5 % by weight) under vigorous stirring for 5 min, followed by the addition of 0.48 mL tetrabutyl titanate (97 % Aldrich) under magnetic stirring for another 5 min. Two pieces of well-cleaned FTO substrates (6.5 × 1.5 × 0.2 cm³) were immersed in the solution, which was transferred into a 100 mL Teflon-lined stainless-steel autoclave and heated at 170 °C for 6 h in an oven. After cooling to room temperature naturally, the rutile nanorods electrode was washed several times with deionized water and was further hydrogenated at 350 °C in a continuous hydrogen and argon (5 % hydrogen) flow for 1 h to obtain hydrogenated rutile nanorod (H-RTNR). For synthesizing anatase H-RTNR (AB@H-RTNR), the H-RTNRs were further put into an aqueous solution mixed by boric acid (H_3BO_3) and ammonium hexafluo-rotitanate ([NH_4]$_2$$TiF_6$) for 40 h at 50 °C. As to anatase-branch@ rutile TiO_2 nanorod (AB@RTNR), RTNRs were put into the aqueous solution, in the same way, to grow the anatase structures before drying at 350 °C for 1 h in air.

2.2. Characterization methods

The morphology and microstructure were characterized by scanning electron microscope (SEM, LEO 1530VP, Germany) and transmission electron microscope (TEM, JEOL JEM-2010 F, Japan). X-ray diffraction (XRD) analysis was performed on an X-ray diffractometer (D/max-IIIA, Japan). The chemical nature of Ti and O was studied using an X-ray photoelectron spectrophotometer (XPS) in Krato Axis Ultra DLD spectrometer with Al Kα X-ray ($h\nu$ = 1486.6 eV) at 15 kV and 150 W. The binding energy was referenced to C $1 s$ line at 284.6 eV for calibration. Raman spectra were examined by a Renishaw inVia Raman microscope. Electrochemical impedance spectroscopy (EIS) was obtained under open-circuit voltage, with 1.0 M NaOH solution and frequency from 0.01 Hz to 1000000 Hz and amplitude of 5 mV (CHI 660e electrochemical station). Mott–Schottky (M-S) analysis was measured with the potential increment of 5×10^{-2} V, the amplitude of 5×10^{-3} V, and the frequency of 1 kHz.

2.3. PEC performance measurement

As it is widely recognized that the oxidation of the TiO_2 photoelectrode under UV irradiation is more powerful and more rapid than that under visible light. With the availability of low cost and stable UV-LED, UV light is adopted as the illumination source for the experiment. All PEC experiments were performed at 23 °C using a three-electrode PEC bulk cell, which consists of electrochemical and optical components. The electrochemical components are made of a TiO_2 working electrode (with a 5 mm diameter circle exposed to the solution and UV light), a Pt net counter electrode, and a saturated Ag/AgCl reference electrode. A standard electrochemical workstation (CV-27) was used for the application of the potential bias, current signal recording, and data processing in the PEC experiment. A UV-LED with a peak wavelength of 365 nm was installed to supply UV illumination for the PEC reaction. The plane of the UV-LED was fixed in parallel to the photoanode surface with a distance of 6.5 mm. The UV intensity at the TiO_2 electrode surface was 6.6 mW/cm². The supporting electrolyte was 0.1 M $NaNO_3$.

3. Results and discussion

3.1. Materials synthesis and characterization

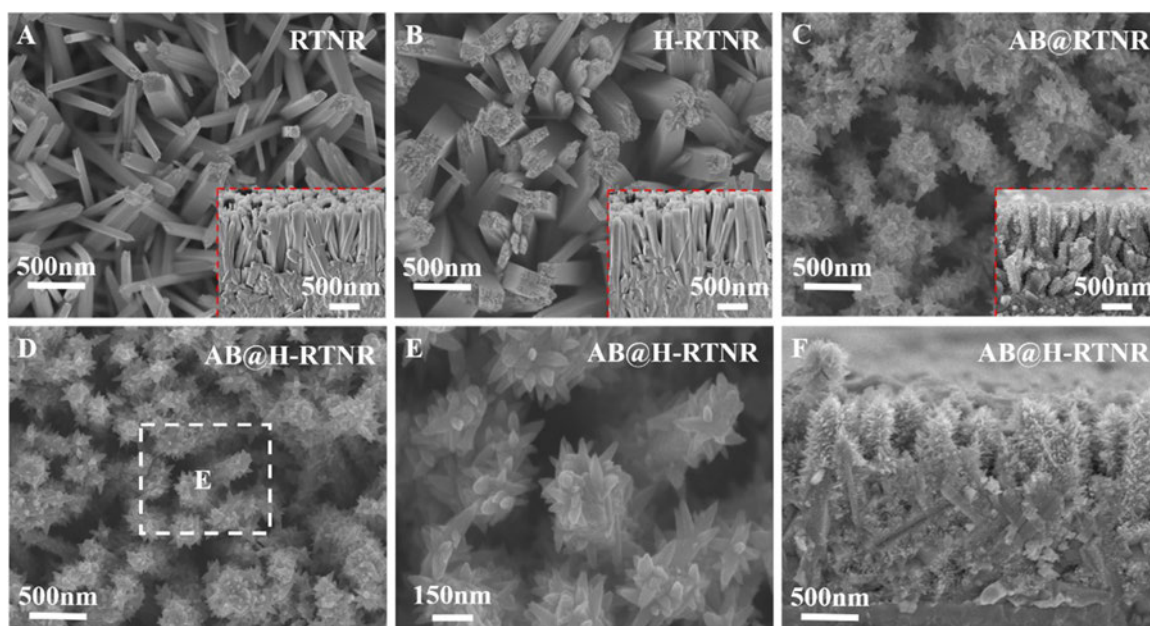The RTNRs are firstly grown on FTO glass by the hydrothermal

Fig. 1. FESEM surface morphologies and cross-sectional view of TiO$_2$ nanostructures (A) RTNR, (B) H-RTNR, (C) AB@RTNR, (D, E) AB@H-RTNR and (F) cross-sectional view of AB@H-RTNR.

method. As it is shown in Fig. 1A, the RTNRs are grown on FTO uniformly with 200 nm in average diameter and 1.5 μm in length, respectively. Subsequent hydrogenation process results in the H-RTNR photoelectrodes. No significant surface morphology changes are observed before and after the hydrogenation treatment (Fig. 1B). The branched structure is achieved by carrying out a second step hydrothermal process on RTNR and H-RTNR, leading to AB@RTNR and AB@H-RTNR, respectively. The similarity of the surface morphologies of AB@RTNR and AB@H-RTNR further confirms that the hydrogenation process does not affect the morphology of nanostructures and the growth of nanobranches (Fig. 1C-E). The in-situ growth of TiO$_2$ ensures the film strongly adhered to the substrate, which improves the lifetime, stability, and reusability of photoanodes. Furthermore, the structure can also reduce the resistance at the interface between TiO$_2$ rods and FTO glass, favoring the photogenerated electrons transferred from photocatalysts to the substrate that facilitates the separation of photogenerated electrons and holes. The SEM images of branched nanostructures (Fig. 1C-F) reveal that the entire surface of nanorods is covered with nanobranches uniformly with an average length of 20 nm. Fig. 1F suggests that the thickness of photocatalysts film on the FTO substrate is approximately 2 μm, and the nanobranches are distributed from the bottom to the up of nanorods, which will significantly increase the surface area of nanostructure and hence promote the light absorption of photocatalysts.

As shown in Figs. 1A- B and 2 E, some of the nanorods are interconnected, especially in the bottom section. Although 1-D nanowires provide direct pathways for fast electrons transportation and facilitate the separation of photogenerated hole-electron pairs, such connections of the nanorods might not affect the vertical transportation of electrons except reducing the distance among the nanorods. We believe such connections will not have a significant influence on the performance of the sensor. The connections will hardly affect the light absorption and mass transport of organic compounds in the photoelectrochemical oxidation of organic compounds because most of these connections occur at the bottom part (close to the FTO current collector).

TEM analyses have been used to study the surface property of different photoelectrodes. Fig. 2A-C exhibit the morphology of pristine RTNR. The surface of RTNR is smooth without disorder layer and a clear lattice spacing of 0.249 nm, corresponding to rutile (101) crystal planes of tetragonal-rutile TiO$_2$ (ICDD No. 73-1232), was observed.

After conducting the hydrogenated process onto RTNR, the TEM image of H-RTNR exhibits that the surface of the nanorod is also smooth, and the diameter is nearly 60 nm (Fig. 2D). A disorder layer with a thickness of 2.1 nm on the surface of the H-RTNRs sample can be observed clearly in Fig. 2E, which is generated from hydrogenation treatment. Great deals of researchers have reported that the disordered layer possesses plenty of oxygen vacancies, which can capture photo-induced electrons and therefore enhance the photocatalytic performance of RTNRs [33,34]. It can also be observed from the figure that the TiO$_2$ nanorods are constituted of many highly ordered tiny single crystal nanowires, which can highly improve the directional transfer of photo-induced charge carriers. The measured lattice spacing of 0.249 nm in Fig. 2E and F correspond to rutile (101) crystal planes of tetragonal-rutile TiO$_2$ (ICDD No. 73-1232). Fig. 2G and J directly prove the branched structures are immobilized on the surface of RTNRs. As it is shown in Fig. 2I and L, there are two lattice fringes with a spacing of 0.249 nm and 0.335 nm, which correspond to the spacing of (101) plane of rutile TiO$_2$ and (101) plane of anatase TiO$_2$, respectively (ICDD No. 73-1232, ICDD No. 71-1166). The only difference is that, for AB@H-RTNR, the disordered layer with a thickness of around 2 nm can be observed on the interface between branches and nanorods, indicating the hydrogenation treatment in the interface. Fig. 2G-L not only proves that the crystal phase of the branch is anatase TiO$_2$ and the trunk is rutile TiO$_2$, but it also gives evidence that the growth of anatase TiO$_2$ branches on the hydrogenated nanorods will not sabotage the disordered layer. This special structure can theoretically improve the density of photogenerated charge carriers and enhance the separation of photogenerated electron/hole pairs.

X-ray diffraction has been used to exhibit the crystal phase of as-prepared photocatalysts (Fig. 3A). After subtracting the diffraction peaks from FTO glass, six diffraction peaks centered at 2θ angles of 26.5°, 36.05°, 41.24°, 54.31°, 62.8°, and 69° are observed in each sample, which are indexed to the characteristic peaks of tetragonal rutile TiO$_2$ (ICDD No.88-1175). For the branched nanostructures, two new peaks centered at 2θ angles of 25.14° and 47.67° proves the existence of the anatase crystal phase (ICDD No. 88-1175). These good correspondences suggest that RTNR and H-RTNR are composed of pure rutile TiO$_2$, while AB@RTNR and AB@H-RTNR consists of rutile and anatase TiO$_2$. The peak centered at 36.05° corresponds to the (101) diffraction that is dominant over all other peaks, providing evidence
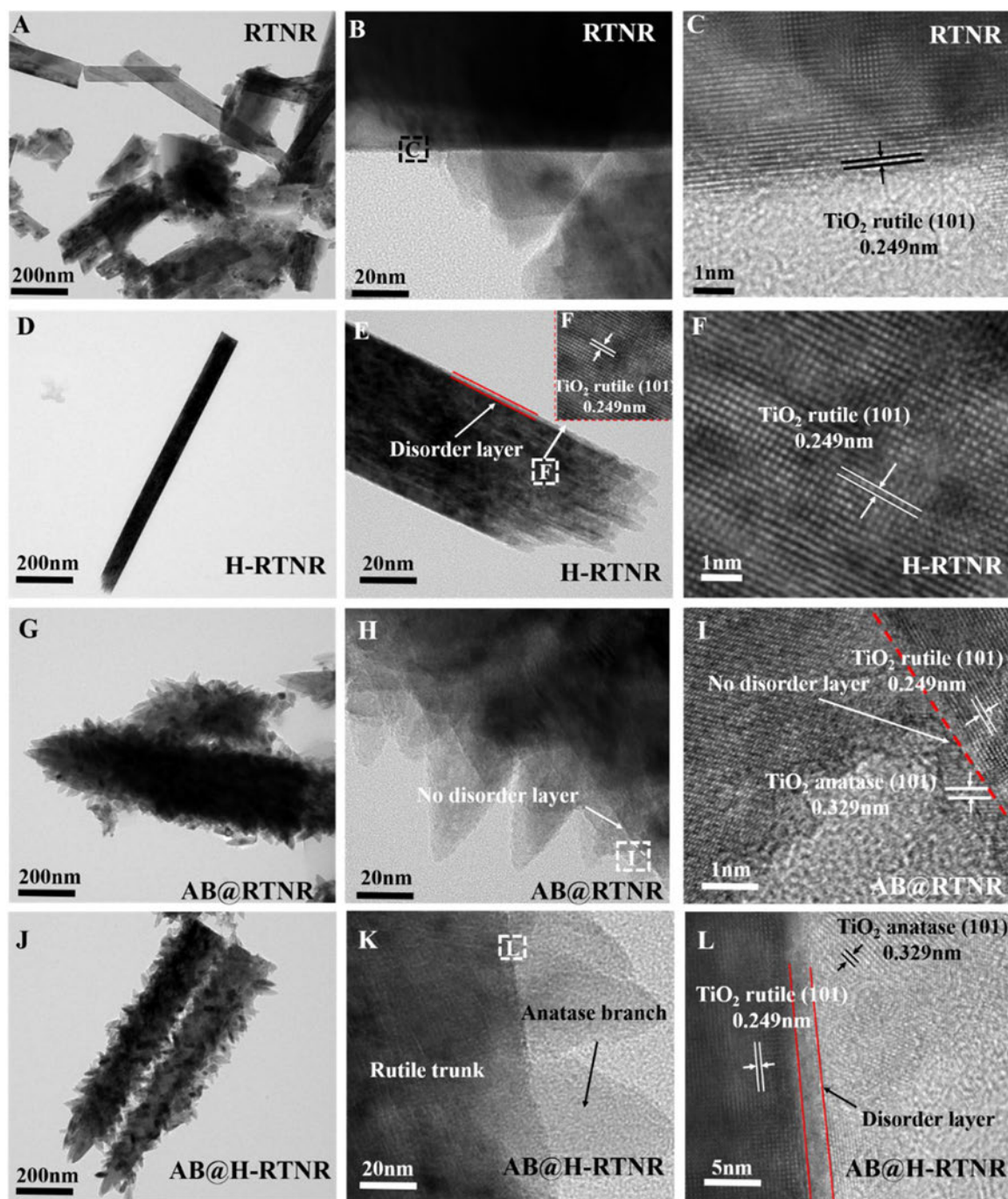
Fig. 2. The TEM and HRTEM images of RTNR (A, B, C), H-RTNR (D, E, F), AB@RTNR (G, H, I) and AB@H-RTNR (J, K, L).

that the RTNRs are highly oriented in the (101) direction on the FTO substrate, which is consistent with the observation from HRTEM images (Fig. 2). Furthermore, the intensity of the peaks representing the anatase crystal phase is comparatively low, which indicates the proportion of anatase TiO_2 is low compared to the rutile crystal phase. The XRD results suggest that anatase TiO_2 appeared in the material after the grown of branches, proving branches are anatase phase TiO_2 structure, and mixed-phase TiO_2 is achieved. However, the difference between the as-prepared materials before and after hydrogenation is not clear, which needs further characterization and analysis.

Raman spectra have been tested to further confirm the phase structure of the samples (Fig. 3B). There are three diffraction peaks centered at 234, 445, and 610 cm^{-1} in all four samples, which correspond to the characteristic peaks of rutile phase TiO_2 [35]. For AB@

RTNR, new peaks appear at 148 cm^{-1} corresponding to the characteristic peak of anatase phase TiO_2; while for AB@H-RTNR, the anatase phase characteristic peak has shifted to 160 cm^{-1}. Moreover, that intensity of characteristic Raman spectra peaks for either anatase or rutile is weakened after hydrogenation treatment. These phenomena of intensity drop and peak shift can be ascribed to the photon confinement and nonstoichiometric because of oxygen vacancy and $Ti-H$ mode generated by the hydrogenation process [27,36,37]. The presence of oxygen vacancies can significantly enhance the separation of photogenerated charge carriers and improve the photocatalytic activity.

High-resolution XPS spectra of different as-prepared TiO_2 samples have shown the core electron peak regions of Ti 2p and O 1s (Fig. 3C and D). For the pristine samples (RTNR and AB@RTNR), the binding energy of Ti 2p electrons (Ti 2p 3/2, 458.8 eV; Ti 2p 1/2, 464.5 eV) is
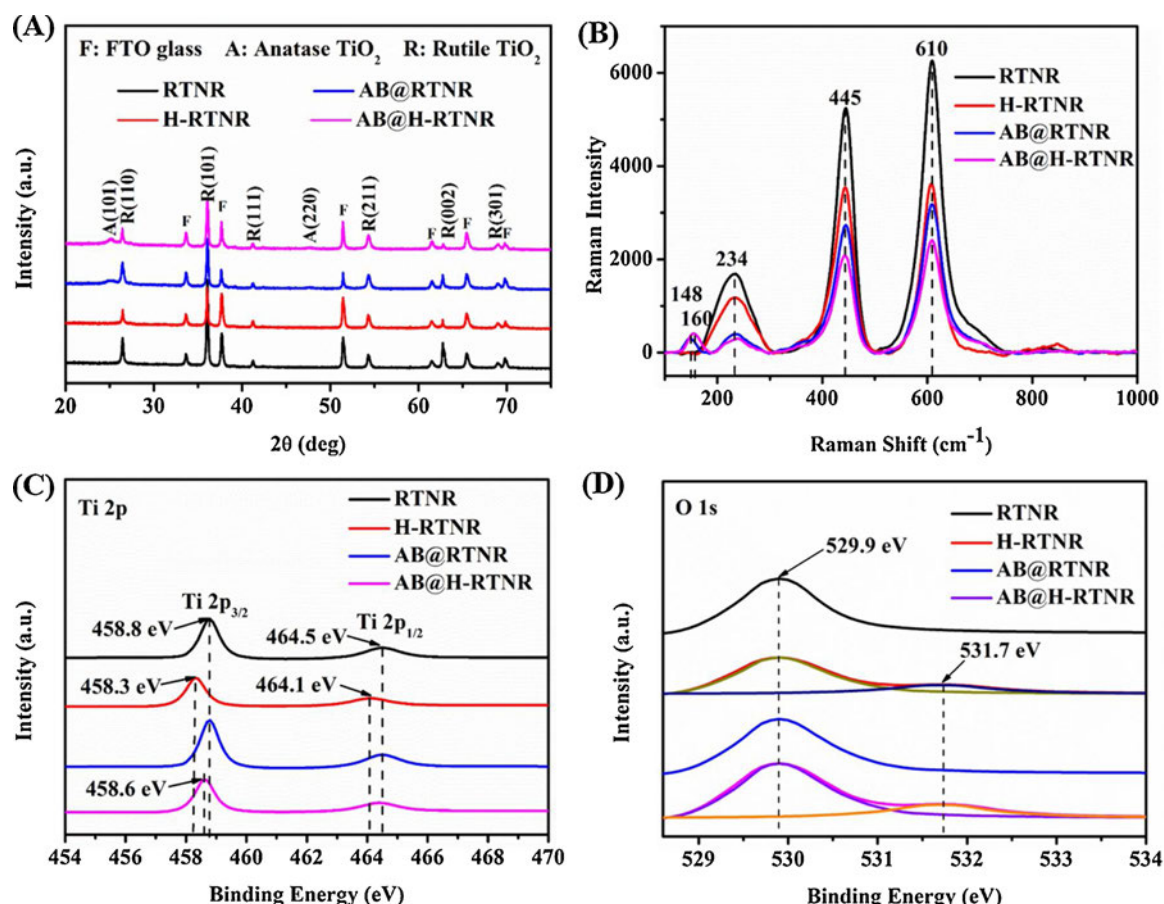
Fig. 3. (A) XRD spectra, (B) Raman spectra and XPS spectra of the as-prepared photocatalysts for (C) Ti 2p and (D) O 1s.

exclusively assigned to Ti^{4+} without the response of Ti^{3+} in the surface layer. While for hydrogenated samples (H-RTNR and AB@H-RTNR), a significant shift of approximately 0.5 eV towards negative direction was observed, suggesting the formation of Ti^{3+} on the surface of the sample [32,38]. A slightly positive shift is observed for AB@H-RTNR compared to H-RTNR, indicating the decrease of Ti^{3+} on the surface of AB@H-RTNR, which can be ascribed to the fact that the disordered layer is covered by anatase TiO_2 branches. In Fig. 3D, the major peaks at 529.9 eV in the O 1s spectrum can be attributed to O in Ti-O bonds [39]. After hydrogenation treatment, a new peak at 531.7 eV appears by deconvoluting the O 1s spectrum of H-RTNR and AB@H-RTNR. This peak can be attributed to Ti-OH that is located at ca. 1.5–1.8 eV higher binding energy comparing with O 1s of the pristine TiO_2. These results further confirm that an oxygen vacancy interface exists between anatase and rutile TiO_2. As it is reported [29], these oxygen vacancies could not only enhance the light absorption but also favor the separation of photo-generated electron-hole pairs, which will significantly improve the PEC activity of the photoelectrode.

Electron paramagnetic resonance (EPR) is also used to confirm the existence of oxygen vacancies and Ti^{3+}. As it is shown in Fig. 4, no obvious peak exists in the EPR spectra of AB@RTNRs,while AB@H-RTNR samples exhibit the EPR signals at the g value of 2.00 which presents the existence oxygen vacancies and Ti^{3+}. This result can clearly indicates that the hydrogenation process can greatly increase the amount of oxygen vacancies and Ti^{3+} in material. This is consistence with the XPS spectra and further proves that AB@H-RTNRs possess large amount of oxygen vacancies which favors the photo-catalytic performance.

UV-Vis absorbance spectra have been used to determine the light absorption situation and band-gap energy of as-prepared photocatalysts to gain greater insight on PEC property of AB@H-RTNR. As it is
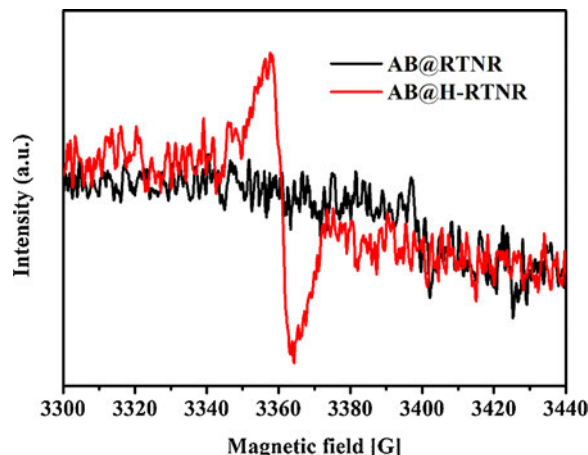

Fig. 4. EPR spectra of AB@RTNRs and AB@H-RTNRs.

displayed in Fig. 5A, the absorbance in the visible light region $(400-700\,nm)$ of H-RTNR and AB@H-RTNR has been significantly enhanced due to the oxygen vacancies produced by the hydrogenation process. It is also recognized that AB@RTNR exhibits promoted light absorbance in the UV region $(200-400\,nm)$ compared to pristine H-RTNR, proving that branched structure possesses superior light-scattering effect which could benefit light absorption for photocatalysts (Fig. 5A). Consequently, the superior performance of AB@H-RTNR on light absorption compared to all the other as-prepared photocatalysts can be attributed to the synergetic effect of branched structure and oxygen vacancy generated by hydrogenation. To obtain the bandgap energy of as-prepared material, the Tauc plots are calculated from
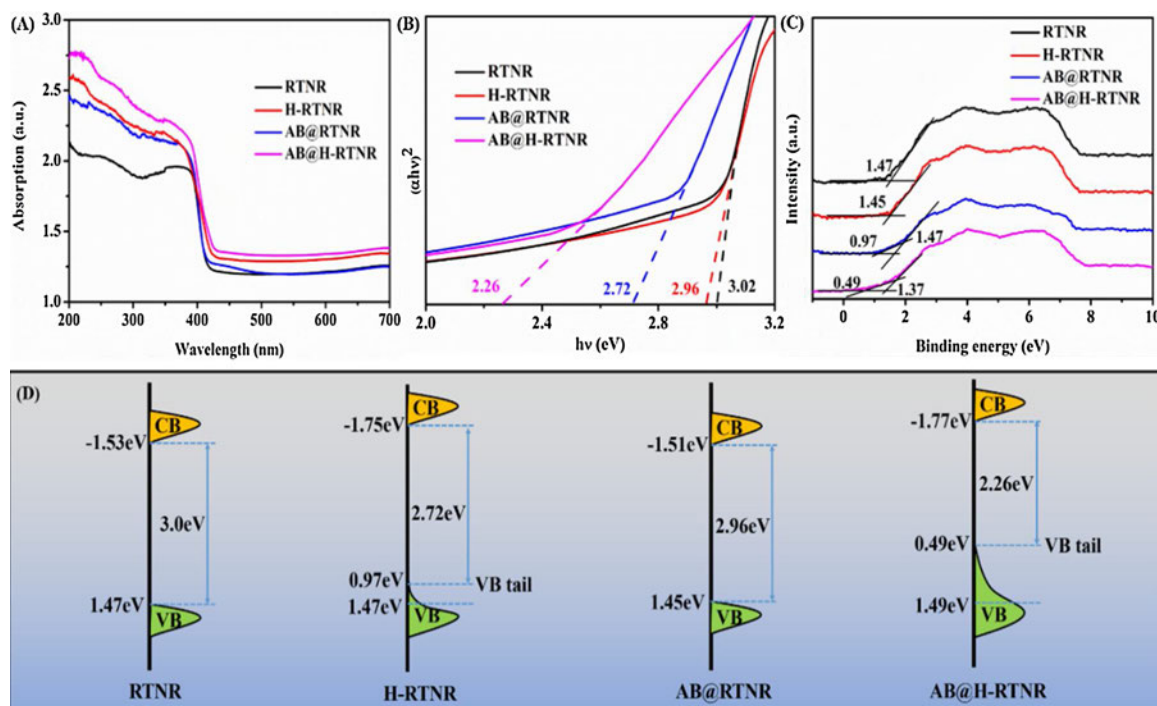
Fig. 5. (A) UV–vis absorbance spectra, (B) Tauc plots derived from Fig. 5A, (C) Valence band-XPS, and (D) Schematic diagrams of the DOS for as-prepared photocatalysts.

UV–vis absorbance spectra by following the Tauc equation [40] (Fig. 5B).

$$(\lambda h\nu)^n = A(h\nu - E_g) \tag{2}$$

Where A is the constant, $h\nu$ is the energy of light, λ is the measured absorption coefficient, n equals to 0.5 for indirect bandgap or 2 for direct bandgap, and E_g is the bandgap energy. From the Tauc plots, it can be recognized that the bandgap energy of AB@H-RTNR is 2.26 eV that is significantly smaller that the pristine TiO_2 bandgap.

To obtain more insight and a better understanding of the bandgap narrowing phenomenon in AB@H-RTNR, valence band XPS (VB-XPS) was conducted, and the density of electronic states (DOS) was obtained based on the UV–vis absorbance spectra and VB-XPS results. RTNR shows valence band DOS characteristics with the edge of the maximum energy at approximately 1.47 eV, which is similar to previous reports [29], whereas the valence band maximum energy of AB@H-RTNR is estimated to be 1.49 eV followed by a band tail at ~ 0.49 eV (Fig. 5C). A schematic illustration of the energy band structure for the different TiO_2 samples is presented in Fig. 5D. The narrowing of the bandgap from 3.0 eV (RTNR) to 2.72 eV (H-RTNR) is contributed to the VB tails and further to 2.26 eV (AB@H-RTNR) as the synergistic effect of heterojunction and oxygen vacancies. The lattice distortion has a great influence on the migration and recombination of charge pairs, and both oxygen vacancies and lattice distortion could greatly improve the photocatalytic activity of AB@H-RTNR.

3.2. Electrochemical characterization

The electrochemical impedance spectra (EIS) have been used to study the interfacial PEC properties on TiO_2 electrodes (Fig. 6A). The Nyquist plots for the four different as-prepared samples under UV light irradiation are obtained with 1.0 M NaOH solution. All Nyquist plots present similarity in the shape of circular arcs with different radius. The circular arc radiuses of hydrogenated TiO_2 nanostructures are much smaller than the pristine samples, suggesting that the introduction of oxygen vacancies by hydrogenation treatment is more beneficial to the separation of photo-induced carriers (h^+-e^-) [41]. Moreover, the

smaller circular arc radius of branched material's plots compared to non-branched material's plots can be attributed to the anatase/rutile TiO_2 heterojunction structure and enlarged surface area of branch structure, which enhances separation of photogenerated charge carriers and provides more active sites for photocatalytic reaction. The inset in Fig. 6A is the corresponding equivalent circuit, where R_s is the system resistance, CPE is the double layer capacitance and R_{ct} is the interface transfer resistance. The R_{ct} results fitted by the equivalent circuit are listed in Table 1. The interface charge transfer resistance of AB@H-RTNR (23.72 Ω) is smaller than that of other electrodes, indicating that the AB@H-RTNR electrode displays greater separation efficiency of photogenerated electron-hole pairs and faster charge transfer than that of the other electrode at the solid-liquid interface. Mott–Schottky (MS) plots (Fig. 6B) have been used to study the flat band potentials of the samples. All the samples show a typical n-type nature in their MS curves with positive slopes. The slope values of all the samples are presented in Table 1. AB@H-RTNR possesses a smaller slope value (0.71) compared to all the other samples, indicating that it has a higher donor density (N_d), according to the following Equation [42].

$$N_d = \frac{2/e_0 \varepsilon \varepsilon_0}{d(1/C^2)/dV} \tag{3}$$

Where N_d is the donor density, e_0 is the electron charge, ε is the dielectric constant of rutile TiO_2 and ε_0 is the permittivity in vacuum. Since the value of e_0, ε and ε_0 are constants, the donor density is inversely proportional to the slope value obtained from the plots [35]. The smallest photo-induced carrier density of AB@H-RTNR is owing to the presence of the disordered layer in bulk and the heterophase structure, which benefits the PEC performance. This result is also consistent with the smallest semicircle radius of the AB@H-RTNR Nyquist plot, which further demonstrates that the hydrogenation of the heterophase interface promoting the transfer of photogenerated carriers.

3.3. Photoelectrochemical characterization

To investigate the PEC properties of different photocatalysts, their performances in photodegrading are characterized in 0.1 M $NaNO_3$
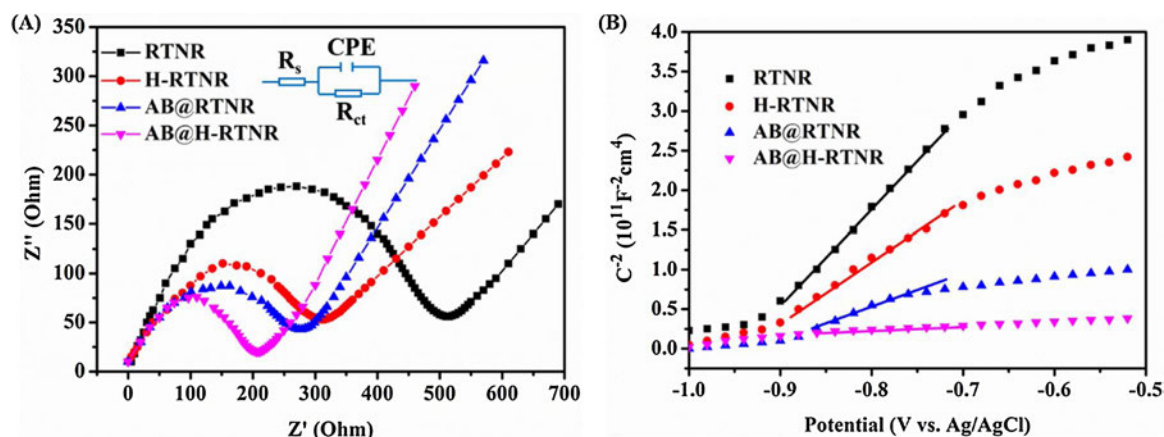
Fig. 6. (A) Nyquist plots of electrochemical impedance and (B) Mott-Schottky plots obtained at 1 kHz of (a) RTNR, (b) H-RTNR and (c) AB@H-RTNR.

Table 1
Interface transfer resistance and slope value of Mott-Schottky plots for three different photocatalysts.

Photocatalysts	RTNR	H-RTNR	AB@RTNR	AB@H-RTNR
R_{ct} (Ω)	75.16	35.28	37.04	23.72
Slope value	11.87	7.33	3.37	0.71

solution under constant UV-LED irradiation with an intensity of $6.6 \, mW/cm^2$. As it is shown in the linear sweep voltammograms (LSV) under UV irradiation (Fig. 7A), the photocurrent increased significantly with the applied potential before reaching a plateau, which is ascribed to the photo-induced holes oxidizing water molecules to produce photocurrent. The photocurrent becomes saturated when the applied potential is more positive than $+0.3$ V (versus Ag/AgCl reference electrode), implying that almost all the electrons generated from oxidizing water molecules by photogenerated holes in the samples are transferred to the counter electrode via electronic circuit at this potential bias. Therefore, a further increase in applied potential would not result in a significant increase in the photocurrent. Consequently, $+0.3$ V (vs. Ag/AgCl reference electrode) has been chosen as the constant applied potential bias for the following PEC experiments. The saturated photocurrent of AB@H-RTNR was higher than that of all the other electrodes, indicating that AB@H-RTNR possesses superior oxidizing ability than other as-prepared photocatalysts.

Fig. 7B exhibits the photocurrent density profiles for all the samples with and without illumination under $+0.3$ V constant potential bias. It is displayed that the photocurrent density of all as-prepared

photoelectrodes can be negligible in the dark. Under UV illumination, the AB@H-RTNR electrode exhibits a photocurrent density $1.79 \, mA/cm^2$, which is 2.42 and 1.42 times higher than that of the H-RTNR electrode ($0.74 \, mA/cm^2$) and the AB@RTNR electrode ($1.26 \, mA/cm^2$), respectively, indicating that AB@H-RTNR has favorable efficient charge separation ability than none branched and none hydrogenated as-prepared photocatalysts. Additionally, Fig. 7B also present that all the photoanodes possess excellent stability during 6000 s test under UV-LED illumination. The favorable photoelectrochemical performance of AB@H-RTNR is mainly attributed to the synergetic effect between the branched heterojunction structure and hydrogenation. The branched anatase TiO_2 structure increases the surface area of the photocatalyst, leading to an increase in both light absorption capacity and activity sites for photocatalytic reaction. The heterophase structure promotes the separation of photogenerated charge carriers of anatase TiO_2 branch and rutile TiO_2 nanorods. Furthermore, hydrogenation treatment produces the oxygen holes that further enhance the range of light absorption and facilitate the separation of photogenerated electrons and holes.

3.4. Analytical principle and performance

An analytical principle is carried out based on the nonexhaustive photocatalytic oxidation model according to our previous work [6]. Briefly speaking, different photocurrent–time profiles can be obtained with and without organic compounds at photoanode in the bulk cell under UV illumination at an applied potential (Fig. 8A). When no illumination is applied to the system, the photocurrent is steady and around zero. After inducing irradiation onto the photocatalyst, the
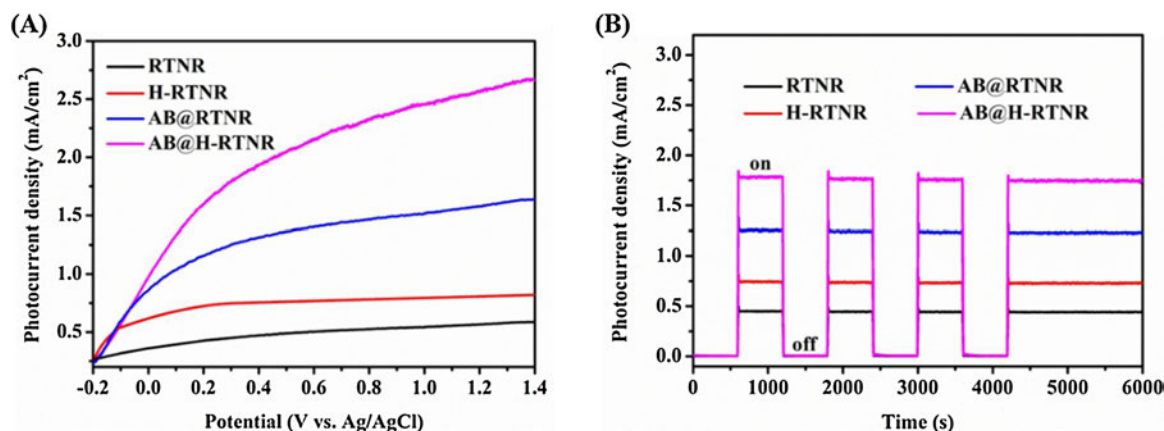

Fig. 7. (A) The linear sweep voltammograms of the as-prepared electrodes in 0.1 M $NaNO_3$ solution under UV light at a scanning rate of 20 mV/s; (B) photocurrent density profiles acquired at $+0.3$ V in the dark and under UV light with as-prepared photocatalysts.
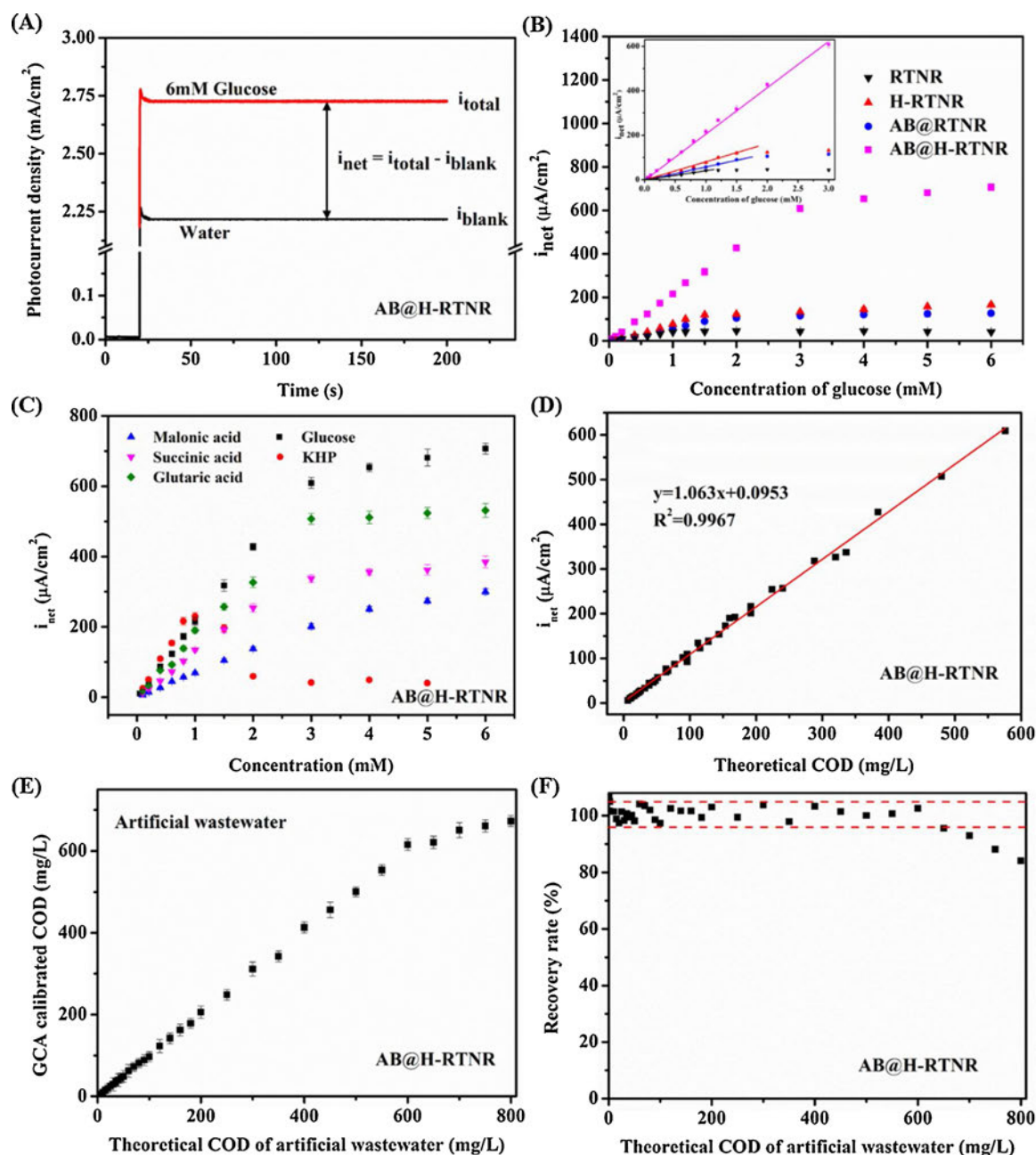
Fig. 8. (A) Typical photocurrent profiles of AB@H-RTNR electrode in water and 6 mM glucose solution; (B) the plot of i_{net} against glucose solution with different concentrations for as-prepared electrodes; (C) the plot of i_{net} against different organic solution with various concentrations for AB@H-RTNR electrode under UV light; (D) linear relationship between i_{net} and theoretical COD values for AB@H-RTNR under UV light; (E) the plot of GCA calibrated COD value against theoretical COD value of artificial wastewater and (F) recovery rate of COD testing with AB@H-RTNR photoelectrode.

photocurrent increases rapidly and then decreased to a steady value. When no organic compounds are injected into the system, the stable background photocurrent i_{blank} is ascribed to the oxidation of water at the surface of the photocatalysts. After injecting organics into the reactor, the net steady-state photocurrent i_{net}, which is generated from degrading organics, can be obtained by subtracting the blank photocurrent i_{blank} from the total photocurrent i_{total}.

$$i_{net} = i_{total} - i_{blank} \tag{4}$$

Under the optimized condition according to several postulates, i_{net} is directly proportional to COD concentrations (Eq. (5)) [6]

$$i_{net} \propto COD \tag{5}$$

To validate this analytical principle on as-prepared photocatalysts,

the COD testing experiments are carried out with different concentrations of glucose solution (Fig. 8B). When the glucose concentration in solution increases, the bare RTNR electrode presents an excellent linear calibration line from 0 to 1.0 mM due to the limiting step of mass transport of organic compounds. Nevertheless, when the concentration of glucose exceeds 1.0 mM, the RTNR electrode reaches its oxidation capacity and the photocurrent becomes steady. With the introduction of anatase TiO_2 branches structure and hydrogenation treatment, i.e., AB@H-RTNR electrode, which results in promoted oxidation capacity of photocatalysts as mentioned before, the linearly increased i_{net} range has been extended to 0 – 3 mM, indicating the promoting of PEC degradation ability can lead to a wider linear detection range for glucose solution. Therefore, using AB@H-RTNR electrode as a PeCOD sensor will further improve the detection range of the photocurrent-based

analytical method.

Besides glucose, the photocurrent response towards other organic compounds is also tested under UV light. As it is shown in Fig. 8C, linear relationships between the net photocurrent at the surface of AB@H-RTNR and substrate concentration are obtained for all cases investigated in a wide extent except for potassium hydrogen phthalate (KHP) of which linear detection range (0-0.8 mM) is smaller due to its chemical stability. Additionally, the slope values of linear detection parts are different when the i_{net} values are plotted against the concentrations of different types of organics. This is due to the varying oxidation number of glucose (24 e⁻), KHP (30 e⁻), malonic acid (8 e⁻), succinic acid (14 e⁻) and glutaric acid (20 e⁻). To calibrate the i_{net} curves, theoretical COD value for each solution is calculated, and subsequently, i_{net} values are normalized and plotted against theoretical COD value (Fig. 8D). As anticipated, the linear fit of data has resulted in an R^2 value of 0.9963. The reproducibility is represented by an average relative standard deviation (RSD) of 1.5 %, obtained from 30 replicated injections of 100 ppm glucose. In the stability test, electrode fouling caused by chemical and biological contamination are not observed in 60 days, and each electrode is capable of ca. 3000 measurements.

An artificial wastewater sample analysis is also carried out to investigate the performance of COD testing with AB@H-RTNR in a real sample. The artificial wastewater consists of six organic matters: 0.075 g glucose, 0.075 g D-ribose, 0.14 g KHP, 0.2 g sodium acetate, 0.24 g L-cysteine, and 0.25 g glycine (per liter of distilled water). The combination of these organic sources could represent the fermentation and hydrolysis products from typical biogenic compounds (proteins, carbohydrates, etc.) [43]. A carbonate buffer solution consists of Na_2CO_3 (1.0 mg/L) is used for adjusting theoretical COD values for the experiment. NH_4Cl and KCl are used for adjusting pH to 8. The theoretical COD of the artificial wastewater is calculated to be 800 mg/L, and the COD value of each composition in the artificial water sample is listed in Table 2. To minimize the interference of changing parameters, e.g., pH, temperature, a standard addition method is chosen for determining the COD value of artificial sample, and Ground Control Approach (GCA) is used for calibration. Fig. 8E shows the correlation between experimental COD values and theoretical COD values. The recovery rate of this calibration method is exhibited in Fig. 8F. Within the detection range (1.25 − 576 ppm COD), the recovery rate fluctuates between 100 % ± 4 %, suggesting the favorable performance of AB@H-RTNR in testing the COD of artificial wastewater sample. The linear detection range, stability, and lifetime are higher than our previous work [6], which is attributed to the oxygen vacancies in crystal lattice generated by the hydrogenation process, as well as the in-situ growth of rutile-nanorod TiO_2 on FTO and of anatase TiO_2 branches on hydrogenated rutile TiO_2.

3.5. Roles of oxygen vacancy on the photocatalytic performance

The roles of oxygen vacancy on the photocatalytic performance can be explained using the energy levels of composition in the as-prepared AB@H-RTNR electrode as shown in Scheme 1. Firstly, we calculated the bandgap energy of AB@H-RTNR from Tauc plot (Fig. 5b) to be 2.26 eV. Secondly, we used VB-XPS (Fig. 5c) to obtain the energy levels of the

Table 2
Composition of artificial wastewater and theoretical COD values of six carbon sources.

Carbon source	Concentration (g/L)	Theoretical COD (mg/L)
Glucose	0.075	80
D-ribose	0.075	80
KHP	0.14	160
Sodium acetate	0.2	160
L-cysteine	0.24	160
Glycine	0.25	160

valence band and mid-band state, which is 1.49 eV and 0.49 eV (vs. RHE), respectively. Finally, the conduction band energy level of AB@H-RTNR is -1.77 eV (vs. RHE), obtained by subtracting 2.26 eV from 0.49 eV (vs. RHE).

According to the results from all the experiment measurements, the enhanced photocatalytic activity of AB@H-RTNR can be ascribed to three aspects. Firstly, the branched structure physically enlarges the surface area of photocatalysts compared to bare nanorods structure, which improves the exposure ratio of nanomaterial to irradiation and creates more active sites for photocatalytic reaction. Moreover, the heterophase structure achieved by the in-situ growth of anatase TiO_2 onto rutile TiO_2 favors the separation of photogenerated electrons and holes. Under UV irradiation, electrons are stimulated from VBs of both anatase and rutile TiO_2 to their CBs, leaving photo-induced holes in VBs. Due to the energy level positions of anatase and rutile TiO_2 (Scheme 1), photo-induced electrons tend to move from CB of anatase (higher energy level) to CB of rutile (lower energy level) and holes transfer from VB of rutile (lower energy level) to VB of anatase (higher energy level). Keeping reduction and oxidation processes in different regions can significantly reduce the recombination of photo-induced electrons and holes. This conclusion has been reported by several studies in the literature [44,45]. Another reason for AB@H-RTNR's favorable photocatalytic activity is the hydrogenation process. After hydrogenation, new energy levels E_{ov} and E_{Ti-OH} will be produced, which are located below the CB and VB of rutile TiO_2 [46]. These new energy levels introduce the mid-gap state of the mixed-phase structure and further enhance the separation of photo-induced electrons and holes (Scheme 1). Based on these three factors, photogenerated electrons are rapidly transferred through the one-dimensional rutile TiO_2 nanorods to the conducting substrate and then to the counter electrode. A large number of photogenerated holes accumulate on the TiO_2 nanobranches, which can rapidly oxidize organic compounds in the sample solution. Therefore, the AB@H-RTNR sensor displays superior photocurrent response to organic compounds and thus holds wider detecting linear range, better stability, and longer lifetime.

An overview of works published on COD sensing as well as our work was shown in Table 3. The AB@H-RTNR photoelectrode exhibits outstanding detection limit and linear range in COD sensing comparing with those none noble metal doped photoelectrode. When comparing with the noble metal doped photoelectrodes, the detection limit of COD sensing using AB@H-RTNR is very close to them. Considering the expense of synthesizing material, AB@H-RTNR is a cost-efficient material for COD testing.
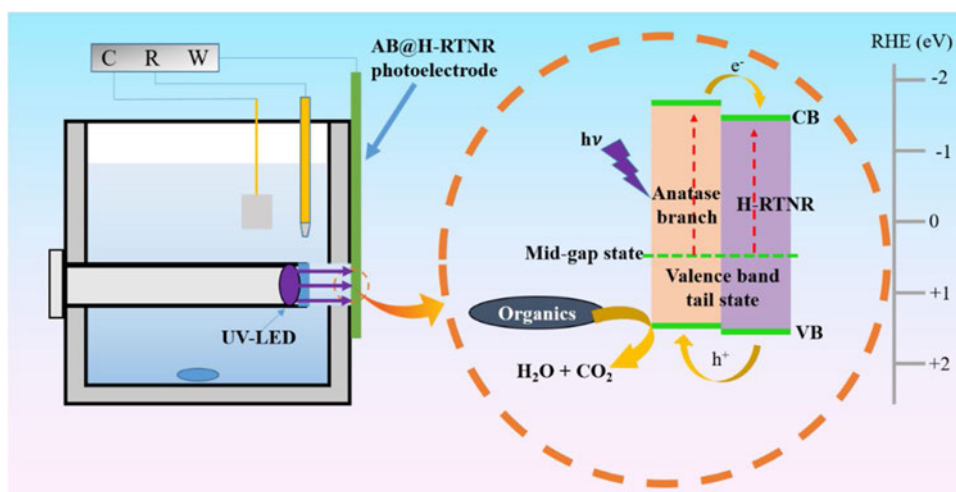
4. Conclusion

An anatase-branch@hydrogenated rutile-nanorod (AB@H-RTNR) TiO_2 electrode has been designed and successfully prepared via a two-step hydrothermal method combined with a hydrogenation process. The role of hydrogenation in AB@H-RTNR is investigated. The as-prepared photoanodes successfully achieved sensitive determination of COD with a detection limit of 0.2 ppm (S/N = 3), an RSD% of 1.5 %, a wide linear detection range of 1.25 − 576 ppm and an average recovery rate fluctuating between 100 % ± 4 % for artificial wastewater sample analyses. Such performances are outstanding in comparison with the standard COD method. Furthermore, AB@H-RTNR photoelectrode has a long lifetime. The superior PEC performance of AB@H-RTNR can be ascribed to the anatase-branch@rutile-nanorod TiO_2 heterophase structure and oxygen vacancy generated by hydrogenation, which increases the number of active sites for photocatalytic reaction, enhance light absorption and facilitate separation efficiency of photogenerated charge carriers. The improved photocatalysts overcome the shortcomings of the previous photocurrent-based PeCOD method with insufficient photocatalytic activity and short lifetime. Moreover, a wider detection range provides the possibility of detecting samples directly without dilution, which favors its commercialization for the real site

Scheme 1. Schematic diagram of the PEC reactor and possible working mechanism for photo-induced electron-hole pairs separation and transport on the interface of AB@H-RTNR under UV light irradiation.

Table 3
PeCOD testing using different processes.

Photocatalyst	Light source	Detection limit (mg/L COD)	Linear range (mg/L COD)	Ref
AB@H-RTNR	$6.6\,mW/cm^2$ UV-LED	0.2	1.25-576	This work
Pt-NPs/TNTAs/Ti	5W UV light	0.12	1.44-672	Si, 2019 [47]
3D Au-NPs/TNTAs		0.18	1.96-3360	Si, 2019 [48]
Nano TiO_2 colloid/H_2O_2	30W UV lamp	–	50-150	Shen, 2018 [49]
Nano-Cu/Cu	–	1.07	2-595	Hassan, 2018 [50]
A-$Bi_2Mo_3O_{12}$/TiO_2	UV-LED	2.05	0.366-208.9	Pang, 2017 [51]
Nano-Cu/GCE	UV light	1.7	15-629.3	Badr, 2017 [52]
Hierarchically-TNTs	4W UV lamp	1	0-300	Heng, 2016 [53]
Nanoporous TiO_2	UV lamp	8	20-250	Zhang, 2016 [54]

industry.

Author contribution statements

Meng Zu, Shengsen Zhang and Shanqing Zhang conceived of the presented idea. Meng Zu and Shengsen designed and developed the experimental plan. Meng Zu and Mengting Zheng carried out the experiment. All the authors discussed the results, analysis of the data and contributed to the final conclsion of this work. Meng Zu and Mengting wrote the manuscript under the supervision of Shengsen Zhang and Shanqing Zhang.

Declaration of Competing Interest

None.

Acknowledgments

References

[1] Y.J. Chan, M.F. Chong, C.L. Law, D.G. Hassell, A review on anaerobic-aerobic treatment of industrial and municipal wastewater, Chem. Eng. J. 155 (2009) 1–18.

[2] A.P. Ligon, S. Zuehlke, M. Spiteller, GC-MS analysis of organic compounds in wastewater and sewage sludge, J. Sep. Sci. 31 (2008) 143–150.

[3] C. Wang, W. Li, M. Huang, High precision wide range online chemical oxygen demand measurement method based on ultraviolet absorption spectroscopy and full-spectrum data analysis, Sens. Actuatosr B-Chem. 300 (2019) 126943.

[4] A.P. Beltrá, J. Iniesta, L. Gras, F. Gallud, V. Montiel, A. Aldaz, A. Canals, Development of a fully automatic microwave assisted chemical oxygen demand (COD) measurement device, Instrum. Sci. Technol. 31 (2003) 249–259.

[5] S. Zhang, D. Jiang, H. Zhao, Development of chemical oxygen demand on-line monitoring system based on a photoelectrochemical degradation principle, Environ. Sci. Technol. 40 (2006) 2363–2368.

[6] S. Zhang, L. Li, H. Zhao, A portable photoelectrochemical probe for rapid determination of chemical oxygen demand in wastewaters, Environ. Sci. Technol. 43 (2009) 7810–7815.

[7] X. Chen, S.S. Mao, Titanium dioxide nanomaterials: synthesis, properties, modifications, and applications, Chem. Rev. 107 (2007) 2891–2959.

[8] H. Zhao, D. Jiang, S. Zhang, W. Wen, Photoelectrocatalytic oxidation of organic compounds at nanoporous TiO_2 electrodes in a thin-layer photoelectrochemical cell, J. Catal. 250 (2007) 102–109.

[9] S. Zhang, W. Wen, D. Jiang, H. Zhao, R. John, G.J. Wilson, G.D. Will, Photoelectrochemical characterisation of TiO_2 thin films derived from microwave hydrothermally processed nanocrystalline colloids, J. Photochem. Photobiol. A Chem. 179 (2006) 305–313.

[10] S. Zhang, H. Zhao, D. Jiang, R. John, Photoelectrochemical determination of chemical oxygen demand based on an exhaustive degradation model in a thin-layer cell, Anal. Chim. Acta 514 (2004) 89–97.

[11] H. Zhao, D. Jiang, S. Zhang, K. Catterall, R. John, Development of a direct photo-electrochemical method for determination of chemical oxygen demand, Anal. Chem. 76 (2004) 155–160.

[12] D. Jiang, H. Zhao, S. Zhang, R. John, Comparison of photocatalytic degradation kinetic characteristics of different organic compounds at anatase TiO_2 nanoporous film electrodes, J. Photochem. Photobiol. A Chem. 177 (2006) 253–260.

[13] Y. Ma, X. Zhu, S. Xu, G. He, L. Yao, N. Hu, Y. Su, J. Feng, Y. Zhang, Z. Yang, Gold nanobipyramid@cuprous oxide jujube-like nanostructures for plasmon-enhanced photocatalytic performance, Appl. Catal. B Environ. 234 (2018) 26–36.

[14] Y. Ma, X. Li, Z. Yang, S. Xu, W. Zhang, Y. Su, N. Hu, W. Lu, J. Feng, Y. Zhang, Morphology control and photocatalysis enhancement by in situ hybridization of cuprous oxide with nitrogen-doped carbon quantum dots, Langmuir 32 (2016) 9418–9427.

[15] M. Li, X. Tu, Y. Wang, Y. Su, J. Hu, B. Cai, J. Lu, Z. Yang, Y. Zhang, Highly enhanced visible-light-driven photoelectrochemical performance of ZnO-modified In_2S_3 nanosheet arrays by atomic layer deposition, Nano Micro Lett. 10 (2018) 45.

[16] X. Zhu, H. Jia, X.-M. Zhu, S. Cheng, X. Zhuo, F. Qin, Z. Yang, J. Wang, Selective Pd deposition on Au nanobipyramids and Pd site-dependent plasmonic photocatalytic activity, Adv. Funct. Mater. 27 (2017).

[17] H. Sutiono, A.M. Tripathi, H.M. Chen, C.H. Chen, W.N. Su, L.Y. Chen, H. Dai, B.J. Hwang, Facile synthesis of [101]-oriented rutile TiO_2 nanorod array on FTO substrate with a tunable anatase-rutile heterojunction for efficient solar water-

splitting, ACS Sustain. Chem. Eng. 4 (2016).

[18] S. Zhang, X. Wang, J. Hu, Z. Xie, H. Lei, F. Peng, Design of two kinds of branched TiO$_2$ nano array photoanodes and their comparison of photoelectrochemical performances, Electrochim. Acta (2017).

[19] J. Liu, X. Yu, Q. Liu, R. Liu, X. Shang, S. Zhang, W. Li, W. Zheng, G. Zhang, H. Cao, Surface-phase junctions of branched TiO$_2$ nanorod arrays for efficient photoelectrochemical water splitting, Appl. Catal. B Environ. 158–159 (2014) 296–300.

[20] J.S. Yang, W.P. Liao, J.J. Wu, Morphology and interfacial energetics controls for hierarchical anatase/rutile TiO$_2$ nanostructured array for efficient photoelectrochemical water splitting, ACS Appl. Mater. Interfaces 5 (2013) 7425–7431.

[21] Y. Gao, Z. Jian, H. An, P. Yan, B. Huang, R. Chen, F. Fan, C. Li, Directly probing charge separation at interface of TiO$_2$ phase junction, J. Phys. Chem. Lett. 8 (2017) 1419–1423.

[22] I.S. Cho, Z. Chen, A.J. Forman, R.K. Dong, P.M. Rao, T.F. Jaramillo, X. Zheng, Branched TiO$_2$ nanorods for photoelectrochemical hydrogen production, Nano Lett. 11 (2011) 4978–4984.

[23] Z. Liu, X. Zhang, S. Nishimoto, M. Jin, D.A. Tryk, T. Murakami, A. Fujishima, Anatase TiO$_2$ nanoparticles on rutile TiO$_2$ nanorods: a heterogeneous nanostructure via layer-by-Layer assembly, Langmuir 23 (2007) 10916–10919.

[24] H. Yao, W. Fu, L. Liu, X. Li, D. Ding, P. Su, S. Feng, H. Yang, Hierarchical photoanode of rutile TiO$_2$ nanorods coupled with anatase TiO$_2$ nanosheets array for photoelectrochemical application, J. Alloys Compd. 680 (2016) 206–211.

[25] S. Pavasupree, S. Ngamsinlapasathian, M. Nakajima, Y. Suzuki, S. Yoshikawa, Synthesis, characterization, photocatalytic activity and dye-sensitized solar cell performance of nanorods/nanoparticles TiO$_2$ with mesoporous structure, J. Photochem. Photobiol. A Chem. 184 (2006) 163–169.

[26] S.J. Kwon, H.B. Im, J.E. Nam, J.K. Kang, T.S. Hwang, K.B. Yi, Hydrothermal synthesis of rutile–anatase TiO$_2$ nanobranched arrays for efficient dye-sensitized solar cells, Appl. Surf. Sci. 320 (2014) 487–493.

[27] S. Chen, D. Li, Y. Liu, W. Huang, Morphology-dependent defect structures and photocatalytic performance of hydrogenated anatase TiO$_2$ nanocrystals, J. Catal. 341 (2016) 126–135.

[28] A. Naldoni, M. Allieta, S. Santangelo, M. Marelli, F. Fabbri, S. Cappelli, C.L. Bianchi, R. Psaro, V. Dal Santo, Effect of nature and location of defects on bandgap narrowing in black TiO$_2$ nanoparticles, J. Am. Chem. Soc. 134 (2012) 7600–7603.

[29] X. Chen, L. Liu, F. Huang, Black titanium dioxide (TiO$_2$) nanomaterials, Chem. Soc. Rev. 44 (2015) 1861–1885.

[30] M. Wang, J. Chen, X. Liao, Z. Liu, J. Zhang, L. Gao, Y. Li, Highly efficient photocatalytic hydrogen production of platinum nanoparticle-decorated SiC nanowires under simulated sunlight irradiation, Int. J. Hydrogen Energy 39 (2014) 14581–14587.

[31] Y.-C. Wang, J.M. Wu, Effect of controlled oxygen vacancy on H$_2$-production through the piezocatalysis and piezophototronics of ferroelectric R$_3$C ZnSnO$_3$ nanowires, Adv. Funct. Mater. 30 (2020) 1907619.

[32] S. Zhang, S. Zhang, B. Peng, H. Wang, H. Yu, H. Wang, F. Peng, High performance hydrogenated TiO$_2$ nanorod arrays as a photoelectrochemical sensor for organic compounds under visible light, Electrochem. Commun. 40 (2014) 24–27.

[33] G. Wang, H. Wang, Y. Ling, Y. Tang, X. Yang, R.C. Fitzmorris, C. Wang, J.Z. Zhang, Y. Li, Hydrogen-treated TiO$_2$ nanowire arrays for photoelectrochemical water splitting, Nano Lett. 11 (2011) 3026–3033.

[34] J. Yan, X. Li, S. Yang, X. Wang, W. Zhou, Y. Fang, S. Zhang, F. Peng, S. Zhang, Design and preparation of CdS/H-3D-TiO$_2$ /Pt-wire photocatalysis system with enhanced visible-light driven H$_2$ evolution, Int. J. Hydrogen Energy 42 (2017) 928–937.

[35] C.C. Wang, P.H. Chou, Effects of various hydrogenated treatments on formation and photocatalytic activity of black TiO$_2$ nanowire arrays, Nanotechnology 27 (2016) 325401.

[36] Z. Lu, C.-T. Yip, L. Wang, H. Huang, L. Zhou, Hydrogenated TiO$_2$ nanotube arrays as high-rate anodes for lithium-ion microbatteries, ChemPlusChem 77 (2012) 991–1000.

[37] T. Leshuk, R. Parviz, P. Everett, H. Krishnakumar, R.A. Varin, F. Gu, Photocatalytic activity of hydrogenated TiO$_2$, ACS Appl. Mater. Interfaces 5 (2013) 1892–1895.

[38] Y. Yan, M. Han, A. Konkin, T. Koppe, D. Wang, T. Andreu, G. Chen, U. Vetter, J.R. Morante, P. Schaaf, Slightly hydrogenated TiO2 with enhanced photocatalytic performance, J. Mater. Chem. A 2 (2014) 12708–12716.

[39] X. Zhang, W. Hu, K. Zhang, J. Wang, B. Sun, H. Li, P. Qiao, L. Wang, W. Zhou, Ti^{3+} self-doped black TiO2 nanotubes with mesoporous nanosheet architecture as efficient solar-driven hydrogen evolution photocatalysts, ACS Sustain. Chem. Eng. 5 (2017) 6894–6901.

[40] J. Tauc, Optical properties and electronic structure of amorphous Ge and Si, Mater. Res. Bull. 3 (1968) 37–46.

[41] Y.K. Lai, J.Y. Huang, H.F. Zhang, V.P. Subramaniam, Y.X. Tang, D.G. Gong, L. Sundar, L. Sun, Z. Chen, C.J. Lin, Nitrogen-doped TiO$_2$ nanotube array films with enhanced photocatalytic activity under various light sources, J. Hazard. Mater. 184 (2010) 855–863.

[42] C. Mao, F. Zuo, Y. Hou, X. Bu, P. Feng, In situ preparation of a Ti^{3+} self-doped TiO$_2$ film with enhanced activity as photoanode by N$_2$H$_4$ reduction, Angew. Chem. Int. Edit. 53 (2014) 10485–10489.

[43] S. Riedl, R.K. Brown, S. Klöckner, K.J. Huber, B. Bunk, J. Overmann, U. Schröder, Successive conditioning in complex artificial wastewater increases the performance of electrochemically active biofilms treating real wastewater, ChemElectroChem 4 (2017) 3081–3090.

[44] T. Miyagi, M. Kamei, T. Mitsuhashi, T. Ishigaki, A. Yamazaki, Charge separation at

[45] D.O. canlon, C.W. Dunnill, J. Buckeridge, S.A. Shevlin, A.J. Logsdail, S.M. Woodley, C.R.A. Catlow, M.J. Powell, R.G. Palgrave, I.P. Parkin, G.W. Watson, T.W. Keal, P. Sherwood, A. Walsh, A.A. Sokol, Band alignment of rutile and anatase TiO$_2$, Nat. Mater. 12 (2013) 798–801.

[46] J. Hu, S. Zhang, Y. Cao, H. Wang, H. Yu, F. Peng, Novel highly active anatase/rutile TiO$_2$ photocatalyst with hydrogenated heterophase interface structures for photoelectrochemical water splitting into hydrogen, ACS Sustain. Chem. Eng. 6 (2018) 10823–10832.

[47] H. Si, N. Pan, X. Zhang, J. Liao, M.N. Rumyantseva, A.M. Gaskov, S. Lin, A real-time on-line photoelectrochemical sensor toward chemical oxygen demand determination based on field-effect transistor using an extended gate with 3D TiO$_2$ nanotube arrays, Sens. Actuators B Chem. 289 (2019) 106–113.

[48] H. Si, X. Zhang, S. Lin, A simple flow injection sensing system for the real-time on-line determination of chemical oxygen demand based on 3D Au-NPs/TiO$_2$ nanotube arrays, Front. Mater. 6 (2019) 238.

[49] W. Shen, F. Huang, X. Zhang, Y. Zhu, X. Chen, N. Akbarjon, On-line chemical oxygen demand estimation models for the photoelectrocatalytic oxidation advanced treatment of papermaking wastewater, Water Sci. Technol. 78 (2018) 310–319.

[50] H.H. Hassan, I.H.A. Badr, H.T.M. Abdel-Fatah, E.M.S. Elfeky, A.M. Abdel-Aziz, Low cost chemical oxygen demand sensor based on electrodeposited nano-copper film, Arab. J. Chem. 11 (2018) 171–180.

[51] Y. Pang, G. Xu, Q. Feng, J. Liu, J. Lv, Y. Zhang, Y. Wu, Synthesis of alpha-Bi$_2$Mo$_3$O$_{12}$/TiO$_2$ nanotube arrays for photoelectrochemical COD detection application, Langmuir 33 (2017) 8933–8942.

[52] I.H.A. Badr, H.H. Hassan, E. Hamed, A.M. Abdel-Aziz, Sensitive and green method for determination of chemical oxygen demand using a nano-copper based electrochemical sensor, Electroanalysis 29 (2017) 2401–2409.

[53] W. Heng, W. Zhang, Q. Zhang, H. Wang, Y. Li, Photoelectrocatalytic microfluidic reactors utilizing hierarchical TiO$_2$ nanotubes for determination of chemical oxygen demand, RSC Adv. 6 (2016) 49824–49830.

[54] Z. Zhang, X. Chang, A. Chen, Determination of chemical oxygen demand based on photoelectrocatalysis of nanoporous TiO$_2$ electrodes, Sens. Actuators B Chem. 223 (2016) 664–670.

Mr. Meng Zu Mr. Meng Zu is currently PhD student in Centre for Clean Environment and Energy, School of Environment and Science, Griffith University, Australia. He received his Master degree from the Department of Civil and Environmental Engineering, Cornell University in 2016. Meng's research interests include the design and development of functional nanomaterials for photoelectrocatalytic sensing and treatment of aquatic pollutants.

A/Prof. Shengsen Zhang Dr. Shengsen Zhang obtained his Ph.D. degree in Industrial Catalysis from South China University of Technology, China in 2012. He is now an associate professor at College of Materials and Energy, South China Agricultural University, China. His research areas include synthesis, modification, and characterization of nanostructured materials for waste water purification, sensing, and energy conversion.

Prof. Shanqing Zhang Prof. Shanqing Zhang obtained his PhD degree in electrochemistry in 2001 at Griffith University, Australia. Since then, he has been working on synthesis, modification, characterization of nanostructured materials for sensing, energy conversion and energy storage devices. As an inventor, Eddie has developed a series of patented and commercialized photoelectrochemical sensors for environmental monitoring based on the functional nanomaterials. He was awarded Australia Research Council Future Fellow in photoelectrocatalysis for 2009-2013. Currently, Prof. Zhang is leading his group carry out a wide spectrum of research in the areas of energy conversion, energy storage and environmental monitoring.

CHAPTER 4

Portable wastewater treatment system based on synergistic photocatalytic and persulphate degradation under visible light

4.1 INTRODUCTORY REMARKS

This chapter includes one published article in *SCIENCE CHINA Materials*, 2021, 1-12.

In this work, photocatalysts, i.e., hydrogenated anatase branched-rutile TiO_2 nanorod (H-AB@RTNR), were fabricated to enable PC degradation to occur under visible light to improve the utilization of solar energy. It was discovered that the addition of PS resulted in the synergistic degradation of tenacious and persistent organics, dramatically improving the extent and kinetics of the degradation. A degradation rate of 100% and a reaction rate constant of 0.0221 min^{-1} for degrading 1 L rhodamine B (20 mg L^{-1}) were achieved in 120 min in a specially designed thin-layer cell under visible light irradiation. This work suggests that the proposed synergistic degradation design is a promising solution for building a portable wastewater treatment system.

4.2 STATEMENT OF CONTRIBUTION

This chapter includes a published paper. The bibliographic details of the co-authored paper, including all authors, are:

<u>Meng Zu</u>, Shengsen Zhang, Changyu Liu, Porun Liu, Dongsheng Li, Chao Xing, Shanqing Zhang

Portable wastewater treatment system based on synergistic photocatalytic and persulphate degradation under visible light

SCIENCE CHINA Materials, 2021, 1-12.

My contribution to the paper involved:

Initial concept and theoretical calculation framework and implementation; Collection and analysis of data; Preparation of manuscript.

(Signed)⬛⬛⬛⬛ (Date) <u>15-04-2021</u>

Name of Student: Meng Zu

(Countersigned)⬛⬛⬛⬛ (Date) <u>15-04-2021</u>

Corresponding author of paper: Shanqing Zhang

(Countersigned)⬛⬛⬛⬛ (Date) <u>15-04-2021</u>

Supervisor: Shanqing Zhang

4.3 Article 3

Portable wastewater treatment system based on synergistic photocatalytic and persulphate degradation under visible light

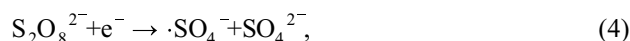Meng Zu[1], Shengsen Zhang[2*], Changyu Liu[3], Porun Liu[1], Dong-Sheng Li[4], Chao Xing[1,5] and Shanqing Zhang[1*]

ABSTRACT   Highly efficient, low-cost, and portable wastewater treatment and purification solutions are urgently needed for aqueous pollution removal, especially at remote sites. Synergistic photocatalytic (PC) and persulphate (PS) degradation under visible light offers an exceptional alternative for this purpose. In this work, we coupled a TiO_2-based PC system with a PS oxidation system into a portable advanced oxidation device for rapid and deep degradation of organic contaminants in wastewater. Using hydrogenation, we fabricated hydrogenated anatase branched-rutile TiO_2 nanorod (H-AB@RTNR) photocatalysts which enable the PC degradation to occur under visible light and improve the utilization of solar energy. We also discovered that the addition of PS resulted in the synergistic degradation of tenacious and persistent organics, dramatically improving the extent and kinetics of the degradation. A degradation rate of 100% and a reaction rate constant of 0.0221 min^{-1} for degrading 1 L rhodamine B (20 mg L^{-1}) were achieved in 120 min in a specially designed thin-layer cell under visible light irradiation. The superior performance of the synergistic PC and PS degradation system was also demonstrated in the degradation of real industrial wastewater. Both remarkable performances can be attributed to the heterophase junction and oxygen vacancies in the photocatalyst that facilitate the catalytic conversion of PS anions into highly active radicals ($\cdot SO_4^-$ and $\cdot OH$). This work suggests that the as-proposed synergistic degradation design is a promising solution for building a portable wastewater treatment system.

Keywords: synergistic effect, hydrogenated TiO_2, oxygen vacancies, persulphate, thin-layer cell, real wastewater

INTRODUCTION

Toxic chemical dyes are frequently used in the textile industry and have severe implications for environmental and human health [1,2]. For some remote textile plants, highly efficient, scalable, portable, and low-cost devices for wastewater treatment and purification are urgently needed [3]. Among numerous wastewater treatment and purification methods, synergistic photocatalytic (PC) and persulphate (PS) degradation technologies (PC-PS) have aroused enormous attention due to their potent degradation ability of tenacious dye contaminants [4,5]. The synergistic effects between PC and PS anions can be explained by two mechanisms. Firstly, the photogenerated electrons (e$^-$) from the PC process can effectively convert PS anions ($S_2O_8^{2-}$, E^0 = 2.01 V vs. normal hydrogen electrode (NHE)) to sulphate radicals ($\cdot SO_4^-$, E^0 = 2.60 V vs. NHE), which enhances the degradation performance. Secondly, the consumption of e$^-$ by the activation process of $S_2O_8^{2-}$ can facilitate the separation of photogenerated electron-hole pairs, which in turn enhances the PC performance [6]. Accordingly, the PC process and PS technology mutually improve the degradation performance of each other and therefore form synergistic effects in the PC-PS systems (Equations (1–6)):

$$\text{Photocatalysts} \xrightarrow{h\nu} \text{h}^+ + \text{e}^-, \tag{1}$$

$$\text{e}^- + O_2 \rightarrow \cdot O_2^-, \tag{2}$$

$$\text{h}^+ + H_2O \rightarrow \cdot OH, \tag{3}$$

$$S_2O_8^{2-} + \text{e}^- \rightarrow \cdot SO_4^- + SO_4^{2-}, \tag{4}$$

[1] Centre for Clean Environment and Energy and School of Environment and Science, Griffith University, Gold Coast, QLD 4222, Australia
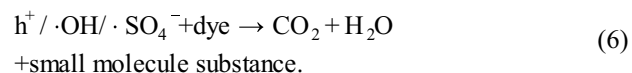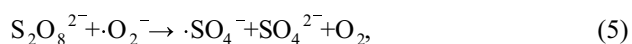[2] College of Materials and Energy, South China Agricultural University, Guangzhou 510643, China
[3] School of Biotechnology and Health Sciences, Wuyi University, Jiangmen 529020, China
[4] College of Materials and Chemical Engineering, Key Laboratory of Inorganic Nonmetallic Crystalline and Energy Conversion Materials, China Three Gorges University, Yichang 443002, China
[5] Key Laboratory of Materials Processing and Mold (Zhengzhou University), Ministry of Education, Zhengzhou 450002, China
* Corresponding authors: (emails: zhangss@scau.edu.cn (Zhang SS); s.zhang@griffith.edu.au (Zhang SQ))

1

$$S_2O_8{}^{2-}+\cdot O_2{}^-\rightarrow \cdot SO_4{}^-+SO_4{}^{2-}+O_2, \tag{5}$$

$$h^+/\cdot OH/\cdot SO_4{}^-+dye\rightarrow CO_2+H_2O \\ +small\ molecule\ substance. \tag{6}$$

To improve the performance of synergistic PC-PS degradation, designing and synthesizing highly efficient photocatalysts plays a critical role. In general, TiO_2 is the most commonly used photocatalyst material due to its appropriate band position, high chemical stability, low cost, and nontoxicity [7]. However, pristine TiO_2 photocatalysts can only be stimulated by UV irradiation because the bandgap of pristine TiO_2 is higher than 3.0 eV, which seriously impedes its utilization in low-cost and environmentally friendly solar energy applications [8]. According to previous studies, building heterojunctions between anatase and rutile TiO_2 effectively enhances solar energy utilization and PC efficiency [9–12]. Though the energy level position of the anatase/rutile heterophase junction is unclear, markedly improved separation rates of photogenerated electrons and holes have been experimentally verified [13–15]. Hydrogenation is another simple method for extending the absorption spectrum of TiO_2-based materials into the visible light region by bringing a disordered layer and oxygen vacancies into photocatalysts [16,17]. On one hand, the synergistic effect of the disordered layer and oxygen vacancies can narrow the bandgap of TiO_2 by introducing a new energy state below the bottom of the conduction band [18]; on the other hand, the electrochemical performance of the photocatalysts can be enhanced after a hydrogenation process, which promotes the separation of photogenerated electron-hole pairs [19,20].

Many studies have confirmed that device design also plays a crucial role in improving the efficiency and reducing the cost of PC reactors [21–23]. A thin-layer reactor, which minimizes the thickness of the aqueous solution and the distance between the irradiation source and photocatalysts, is a promising device design for effective utilization of irradiation [24]. According to Beer's Law, light loss in aqueous solution is inevitable (Equation (7)):

$$A=\varepsilon bc, \tag{7}$$

where A is the absorbance of light; ε is the molar absorptivity; b is the thickness of aqueous solution, and c is the electrolyte concentration. It can be directly inferred from Equation (7) that reducing the thickness of the aqueous solution can directly minimize the light loss in the electrolyte, which demonstrates that the thin-layer reactor will further improve the performance of PC dye degradation.

In this work, a highly efficient, scalable, portable, and low-cost wastewater treatment device was designed for small-scale textile plants at remote sites. Hydrogenated anatase branched-rutile TiO_2 nanorod (H-AB@RTNR) photocatalysts were fabricated and applied to improve the degradation efficiency of rhodamine B (RhB) under visible light irradiation. The effects of mixed-phase TiO_2 and oxygen vacancies generated by the hydrogenation process on the PC pathways were investigated. In addition, the introduction of PS into the PC system synergistically promoted the degradation efficiency of RhB. A thin-layer reactor was designed and built for the practical application of the PC-PS technology, which improved the efficiency, scalability, portability and cost-effectiveness of the reactor. The designed thin-layer reactor circulating flux of 5 L h^{-1} is capable of fully degrading 1 L RhB solution (20 mg L^{-1}) in 120 min with a high reaction rate constant of 0.0221 min^{-1}. Moreover, the thin-layer reactor showed excellent PC degradation capacity for real textile mill wastewater with good removal rates of total organic carbon (TOC, 62.3%) and chemical oxygen demand (COD, 74.8%) in 240 min operation with a circulating flux of 5 L h^{-1}.

EXPERIMENTAL SECTION

Materials and reagents

Fluorine-doped tin oxide (FTO) glass (with a resistance of 8 Ω per square and a thickness of 2.2 mm) was purchased from Delta Technologies Limited (USA) and used as a substrate for TiO_2 film growth. Tetrabutyl titanate (97%) was supplied by Sigma-Aldrich (USA) and employed as the precursors of TiO_2. RhB of commercial-grade was obtained from Sigma-Aldrich (USA). The characteristics of RhB are displayed in Table S1. Other chemical reagents, including hydrochloric acid (HCl, 36.5% by weight), boric acid (H_3BO_3), ammonium hexafluoro-rotitanate ($[NH_4]_2TiF_6$), and sodium nitrate ($NaNO_3$) were of analytical grade and purchased from Sigma-Aldrich (USA). All reagents obtained from Sigma-Aldrich were used as received without further treatment unless otherwise stated. High-purity distilled water (Millipore Corp., 18 MΩ cm) was used in the preparation and dilution of solutions. The real water sample was taken from a textile mill in Queensland, Australia, and represents the original disposal from the textile furnishing process. The sample was stored in a refrigerator at 4°C according to standard method guidelines. The physiochemical properties of the real water sample are displayed in Table S2.

Synthesis of photocatalysts

Rutile TiO_2 nanorod arrays (RTNRs) were prepared according to a previously reported method [25]. Briefly, 20 mL distilled water was mixed with 20 mL HCl (11.9 mol L^{-1}) under vigorous stirring for 20 min. Then, 0.5 mL tetrabutyl titanate (2.94 mol L^{-1}) was added into the well-mixed solution. After stirring for another 20 min, the solution was transferred into a Teflon-lined stainless steel autoclave. Two pieces of well-cleaned FTO glass were half-immersed in the as-prepared solution and heated at 180°C for 12 h in an oven. To synthesize anatase RTNRs (AB@RTNRs), the RTNRs were put into a mixed solution consisting of 24.1 mol L^{-1} H_3BO_3 and 5.3 mol L^{-1} $[NH_4]_2TiF_6$ and subjected to hydrothermal treatment at 60°C for 24 h. The as-prepared samples were cooled to room temperature naturally, then washed several times with distilled water and dried in air. The hydrogenation process was conducted at 200°C in a tube furnace with a mixed gas flow consisting of 5% hydrogen and 95% argon for 1 h to obtain hydrogenated rutile nanorods (H-AB@RTNRs).

Characterizations

The nanostructured morphology was characterized by scanning electron microscopy (SEM, LEO 1530VP, Germany). The crystallographic phase and structure of photocatalysts were tested by X-ray diffraction (XRD) with an X-ray diffractometer (D/max-IIIA, Japan). The Raman spectra were obtained on a Renishaw in Via Raman microscope. X-ray photoelectron spectrophotometer (XPS) analysis was carried out with a Krato Axis Ultra DLD spectrometer with Al Kα X-ray ($h\nu$ = 1486.6 eV) at 15 kV and 150 W to characterize the chemical nature of the Ti and O states. Electron paramagnetic resonance (EPR) spectra were obtained with an E500 (Bruker, Germany) at 77 K and a radiofrequency of 9.442 GHz. UV-visible (UV-vis) spectra were obtained with a UV-vis spectrophotometer (Agilent Cary 300, USA) to characterize the bandgap energy of photocatalysts. The incident photo-to-current conversion efficiency (IPCE) spectra were obtained via an Oriel's QEPVSI-b monochromator system (Oriel Cornerstone™, USA). Fluorescence (FL) spectra were characterized via an F-4500 spectrophotometer (Hitachi, Japan) with an excitation wavelength of 260 nm. To evaluate the charge transportation situation, electrochemical impedance spectroscopy (EIS) testing was carried out under open-circuit voltage, with a 1.0 mol L^{-1} NaOH solution, with frequency ranging from 10 mHz to 1 MHz, and an amplitude of 5 mV on a CHI 660e electrochemical station (CH Instruments™, USA). Mott-

Schottky (M-S) analysis was performed with a potential increment of 5×10^{-2} V, an amplitude of 5×10^{-3} V, and a frequency of 1 kHz.

Dye degradation performance measurement

The evaluation of liquid-phase PC oxidation of RhB was carried out in XPA-system Photochemical Reactors (Nanjing, China). The degraded RhB concentration was analyzed using a Cary 50 spectrophotometer (Varian Co., USA). The percentage of degradation was reported as C/C_0. C is the absorption of RhB at each irradiated time interval of the maximum peak of the absorption spectrum, and C_0 is the absorption of the initial concentration when adsorption/desorption equilibrium is achieved. The TOC and COD represent the amounts of organic compounds in the water sample. The TOC was tested with TOC-V_{CPN} Total Organic Carbon Analyzer (Shimadzu Corp., Japan), and the COD value was examined by an EPA-approved COD analyzer (Merck NOVA 30, USA). The PC dye degradation performance of H-AB@RTNRs was also tested with a homemade thin-layer cell system (Figs S1 and S2). The optical-electronic parameters and spectrum of the LED panel are displayed in Table S3. The details of the homemade thin-layer cell system are available in the Supplementary information.

RESULTS AND DISCUSSION

Materials characterization

Crystalline phase structure and morphology characterization

The crystalline nature and phase of the as-prepared nanocomposite photocatalysts were analyzed by XRD (Fig. 1a). After subtracting the diffraction peaks from FTO glass, the XRD peaks of the pure TiO_2 (RTNRs) were observed at 2θ = 25.6°, 36.1°, 41.2°, 54.3°, 62.8°, and 69.2°, which correspond to the characteristic peaks of tetragonal rutile crystalline phase (ICDD No. 88-1175). The results prove that pure rutile TiO_2 photocatalysts were synthesized on the surface of FTO glass. In the patterns of AB@RTNRs and H-AB@RTNR nanocomposites, new diffraction peaks in addition to the peaks of rutile TiO_2 were simultaneously observed at 2θ = 25.1°, 38.2°, and 47.7°, which are indexed to the characteristic peaks of anatase crystalline phase TiO_2 (ICDD No. 88-1175). The XRD patterns provide evidence that the anatase crystalline TiO_2 nanostructures exist in the branched-photocatalysts. Moreover, no additional peak was observed after the hydrogenation process, indicating that hydro-
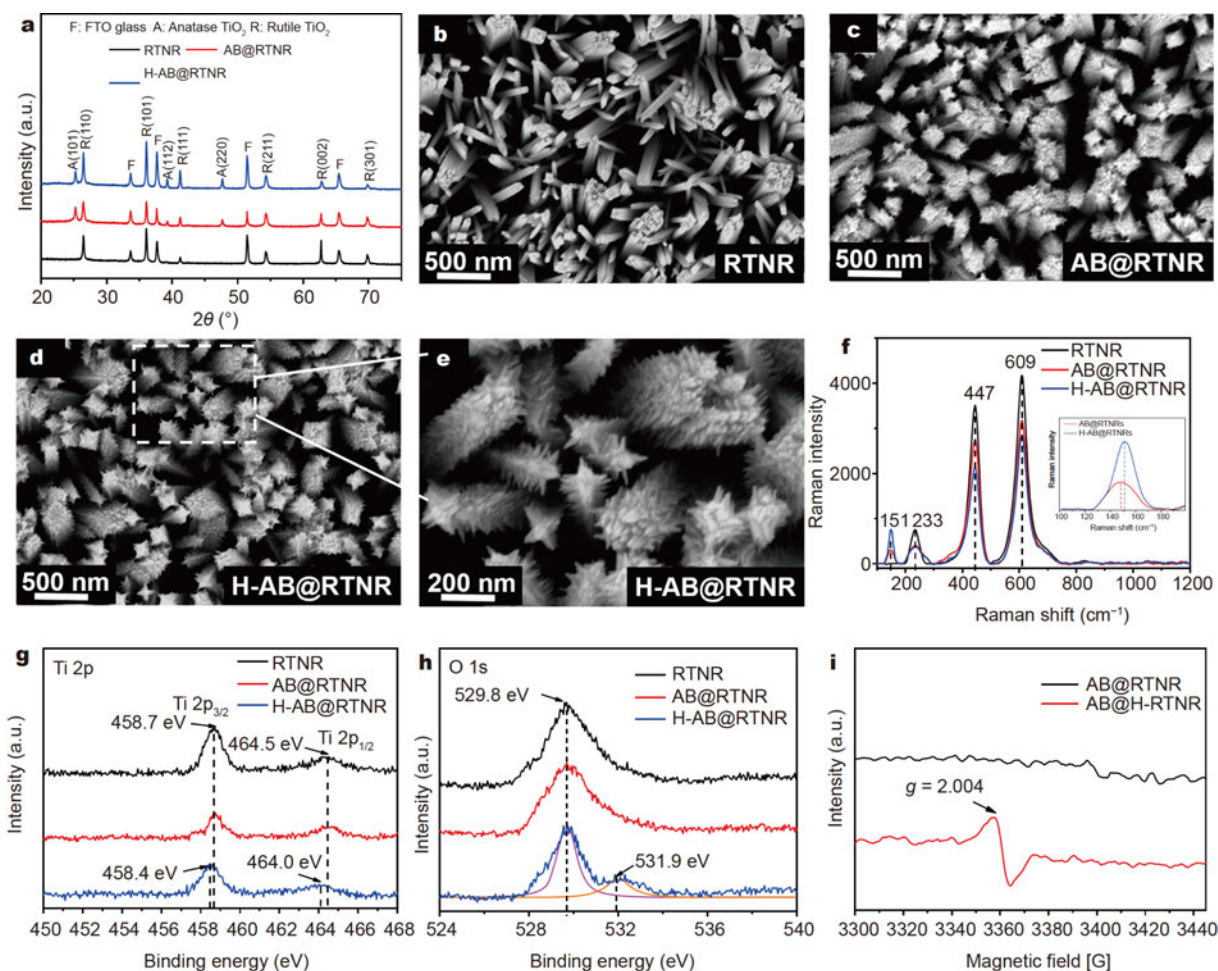
Figure 1 (a) XRD patterns; (b–e) FESEM surface morphologies; (f) Raman spectra (the inset exhibits the enlarged view of E_g peaks in the Raman spectra); XPS spectra for (g) Ti 2p and (h) O 1s; (i) EPR spectra of the as-prepared photocatalysts.

genation does not affect the crystal phase structure of the as-prepared materials. As a result, the diffraction peaks of the samples in Fig. 1a concur with the reports of rutile and anatase TiO_2 crystals in the literature [7,26].

The microstructure and surface morphology of the as-prepared nanocomposite were observed using field emission FEM (FESEM), with the results displayed in Fig. 1b–e. As revealed in Fig. 1b, smooth rutile TiO_2 nanorods with a length of 1.5 μm and a diameter of 200 nm were grown on FTO glass *via* a hydrothermal process. After the growth of anatase TiO_2 on the surface of the nanorods, branch-like TiO_2 were observed around the nanorods (Fig. 1c). The anatase branches were vertically grown and uniformly distributed on the surface of the nanorods, inferring that the surface area for absorbing light of branched nanorods was larger than that of RTNRs, which favours light absorption and extends the

active reaction area. Fig. 1d and e display the morphology of the photocatalysts after the hydrogenation process, which is denoted as H-AB@RTNRs. It can be observed from the FESEM images that the hydrogenation process does not change the morphology of the photocatalysts.

Raman spectra were obtained to characterize the structural features and the vibrational modes of the as-prepared samples (Fig. 1f). Generally, in all photocatalyst patterns, three diffraction peaks centered at 233, 447, and 609 cm^{-1} were observed, which correspond to the Raman-active modes of rutile phase TiO_2 [27]. For the materials after the growth of anatase branches, a new peak appeared at 151 cm^{-1} which is indexed to the characteristic peaks of symmetric stretching vibrations of oxygen atoms in the O–Ti–O bond in anatase phase TiO_2. As shown in the inset in Fig. 1f, the E_g Raman peak at 151 cm^{-1} from the sample before hydrogenation shifted to a slightly

higher wavenumber after the hydrogenation process. The phenomenon can be attributed to the replacement of Ti ions which facilitates the formation of oxygen vacancies in hydrogenated materials because of the drop in O/Ti ratio [28,29].

Surface electron analysis
XPS analysis was conducted to confirm the detailed surface composition and elemental valence states of the as-prepared nanocomposite. As can be observed in Fig. 1g, the peaks located at 458.7 and 464.5 eV correspond to Ti $2p_{3/2}$ and Ti $2p_{1/2}$, respectively. The results imply the Ti exists as Ti^{4+} without the presence of Ti^{3+} in the surface layer of RTNRs and AB@RTNRs. After the hydrogenation process, the major peaks of XPS spectra shifted to 458.4 and 464.0 eV for Ti $2p_{3/2}$ and Ti $2p_{1/2}$, respectively, indicating the generation of Ti^{3+} on the surface layer of hydrogenated samples [25]. The O 1s spectra of the as-prepared photocatalysts are presented in Fig. 1h. The major peak at 529.8 eV in the O 1s spectrum provides evidence of the presence of Ti–O bonds in all the three as-prepared samples [30]. After the hydrogenation process, a new peak was obtained by deconvolution of the XPS spectrum of H-AB@RTNRs. The new peak appearing at 531.9 eV is attributed to Ti–OH bonds in H-AB@RTNRs, indicating that oxygen vacancies are formed during the hydrogenation process [31].

EPR analysis was applied to further illustrate the oxygen vacancies and Ti^{3+} on the surface layer of the photocatalysts (Fig. 1i). Before the hydrogenation, no significant major peaks were observed in the EPR spectrum of AB@RTNRs. Conversely, the hydrogenated samples exhibited a noticeable signal at the proportionality factor (*g*) value of 2.004, further proving the increase of oxygen vacancies and Ti^{3+} after the hydrogenation process. The results were compatible with the Raman and XPS patterns, which all provided evidence of the increased oxygen vacancies and Ti^{3+} on the surface layer of the photocatalysts. The detected oxygen vacancies and Ti^{3+} explain the superior PC performance of H-AB@RTNRs because those intrinsic defects significantly extend the light absorption range to the visible light region and facilitate the separation of photoinduced charge carriers, which therefore enhances the PC efficiency of the photocatalysts [32].

Optical features
The optical features of the materials were examined by UV-vis spectroscopy to investigate the light-harvesting ability of the as-prepared materials (Fig. 2a). As shown in the UV-vis spectra, the RTNRs only exhibit strong absorbance in the UV area, while the visible-light absorption was the lowest among all the three photocatalysts owing to its wide bandgap. The AB@RTNR sample displayed a noticeable increase in UV light absorption and a little enhancement in the visible light region. This phe-
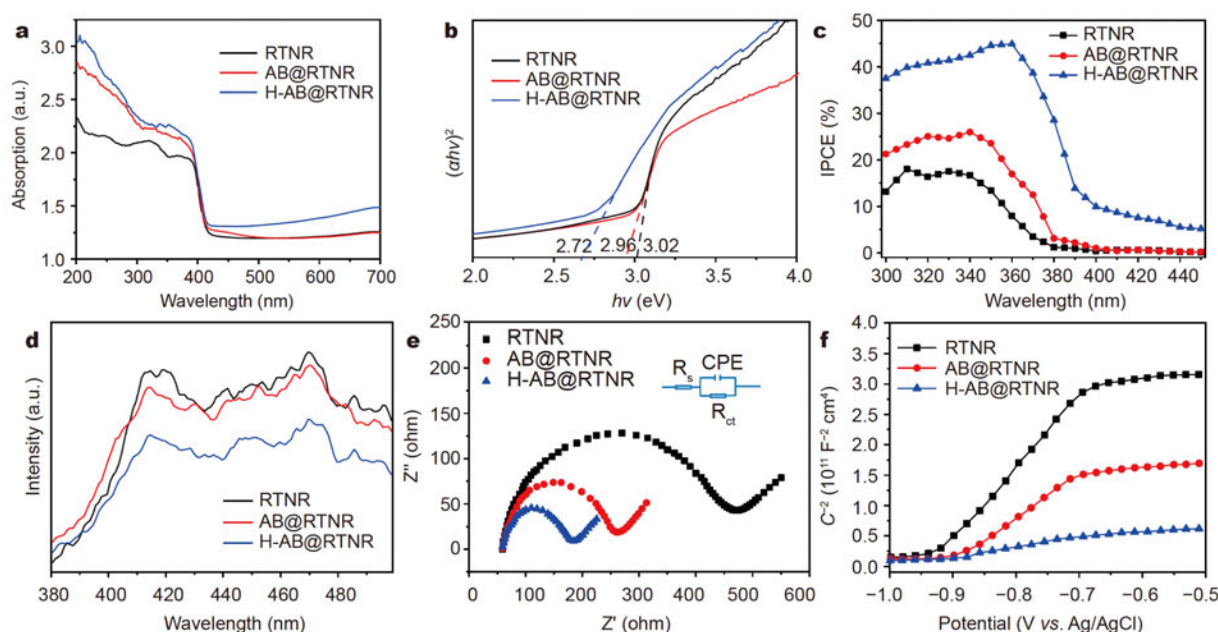

Figure 2 (a) UV-vis absorbance spectra; (b) Tauc plots derived from (a); (c) IPCE plots measured at 1.02 V *vs.* RHE applied bias; (d) FL, (e) EIS and (f) M-S spectra of RTNRs, AB@RTNRs, and H-AB@RTNRs.

nomenon could be attributed to the enlarged specific surface area from the branched structure and the alignment of different energy level positions of anatase and rutile, which slightly decrease the bandgap energy of the photocatalysts [15]. After the introduction of oxygen vacancies by the hydrogenation process, the H-AB@RTNR photocatalysts showed enhanced absorption in both UV light region and visible light region, which is consistent with the previous report [33]. The superior performance in light absorption of H-AB@RTNRs can be attributed to the narrowing of the bandgap by the introduction of oxygen vacancies and Ti^{3+} *via* the hydrogenation process as well as the enhanced light-harvesting capability of the branched structure. The results of H-AB@RTNR samples show impressive PC efficiency compared with the pristine RTNRs sample under visible-light irradiation due to the synergistic effects between the hydrogenation process and branched morphology.

To further investigate the bandgap energy of the as-prepared samples, the Tauc plots (Fig. 2b) were derived from the UV-vis spectra with the Tauc equation (Equation (8)) [34]:

$$(\lambda h\nu)^n = A(h\nu - E_g), \tag{8}$$

where A represents a constant, $h\nu$ represents the energy of irradiation, λ represents the measured absorption coefficient, and n equals 0.5 because the TiO_2 bandgap type is indirect [35]. The E_g of the as-prepared samples were obtained by extrapolation of the linear parts of the Tauc plots. As can be observed in Fig. 2b, the estimated E_g value for H-AB@RTNRs ($E_g \sim 2.72$ eV) is narrower than that of RTNRs ($E_g \sim 3.02$ eV) and AB@RTNRs ($E_g \sim 2.96$ eV). Therefore, the results further suggest that the bandgap of the as-prepared samples decrease with the introduction of oxygen vacancies and Ti^{3+} *via* the hydrogenation process, leading to enhanced light absorption in the region of visible light.

To investigate the quantum efficiency of the as-prepared photocatalysts, IPCE spectra were obtained and are exhibited in Fig. 2c. In the UV light region (before the wavelength of 380 nm), the H-AB@RTNRs exhibited the highest IPCE value among all the photocatalysts. Furthermore, the AB@RTNRs samples also showed an obvious light response within the visible light region (400–450 nm). This phenomenon could result from the synergistic effects between the well-aligned bandgap of mixed-phase TiO_2 and oxygen vacancies brought by the hydrogenation process.

The bandgap energy and recombination rate of charge carriers were investigated by FL spectra (Fig. 2d). Two

major peaks were observed at the wavelength of 413 and 471 nm, which are equivalent to 3.00 and 2.63 eV, respectively. The first peak appearing at 413 nm is referred to as the bandgap energy of rutile TiO_2 (3.02 eV), which proves that the photocatalysts were basically composed of the rutile phase TiO_2. It could be observed that the intensity of the FL spectra of the branched structure (AB@RTNRs and H-AB@RTNRs) is more potent than that of the non-branched structure (RTNRs) in the range of 380–390 nm. The phenomenon could be explained by the introduction of anatase branches with higher bandgap energy (3.2 eV), which correspond to the wavelength of 387 nm. However, the proportion of the anatase branch was comparatively low compared with rutile nanorods, so no major characteristic peaks corresponding to anatase phase TiO_2 were observed at 387 nm. The FL spectra integral intensities of H-AB@RTNRs were lower than those of other as-prepared samples, implying that the recombination rate of photogenerated charge carriers for H-AB@RTNRs was the lowest among all the as-prepared photocatalysts.

Electrochemical properties

EIS was used to study the interfacial PEC properties, such as recombination and transmission of charge carriers, on the interface between photocatalysts and electrolyte (Fig. 2e). The Nyquist plots of the RTNRs, AB@RTNRs, and H-AB@RTNRs were fitted to the proposed equivalent circuit, the simplified Randles cell, which is displayed in the inset of Fig. 2e. In the simplified Randles cell, CPE represents the double layer capacitance, R_s represents the solution resistance, and R_{ct} represents the charge-transfer resistance, which corresponds to the radius of arcs in the Nyquist plots. It could be also observed from Fig. 2e that the order of the radius of arcs for different photocatalysts was RTNRs < AB@RTNRs < H-AB@RTNRs, indicating that the transmission resistance of charge carriers in the interface between TiO_2 and electrolyte decreased after the modification of morphology and bandgap structure.

M-S plots were applied to investigate the flat band potentials (E_{fb}) and types of semiconductors (Fig. 2f). The M-S plots clearly illustrates that all the as-prepared samples are typical n-type semiconductors because of the positive slopes of the M-S curves [36]. The donor density (N_d) of all samples was calculated *via* Equation (9):

$$N_d = \frac{2/e_0\varepsilon\varepsilon_0}{d(1/C^2)/dV}, \tag{9}$$

where e_0 represents the charge of an electron (1.602 × 10^{-19} C), ε represents the dielectric constant of rutile

TiO$_2$, ε_0 represents the permittivity of free space in vacuum (8.854×10^{-12} F m^{-1}), and $d(1/C^2)/dV$ represents the slope by extrapolating the linear parts of M-S curves. Considering the values of e$_0$, ε and ε_0 are constants, it could be easily inferred that N_d was inversely proportional to $d(1/C^2)/dV$. Consequently, the smallest slope value of H-AB@RTNRs indicates that the donor density of H-AB@RTNRs was the highest among all the photocatalysts, which arises from the intrinsic defects brought about by the hydrogenation of the mixed-phase TiO$_2$. The results were also compatible with the smallest arc radius of H-AB@RNTRs from the Nyquist plots.

Performance of dye degradation by different processes

PC degradation
PC degradation of the as-prepared photocatalyst was investigated by degrading RhB under visible light. As illustrated in Fig. 3a, the removal efficiency of the photolysis process without adding any photocatalyst was negligible. After the introduction of RTNR photocatalysts, 2.2% of the RhB was eliminated after 240 min, which was similar to the removal rate of bare photolysis, indicating that the bare RTNRs hardly respond to visible light. Moreover, the degradation rate of RhB by the AB@RTNRs was 5.2% after 240 min, which is only a slight improvement compared with the bare RTNRs, showing that branched structure and mixed-phase strategy could slightly narrow the bandgap of the photocatalyst and moderately responds to visible light. However, the enhancement was not significant and further modification of the bandgap energy is needed. The visible light responses of RTNRs and AB@RTNRs were consistent with the IPCE results (Fig. 2c). After the hydrogenation process, the H-AB@RTNRs outperformed all the other as-prepared photocatalysts with an RhB removal rate of 95.2% in 240 min under visible light irradiation. To gain more insights into the procedure of PC degradation on H-AB@RTNRs, UV-vis spectra of the solutions collected at different time intervals are exhibited in Fig. 3b. Since the intensity of absorption spectra gradually decreased with irradiation time and the position of major peaks did not shift horizontally, it could be inferred that the PC degradation process of RhB followed the aromatic ring-opening mechanism [37].

PC-PS degradation kinetics
The synergistic effects between photocatalysts and PS anions were investigated by adding potassium persulphate (K$_2$S$_2$O$_8$) into the aqueous solution. As shown in Fig. 3c, the degradation rates of RhB on all as-prepared samples significantly increased after adding
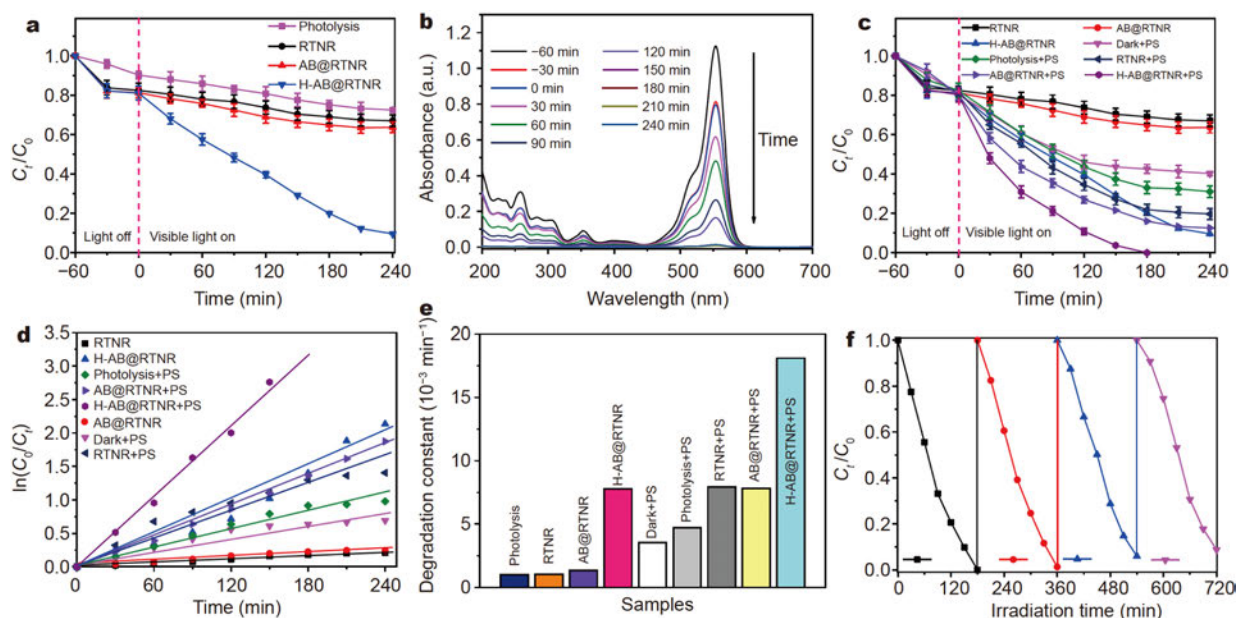

Figure 3 (a) PC degradation of RhB on the as-prepared photocatalysts; (b) UV-vis spectral changes for removal of RhB on the H-AB@RTNR; (c) PC degradation of RhB on the as-prepared photocatalysts in the presence and absence of PS; (d) Pseudo-first-order kinetics plots for the removal of RhB with the as-prepared samples; (e) the reaction rate constants of RhB for all the samples; (f) recycling runs for the H-AB@RTNRs photocatalyst on the PC-PS degradation of RhB.

1.48 mmol L^{-1} of K$_2$S$_2$O$_8$ solution, with the H-AB@RTNR photocatalysts achieving a degradation rate of 100% RhB after 180 min under visible light. The performance of dye degradation on different photocatalysts was explicitly investigated by using the pseudo-first-order kinetics model, as shown in Equation (10):

$$\ln(C_0 / C) = kt, \tag{10}$$

where C_0 represents the initial concentration of dye solution, C represents the concentration of dye solution at time t, t represents the reaction time, and k represents the pseudo-first-order reaction rate constant. According to Equation (10), the kinetics plots for all the as-prepared photocatalysts, both in the presence and absence of PS anions, are exhibited in Fig. 3d. The linear relationship in kinetics plots provides evidence that the dye degradation process on the as-prepared samples obeyed the pseudo-first-order kinetics model. The degradation rates of all the samples were calculated from the kinetics plots and are displayed in Fig. 3e. It can be observed that the reaction rate constant of H-AB@RTNR photocatalyst with PS anions (18.2×10^{-3} min^{-1}) was much higher than that of RTNRs (7.4×10^{-3} min^{-1}) and AB@RTNRs (7.2×10^{-3} min^{-1}) as well as the samples without PS anions. The results prove that the synergistic effects between photocatalysts and PS anions could sharply increase the degradation rate of RhB on H-AB@RTNRs under visible light. The stability of photocatalysts during PC degradation is crucial for practical applications. Consequently, the recyclability of the H-AB@RTNRs for RhB degradation with PS anions was tested under identical conditions (Fig. 3f). The plots show no significant decrease in degradation performance of H-AB@RTNRs in the four recycled runs, exhibiting its superior stability in PC-PS degradation of RhB under visible light.

Design of PC-PS thin-layer reactor
The influential factors of the thin-layer cell system performance, such as the angle of the slanted bed and the thickness of aqueous solution, were investigated, and the results are displayed in Figs S3 and S4. The comparison of the performance of PC-PS degradation of RhB in a conventional bulk cell and the thin-layer cell was studied in the following experiments. RhB solutions with identical concentration (20 mg L^{-1}) were treated by these two processes, and the results are displayed in Fig. S5. As shown in Fig. S5a, the degradation rate of RhB in the thin-layer cell was higher than that of the conventional bulk cell. The result was attributed to the design of the thin-layer cell, which minimized the thickness of the

water film layer and therefore reduced the light loss in aqueous solution. The pseudo-first-order kinetics plots are exhibited for intuitively illustrating the comparison of degradation performance between the two processes (Fig. S5b). The slope value of the pseudo-first-order kinetics plot for the thin-layer cell process was greater than that of the conventional bulk cell process, which proves that the thin-layer cell system could considerably improve the PC-PS degradation of RhB and achieved a degradation rate of 100% and a reaction rate constant of 0.0221 min^{-1} in 120 min under visible light.

PC-PS degradation mechanism
With the results presented above, a hypothetical explanation (Fig. 4) of the PC performance of H-AB@RTNRs in visible light region and the synergistic effects between H-AB@RTNRs and PS anions is proposed through two aspects. Firstly, from the perspective of photocatalysts, although the position of energy level alignment in mixed-phase anatase/rutile TiO$_2$ is controversial, it is widely accepted that the mixed-phase heterostructure could significantly improve the charge separation rate and slightly narrow the bandgap of photocatalysts, which favours the PC performance [13–15,38]. Furthermore, the hydrogenation process on the photocatalysts brought in abundant oxygen vacancies and Ti^{3+} in the surface layer of photocatalysts, which acted as a trapping site for capturing the photogenerated electrons and impeded the recombination of electron-hole pairs. The hydrogenation process also pronouncedly reduced the bandgap energy, which favoured its response to visible light. Secondly, from the perspective of synergistic effects in the PC-PS system, the reaction mechanism is displayed in Equations (1–6). Briefly, the photogenerated holes (h^+) reacted with H$_2$O to produce hydroxyl radicals (·OH), which possess high oxidation potential ($E^0 =$ 2.80 V *vs.* NHE). The oxygen molecules (O$_2$) were reduced by photogenerated electrons (e^-) to produce superoxide anion radicals (·O$_2^-$). Then e^- and ·O$_2^-$ further reacted with S$_2$O$_8^{2-}$ to produce ·SO$_4^-$, which possess a high oxidation potential ($E^0 =$ 2.60 V *vs.* NHE). Therefore, the ·OH and ·SO$_4^-$ both played a principal role in the degradation process due to their superior oxidation potentials. The h^+ played a crucial role in generating ·OH by oxidizing water at the lower valence band of the photocatalysts. Moreover, ·O$_2^-$ was a major assistant in transforming the S$_2$O$_8^{2-}$ in solution into ·SO$_4^-$. In this way, the organic contaminant could be indiscriminately oxidized to the small-molecule substance. In turn, S$_2$O$_8^{2-}$ also acted as a trapping site for photogenerated electrons, which
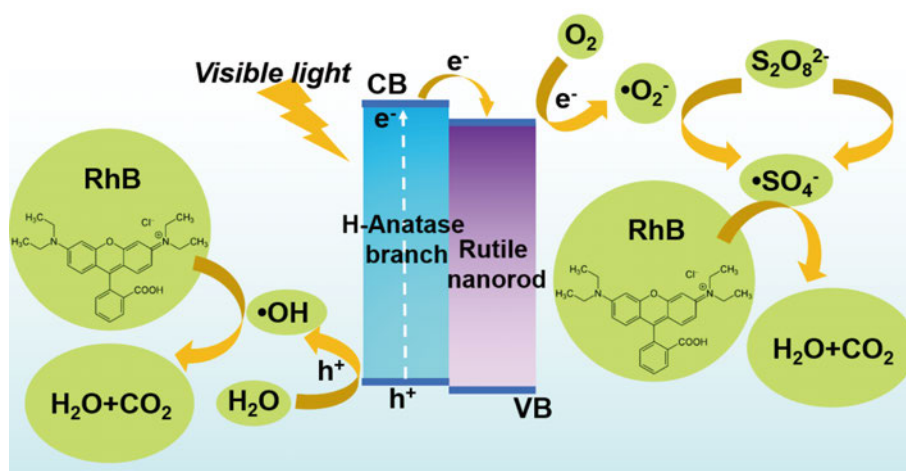
Figure 4 The mechanism of the synergistic PC-PS degradation of dye RhB.

improved the separation rate of photoinduced electron-hole pairs. In this way, the PS anions and H-AB@RTNR photocatalysts synergistically enhanced the degradation performance on RhB under visible light irradiation.

PC-PS degradation pathway of RhB
To investigate the degradation pathway of RhB under visible light irradiation, an LC/MS analysis was used to gain insights into the intermediate compounds generated during the PC-PS degradation process. Combining the results from the mass spectrograms of the intermediates during the degradation of RhB (Fig. S6) and the m/z values corresponding to the proposed intermediates' peaks (Table S4), a proposed degradation pathway can be acquired (Fig. 5), concurring with the results in previous studies [39]. There are four steps for RhB degradation. Firstly, the ethyl groups in RhB were attacked by radicals with high oxidation potential and experienced an *N*-de-ethylation process to generate phenyl oxonium inter-mediates (I–V). During the PC-PS process, five *N*-de-ethyl products were detected and their maximum peaks appeared in successive order, which demonstrated that the *N*-de-ethylation of RhB was a stepwise process. Secondly, in the chromophore cleavage process, the central carbon in the V was oxidized by active species, such as $\cdot SO_4^-$, $\cdot O_2^-$ and $\cdot OH$, generating major phenolic inter-mediates (VI–VIII). It can be also observed from Fig. S6 that during the whole degradation process, the chromo-phore cleavage of the RhB occurred simultaneously, re-flecting the superior degradation ability of the PC-PS system. The photogenerated h^+, $\cdot O_2^-$, and $\cdot OH$ as well as the PS-generated $\cdot SO_4^-$ directly attack the central carbon

of the dye molecule. These active radicals could also react with the *N*-de-ethylation intermediates and generate the primary products, such as phthalic acid, benzoic acid, and 1,2-dimethylbenzene. The third process of RhB de-gradation was the ring opening process, where the low-molecular-weight intermediates generated in the previous process were further attacked by active radicals and formed the broken-ring intermediates (IX–XII). The last process was the mineralization of those broken-ring products to produce small molecule substances, such as CO_2 and H_2O.

PC-PS treatment of real wastewater sample
The practical applicability of the thin-layer cell system with the H-AB@RTNR photocatalysts was tested using a real wastewater sample discharged from a textile industry. As shown in Fig. S7, the COD and TOC removal of 74.8% and 62.3%, respectively, were achieved after 240 min de-gradation with H-AB@RTNRs in the thin-layer cell sys-tem under visible light irradiation. Moreover, the biodegradability variation of the wastewater sample was analyzed by calculating the average oxidation state (AOS) and carbon oxidation state (COS) by Equations (11) and (12):

$$AOS = 4 - 1.5 \times COD/TOC, \tag{11}$$

$$COS = 4 - 1.5 \times COD/TOC_0, \tag{12}$$

where COD and TOC represent the values recorded after 240 min degradation, TOC_0 represents the initial TOC value of the raw wastewater sample. The AOS and COS values varied within ± 4, which represent the most oxi-dized form (CO_2) and the most reduced form (CH_4) of
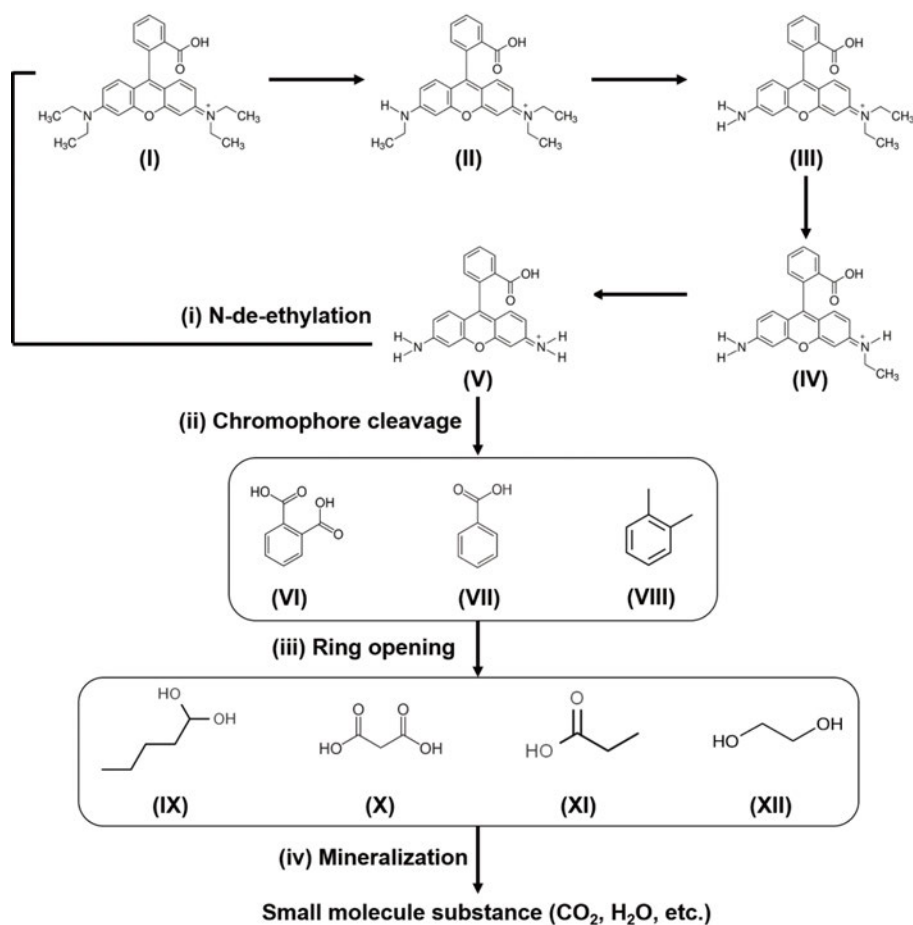
Figure 5 Proposed degradation pathway and intermediates during RhB degradation reaction with H-AB@RTNRs under visible light irradiation.

organic compounds. According to the experimental results, the AOS value was calculated to be 1.25 for raw wastewater samples. After a 240-min treatment process, the AOS and COS values of the solution were 2.16 and 3.31, respectively, which demonstrated that the biodegradability of raw wastewater was enhanced after PC-PS degradation in the thin-layer cell system.

CONCLUSION

A comprehensive study on designing a highly efficient, scalable, portable, and low-cost wastewater treatment and purification device for small-scale textile plants was carried out, and several conclusions are summarized as follows. Firstly, to improve the efficiency of contaminant degradation and reduce the cost of the operating device, the H-AB@RTNRs nanocomposites were successfully fabricated *via* a hydrothermal route. The H-AB@RTNRs were characterized by different methods to prove that the

photocatalysts possessed abundant oxygen vacancies and Ti^{3+}, which facilitated the separation rate of electron-hole pairs and enhanced the light absorption in the visible region. In this way, clean and low-cost solar energy can be utilized for wastewater treatment with H-AB@RTNRs. Secondly, the introduction of PS anions into the PC degradation process enables the reactor to degrade refractory organic contaminants that could not be achieved by the PC process alone. The phenomenon can be attributed to the synergistic effects between H-AB@RTNRs and PS anions, where the photogenerated electrons act as the reactive sites for PS anions to generate active radicals ($\cdot SO_4^-$), which possess a high oxidation potential ($E^0 = 2.60$ V *vs.* NHE) and therefore exhibit superior degradation performance for persistent organic contaminants. Thirdly, the thin-layer cell design could reduce the light loss in the aqueous solution by minimizing the thickness of the water film between the irradiation source and

photocatalysts, which maximizes light absorption by the photocatalysts and therefore achieves a better degradation performance compared with the conventional bulk cell. The device design also improves the portability of the reactor and exhibits its potential for up-scaling. Finally, according to the results of the real wastewater treatment experiments, it can be shown that the H-AB@RTNRs photocatalysts and PC-PS degradation system in the thin-layer cell have significant potential for practical PC removal of organic dye contaminants in the environment.

1   Sabri M, Habibi-Yangjeh A, Chand H, et al. Activation of persulfate by novel TiO$_2$/FeOCl photocatalyst under visible light: Facile synthesis and high photocatalytic performance. Separ Purif Tech, 2020, 250: 117268

2   Li Q, Hou X, Fang Z, et al. Construction of layered h-BN/TiO$_2$ hetero-structure and probing of the synergetic photocatalytic effect. Sci China Mater, 2020, 63: 276–287

3   Zhao Y, Kang S, Qin L, et al. Self-assembled gels of Fe-chitosan/montmorillonite nanosheets: Dye degradation by the synergistic effect of adsorption and photo-Fenton reaction. Chem Eng J, 2020, 379: 122322

4   Tang Q, An X, Lan H, et al. Polyoxometalates/TiO$_2$ photocatalysts with engineered facets for enhanced degradation of bisphenol A through persulfate activation. Appl Catal B-Environ, 2020, 268: 118394

5   Anipsitakis GP, Dionysiou DD. Radical generation by the interaction of transition metals with common oxidants. Environ Sci Technol, 2004, 38: 3705–3712

6   Li X, Huang X, Xi S, et al. Single cobalt atoms anchored on porous N-doped graphene with dual reaction sites for efficient Fenton-like catalysis. J Am Chem Soc, 2018, 140: 12469–12475

7   Zu M, Zheng M, Zhang S, et al. Designing robust anatase-branch@hydrogenated-rutile-nanorod TiO$_2$ as accurate and sensitive photoelectrochemical sensors. Sens Actuat B-Chem, 2020, 321: 128504

8   Liu L, Liu X, Chai Y, et al. Surface modification of TiO$_2$ nanosheets with fullerene and zinc-phthalocyanine for enhanced photocatalytic reduction under solar-light irradiation. Sci China Mater, 2020, 63: 2251–2260

9   He J, Du YE, Bai Y, et al. Facile formation of anatase/rutile TiO$_2$ nanocomposites with enhanced photocatalytic activity. Molecules, 2019, 24: 2996

10 Zhou T, Chen S, Li L, et al. Carbon quantum dots modified anatase/rutile TiO$_2$ photoanode with dramatically enhanced photoelectrochemical performance. Appl Catal B-Environ, 2020, 269: 118776

11 Ai C, Xie P, Zhang X, et al. Explaining the enhanced photoelectrochemical behavior of highly ordered TiO$_2$ nanotube arrays: Anatase/rutile phase junction. ACS Sustain Chem Eng, 2019, 7: 5274–5282

12 Zhong Y, Ma S, Chen K, et al. Controlled growth of plasmonic heterostructures and their applications. Sci China Mater, 2020, 63: 1398–1417

13 Miyagi T, Kamei M, Mitsuhashi T, et al. Charge separation at the rutile/anatase interface: a dominant factor of photocatalytic activity. Chem Phys Lett, 2004, 390: 399–402

14 Kawahara T, Konishi Y, Tada H, et al. A patterned TiO$_2$(anatase)/TiO$_2$(rutile) bilayer-type photocatalyst: Effect of the anatase/rutile junction on the photocatalytic activity. Angew Chem, 2002, 114: 2935–2937

15 Scanlon DO, Dunnill CW, Buckeridge J, et al. Band alignment of rutile and anatase TiO$_2$. Nat Mater, 2013, 12: 798–801

16 Wang X, Mayrhofer L, Hoefer M, et al. Facile and efficient atomic hydrogenation enabled black TiO$_2$ with enhanced photo-electrochemical activity via a favorably low-energy-barrier pathway. Adv Energy Mater, 2019, 9: 1900725

17 Xiao F, Zhou W, Sun B, et al. Engineering oxygen vacancy on rutile TiO$_2$ for efficient electron-hole separation and high solar-driven photocatalytic hydrogen evolution. Sci China Mater, 2018, 61: 822–830

18 Pan J, Dong Z, Wang B, et al. The enhancement of photocatalytic hydrogen production via Ti^{3+} self-doping black TiO$_2$/g-C$_3$N$_4$ hollow core-shell nano-heterojunction. Appl Catal B-Environ, 2019, 242: 92–99

19 Lu Y, Yin WJ, Peng KL, et al. Self-hydrogenated shell promoting photocatalytic H$_2$ evolution on anatase TiO$_2$. Nat Commun, 2018, 9: 2752

20 Zhuang G, Chen Y, Zhuang Z, et al. Oxygen vacancies in metal oxides: Recent progress towards advanced catalyst design. Sci China Mater, 2020, 63: 2089–2118

21 Bhatkhande DS, Pangarkar VG, Beenackers AACM. Photocatalytic degradation for environmental applications—A review. J Chem Technol Biotechnol, 2002, 77: 102–116

22 Zhao W, Wang X, Ma L, et al. WO$_3$/p-type-GR layered materials for promoted photocatalytic antibiotic degradation and device for mechanism insight. Nanoscale Res Lett, 2019, 14: 146

23 Li H, Long B, Ye KH, et al. A recyclable photocatalytic tea-bag-like device model based on ultrathin Bi/C/BiOX (X = Cl, Br) nanosheets. Appl Surf Sci, 2020, 515: 145967

24 Wang Y, Zu M, Zhou X, et al. Designing efficient TiO$_2$-based photoelectrocatalysis systems for chemical engineering and sensing. Chem Eng J, 2020, 381: 122605

25 Zhang S, Zhang S, Peng B, et al. High performance hydrogenated TiO$_2$ nanorod arrays as a photoelectrochemical sensor for organic compounds under visible light. Electrochem Commun, 2014, 40: 24–27

26 Lin J, Sun T, Li M, et al. More efficiently enhancing photocatalytic activity by embedding Pt within anatase–rutile TiO$_2$ heterophase junction than exposing Pt on the outside surface. J Catal, 2019, 372: 8–18

27 Wang CC, Chou PH. Effects of various hydrogenated treatments on formation and photocatalytic activity of black TiO$_2$ nanowire arrays. Nanotechnology, 2016, 27: 325401

28 Chen S, Li D, Liu Y, et al. Morphology-dependent defect structures and photocatalytic performance of hydrogenated anatase TiO$_2$ nanocrystals. J Catal, 2016, 341: 126–135

29 Ye K, Li K, Lu Y, et al. An overview of advanced methods for the characterization of oxygen vacancies in materials. TrAC Trends Anal Chem, 2019, 116: 102–108

30 Zhang X, Hu W, Zhang K, et al. Ti^{3+} self-doped black TiO$_2$ nanotubes with mesoporous nanosheet architecture as efficient solar-driven hydrogen evolution photocatalysts. ACS Sustain Chem Eng, 2017, 5: 6894–6901

31 Chen X, Liu L, Huang F. Black titanium dioxide (TiO$_2$) nano-

materials. Chem Soc Rev, 2015, 44: 1861–1885

32 Chen X, Liu L, Yu PY, *et al.* Increasing solar absorption for photo-catalysis with black hydrogenated titanium dioxide nanocrystals. Science, 2011, 331: 746–750

33 Hu J, Zhang S, Cao Y, *et al.* Novel highly active anatase/rutile TiO_2 photocatalyst with hydrogenated heterophase interface structures for photoelectrochemical water splitting into hydrogen. ACS Sustain Chem Eng, 2018, 6: 10823–10832

34 Tauc J. Optical properties and electronic structure of amorphous Ge and Si. Mater Res Bull, 1968, 3: 37–46

35 Reyes-Coronado D, Rodríguez-Gattorno G, Espinosa-Pesqueira ME, *et al.* Phase-pure TiO_2 nanoparticles: anatase, brookite and rutile. Nanotechnology, 2008, 19: 145605

36 Yan J, Han X, Qian J, *et al.* Preparation of 2D graphitic carbon nitride nanosheets by a green exfoliation approach and the enhanced photocatalytic performance. J Mater Sci, 2017, 52: 13091–13102

37 Asadzadeh-Khaneghah S, Habibi-Yangjeh A, Seifzadeh D. Graphitic carbon nitride nanosheets coupled with carbon dots and BiOI nanoparticles: Boosting visible-light-driven photocatalytic activity. J Taiwan Institute Chem Engineers, 2018, 87: 98–111

38 Li K, Lu X, Zhang Y, *et al.* Bi_3TaO_7/Ti_3C_2 heterojunctions for enhanced photocatalytic removal of water-borne contaminants. Environ Res, 2020, 185: 109409

39 Isari AA, Payan A, Fattahi M, *et al.* Photocatalytic degradation of rhodamine B and real textile wastewater using Fe-doped TiO_2 anchored on reduced graphene oxide (Fe-TiO_2/rGO): characterization and feasibility, mechanism and pathway studies. Appl Surf Sci, 2018, 462: 549–564

Meng Zu is currently a PhD student at the Centre for Clean Environment and Energy, School of Environment and Science, Griffith University, Australia. He received his Master degree from the Department of Civil and Environmental Engineering, Cornell University in 2016. His research interests include the design and development of functional nanomaterials for photoelectrocatalytic sensing and treatment of aquatic pollutants.

Shengsen Zhang obtained his PhD degree from South China University of Technology, China in 2012. He is now an associate professor at the College of Materials and Energy, South China Agricultural University, China. His research interests include the synthesis, modification, and characterization of nanostructured materials for wastewater purification, sensing, and energy conversion.

Shanqing Zhang obtained his PhD degree in electrochemistry in 2001 at Griffith University, Australia. He is now a professor at Griffith University. His research interests include energy conversion, energy storage, and environmental monitoring.

可见光光催化剂-过硫酸盐协同净化污水系统

祖萌[1], 张声森[2*], 刘长宇[3], 刘珀润[1], 李东升[4], 邢超[1,5], 张山青[1*]

摘要 本文报道了一种氢化金红石/锐钛矿混晶结构的TiO_2薄膜光催化材料(H-AB@RTNR)与过硫酸盐协同降解有机污染物的新方法, 设计了一套薄层式反应器以提高该方法对污染物的降解效率, 建立了可见光光催化剂-过硫酸盐协同净化污水系统. 实验结果表明, 在可见光(λ>420 nm)的照射下, 120分钟内可完全净化1 L浓度为20 mg L^{-1}的罗丹明B溶液, 反应速率常数达到0.0221 min^{-1}. 在对实际工业废水的处理实验中, 此系统也表现出优异的净化效果. 机理分析表明此系统优异的净化污水性能主要归功于反应中生成的大量硫酸根自由基 ($\cdot SO_4^-$)和羟基自由基 ($\cdot OH$). 最后本文对降解过程中的中间产物进行了分析, 明确了降解有机物的反应路径.

Supporting information

Portable wastewater treatment system based on synergistic photocatalytic and persulphate degradation under visible light

Meng Zu [1], Shengsen Zhang [2, *], Changyu Liu [3], Rorun Liu [1], Dong-Sheng Li [4], Chao Xing [1,5],

Shanqing Zhang [1, *]

[1] Centre for Clean Environment and Energy and Griffith School of Environment, Griffith University,

Gold Coast, QLD 4222, Australia

[2] College of Materials and Energy, South China Agricultural University, Guangzhou 510643,

Guangdong, China

[3] School of Biotechnology and Health Sciences, Wuyi University, Jiangmen 529020, China

[4] College of Materials and Chemical Engineering, Key Laboratory of Inorganic Nonmetallic

Crystalline and Energy Conversion Materials, China Three Gorges University, Yichang, 443002,

China)

[5] Key Laboratory of Materials Processing and Mold (Zhengzhou University), Ministry of

Education, Zhengzhou, 450002, China

*Corresponding author: zhangss@scau.edu.cn, s.zhang@griffith.edu.au

Dye degradation performance experiment

The evaluation of liquid-phase PC oxidation of RhB was carried out in XPA-system Photochemical Reactors (Nanjing, China). A series of quartz glass tubes containing the RhB solution and photocatalyst was placed uniformly on the supporting shelf, surrounding the central light source. A 300 W Xe lamp equipped with a UV-cutoff filter ($\lambda > 420$ nm) was used as the visible light source and placed in a cylindrical glass vessel in which cold water was circulated to avoid overheating. To maintain the temperature of the aqueous solution at 25°C during the reaction, the quartz glass tubes were put in a water tank with cold water circulating. Before irradiation, the suspensions were magnetically stirred in the dark for 1 h to reach an adsorption/desorption equilibrium. At given irradiation time intervals, a 0.5 mL sample solution was collected and centrifuged to remove the unexpected solid particles. The PC dye degradation performance of H-AB@RTNRs was also tested with a homemade thin-layer cell system. The sample solution stored in the water tank was driven by a centrifugal pump and transported in the direction shown in Fig. S1. The thin-layer cell consisted of an inlet reservoir, a slanted bed for mounting the FTO glass with the photocatalysts, and an outlet reservoir (Fig. S2a and b). The whole system was mounted on a wheeled trolley, improving the mobility of the PC reactor (Fig. S2c). Due to the enhanced mobility of the PC reactor, the thin-layer reactor system can be moved outside under sunshine, which could provide two irradiation modes for the PC reaction: artificial light mode and natural sunlight mode. The artificial light mode was driven by a visible light LED panel (Xigang, China) mounted right above the thin-layer cell to stimulate the PC reaction (Fig. S2d). The optical and electronic parameters of the LED panel are displayed in Table S3. The circulating flux of the thin-layer cell system was 5 L h^{-1}.

2

PC-PS thin-layer reactor system

Briefly, FTO glass with the H-AB@RTNRs photocatalysts was mounted on a slanted bed in the thin-layer cell. During the experiment, the sample solution in the tank was pumped up and circulated through the whole system. The solution was stored in the inlet reservoir at the beginning. When the water level was higher than the edge of the reservoir, the solution would be driven downwards by the slanted FTO glass with the H-AB@RTNRs film by gravity. The slanted bed was placed at a fixed angle of 15° to achieve a continuous layer flow and maintain a constant flow rate on the surface of the photocatalysts. As shown in Fig. S3, the degradation efficiency changed with the slanted bed angle in the range of 10°–30° under a constant light intensity and flow rate. When the slant angle increased to over 30°, the continuous layer flow was hard to maintain, which made the degradation efficiency decline dramatically. Since the circulating flux was not relatively high 5 L h^{-1}), a thin layer of aqueous solution film would form on the surface of the photocatalysts. According to Fig. S4, the thickness of the aqueous solution layer significantly influenced the degradation efficiency, which concurred with the Beer's Law mentioned previously. The decrease in the thickness of the aqueous solution could significantly reduce the light loss before reaching the photocatalysts, and therefore favoured dye degradation (Equation 7).
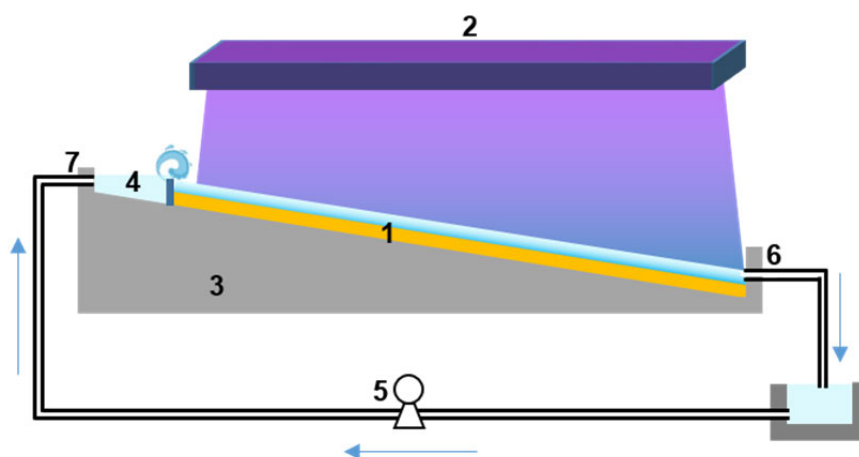
Figure S1. Schematic illustration of the side view of the thin-layer reactor system, including 1: FTO glass with H-AB@RTNRs; 2: LED panel; 3: thin-layer cell; 4: inlet reservoir; 5: centrifugal pump; 6: water outlet; 7: water inlet.
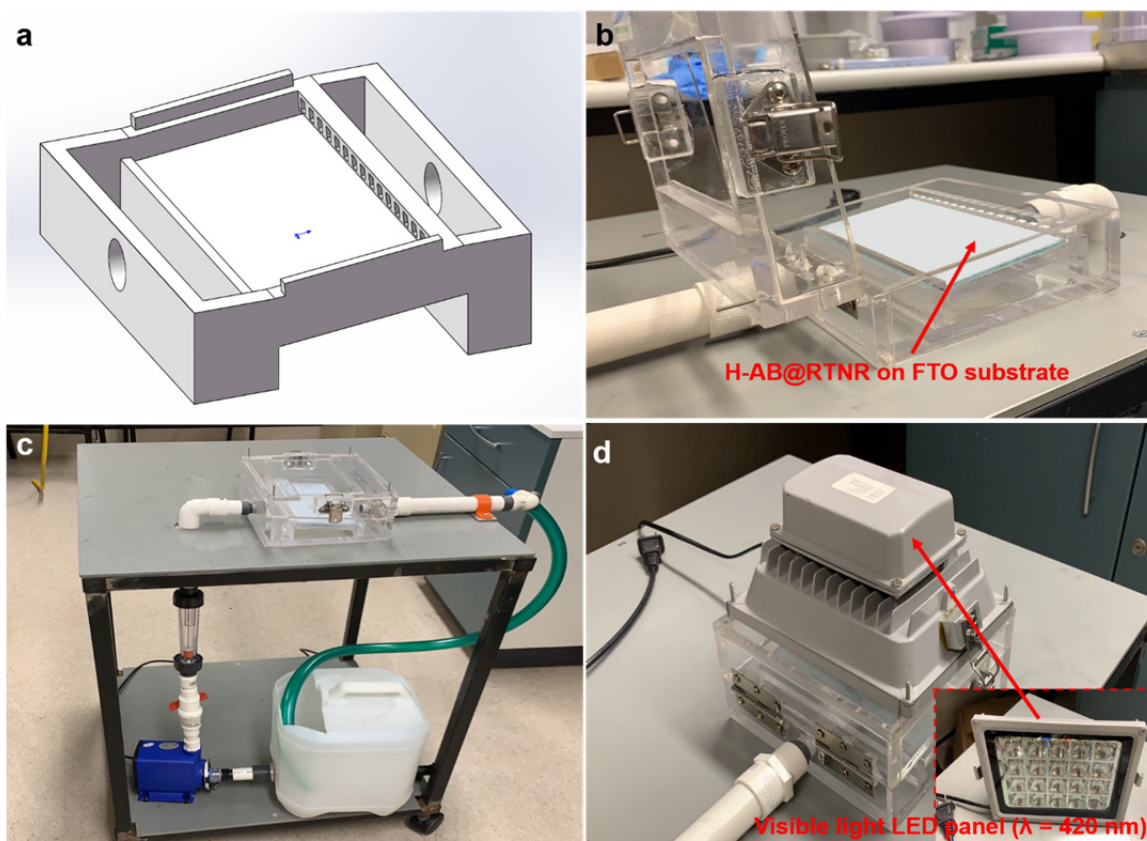

Figure S2. (a) Schematic diagram of the thin-layer cell, (d) the flexible design of thin-layer cell lid, (c) the thin-layer reactor system mounted on a wheeled trolley, and (d) thin-layer cell with LED panel mounted above (the inset exhibits the visible light LED panel).
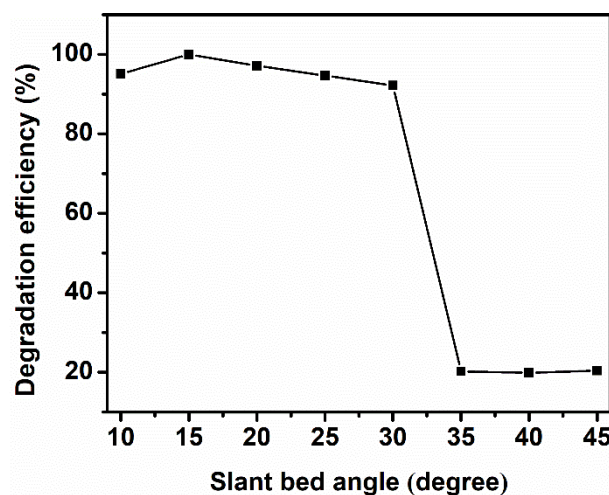
4

Figure S3. Plots of the degradation efficiency changing with the slant bed angle. (operation time: 2 h,

circulating flux: 5 L/h, initial concentration of RhB: 20 mg/L)
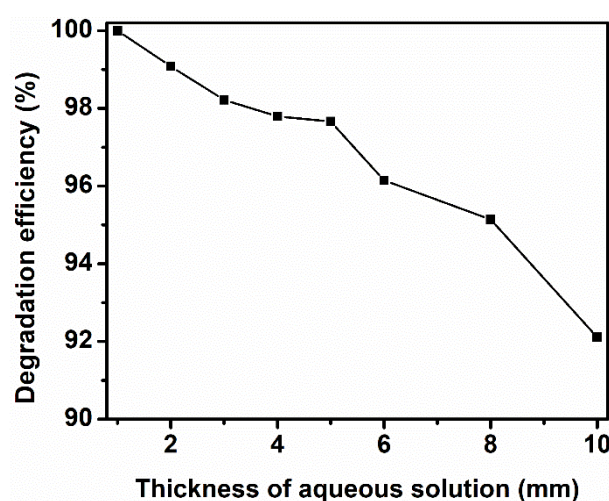
Figure S4. Plots of the degradation efficiency changing with the thickness of the aqueous solution.

(operation time: 2 h, circulating flux: 5 L/h, initial concentration of RhB: 20mg/L)

5
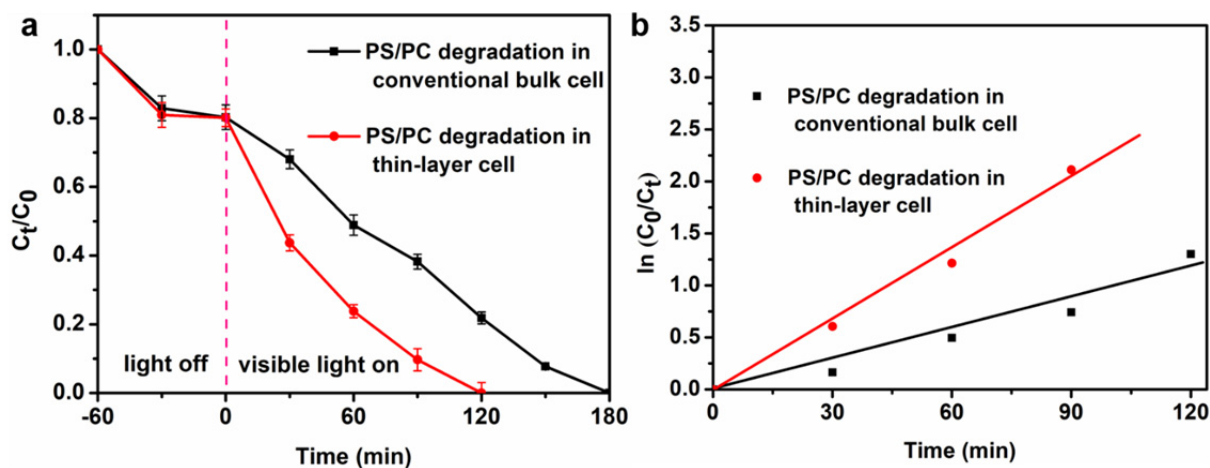
Figure S5. (a) PC-PS degradation of RhB on H-AB@RTNRs and (b) Pseudo-first-order kinetic plots for the removal of RhB on H-AN@RTNRs in the conventional bulk cell and thin-layer cell.
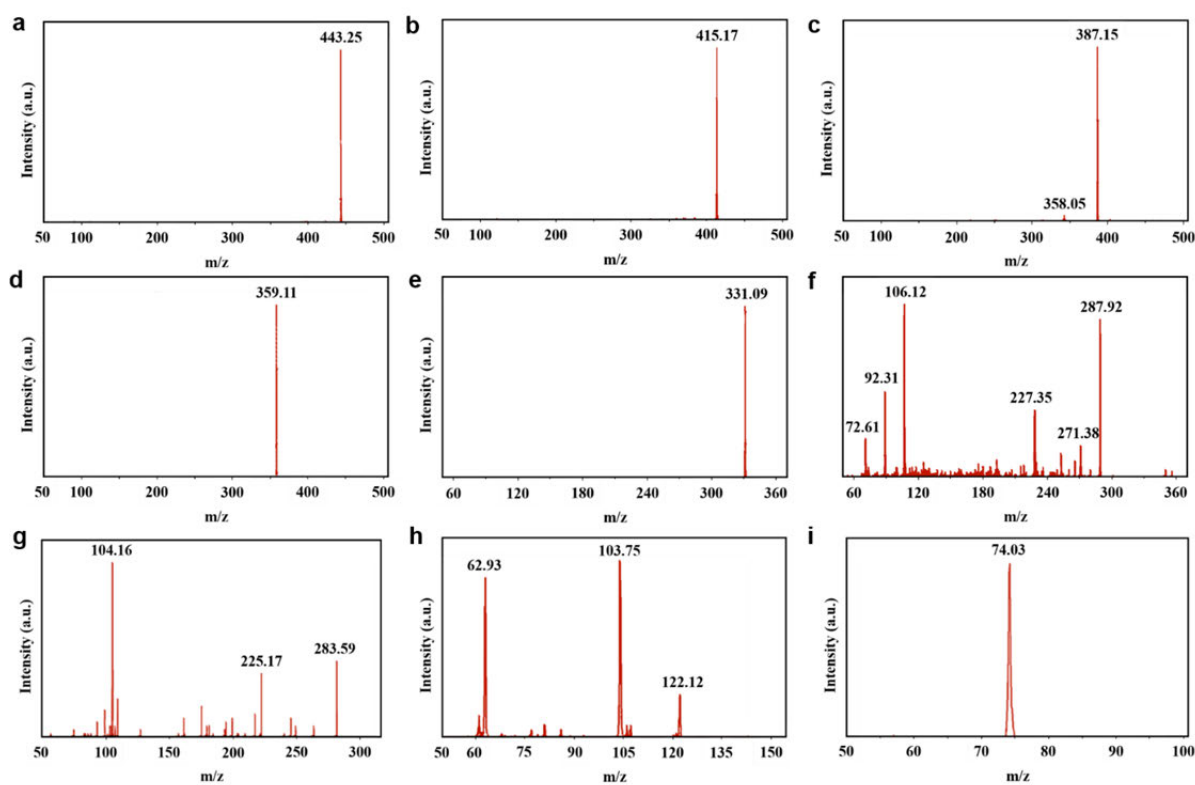
Figure S6. Mass spectrograms analysis of reaction intermediates during the PC/PS degradation of RhB by H-AB@RNTRs under visible light irradiation.

6
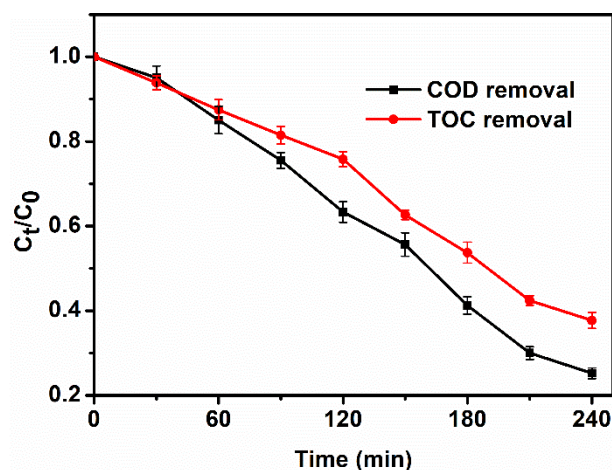
Figure S7. COD and TOC removal rate of a real wastewater sample degraded with H-AB@RTNRs photocatalysts in the thin-layer cell system under visible light irradiation.

Table S1. The characteristics of rhodamine B

Name	Rhodamine B
Formula	$C_{28}H_{31}ClN_2O_3$
Molecular weight	479.01 g/mol
IUPAC name	9-(2-Carboxyphenyl)-3,6-bis(diethylamino)xanthylium chloride
LD_{50} (mouse)	887 mg/kg
LD_{L0} (rat)	500 mg/kg
Chemical structure	

Table S2. Physiochemical properties of the real water sample

Parameter	Value	
	Range	Average
Total COD (mg/L)	1358-2139	1749
BOD_5 (mg/L)	105-160	130
BOD_5/COD	–	0.074
TOC (mg/L)	875-1034	955
Turbidity (NTU)	12-20	16
TDS (mg/L)	1504-1977	1741
TSS (mg/L)	205-258	232
pH	6.5-7.7	7.1

Table S3. Optical-electronic parameters and spectrum of the LED panel
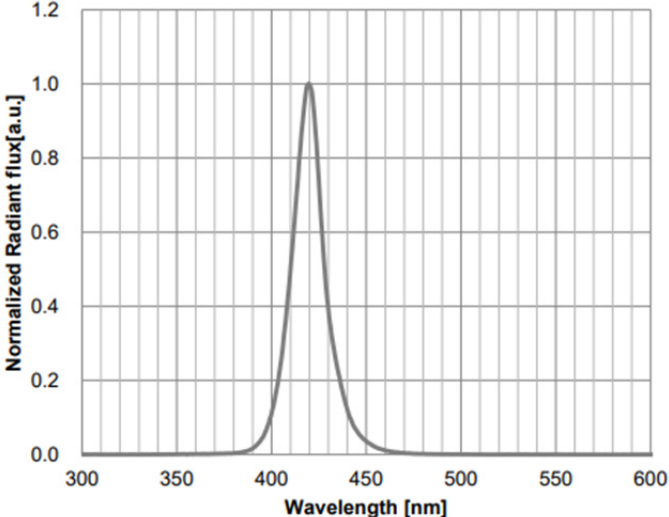
Parameter	Value
Peak wavelength	420 nm
LED quantity	4*5
Radiant flux	1040 mW
Forward voltage	3.5 V
Spectrum half width	10 nm
View angel	45 °
Spectrum (Ta = 25 °C, I_f = 500mA)	

Table S4. Proposed intermediates produced during PC-PS degradation of RhB under visible light irradiation

Sequence	*m/z*	Proposed intermediates
I	443.25	RhB
II	415.17	N,N-diethyl-N'-ethylrhodamine
III	387.15	N,N-diethylrhodamine
IV	359.11	N-ethylrhodamine
V	331.09	Rhodamine
VI	165.53	Phthalic acid
VII	122.12	Benzoic acid
VIII	106.12	1,2-dimethylbenzene
IX	104.16	1,1-pentanediol
X	103.75	Malonic acid
XI	74.03	Propionic acid
XII	62.93	Ethylene glycol

CHAPTER 5

Efficient removal of antibiotics via a synergetic process combining visible-light-driven TiO$_2$/WO$_3$ nanofibers photocatalysis and chlorination

Chemical Engineering Journal, in review.

5.1 INTRODUCTORY REMARKS

This chapter includes one submitted manuscript (**M. Zu**, S. Zhang, C. Liu, C. Xing, D. Li, P. Liu, S. Zhang, Efficient removal of antibiotics via a synergetic process combining visible-light-driven TiO$_2$/WO$_3$ nanofibers photocatalysis and chlorination, ***Chemical Engineering Journal***).

In this work, we successfully designed and synthesized TiO$_2$/WO$_3$ nanofibers as the photocatalyst and fabricated an antibiotic degradation system by combining the TiO$_2$/WO$_3$ photocatalysis system powered by visible light LED arrays and traditional chlorination, resulting in a TiO$_2$/WO$_3$ PC-chlorination system. The system could efficiently produce highly oxidizing free radicals (i.e., •OH and •ClO) at the photocatalyst in the presence of free chlorine in water under visible light (>420 nm) illumination. In the course of the degradation of tetracycline hydrochloride, a model antibiotic, the pseudo-first-order degradation rate constant of the PC-chlorination system has reached 21.438 min^{-1}, which is 3.66 and 86.57 times higher than that in pure TiO$_2$/WO$_3$ photocatalysis and traditional chlorination processes, respectively. The superior performance of the PC-chlorination system can be ascribed to the synergetic effect established between the photocatalysis system and the traditional chlorination. The activation of free chlorine by photocatalysts can significantly boost the yield of active radicals, which favors the degradation efficiency of antibiotics. Effects of water quality (pH) and other operational conditions (e.g., chlorine dose, irradiation wavelength) are also investigated, suggesting the optimal working conditions for the PC-chlorination system (photocatalyst concentration at 0.5 g L^{-1}, chlorine concentration at 4 mmol L^{-1}, and initial pH at 4). Results suggest that the proposed visible-light-driven photocatalytic oxidation combined with traditional chlorination treatment could offer an exceptional solution to realize the complete removal of antibiotics from water and upgrade the antibiotic removal capability of existing wastewater treatment plants.

5.2 STATEMENT OF CONTRIBUTION

My contribution to the paper involved:

Initial concept; Experimental design and implementation; Collection and analysis of data;

Preparation of manuscript.

(Signed)_____█████████████_____(Date) <u>15-04-2021</u>

Name of Student: Meng Zu

(Countersigned)____███████████____(Date) <u>15-04-2021</u>

Supervisor: Shanqing Zhang

5.3 Article 4

Efficient removal of antibiotics via a synergetic process combining visible-light-driven TiO₂/WO₃ nanofibers photocatalysis and chlorination

Meng Zu [1], Shengsen Zhang [2, *], Changyu Liu [3], Rorun Liu [1], Dongsheng Li [4], Chao Xing [1,5], Shanqing Zhang [1, *]

[1] Centre for Clean Environment and Energy and Griffith School of Environment, Griffith University, Gold Coast, QLD 4222, Australia

[2] College of Materials and Energy, South China Agricultural University, Guangzhou 510643, Guangdong, China

[3] School of Biotechnology and Health Sciences, Wuyi University, Jiangmen 529020, China

[4] College of Materials and Chemical Engineering, Key Laboratory of Inorganic Nonmetallic Crystalline and Energy Conversion Materials, China Three Gorges University, Yichang, 443002, China)

[5] Key Laboratory of Materials Processing and Mold (Zhengzhou University), Ministry of Education, Zhengzhou, 450002, China

*Corresponding author: zhangss@scau.edu.cn, s.zhang@griffith.edu.au

Abstract

The traditional chlorination process in wastewater treatment could not efficiently remove the antibiotics originated from pharmaceuticals, pesticides, and personal care products in aquatic environments, which has posed a significant threat to public health and the environment. Low-cost and high-efficient technologies in removing the antibiotics and assuring the effluent quality of the wastewater treatment plant are urgently needed. In this work, we designed and synthesized TiO_2/WO_3 nanofibers as the photocatalyst and fabricated an antibiotic degradation system by combining the TiO_2/WO_3 photocatalysis system powered by visible light LED arrays and traditional chlorination, resulting in a TiO_2/WO_3 photocatalytic (PC)-chlorination system. The proposed system could efficiently produce abundant highly oxidizing free radicals (i.e., •OH and •ClO) at the photocatalyst in the presence of free chlorine in water under visible light (>420 nm) illumination. In the course of the degradation of tetracycline hydrochloride, a model antibiotic, the pseudo-first-order degradation rate constant of the PC-chlorination system has reached 21.44 min^{-1}, which is by 3.66 and 86.57 times higher than that in the pure TiO_2/WO_3 photocatalysis and traditional chlorination processes, respectively. The superior performance of the PC-chlorination system can be ascribed to a synergetic effect established between the photocatalysis system and the traditional chlorination. The activation of the free chlorine by photocatalysts can significantly boost the yield of active radicals, which favors the degradation efficiency of antibiotics. The proposed PC-chlorination treatment could offer an exceptional improvement to the traditional chlorination process and realize the complete removal of antibiotics in water, affording the antibiotic removal capability to the conventional wastewater treatment plant.


Key Words: Photocatalysts, free chlorine, antibiotics degradation, visible light, synergistic

1. Introduction

With industrialization progressing in the past few decades, more and more micropollutants, such as pharmaceuticals, antibiotics, and personal care products, have been widely detected in the aquatic environment [1]. In the conventional water treatment plant (WTP), the chlorination process is always applied as a disinfection method for removing bacteria from drinking water [2]. However, several studies suggest that chlorination cannot effectively remove the antibiotics from water [3-5]. Moreover, low-level residual free chlorine (FC) in water will accelerate the converting of antibiotics into toxins during water distribution [6, 7]. Therefore, an alternative strategy to remove the antibiotics during the chlorination process is needed rather than the traditional chlorination process. Recently, applying the UV/chlorine process instead of the traditional chlorination process appears to be a sustainable and economically friendly approach for degrading antibiotics in WTP due to two reasons [8-10]. Firstly, the photolysis of FC (HClO and ClO$^-$) under UV irradiation can produce abundant active radicals with high oxidation potential ($\bullet$OH, E_0 = 2.8 V; $\bullet$Cl, E_0 = 2.4 V), and some secondary radicals ($\bullet$Cl$_2^-$, E_0 = 2.0 V; $\bullet$ClO, E_0 = 1.5-1.8 V) generated from the reaction between $\bullet$Cl and ClO$^-$ [11, 12]. Those active radical species will attack the antibiotics in water and degrade them into small molecular substances. Secondly, the water effluent of the disinfection process in most conventional WTPs contains abundant FC residuals, making it possible to directly incorporate the UV/chlorine process in the disinfection process, resulting in a cost-effective technology upgrade [13]. However, the building and operation cost of the UV/chlorine system is considerably high, which impedes large-scale implementation.

To further reducing the cost of the UV/chlorine system, the solar/chlorine system was investigated and

reported by many researchers because solar irradiation is more cost-effectively and available worldwide [14-16]. However, the utilization of solar irradiation in previous reported solar/chlorine systems majorly rely on the UV region of the solar light, which takes only a small proportional (less than 4%) of the full spectrum [17], because reactive species are generated due to the UV photolysis of FC [12]. According to Long's theoretical calculation [18], HOCl and ClO$^-$ (pK$_a$ = 7.5) can be activated by superoxide radicals ($\bullet$O$_2{}^-$) to generate hydroxyl radicals ($\bullet$OH) at $7.5 \pm 0.38 \times 10^6$ M^{-1} s^{-1} and by photo-induced electrons (e$^-$) to produce $\bullet$O$^-$ at 7.2×10^9 M^{-1} s^{-1}, respectively (Eq. 1 and 2).

$$HOCl + \cdot O_2{}^- \rightarrow \cdot OH + \cdot Cl + O_2 \tag{1}$$

$$ClO^- + e^- \rightarrow \cdot O^- + Cl^- \tag{2}$$
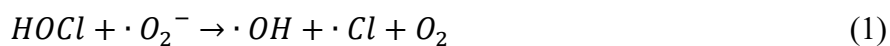
Therefore, we assume that e$^-$ and $\bullet$O^{2-} generated from the visible-light-driven photocatalytic (PC) process can generate greater amounts of $\bullet$OH *via* chlorine activation in water solution than the PC process or traditional chlorination process.

To produce photogenerated carriers for providing e$^-$ and $\bullet$O^{2-} under visible light, it is highly desirable to develop and synthesize advanced photocatalysts, which possess enhanced PC activities activated by visible-light irradiation [19]. Recently, numerous efforts have been made in designing and developing visible-light-driven photocatalysts with narrow band-gap. Coupling TiO$_2$ with a narrow band-gap semiconductor to extend the light absorption range and facilitate the separation of photogenerated electrons and holes has attracted considerable attention. Some heterostructural TiO$_2$-based photocatalysts, i.e., TiO$_2$/CdS, TiO$_2$/BiVO$_4$, TiO$_2$/SnO$_2$, and TiO$_2$/WO$_3$, are widely studied [20-23]. WO$_3$ seems to be a promising semiconductor for coupling TiO$_2$ due to several advantages: lower cost in synthesizing, narrower band-gap, higher stability, and strong photo-corrosion resistance compared to other semiconductors [23,

24]. Furthermore, the morphology modification of photocatalysts can also influence PC activity. The 1-D nanostructures (e.g., nanorods, nanotubes, and nanofibers) have superior PC activity because of the fast electron transfer *via* the direct pathway along the radial direction [25]. This property results in the fast separation of photogenerated charge carriers, enhancing the PC performance of photocatalysts compared to other nanostructures.

Herein, 1-D TiO_2/WO_3 nanofibers were synthesized and studied as the photocatalyst capable of generating photogenerated charge carriers and active radicals for activating FC in the aqueous solution to degrade tetracycline hydrochloride (TC-HCl), a model antibiotic, under visible light irradiation. TC-HCl is selected as a model compound because it is a frequently detected refractory antibiotic in water bodies. In this study, we designed an antibiotic degradation system by integrating the TiO_2/WO_3 nanofibers photocatalysis system with the traditional chlorination process, noted as visible-light-driven PC/chlorination process (V-PC/C-P). The photolysis of FC cannot be activated to produce highly oxidizing agents under visible irradiation; in contrast, the introduction of TiO_2/WO_3 photocatalysts can significantly boost the yield of active radicals, which plays the same or even better role compared to UV photolysis of FC. During the process, abundant highly oxidizing free radicals (i.e., •OH and •ClO) are produced at the photocatalyst in the presence of FC in water under visible light (>420 nm) irradiation. The influences of water quality (pH) and other operational conditions (e.g., photocatalysts concentration, initial antibiotics concentration, and FC concentration) on degrading the TC-HCl were investigated. Under the optimal working conditions, the degradation rate of the removal of TC-HCl has reached 100% after 120 min reaction, and the pseudo-first-order rate constant of the V-PC/C-P is 21.44 min^{-1}. The superior performance of the PC-chlorination system can be attributed to the synergetic effect established between the photocatalysis system and the chlorination

process.

2. Materials and methods

2.1 Chemicals and reagents

TiO$_2$ powder (P25, commercial-grade) was purchased from Degussa, Germany. Sodium hydroxide (NaOH), hydrochloric acid (HCl, 36.5% by weight), tungstic acid (H$_2$WO$_4$), and methenamine (C$_6$H$_{12}$N$_4$) were obtained from Sigma-Aldrich of analytical reagent (AR) grade and used as received. High-purity distilled water (Millipore Corp., 18 MΩ cm) was used to prepare and dilute solutions. Tetracycline hydrochloride (TC-HCl, AR) was also purchased from Sigma-Aldrich and used as the model antibiotics for degradation.

2.2 Synthesizing procedure

The anatase TiO$_2$ nanofiber was synthesized by a two-step hydrothermal process similar to that described by Yu and Tian [26, 27]. In the first hydrothermal step, fibrous Na-titanate was synthesized. Briefly, 20 mL distilled water was mixed with 60 mL NaOH (10 mol L^{-1}) and 1.8 g commercial-grade TiO$_2$ powder (P25, Degussa) under vigorous stirring for 30 min to form a suspension. After stirring, the suspension was transferred into a 100 mL autoclave for a hydrothermal process at 200 °C for 20 h. The as-prepared samples were cooled naturally, then separated by filtration and washed several times with HCl (0.1 mol L^{-1}) solution until the pH of the solution became neutral and dried in a vacuum oven at 60 °C overnight. After drying, the sample was mixed with 50 mL HCl (0.1 mol L^{-1}) and then subjected to the second hydrothermal treatment at 180 °C for 24 h. After cooling down to room temperature naturally, the as-prepared material was separated and washed several times with large distilled water.

For the synthesize of TiO$_2$/WO$_3$ nanocomposites, 20 mL H$_2$O$_2$ and 2.5 g H$_2$WO$_4$ powders were added

into a beaker under vigorous stirring at 90 °C for 1 h. After stirring, the well-mixed solution was added into 60 mL distilled water dropwise, obtaining a transparent sol. After dipping the as-prepared TiO_2 nanofibers into the as-prepared sol for 45 min, a layer of WO_3 seed was successfully deposited onto the surface of TiO_2 nanofibers. After that, the TiO_2 fibers with the WO_3 seed layer were collected and calcined at 300 °C for 1 h in air. After the calcined TiO_2 nanofibers cooled to room temperature naturally, the samples were added into 60 mL distilled water and then well-mixed with 20 mL as-prepared sol and 0.168 g $C_6H_{12}N_4$ powders under vigorous stirring for 30 min. Then the suspension was transferred into a 100 mL autoclave for another hydrothermal treatment at 150 °C for 16 h. The obtained materials were separated and washed several times by ethanol and distilled water and dried in the vacuum oven at 60 °C overnight.

2.3 Characterization

The nanostructured morphology was characterized by scanning electron microscopy (SEM, JEOL JSM-7001F, Japan). To further investigate the composition of the material, the transmission electron microscope (TEM, JEOL JEM-2010 F, Japan) was applied. The crystallographic phase and structure of photocatalysts were tested by X-ray diffraction (XRD) with an X-ray diffractometer [Cu-Kα radiations (wavelength, 1.5406 Å) on a Bruker D8 System]. The Raman test was carried out on a Raman microscope (Renishaw). X-ray photoelectron spectrophotometer (XPS) results were obtained in a Krato Axis Ultra DLD spectrometer at 15 kV and 150 W. UV-visible (UV-vis) experiments were conducted with Agilent Cary 300 UV-vis spectrophotometer to gain more insights on the band-gap condition. Electrochemical impedance spectroscopy (EIS) plots were obtained on an electrochemical station (CHI 660e) to study the charge transfer of the photocatalysts. Mott-Schottky (M-S) analysis was carried out in a quartz cell 0.1 mol L^{-1} $NaNO_3$ solution, applying a three-electrode configuration with a frequency of 1 kHz.

2.4 Experimental setup and procedures

The study on PC degradation performance on TC-HCl was applied in XPA-system Photochemical Reactors (Nanjing, China). A series of quartz glass tubes containing the TC-HCl solution and photocatalyst was placed uniformly on the supporting shelf surrounding the central light source. A series of LED arrays (45W, λ_{max} = 420 nm, Xigang, China) was used as the visible light source and placed in the reactor center. FC concentrations were adjusted by adding hypochlorous acid (HClO) in water solution and were determined by a DPD colorimetric method with a detection limit of 0.10 μmol L^{-1}. To maintain the temperature of the aqueous solution at 25°C during the reaction, the quartz glass tubes were put in a water tank with cold water circulating. Before introducing visible light, the solution was stirred in the dark for 40 min to reach an adsorption/desorption equilibrium. A 0.5 mL sample solution was collected and centrifuged to remove the unexpected solid particles every 20 min. The degraded TC-HCl concentration was analyzed using a Cary 50 spectrophotometer (Varian Co., USA). The reusability and stability of TiO_2/WO_3 were examined by conducting four consecutive TC-HCl degradation experiments under the same experimental conditions.

3. Results and discussion
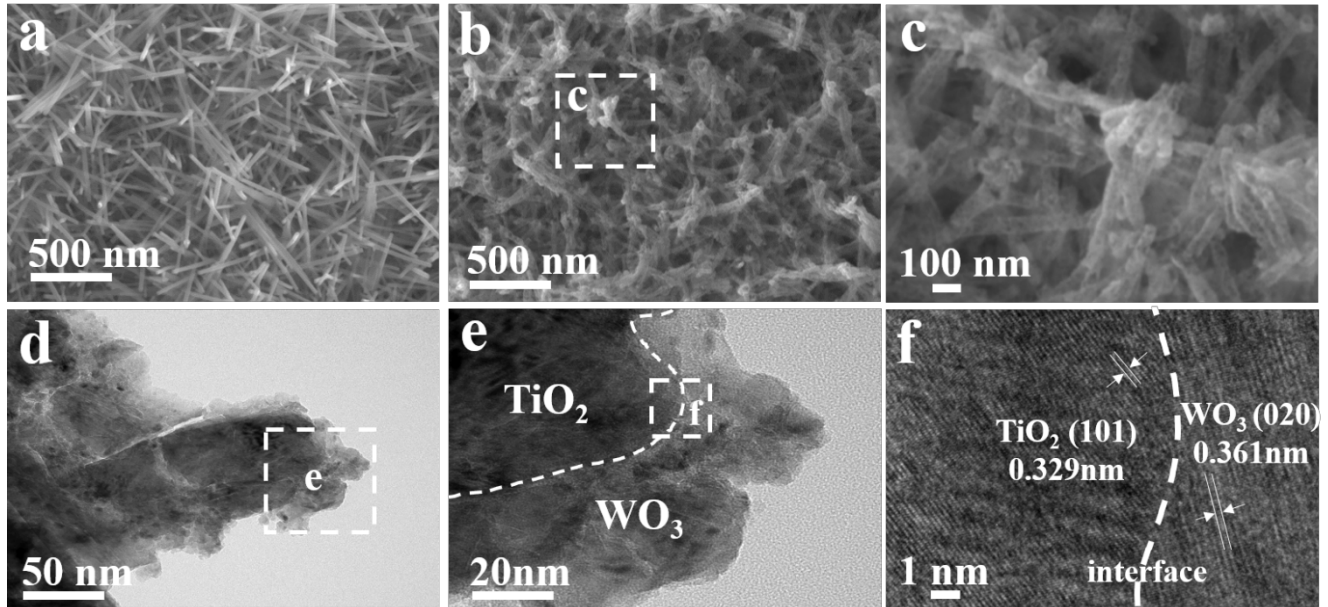
3.1 Photocatalyst synthesis and characterization

Fig. 1. FESEM images of (a) bare TiO_2; (b) (c) TiO_2/WO_3; and (d) (e) (f) TEM images of TiO_2/WO_3

The TiO_2 nanofibers are firstly fabricated *via* a two-step hydrothermal method. As shown in Fig. 1a, the TiO_2 nanofibers have similar fibrous morphology with diameters of 50–100 nm and lengths of 800-1000 nm. After the growth of WO_3, WO_3 nanoparticles are uniformly coated onto the surface of TiO_2 nanofibers (Fig. 1b and c) without changing the alignment of TiO_2 nanofibers. The thickness of WO_3 coating is around 5 nm, and the surface of TiO_2/WO_3 nanocomposites becomes uneven when compared to the smooth TiO_2 nanofibers in Fig. 1a. Moreover, the WO_3 coating film exhibits a compact surface with a fine-grained structure. The structural characteristics of TiO_2/WO_3 nanofibers are further investigated by TEM, as shown in Fig. 1d-f. From the low magnification image (Fig. 1d and e), the deep colour section is the TiO_2 nanofiber, while the shallow colour section represents the WO_3 coating. The HRTEM images collected from the individual nanofiber exhibit that the nanocomposite is completely crystalline along its entire length and reveals clear lattice fringes with interplanar spacings of 0.329 nm and 0.361 nm, which correspond to the

d-spacings of (101) lattice planes of anatase TiO_2 and (020) lattice planes of WO_3 (Fig. 1f). The TEM image

reveals the TiO_2/WO_3 photocatalysts are composed majorly by anatase TiO_2 nanofibers core and compact
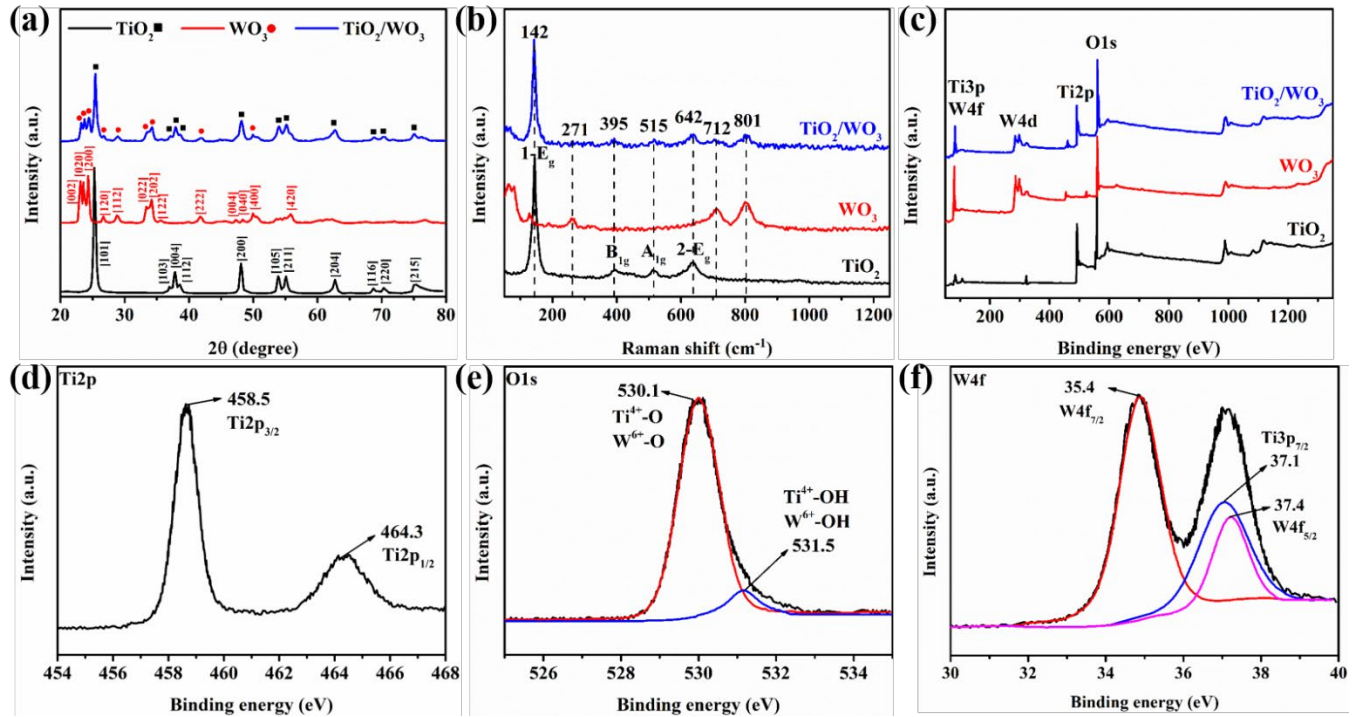
WO_3 coating.

Fig. 2. (a) XRD patterns, (b) Raman spectra, and (c) XPS survey spectrum of TiO_2, WO_3, and TiO_2/WO_3. High-resolution

XPS spectra of (d) Ti2p, (e) O1s, and (f) W4f of TiO_2/WO_3 sample.

X-ray diffraction (XRD) analysis has been used to investigate the crystal phases of as-prepared

photocatalysts (Fig. 2a). As shown in Fig. 2a, the XRD pattern of the bare TiO_2 nanofibers exhibits several

characteristic diffraction peaks, which can be indexed as anatase TiO_2 (ICDD-21-1272) [28]. Notably, the

major peak of the TiO_2 XRD pattern appears at 25.1°, which corresponds to the (101) planes of anatase

TiO_2. This result exhibits excellent consistency with the HRTEM image (Fig. 1f). After the growth of WO_3,

the XRD patterns of the TiO_2/WO_3 nanocomposites displays several new characteristic diffraction peaks

when compared to the bare TiO_2 XRD pattern (Fig. 2a). These new characteristic peaks at 23.2°, 23.9°,

24.4°, 28.8°, 34.1°, and 49.8° can be indexed as monoclinic WO_3 (ICDD-43-1035) [28]. The XRD patterns

further confirm the successful growth of monoclinic WO_3 on the surface of anatase TiO_2 nanofibers (Fig. 2a). For the sake of further investigation of the sample's phase structure, Raman spectra of bare TiO_2 nanofibers and TiO_2/WO_3 nanocomposites are displayed in Fig. 2b. As it is shown in Fig. 2b, TiO_2 is formed at its anatase phase and exhibit phonon frequencies at 142 cm^{-1} (E_g), 395 cm^{-1} (B_{1g}), 515 cm^{-1} (A_{1g}), and 642 cm^{-1} (E_g), which are consistence with the literature within ±1% deviation [29]. After coupling the WO_3 nanocomposites, the monoclinic WO_3 phase appears at 271 cm^{-1}, 712 cm^{-1}, and 801 cm^{-1}, which can be ascribed to the formation of W-O-W bending mode (bridging oxide ions) and W-O-W stretching mode (tungsten oxide network) [30].

To investigate the detailed surface composition and elemental bonding condition of the as-prepared nanocomposite, XPS analysis was conducted and shown in Fig. 2c-f. Fig. 2c exhibits the wide range XPS spectrum of the TiO_2/WO_3 nanocomposite. The XPS survey spectrum displays distinctive peaks of Ti, O, and W in the as-prepared nanofibers, proving the presence of titanium, oxygen, and tungsten elements. The Ti 2p spectrum of the TiO_2/WO_3 nanofibers is shown in Fig. 2d. Two peaks at binding energies of 458.5 eV and 464.3 eV correspond to the Ti $2p_{3/2}$ and Ti $2p_{1/2}$ peaks, respectively. The splitting of the 2p doublet is 5.8 eV, suggesting the existence of the Ti^{4+} oxidation state in the as-prepared TiO_2/WO_3 nanofibers [31]. As exhibited in the XPS spectra of O 1s (Fig. 2e), the O 1 s spectra can be fitted with two peaks: 530.1 eV and 531.5 eV. The former corresponds to the Ti-O and W-O bonds, while the latter can be attributed to both the Ti-OH and W-OH bonds. Fig. 2f shows the W 4f spin-orbit spectra and their deconvolution analysis. The binding energy peak at 35.4 eV results from the emission of W $4f_{7/2}$ core-level, which can be attributed to the W^{6+} oxidation state of tungsten atoms. Another peak at 37.4 eV is indexed to W $4f_{5/2}$, and the splitting of the 4f doublet is 2.0 eV, indicating that the tungsten is in the W^{6+} valance state [31]. These XPS results

provide evidence that the TiO$_2$/WO$_3$ nanofibers were successfully synthesized with the composition of TiO$_2$ and WO$_3$.

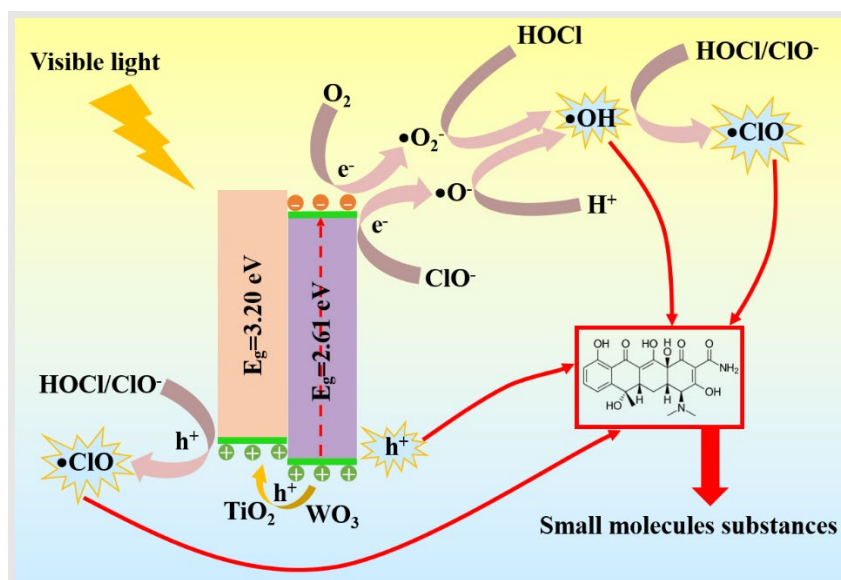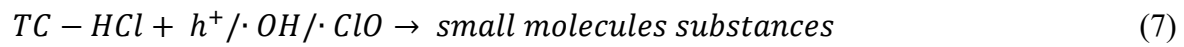## 3.2 Production mechanism of free radicals

Fig. 3. Proposed mechanism of the highly oxidizing •OH and •ClO radicals for the synergistic degradation of TC-HCl in the PC-chlorination system.

The proposed mechanism of the PC/chlorination process with TiO$_2$/WO$_3$ nanofibers under visible light is exhibited in Fig. 3. After introducing the visible light, the electrons (e$^-$) in the valence band (VB) of WO$_3$ are stimulated to the conduction band (CB). Due to the band edge position of TiO$_2$ and WO$_3$, the photogenerated holes (h$^+$) left in the VB of WO$_3$ can be smoothly transferred to the VB of TiO$_2$. In this way, the recombination rate of photogenerated electron and hole pairs is significantly impeded, favoring the PC activity of TiO$_2$/WO$_3$ nanocomposites under visible irradiation. When adding FC (HClO/ClO$^-$) into the PC system, the photo-induced holes in the VB of TiO$_2$ start to oxidize the HClO/ClO$^-$ into chlorine monoxide radical (•ClO), while the e$^-$ in the CB of WO$_3$ reacts with the O$_2$ to produce •O$_2^-$ (Eq. 3 and 4) [32]. As mentioned before (Eq. 1 and 2), the HOCl and ClO$^-$ in water solution will further react with •O^{2-} and e$^-$ to

generate •OH and •O⁻, respectively. Since the solution is in the acidic condition, the •O⁻ radicals can be easily converted into •OH (Eq. 5). The formed •OH may either attack TC-HCl directly or further react with HOCl/ClO⁻ to generate •ClO (Eq. 6) [32], which can also attack the TC-HCl into small molecules. In this way, the TC-HCl compounds will be attacked and degraded by photogenerated holes and active radicals with high oxidation potential (•OH, E_0 = 2.8 V; •ClO, E_0 = 1.5-1.8 V) into small molecules substances (Eq. 7).

$$HOCl/ClO^- + h^+ \rightarrow \cdot ClO \tag{3}$$

$$O_2 + e^- \rightarrow \cdot O_2^- \tag{4}$$

$$\cdot O^- + H^+ \rightarrow \cdot OH \tag{5}$$

$$HOCl/ClO^- + \cdot OH \rightarrow \cdot ClO \tag{6}$$

$$TC - HCl + h^+/\cdot OH/\cdot ClO \rightarrow small\ molecules\ substances \tag{7}$$
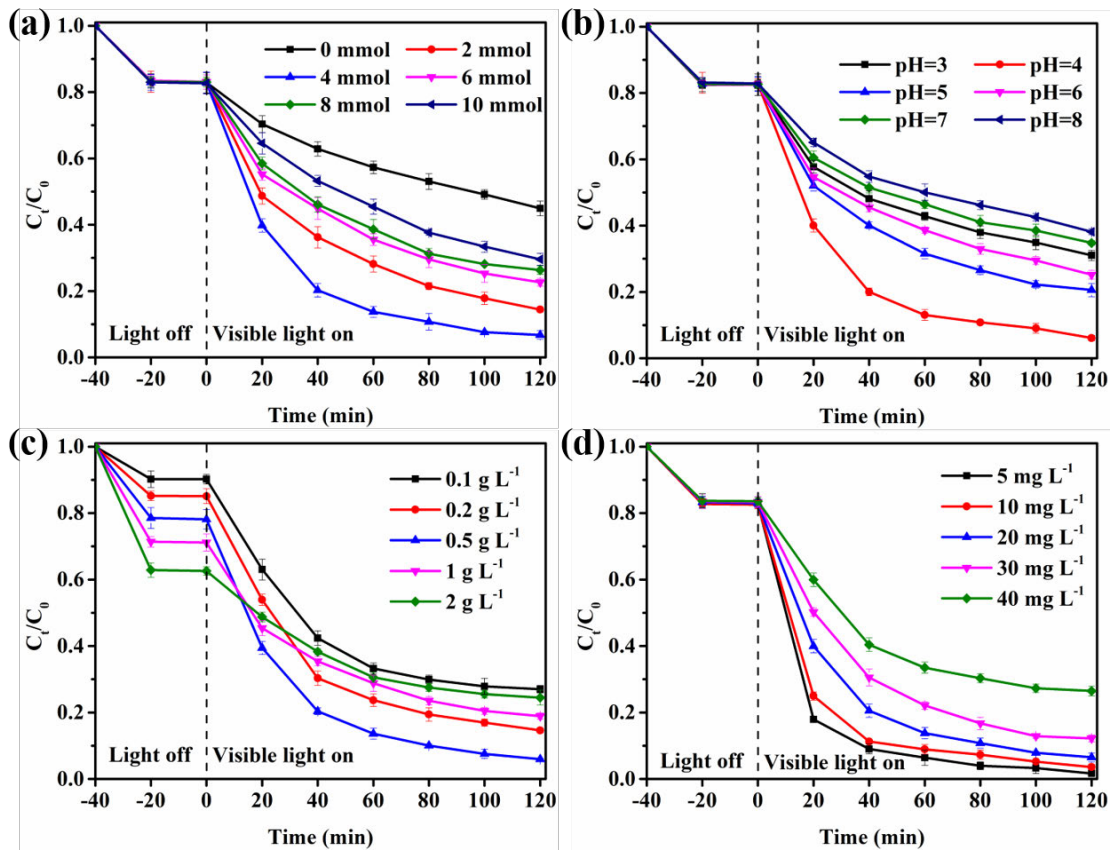
3.3 Influencing factors on V-PC/C-P

Fig. 4. The effect of (a) FC concentration, (b) initial pH, (c) TiO$_2$/WO$_3$ concentration, and (d) initial concentration of TC-HCl on the degradation process of TC-HCl.

To better understand the effect of different influential factors on V-PC/C-P, several optimization experiments are carried out. Firstly, the effect of FC concentrations (0, 2, 4, 6, and 10 mmol L^{-1}) on TC-HCl removal experiments are carried out (Fig. 4a). The TiO$_2$/WO$_3$ concentration is 0.5 mg L^{-1}, the initial pH is 4, and the initial antibiotic concentration is 20 mg L^{-1}. With the concentration of FC increases from 0 to 4 mmol L^{-1}, the degradation rate of TC-HCl after 120 min increases from 45.8% to 91.8%. The results can be ascribed to the boosting of the yield of active radicals (•OH and •ClO) when increasing the FC concentration in the system. Nevertheless, when the FC concentration is higher than 4 mmol L^{-1}, further increasing the FC concentration will jeopardize the degradation performance of TC-HCl. This phenomenon

can be resulted from the consumption of •OH by excessive amounts of FC in water. As it is mentioned before in the mechanism of V-PC/C-P, part of the •OH radicals will attack and degrade antibiotics, while other •OH radicals are going to be captured by $HClO/ClO^-$ in water to generate •ClO. When the FC concentration is too high, most •OH radicals will be converted to •ClO, an active radical with comparatively lower oxidation potential (•ClO, $E_0 = 1.5\text{-}1.8$ V compared to •OH, $E_0 = 2.8$ V), and therefore the degradation performance will be decelerated.

Since the $•O^-$ radicals, generated by the reduction of ClO^-, will react with the H^+ in water solution to produce •OH, the pH of the solution is an essential parameter to improve the yield of •OH radicals in V-PC/C-P [33]. Therefore, the effect of initial pH (3 - 8) on TC-HCl degradation is studied (Fig. 4b). The pH value of the water samples is controlled *via* HCl (0.1 mol L^{-1}) and NaOH (0.1 mol L^{-1}) solutions. The TiO_2/WO_3 concentration is 0.5 g L^{-1}, the FC concentration is 4 mmol L^{-1}, and the initial TC-HCl concentration is 20 mg L^{-1}. Apparently, the performance of TC-HCl degradation under the acidic condition is better than that under the neutral and alkaline condition since a smaller pH value represents a larger amount of H^+ in water and therefore improve the •OH generation. However, when the pH value of the solution decreases to 3, the degradation rate of TC-HCl dramatically declined. This phenomenon can be ascribed to the following reason. The pK_a values for TC-HCl are 3.3, 7.7, and 9.7, so the TC-HCl molecule is neutral when the pH value is between 3.3 and 7.7 [34]. When the pH of the solution is below 3.3, the TC-HCl and photocatalysts are mainly in the cation form, which makes them repel each other. In this way, the degradation efficiency of TC-HCl is impeded and resulting in the optimized initial pH value for V-PC/C-P is 4.

We also investigate the influence of different amounts of photocatalysts (0.1, 0.2, 0.5, 1, and 2 g L^{-1}) on

the degradation efficiency of TC-HCl. The initial pH is 4, the FC concentration is 4 mmol L^{-1}, and the initial TC-HCl concentration is 20 mg L^{-1}. As shown in Fig. 4c, before illumination, the adsorption capacity of photocatalysts is enhanced with the increase of the initial concentration of TiO_2/WO_3 nanofibers. After introducing visible light, the degradation performance of TC-HCl has been improved from 70.1% to 92.4% when the TiO_2/WO_3 concentrations increased from 0.1 to 0.5 g L^{-1}. When further adding photocatalysts concentration (1 and 2 g L^{-1}), the degradation rate of V-PC/C-P drops to 73.4% and 60.9%, respectively. The results can be ascribed to the aggregation of an excessive amount of photocatalysts, which blocks the irradiation light and hinders the generation of photo-induced electrons and holes. In this way, the degradation rate of V-PC/C-P is slowed down.

Additionally, different initial concentrations of TC-HCl solution (5, 10, 20, 30, and 40 mg L^{-1}) were used to investigate their effects on the performance of the PC/chlorination degradation system. The TiO_2/WO_3 concentration is 0.5 g L^{-1}, the FC concentration is 4 mmol L^{-1}, and the initial pH is 4. As shown in Fig. 4d, When the initial concentration of the antibiotic increases from 5 to 40 mg L^{-1}, the TC-HCl degradation rate decreases from 98.0% to 68.3%, which can be ascribed to two reasons. Firstly, when the TC-HCl concentration increases, the by-products of TC-HCl increase as well, which is going to compete with the target antibiotics for capturing active radicals. In this way, the degradation process is severely impeded, and the TC-HCl degradation rate decrease significantly. Secondly, the intermediates produced during the degradation process can cover the surface of the photocatalyst. With the increasing initial concentration of TC-HCl, more and more photocatalysts will be fully covered by the intermediates, which impede the PC process of the photocatalysts and, therefore, slow down the degradation performance of the system. With all the optimization experiments results, we can conclude that the optimized condition for V-PC/C-P is with

the initial FC concentration of 4 mmol L^{-1}, the initial pH of 4, the initial photocatalysts concentration of 0.5 g L^{-1}, and the initial antibiotics concentration of 5 mg L^{-1}.

3.4 TC-HCl degradation performance with V-PC/C-P under optimized condition
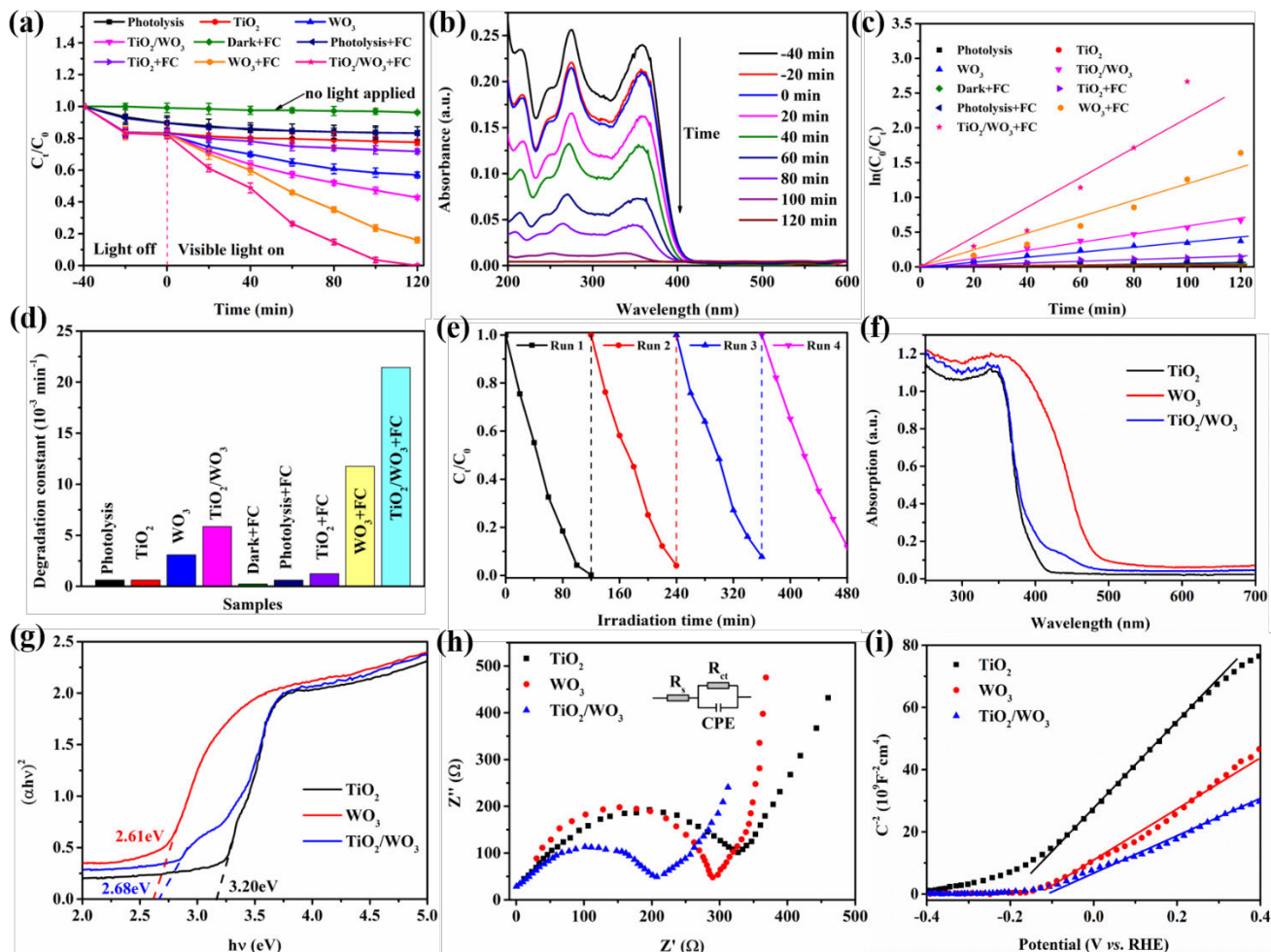
Fig. 5. (a) PC removal of TC-HCl on the materials under the different conditions; (b) The UV–vis absorption curves for degradation of TC-HCl with TiO$_2$/WO$_3$ at different irradiation time; (c) Pseudo-first-order kinetics for the degradation of TC-HCl under visible irradiation; (d) the degradation rate constants derived from Fig. 5c; (e) stability tests for the TiO$_2$/WO$_3$ nanofibers on the removal of TC-HCl. (f) UV-vis absorbance curves, (g) Tauc plots, (h) EIS spectra, and (i) M-S spectra of TiO$_2$, WO$_3$, and TiO$_2$/WO$_3$

PC activity of the TiO$_2$/WO$_3$ nanofibers has been investigated by degrading TC-HCl under optimized conditions (Fig. 5a). Before adding the photocatalysts, the removal efficiency of the photolysis process was

negligible. After introducing TiO₂ nanofibers, 1.8% of the TC-HCl was eliminated after 120 min, indicating that the pristine TiO₂ nanofibers hardly respond to visible light illumination. When changing the photocatalyst from pristine TiO₂ nanofibers to TiO₂/WO₃ nanofibers, the degradation rate of TC-HCl increases to 49.4%, which proves that the coupling of TiO₂ with WO₃ significantly improve the light absorption range of the photocatalyst and further enhance the photogenerated charge carrier's separation rate. The traditional chlorination process is simulated by carrying out the experiment under the "Dark+FC" condition. As shown in Fig. 5a, the degradation rate on TC-HCl by the traditional chlorination process is also negligible, which proves that the traditional chlorination process can hardly remove antibiotics from water bodies. The performance of either merely PC degradation or the traditional chlorination process on TC-HCl is not outstanding, and therefore the synergistic degradation integrating PC and chlorination is needed. As exhibited in Fig. 5a and b, the performance of antibiotics removal is facilitated after adding 2.51 mmol HClO. Notably, the TiO₂/WO₃ nanofibers successfully degrade 100% TC-HCl after 120 min under visible light irradiation with the assistance of FC in water solution. To better study the performance of antibiotics removal on different photocatalysts, the pseudo-first-order kinetics model is applied, as shown in Eq. 8:

$$\ln (C_0/C_t) = kt \tag{8}$$

where C_0 represents the initial concentration of TC-HCl solution, C_t represents the antibiotics concentration at time t, and k represents the degradation rate constant. As presented in Fig. 5c, the kinetics plots are obtained based on Eq. 8. The degradation rate constant of each system is calculated from the kinetics plots (Fig. 5c) and displayed in Fig. 5d. The reaction rate constant of TiO₂/WO₃ nanofibers with the presence of FC is 21.44×10^{-3} min⁻¹, which was much higher than that of TiO₂ (1.24×10^{-3} min⁻¹) and WO₃ ($11.75 \times$

10^{-3} min^{-1}) as well as the TiO$_2$/WO$_3$-based PC degradation system without FC addition (5.86×10^{-3} min^{-1}). The outcomes provide evidence that the synergistic effects between PC degradation and chlorination could significantly enhance the removal rate of TC-HCl on TiO$_2$/WO$_3$ nanofibers under visible light. The repeatability of PC performance for V-PC/C-P was investigated by repeating the degradation experiments toward 5 mg L^{-1} TC-HCl under visible light (Fig. 5e). Photocatalyst is collected and washed several times with distilled water and ethanol after each test. The plots show no significant decrease with only a 7.8% drop in degradation rate after four cycles. The drop in degradation rates can be ascribed to the photocatalyst loss during the washing process.

The superior performance of TiO$_2$/WO$_3$ nanofibers in degradation of TC-HCl under visible light is hypothesized to result from the outstanding optical, electrochemical, and photoelectrochemical properties of the material. Therefore, a series of characterization methods are used to provide evidence for this assumption. For the optical feature's characterization, Fig. 5f shows the UV-vis absorption curvesDRS of as-prepared photocatalysts. It can be observed that TiO$_2$/WO$_3$ nanocomposite exhibits better absorbance in the visible light region (λ = 400-500 nm) compared to that of the pristine TiO$_2$ nanofibers. Tauc plots (Fig. 5g) were derived from UV-vis spectra according to the Tauc equation (Eq. 9) [35]:

$$(\lambda h\upsilon)^n = A(h\upsilon - E_g) \tag{9}$$

where A is a constant, $h\upsilon$ represents the light energy, λ represents the wavelength of light, and n is 0.5 because of the indirect band-gap type of anatase TiO$_2$. The E$_g$ of the as-prepared samples can be obtained by extrapolating the linear parts of the Tauc plots. As shown in Fig. 5g, the E$_g$ value for the bare TiO$_2$ nanofibers is estimated to be 3.20 eV, which corresponds to the band-gap of anatase TiO$_2$. After the growth of WO$_3$ (E$_g$ = 2.61 eV), the TiO$_2$/WO$_3$ nanofibers present an E$_g$ value located at about 2.68 eV. The UV-vis

spectra display that the TiO_2/WO_3 nanocomposites extend the light absorption range of photocatalysts and result in a higher PC activity under visible irradiation.

To further investigate the electrochemical properties of the photocatalysts, EIS measurements were applied with a frequency ranging from 10 mHz to 1 MHz and an amplitude of 5 mV. All the Nyquist plots (TiO_2, WO_3, and TiO_2/WO_3 nanomaterials) exhibited in Fig. 5h exhibits a similar shape with a semicircle, which corresponds to the charge carrier transmission properties of materials in the high-frequency region. The Nyquist plots exhibit that the TiO_2/WO_3 nanocomposites possess the smallest charge transmission impedance on the interface between photocatalyst and electrolyte since the radius of the semicircle of TiO_2/WO_3 is the smallest, which means it possesses the lowest charge transfer resistance [36]. The comparatively low charge transmission resistance can be ascribed to the enhanced separation rate of photogenerated electron-hole pairs from TiO_2/WO_3 and the fast charge transfer speed of the 1-D nanofiber morphology.

To gain more insights on the flat band potentials (E_{fb}) of as-prepared materials, Mott-Schottky (M-S) plots were investigated (Fig. 5i). The positive slopes of the M-S curves in Fig. 5i illustrate that all the as-prepared photocatalysts are typical n-type semiconductors [37]. The donor density (N_d) of all samples was calculated *via* Eq. 10:

$$N_d = \frac{2/e_0\varepsilon\varepsilon_0}{d(1/C^2)/dV} \tag{10}$$

Where e_0, ε, and ε_0 are constants, representing the electron charge, the dielectric constant, and the permittivity of free space in vacuum, respectively. $d(1/C^2)/dV$ represents the slope of extrapolating the linear parts of M-S curves. Since the values of e_0, ε_0 and ε are constants, it could be deduced that N_d was inversely proportional to $d(1/C^2)/dV$, which means a smaller slope of the plot represents higher donor

density of the corresponding material. Herein, the TiO$_2$/WO$_3$ nanocomposites exhibit the highest donor density among all as-prepared photocatalysts, consistent with the results obtained from the Nyquist plots (Fig. 5h). All these characterization results prove that the TiO$_2$/WO$_3$ nanofibers possess superior optical and electrochemical properties compared to other as-prepared photocatalysts, which explains the favorable PC performance of TiO$_2$/WO$_3$ nanofibers in degradation antibiotics under visible light irradiation.

3.5 Degradation Pathways of TC-HCl in V-PC/C-P

To further investigate the degradation pathway and intermediate produced during the V-PC/C-P, an LC/MS analysis is applied to gain more insight into the TC-HCl degradation process. The reaction solution is collected at different time points, and the MS spectra of the degradation intermediates are exhibited in Fig. S1. According to the mass spectrograms of the intermediate, it can be inferred that there are two potential pathways for the degradation of TC-HCl (Fig. 6). Firstly, since the double bond functional groups are vulnerable to the attack from active radicals because of their high electron density [38], abundant •OH in the solution will attack the double bond in TC-HCl and hydroxylates the antibiotics into P1 (*m/z* 461). Subsequently, the P1 is further oxidized by •OH, •ClO, and h$^+$ in water and produces P2 (*m/z* 431). After that, P3 (*m/z* 376) and P4 (*m/z* 365) are further formed *via* the ring-opening reaction at the cyclotrione structure [39]. Meanwhile, an N-demethylation process simultaneously occurred by attacking the N-C bond in TC-HCl due to its comparatively weak binding energy, producing P5 (*m/z* 417) [39]. Then the active radicals in the solution are going to attack the vulnerable amine group in P5 and further deaminate it into P6 (*m/z* 358), which will experience a dehydroxylation process to produce P7 (m/z 327) subsequently. The intermediate products P8 (*m/z* 242), P9 (*m/z* 213), and P10 (*m/z* 175) are generated *via* a series of ring-opening and oxidizing processes from P3, P4, and P7 [34]. Finally, several small molecular intermediates

such as P11 (*m/z* 122) and P12 (*m/z* 60) are generated and then easily degraded into H_2O and CO_2 by the
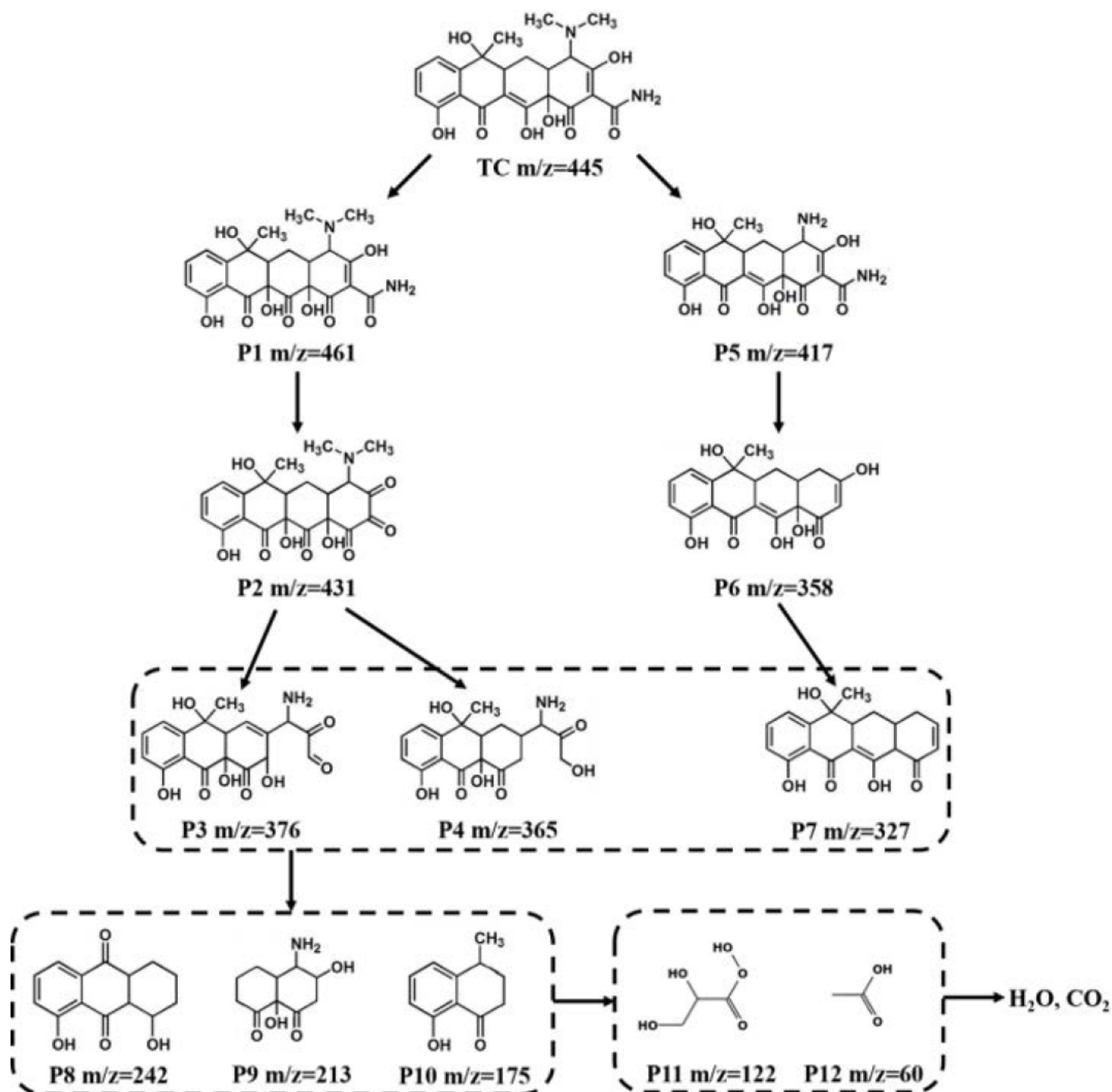
h^+ and active radicals in the V-PC/C-P.

Fig. 6. Proposed degradation pathways and intermediates during V-PC/C-P

4. Conclusion

A study on designing an efficient, low-cost, and easily implementable antibiotics degradation system

based on synergistic effect between photocatalysis and chlorination was carried out, and the results can be summarized as follows. Firstly, to extend the light absorption range of photocatalysts, the TiO_2/WO_3 nanofibers were successfully fabricated *via* a two-step hydrothermal method. The material was characterized by different approaches to prove that the photocatalysts possessed 1-D morphology, resulting in fast charge transfer along the radial direction, facilitating the separation rate of photogenerated electrons and holes. Moreover, the photocatalysts were also characterized to prove that TiO_2/WO_3 nanofibers efficiently respond to visible light irradiation. Secondly, although the photolysis in the traditional chlorination process cannot be triggered by visible illumination, the introduction of visible-light-driven photocatalysts could achieve that goal. When adding TiO_2/WO_3 nanofibers into the chlorination system, the HOCl and ClO^- can be activated to produce •OH and $•O^-$ with the assistance of $•O_2^-$ and e^- generated by the photocatalysis process under visible irradiation. Hence, large amounts of active radicals were produced and well-functioned in degrading antibiotics under visible light irradiation, resulting in efficient antibiotic removal. Additionally, the V-PC/C-P can be easily integrated into the chlorination tank in existing WTPs in a facile and low-cost way. This work provides us an alternative solution to add the antibiotic removal capability to the traditional WTPs.

Reference:

[1] A. Kumar, M. Khan, J. He, I.M. Lo, Recent developments and challenges in practical application of visible–light–driven TiO_2–based heterojunctions for PPCP degradation: A critical review, Water. Res., 170 (2020) 115356.

[2] J. Jiang, J. Han, X. Zhang, Nonhalogenated aromatic DBPs in drinking water chlorination: a gap between NOM and halogenated aromatic DBPs, Environ. Sci. Technol., 54 (2020) 1646-1656.

[3] L. Xu, W. Ouyang, Y. Qian, C. Su, J. Su, H. Chen, High-throughput profiling of antibiotic resistance genes in drinking water treatment plants and distribution systems, Environ. Pollut., 213 (2016) 119-126.

[4] W. Lin, M. Zhang, S. Zhang, X. Yu, Can chlorination co-select antibiotic-resistance genes?, Chemosphere, 156 (2016) 412-419.

[5] T. Zhang, Y. Hu, L. Jiang, S. Yao, K. Lin, Y. Zhou, C. Cui, Removal of antibiotic resistance genes and control of horizontal transfer risk by UV, chlorination and UV/chlorination treatments of drinking water, Chem. Eng. J., 358 (2019) 589-597.

[6] Y. Chen, J.-Q. Su, J. Zhang, P. Li, H. Chen, B. Zhang, K.Y.-H. Gin, Y. He, High-throughput profiling of antibiotic resistance gene dynamic in a drinking water river-reservoir system, Water. Res., 149 (2019) 179-189.

[7] Y. Zhang, A.Z. Gu, M. He, D. Li, J. Chen, Subinhibitory concentrations of disinfectants promote the horizontal transfer of multidrug resistance genes within and across genera, Environ. Sci. Technol., 51 (2017) 570-580.

[8] W.-W. Cai, T. Peng, B. Yang, C. Xu, Y.-S. Liu, J.-L. Zhao, F.-L. Gu, G.-G. Ying, Kinetics and mechanism of reactive radical mediated fluconazole degradation by the UV/chlorine process: Experimental and theoretical studies, Chem. Eng. J., 402 (2020) 126224.

[9] Z. Hua, D. Li, Z. Wu, D. Wang, Y. Cui, X. Huang, J. Fang, T. An, DBP formation and toxicity alteration during UV/chlorine treatment of wastewater and the effects of ammonia and bromide, Water. Res., 188 (2021) 116549.

[10] H. Wang, J. Wang, S. Li, G. Ding, K. Wang, T. Zhuang, X. Huang, X. Wang, Synergistic effect of UV/chlorine in bacterial inactivation, resistance gene removal, and gene conjugative transfer blocking, Water. Res., 185 (2020) 116290.

[11] M.J. Watts, K.G. Linden, Chlorine photolysis and subsequent OH radical production during UV treatment of chlorinated water, Water. Res., 41 (2007) 2871-2878.

[12] J. Fang, Y. Fu, C. Shang, The roles of reactive species in micropollutant degradation in the UV/free chlorine system, Environ. Sci. Technol., 48 (2014) 1859-1868.

[13] D.K. Roth, D.A. Cornwell, DBP impacts from increased chlorine residual requirements, J. Am. Water. Works. Ass., 110 (2018) 13-28.

[14] X. Kong, L. Wang, Z. Wu, F. Zeng, H. Sun, K. Guo, Z. Hua, J. Fang, Solar irradiation combined with chlorine can detoxify herbicides, Water. Res., (2020) 115784.

[15] Z. Hua, K. Guo, X. Kong, S. Lin, Z. Wu, L. Wang, H. Huang, J. Fang, PPCP degradation and DBP formation in the solar/free chlorine system: Effects of pH and dissolved oxygen, Water. Res., 150 (2019) 77-85.

[16] X. Zhang, J. He, Y. Lei, Z. Qiu, S. Cheng, X. Yang, Combining solar irradiation with chlorination enhances the photochemical decomposition of microcystin-LR, Water. Res., 159 (2019) 324-332.

[17] M. Zu, M. Zheng, S. Zhang, C. Xing, M. Zhou, H. Liu, X. Zhou, S. Zhang, Designing robust anatase-branch@ hydrogenated-rutile-nanorod TiO_2 as accurate and sensitive photoelectrochemical sensors, Sens. Actuators B Chem., (2020) 128504.

[18] C.A. Long, B.H. Bielski, Rate of reaction of superoxide radical with chloride-containing species, J. Phys. Chem., 84 (1980) 555-557.

[19] Y. Qian, L. Wang, J. Du, H. Yang, M. Li, Y. Wang, D.J. Kang, A high catalytic activity photocatalysts based on porous metal sulfides/TiO_2 heterostructures, Adv. Mater. Interfaces, 8 (2021) 2001627.

[20] H. Yin, Y. Cao, T. Fan, B. Qiu, M. Zhang, J. Yao, P. Li, X. Liu, S. Chen, Construction of carbon bridged TiO_2/CdS tandem Z-scheme heterojunctions toward efficient photocatalytic antibiotic degradation and Cr (VI) reduction, J. Alloys. Compd., 824 (2020) 153915.

[21] Q. Pan, A. Li, Y. Zhang, Y. Yang, C. Cheng, Rational design of 3D hierarchical ternary SnO_2/TiO_2/$BiVO_4$ arrays photoanode toward efficient photoelectrochemical performance, Adv. Sci., 7 (2020) 1902235.

[22] M. Khalil, F. Naumi, U. Pratomo, T.A. Ivandini, G.T. Kadja, J.Y. Mulyana, Coexposed TiO_2's (001) and (101) facets in TiO_2/$BiVO_4$ photoanodes for an enhanced photocatalytic fuel cell, Appl. Surf. Sci., 542 (2021) 148746.

[23] Y. You, W. Tian, L. Min, F. Cao, K. Deng, L. Li, TiO_2/WO_3 bilayer as electron transport layer for efficient planar perovskite solar cell with efficiency exceeding 20%, Adv. Mater. Interfaces, 7 (2020) 1901406.

[24] L. Kang, X.Y. Liu, A. Wang, L. Li, Y. Ren, X. Li, X. Pan, Y. Li, X. Zong, H. Liu, Photo–thermo catalytic oxidation over a TiO_2‑WO_3‑supported platinum catalyst, Angew. Chem., 132 (2020) 13009-13016.

[25] Z. Yu, H. Liu, M. Zhu, Y. Li, W. Li, Interfacial charge transport in 1D TiO_2 based photoelectrodes for photoelectrochemical water splitting, Small, 17 (2021) 1903378.

[26] J. Yu, H. Yu, B. Cheng, X. Zhao, Q. Zhang, Preparation and photocatalytic activity of mesoporous anatase TiO_2 nanofibers by a hydrothermal method, J. Photochem. Photobiol. A, 182 (2006) 121-127.

[27] T. Cao, Y. Li, C. Wang, C. Shao, Y. Liu, A facile in situ hydrothermal method to $SrTiO_3$/TiO_2 nanofiber heterostructures with high photocatalytic activity, Langmuir, 27 (2011) 2946-2952.

[28] H. Khan, M.G. Rigamonti, G.S. Patience, D.C. Boffito, Spray dried TiO_2/WO_3 heterostructure for photocatalytic applications with residual activity in the dark, Appl. Catal. B, 226 (2018) 311-323.

[29] V.O. Odhiambo, A. Ongarbayeva, O. Kéri, L. Simon, I.M. Szilágyi, Synthesis of TiO_2/WO_3 composite nanofibers by a water-based electrospinning process and their application in photocatalysis, Nanomaterials, 10 (2020) 882.

[30] C. Wang, Y. Li, P. Qiu, L. Duan, W. Bi, Y. Chen, D. Guo, Y. Liu, W. Luo, Y. Deng, Controllable synthesis of highly crystallized mesoporous TiO_2/WO_3 heterojunctions for acetone gas sensing, Chin. Chem. Lett., 31 (2020) 1119-1123.

[31] H. Gao, P. Zhang, J. Hu, J. Pan, J. Fan, G. Shao, One-dimensional Z-scheme TiO_2/WO_3/Pt heterostructures for enhanced hydrogen generation, Appl. Surf. Sci., 391 (2017) 211-217.

[32] Z. Cheng, L. Ling, Z. Wu, J. Fang, P. Westerhoff, C. Shang, Novel visible light-driven photocatalytic chlorine activation process for Carbamazepine degradation in drinking water, Environ. Sci. Technol., 54 (2020) 11584-11593.

[33] S.P. Onkani, P.N. Diagboya, F.M. Mtunzi, M.J. Klink, B.I. Olu-Owolabi, V. Pakade, Comparative study

of the photocatalytic degradation of 2–chlorophenol under UV irradiation using pristine and Ag-doped species of TiO_2, ZnO and ZnS photocatalysts, J. Environ. Manage., 260 (2020) 110145.

[34] T. Zhang, Y. Liu, Y. Rao, X. Li, D. Yuan, S. Tang, Q. Zhao, Enhanced photocatalytic activity of TiO_2 with acetylene black and persulfate for degradation of tetracycline hydrochloride under visible light, Chem. Eng. J., 384 (2020) 123350.

[35] J. Tauc, Optical properties and electronic structure of amorphous Ge and Si, Mater. Res. Bull., 3 (1968) 37-46.

[36] F. Chen, T. Ma, T. Zhang, Y. Zhang, H. Huang, Atomic-level charge separation strategies in semiconductor-based photocatalysts, Adv. Mater., 33 (2021) 2005256.

[37] H. Zhao, Z. Xing, S. Su, S. Song, Z. Li, W. Zhou, Gear-shaped mesoporous NH_2-MIL-53(Al)/CdS P-N heterojunctions as efficient visible-light-driven photocatalysts, Appl. Catal. B, 291 (2021) 120106.

[38] J. Wang, D. Zhi, H. Zhou, X. He, D. Zhang, Evaluating tetracycline degradation pathway and intermediate toxicity during the electrochemical oxidation over a Ti/Ti_4O_7 anode, Water. Res., 137 (2018) 324-334.

[39] J. Chen, X. Xiao, Y. Wang, Z. Ye, Ag nanoparticles decorated WO_3/g-C_3N_4 2D/2D heterostructure with enhanced photocatalytic activity for organic pollutants degradation, Appl. Surf. Sci., 467 (2019) 1000-1010.

Efficient removal of antibiotics via a synergetic process combining visible-light-driven TiO₂/WO₃ nanofibers photocatalysis and chlorination

Meng Zu [1], Shengsen Zhang [2, *], Changyu Liu [3], Rorun Liu [1], Dongsheng Li [4], Chao Xing [1,5], Shanqing Zhang [1, *]

[1] Centre for Clean Environment and Energy and Griffith School of Environment, Griffith University, Gold Coast, QLD 4222, Australia

[2] College of Materials and Energy, South China Agricultural University, Guangzhou 510643, Guangdong, China

[3] School of Biotechnology and Health Sciences, Wuyi University, Jiangmen 529020, China

[4] College of Materials and Chemical Engineering, Key Laboratory of Inorganic Nonmetallic Crystalline and Energy Conversion Materials, China Three Gorges University, Yichang, 443002, China)

[5] Key Laboratory of Materials Processing and Mold (Zhengzhou University), Ministry of Education, Zhengzhou, 450002, China

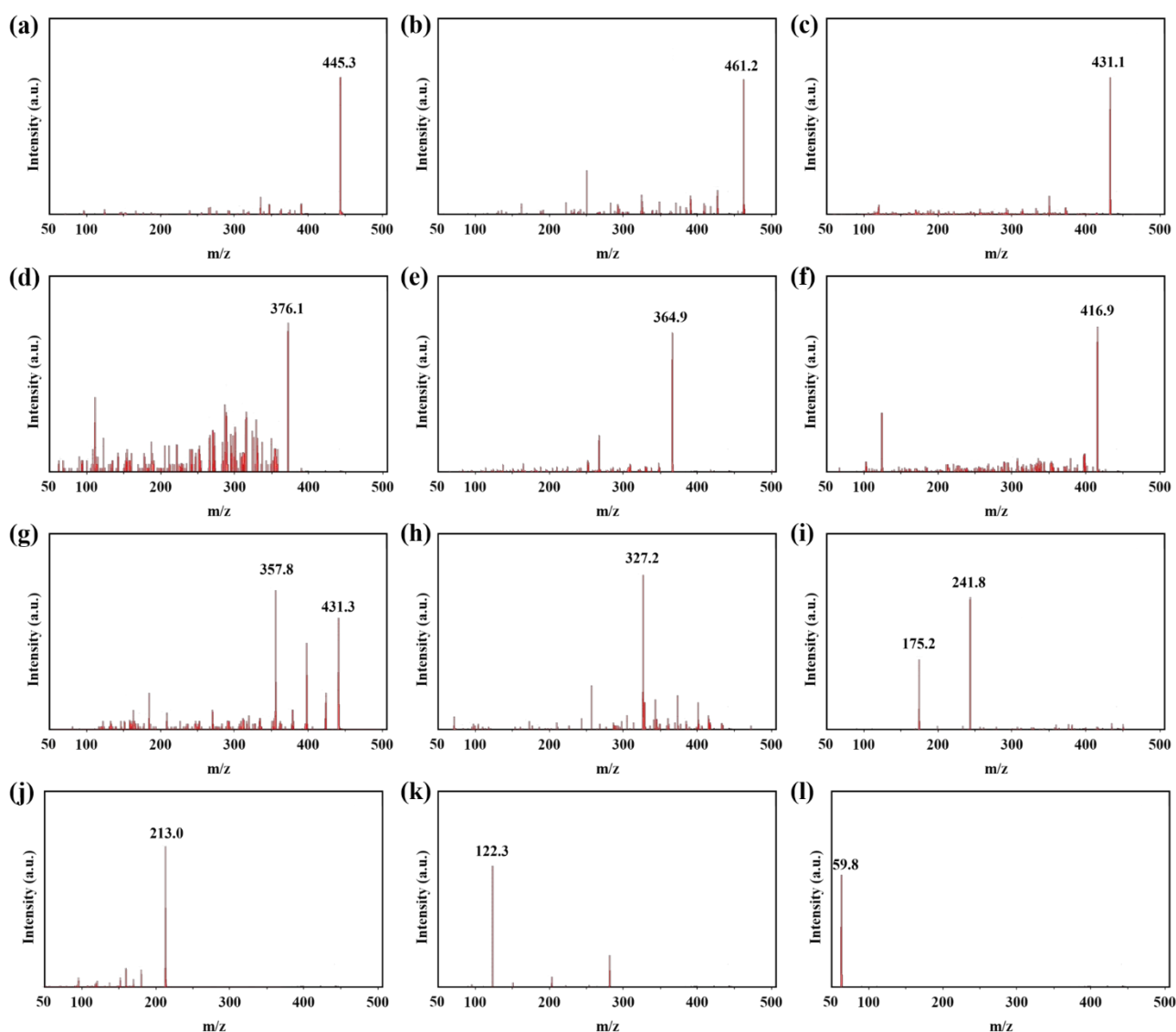*Corresponding author: zhangss@scau.edu.cn, s.zhang@griffith.edu.au

Figure S1. Mass spectrograms analysis of reaction intermediates during the PC/chlorine degradation of TC-HCl by TiO$_2$/WO$_3$ nanofibers under visible light irradiation.

CHAPTER 6

N-doped carbon wrapped FeNi nanoparticles co-catalysts for the photodegradation of antibiotics under visible-light irradiation

6.1 INTRODUCTORY REMARKS

The findings and developments in this chapter are summarized in an article form for submission to *ACS Sustainable Chemistry & Engineering*.

In this work, we fabricated noble-metal free co-catalysts, i.e., N-doped carbon wrapped FeNi nanoparticles (FeNi@NGC), via a pyrolysis method. Hydrogenated TiO_2 (H-TiO_2) was synthesized as the host photocatalysts and coupled with as-prepared FeNi@NGC to obtain superior PC activity in the degradation of tetracycline hydrochloride (TC-HCl), a model antibiotic. The FeNi@NGC/H-TiO_2 system achieved a degradation rate of 100% within 120 min on degrading 100 mL 20 mg L^{-1} TC-HCl under visible light irradiation (λ>420 nm). The degradation rate constant of the FeNi@NGC/H-TiO_2 system reached 23.18 min^{-1}, which was 33.99, 26.98, and 2.23 times compared to that of TiO_2, FeNi@NGC/TiO_2, and H-TiO_2 system. The favorable performance of the FeNi@NGC/H-TiO_2 system can be ascribed to two reasons: the secondary electron transfer in the FeNi intermetallic compounds that facilitates the photo-induced charge separation in photocatalysts; and the enhanced visible light absorption ability resulted from the N-doped graphitized carbon shell. Moreover, the oxygen vacancies brought by the hydrogenation process also improves the visible light absorbance of the photocatalysts, which favors the degradation performance. This study suggests that coupling FeNi@NGC co-catalyst with H-TiO_2 is a promising strategy for improving the photocatalytic degradation performance on antibiotics.

6.2 STATEMENT OF CONTRIBUTION

My contribution to the paper involved:

Initial concept and experimental design and implementation; Collection and analysis of data;

Preparation of manuscript.

(Signed)_____███████████____(Date) 15-04-2021

Name of Student: Meng Zu

(Countersigned)_____███████████___(Date) 15-04-2021

Supervisor: Shanqing Zhang

6.3 Article 5

N-doped carbon wrapped FeNi nanoparticles co-catalysts for the photodegradation of antibiotics under visible-light irradiation

Meng Zu [1], Shengsen Zhang [2, *], Changyu Liu [3], Rorun Liu [1], Dong-Sheng Li [4], Chao Xing [1,5], Shanqing Zhang [1, *]

[1] Centre for Clean Environment and Energy and Griffith School of Environment, Griffith University, Gold Coast, QLD 4222, Australia

[2] College of Materials and Energy, South China Agricultural University, Guangzhou 510643, Guangdong, China

[3] School of Biotechnology and Health Sciences, Wuyi University, Jiangmen 529020, China

[4] College of Materials and Chemical Engineering, Key Laboratory of Inorganic Nonmetallic Crystalline and Energy Conversion Materials, China Three Gorges University, Yichang, 443002, China)

[5] Key Laboratory of Materials Processing and Mold (Zhengzhou University), Ministry of Education, Zhengzhou, 450002, China

*Corresponding author: zhangss@scau.edu.cn, s.zhang@griffith.edu.au

Abstract

During the last decades, the photocatalytic (PC) degradation method has become a promising strategy in removing refractory organic compounds, i.e., antibiotics, because of its inherent characteristics, such as low-cost, environmentally friendly, and easily implementable. Coupling noble-metal co-catalysts with the photocatalysts seems to be an efficient approach to improve the PC degradation performance. Nevertheless, the low cost-effectiveness of noble-metal co-catalysts has impeded the sustainable development of this approach. Herein, we fabricated noble-metal free co-catalysts, i.e., N-doped carbon wrapped FeNi nanoparticles (FeNi@NGC), *via* a pyrolysis method. Hydrogenated TiO_2 (H-TiO_2) was synthesized as the host photocatalysts and coupled with as-prepared FeNi@NGC to obtain superior PC activity in the degradation of tetracycline hydrochloride (TC-HCl), a model antibiotic. The FeNi@NGC/H-TiO_2 system achieved a degradation rate of 100% within 150 min on degrading 100 mL 20 mg L^{-1} TC-HCl under visible light irradiation ($\lambda > 420$ nm). The degradation rate constant of the FeNi@NGC/H-TiO_2 system reached 23.18 min^{-1}, which was 33.99, 26.98, and 2.23 times compared to that of TiO_2, FeNi@NGC/TiO_2, and H-TiO_2 system. The favorable performance of the FeNi@NGC/H-TiO_2 system can be ascribed to two reasons: the secondary electron transfer in the FeNi intermetallic compounds that facilitates the photo-induced charge separation in photocatalysts; and the enhanced visible light absorption ability resulted from the N-doped graphitized carbon shell. Moreover, the oxygen vacancies brought by the hydrogenation process also improves the visible light absorbance of the photocatalysts, which favors the degradation performance. This study suggests that coupling FeNi@NGC co-catalyst with H-TiO_2 is a promising strategy for improving the photocatalytic degradation performance on antibiotics.

Key Words: hydrogenation, noble-metal free, antibiotics degradation, co-catalysts, visible light

1. Introduction

As the process of industry development accelerates, the concentration of the antibiotic in water bodies has far exceeded the standard and arouses increasing concerns all over the world [1, 2]. Photocatalytic (PC) degradation appears to be a promising strategy for efficient degradation of refractory antibiotics due to numerous advances, such as cost-effectiveness, high efficiency, and potential for utilizing solar energy [3, 4]. Despite those advantages, designing the photocatalytic system with a high separation rate of photogenerated charge carriers and enhanced light absorption capability is still challenging [5]. Coupling the host photocatalysts with noble-metal co-catalysts seems to be an alternative strategy for improving the PC activity on the degradation of antibiotics, resulted from the enhanced separation rate of photogenerated electrons and holes [6, 7]. However, the high cost of synthesizing noble-metal co-catalysts severely hinders the sustainable development of this technique. Consequently, various studies have focused on the noble-metal free co-catalysts, such as Fe, Ni, Co, and their oxides, to diminish the spending on synthesizing [8-10]. Among those nonprecious metal elements, Ni appears to be a promising substitute element for Pt in traditional noble-metal-based co-catalysts due to its considerably high work function (5.15 eV) [11].

Nevertheless, the Ni atom's particle size is comparatively small and large amounts of Ni co-catalysts cannot be utilized into the degradation process, which impedes its further application. Therefore, designing intermetallic compounds co-catalysts can effectively address this problem and significantly improves the activity of the co-catalysts due to several reasons [12]. Firstly, the electronegativity between the two elements in the intermetallic compounds provides a potential for the electrons in one element being transferred to the other element. In this way, the electrons can be effectively accumulated in the active sites of the intermetallic co-catalysts [13].

Moreover, the photogenerated electrons will engage in a secondary transmission process transfer to the intermetallic co-catalysts because of the variation of electronegativities between them, facilitating the separation of photogenerated electrons and holes [14]. To improve the light absorption of the co-catalysts,

great amounts of efforts have been made in designing the carbon-based shell wrapped co-catalysts [15-17]. The carbon-based shell possesses a wide spectrum of light absorption range and fine conductivity, which improves the potential of host photocatalysts in utilizing solar energy. Moreover, the shell structure is capable of trapping the irradiation inside and dramatically increase the light utilization rate compared to other morphology. As to further improve the visible light utilization of the PC system, hydrogenated TiO_2 (H-TiO_2) is fabricated as the host catalysts since the hydrogenation on the surface of photocatalysts could bring in abundant oxygen vacancies in the crystal lattice and result in an increase in electron donor density and visible light absorption capability [18, 19].

Herein, we fabricated the N-doped graphitized carbon-wrapped FeNi intermetallic compounds (FeNi@NGC) *via* a pyrolysis method. The FeNi@NGC co-catalysts were incorporated with the host photocatalysts H-TiO_2 *via* mechanical ball-milling to investigate the performance of the co-catalysts on assisting H-TiO_2 in the degradation of antibiotics. The FeNi@NGC/H-TiO_2 photocatalyst exhibits favorable PC degradation performance in the removal of tetracycline hydrochloride (TC-HCl) with a degradation rate of 100% within 150 min and a reaction rate constant of 23.18 min^{-1}. The satisfying result can be ascribed to the enhanced separation rate of photogenerated electron-hole pairs and extended light absorption range with the assistance of FeNi@NGC co-catalysts.

2. Materials and methods

2.1 Chemical reagents

Tetrabutyl titanate (Ti(C_4H_9O)$_4$), hydrochloric acid (HCl, 36.5% by weight), potassium ferricyanide ($K_3[Fe(CN)_6]$), sodium citrate ($C_6H_5Na_3O_7$), nickel nitrate hexahydrate (Ni(NO_3)$_2 \cdot 6H_2O$), ferric ferrocyanide ($Fe_4[Fe(CN)_6]_3$), and urea were purchased from Sigma-Aldrich of analytical reagent (AR) grade. TiO_2 powder (P25, commercial-grade) was obtained from Degussa. All the chemical reagents were used as received without further purification unless otherwise stated.

2.2 Synthesis process

Preparation of Ni$_3$[Fe(CN)$_6$]$_2 \cdot$H$_2$O nanocubes and FeNi@NGC nanoparticles.

Ni$_3$[Fe(CN)$_6$]$_2$·H$_2$O nanocubes were prepared by a method similar to that presented in the literature [12]. Briefly, a 120 mL 6 mmol L^{-1} Ni(NO$_3$)$_2$·6H$_2$O solution and 20 mL 5 mmol L^{-1} C$_6$H$_5$Na$_3$O$_7$ were put in a beaker mixed with 100 ml 5 mmol L^{-1} K$_3$Fe(CN)$_6$ solution under vigorous stirring for 30 min. Then the well-mixed solution was aged overnight. After aging, the precipitates were separated by centrifugation and washed several times before dried in a vacuum oven at 60 °C. The pyrolysis of as-prepared nanocubes obtained the FeNi@NGC nanoparticles. Briefly, the Ni$_3$[Fe(CN)$_6$]$_2$·H$_2$O powder was fine-grinded and calcined at 500 °C in a continuous N$_2$ flow for 2 h. The black powder obtained was FeNi@NGC nanoparticles.

Preparation of H-TiO$_2$

The anatase TiO$_2$ nanorods were synthesized by a two-step hydrothermal process similar to that described by Yu [20]. Briefly, 20 mL distilled water was mixed with 40 mL NaOH (10 mol L^{-1}) and 1.8 g commercial-grade TiO$_2$ powder under vigorous stirring for 30 min to form a suspension. After stirring, the suspension was transferred into a 100 mL autoclave for a hydrothermal process at 180 °C for 48 h. The as-prepared samples were cooled naturally, then separated by filtration and washed several times with HCl (0.1 mol L^{-1}) solution until the pH of the solution became neutral and dried in a vacuum oven at 60 °C overnight. After drying, the sample was mixed with 50 mL HCl (0.1 mol L^{-1}) and then subjected to the second hydrothermal treatment at 180 °C for 48 h. After cooling down to room temperature naturally, the as-prepared material was separated and washed several times with large amount of distilled water. The H-TiO$_2$ nanorods were fabricated by calcinating the as-prepared TiO$_2$ nanorods at 350 °C in a continuous hydrogen and argon (5 % hydrogen) flow for 1 h.

Preparation of FeNi@NGC/TiO$_2$ and Fe@NGC/H-TiO$_2$

The mechanical ball-milling method was applied in mixing as-prepared TiO$_2$ and FeNi@NGC for 1 h to form FeNi@NGC. The Fe@NGC/H-TiO$_2$ photocatalysts were obtained with an identical method.

2.3 Characterization

The nanostructured morphology was characterized by scanning electron microscopy (SEM, JEOL JSM-7001F, Japan). To further investigate the composition of the material, the transmission electron microscope (TEM, JEOL JEM-2010 F, Japan) was applied. The crystallographic phase and structure of photocatalysts were tested by X-ray diffraction (XRD) with an X-ray diffractometer [Cu-Kα radiations (wavelength, 1.5406 Å) on a Bruker D8 System]. The Raman test was carried out on a Raman microscope (Renishaw). X-ray photoelectron spectrophotometer (XPS) results were obtained in a Krato Axis Ultra DLD spectrometer at 15 kV and 150 W. UV-visible (UV-vis) experiments were conducted with Agilent Cary 300 UV-vis spectrophotometer to gain more insights on the band-gap condition. Electrochemical impedance spectroscopy (EIS) plots were obtained on an electrochemical station (CHI 660e) to study the charge transfer of the photocatalysts. Mott-Schottky (M-S) analysis was carried out in a quartz cell in 0.1 mol L^{-1} $NaNO_3$ solution, applying a three-electrode configuration with a frequency of 1 kHz.

2.4 Experimental procedure

The study on PC degradation performance on TC-HCl was applied in XPA-system Photochemical Reactors (Nanjing, China). FC concentrations were adjusted by adding hypochlorous acid (HClO) in water solution and were determined by a DPD colorimetric method with a detection limit of 0.10 μmol L^{-1}. To maintain the temperature of the aqueous solution at 25°C during the reaction, the quartz glass tubes were put in a water tank with cold water circulating. Before introducing visible light, the solution was stirred in the dark for 40 min to reach an adsorption/desorption equilibrium. A 0.5 mL sample solution was collected and centrifuged to remove the unexpected solid particles every 30 min. The degraded TC-HCl concentration was analyzed using a Cary 50 spectrophotometer (Varian Co., USA). The reusability and stability of FeNi@NGC/H-TiO$_2$ were examined by conducting four consecutive TC-HCl degradation experiments under the same experimental conditions.

3. Results and discussion
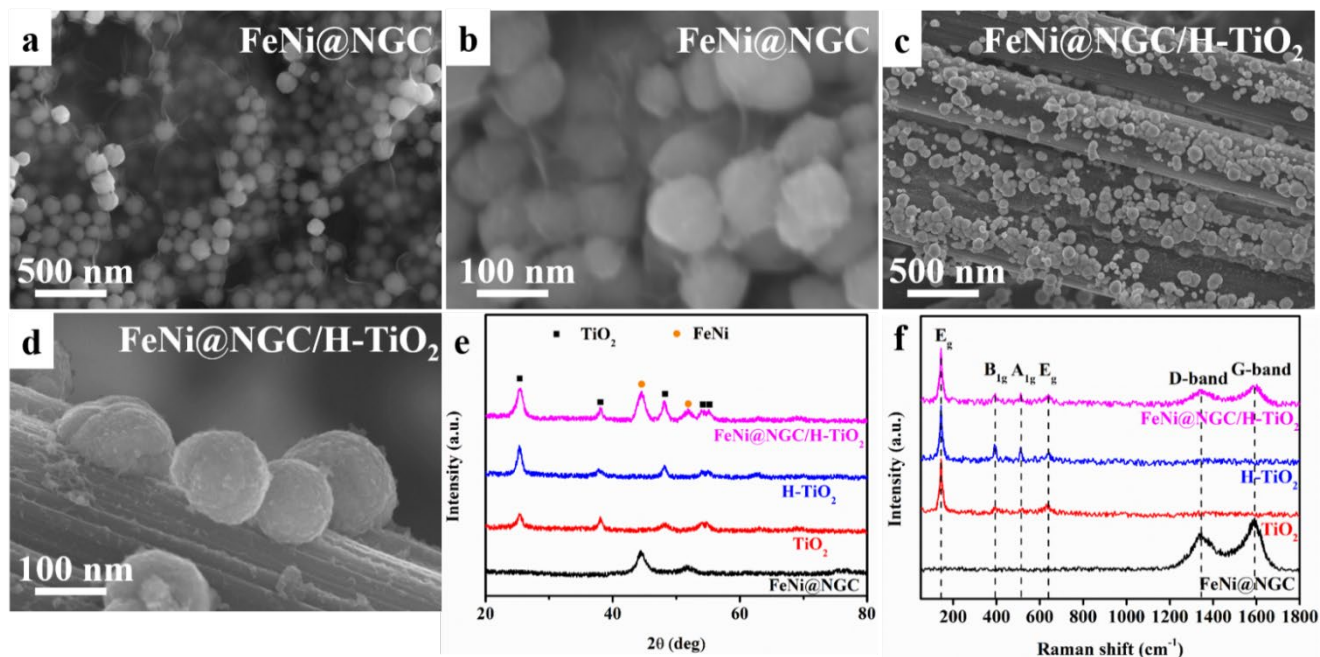
3.1 Photocatalysts characterization

Figure 1. FESEM images of (a) (b) FeNi@NGC and (c) (d) FeNi@NGC/H-TiO$_2$. (e) XRD patterns and (f) Raman spectra of as-prepared materials.

The FeNi@NGC co-catalysts are fabricated by a pyrolysis method with Ni(NO$_3$)$_2$·6H$_2$O and C$_6$H$_5$Na$_3$O$_7$ solution. As shown in Fig. 1a and b, the size of FeNi@GNC nanoparticles is about 100 nm, and the structure of graphitized carbon shells can be observed. After grinding the co-catalysts with H-TiO$_2$ nanorods, it can be observed that the co-catalysts cover the majority surface of the H-TiO$_2$ nanorods (Fig. 1c). The diameter of the H-TiO$_2$ is around 500 nm with a smooth surface. Fig. 1d exhibits the magnified morphology image of FeNi@NGC/H-TiO$_2$, from where we can figure out that the co-catalysts and H-TiO$_2$ nanorods are in close contact. The XRD pattern as-prepared materials (Fig. 1e) provides evidence that FeNi@NGC/H-TiO$_2$ is composed of FeNi intermetallic compounds, N-doped carbon, and H-TiO$_2$. As displayed in Fig. 1e, the XRD pattern for FeNi@NGC corresponds to that of the intermetallic compounds with a Fe/Ni atomic ratio of 1: 1 (PDF#47-1417) [21]. The peak appearing at 51.24° results from the (200) lattice plane of graphitized carbon (PDF#41-1405) [21]. The XRD patterns of the TiO$_2$ and H-TiO$_2$ nanorods exhibit several characteristic diffraction peaks, indexed as anatase TiO$_2$ (ICDD-21-1272) [22]. No obvious differences can

be observed in the XRD patterns before and after the hydrogenation process, suggesting that the hydrogenation process has not altered the crystalline structure of the material. The Raman spectra of FeNi@NGC exhibits two distinguishing peaks at 1321 cm^{-1} and 1585 cm^{-1} (Fig. 1f), which correspond to the D-band and G-band of FeNi@NGC, respectively, proving that the N-doped carbon shell possesses a graphene-like structure. As to the Raman spectra of TiO$_2$ and H-TiO$_2$, the TiO$_2$ nanorods are formed at the anatase phase and exhibit phonon frequencies at 142 cm^{-1} (E$_g$), 395 cm^{-1} (B$_{1g}$), 515 cm^{-1} (A$_{1g}$), and 642 cm^{-1} (E$_g$), which are consistence with the literature within ±1% deviation [23]. All the SEM, XRD, and Raman results exhibit that the FeNi@NGC/H-TiO$_2$ is successfully synthesized with N-doped graphitic carbon shell, FeNi intermetallic compounds, and H-TiO$_2$ nanorods.
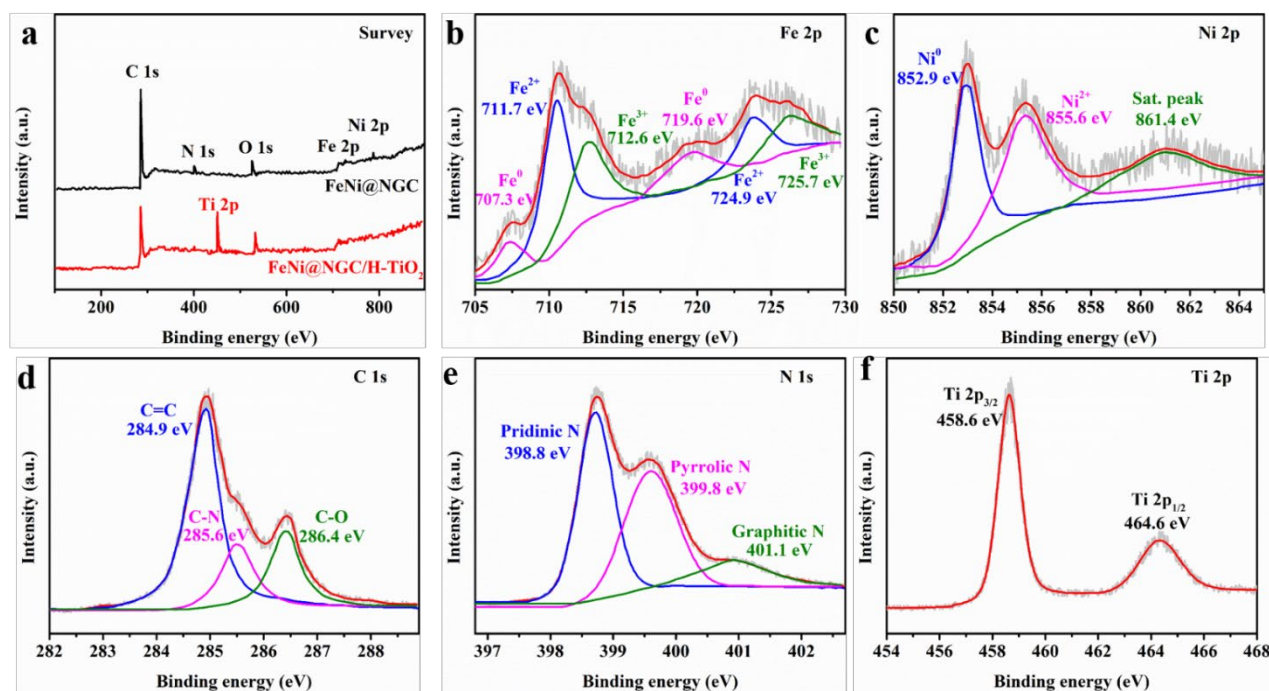

Figure 2. (a) XPS survey spectrum of FeNi@NGC and FeNi@NGC/H-TiO$_2$. High-resolution XPS spectra of (b) Fe 2p, (c) Ni 2p, (d) C 1s, (e) N 1s and (f) Ti 2p of FeNi@NGC/H-TiO$_2$ samples.

To study the surface chemical composition of the FeNi@NGC and FeNi@NGC/H-TiO$_2$ photocatalysts, the XPS investigation is applied (Fig. 2). As shown in the XPS survey spectrum (Fig. 2a), both FeNi@NGC and FeNi@NGC/H-TiO$_2$ contain C, N, and O, with a C/N atomic ratio of 8/1. Obvious peaks for Fe and Ni can be observed in the XPS survey of FeNi@NGC while not in that of FeNi@NGC/H-TiO$_2$, which can be ascribed to the comparatively low content of FeNi@NGC in the latter photocatalysts. As shown in the Fe

2p spectrum of FeNi@NGC/H-TiO$_2$ (Fig. 2b), the spectra can be deconvoluted into six peaks. The two peaks appearing at 707.3 eV and 719.6 eV correspond to Fe^0, which suggests the presence of metallic Fe. The other two peaks at 711.7 eV and 724.9 eV can be ascribed to Fe^{2+}, and peaks at 712.6 eV and 725.7 eV are associated with Fe^{3+}. Fig. 2c displays the Ni 2p spectrum of FeNi@NGC/H-TiO$_2$ photocatalysts, which consisting of three major peaks. The peak appearing at 852.9 eV can be ascribed to Ni^0, indicating that the metallic Ni is successfully formed in the FeNi intermetallic compounds. The other two peaks at 855.6 eV and 861.4 eV are associated with Ni^{2+} and the Ni element's saturation peak. Furthermore, to investigate the chemical composition of carbon-based shells, the C 1s spectrum is presented in Fig. 2d. The peak located at 284.9 eV results from the C=C bond, proving that the carbon shell is graphitized. The other two peaks at 285.6 eV and 286.4 eV are caused by the C-N bond and C-O bond, ascribed to the N-doped carbon structure. Fig. 2e exhibits the N 1s spectrum of FeNi@NGC/H-TiO$_2$. After deconvolution, three peaks can be obtained from the XPS spectrum, which are at 398.8 eV, 399.8 eV, and 401.1 eV, corresponding to pyridinic N, pyrrolic N, and graphitic N, respectively. These results prove that the photocatalysts are successfully doped with N elements. In addition, the Ti 2p spectrum of FeNi@NGC/H-TiO$_2$ is exhibited in Fig. 2f. Two peaks at binding energies of 458.6 eV and 464.6 eV correspond to the Ti 2p$_{3/2}$ and Ti 2p$_{1/2}$ peaks, respectively. The splitting of the 2p doublet is 6.0 eV, suggesting the existence of the Ti^{4+} oxidation state in the as-prepared photocatalysts [24].
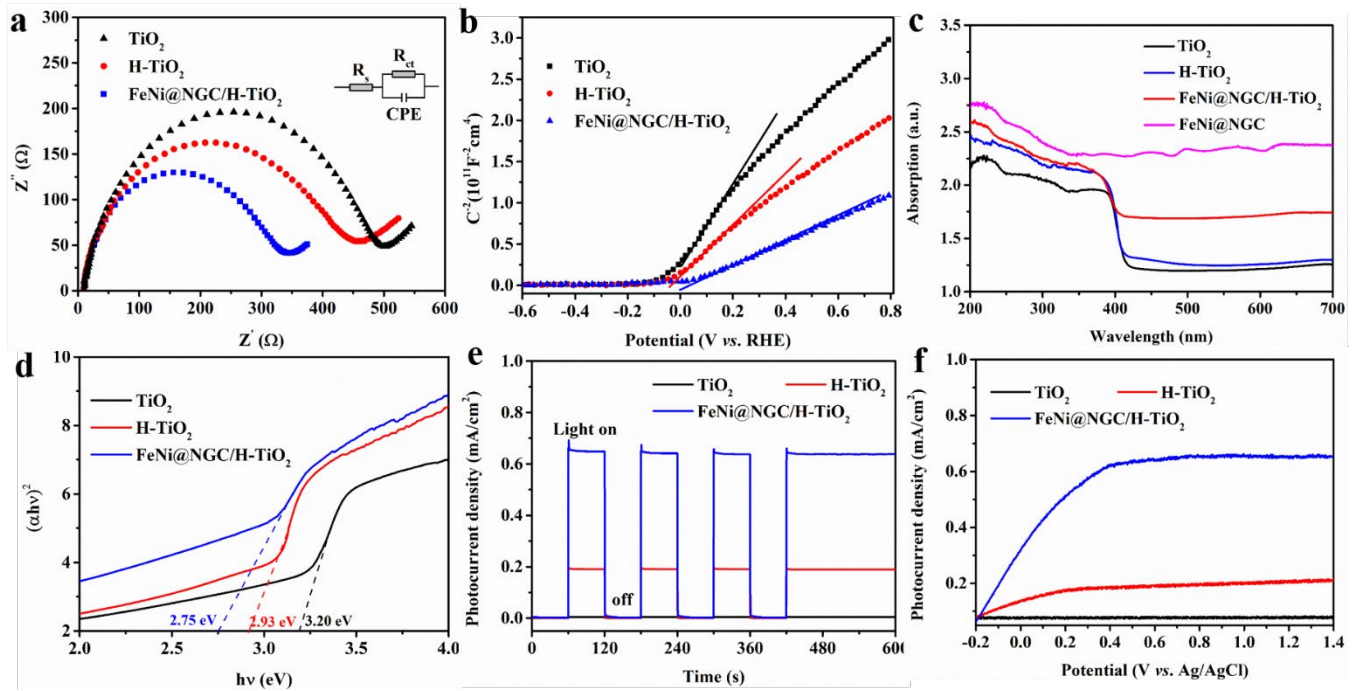
Figure 3. (a) EIS spectra, (b) Mott-Schottky plot, (c) UV-vis spectra, (d) Tauc plots derived from Fig. 3c, (e) transient photocurrent plots, and (f) linear sweep voltammetry of as-prepared photocatalysts.

To study the electrochemical properties of the as-prepared photocatalysts, EIS measurements are conducted. As shown in Fig. 3a, all the Nyquist plots share a similar shape with a semicircle and a straight line afterward. As widely accepted, the smaller radius of the semicircle arc represents the lower charge transmission resistance on the interface between the photocatalysts and electrolytes [25]. Therefore, the FeNi@NGC/H-TiO$_2$ photocatalysts display the lowest charge transfer impedance among all as-prepared photocatalysts, which can be ascribed to the improved separation rate of photo-induced charge carriers by coupling co-catalysts with H-TiO$_2$ nanorods. The Mott-Schottky (M-S) plots were also studied to investigate the flat band potentials (E$_{fb}$) of as-prepared materials Fig. 3b. From the M-S plots, the donor density (N$_d$) of all samples can be obtained via Eq. 1:

$$N_d = \frac{2/e_0\varepsilon\varepsilon_0}{d(1/C^2)/dV} \tag{1}$$

Where e$_0$, ε, and ε$_0$ are constants, representing the electron charge, the dielectric constant, and the permittivity of free space in vacuum, respectively. d(1/C^2)/dV represents the slope of extrapolating the linear parts of M-S curves. Since the values of e$_0$, ε$_0$, and ε are constants, the N$_d$ was inversely proportional

to the slope of the linear part of the M-S curves. Therefore the smallest slope of the M-S curve of FeNi@NGC/H-TiO$_2$ photocatalyst represents its highest donor density among all as-prepared materials, corresponding to the results obtained from the Nyquist plots (Fig. 3a). These characterization results on the electrochemical properties of the prepared materials prove that the FeNi@NGC/H-TiO$_2$ photocatalysts exhibit superior charge separation rate and abundant donor density, favoring the PC degradation performance of FeNi@NGC/H-TiO$_2$ photocatalysts in the degradation of antibiotics under visible light irradiation.

To investigate the light absorption capacity and band-gap energy of as-prepared photocatalysts, the UV-vis absorbance of as-prepared samples is characterized (Fig. 3c). As shown in the figure, the FeNi@NGC co-catalyst displays strong light absorbance over a wide spectrum of ranges. The TiO$_2$ nanorods exhibit strong absorption in the UV irradiation range, while the absorbance sharply declined when the irradiation wavelength is higher than 420 nm. The H-TiO$_2$ photocatalysts show slightly better light absorption ability in the visible light region than pristine TiO$_2$. After coupling the co-catalysts with H-TiO$_2$, the visible light absorption capacity is highly enhanced, suggesting that the FeNi@NGC/H-TiO$_2$ photocatalysts possess superior PC activity under visible light irradiation. By deriving Fig. 3c into Tauc plots (Fig. 3d), we can obtain more insights into the materials' band gap energy. As shown in the figure, the band-gap of TiO$_2$ and H-TiO$_2$ are 3.02 eV and 2.93 eV, respectively. The result further proves that the composition of the TiO$_2$ nanorods is majorly anatase crystalline phase TiO$_2$, and the hydrogenation process brings in abundant oxygen vacancies into the photocatalysts, which narrows the band-gap and enhances the visible light absorption capacity of bare TiO$_2$. After coupling the FeNi@NGC co-catalysts with H-TiO$_2$, the band-gap energy is further narrowed, resulting from the strong light absorption ability of carbon-based shell structure in the co-catalysts.

The transient photocurrent intensity experiments are carried out in a 0.1 mol L^{-1} NaNO$_3$ solution under visible light irradiation to investigate the PEC properties of as-prepared photocatalysts. As shown in Fig. 3e, the FeNi@NGC/H-TiO$_2$ photocatalysts display a photocurrent density of 0.64 mA cm^{-2} under visible

light irradiation, which is 3.37 times higher than that of H-TiO₂ (0.19 mA cm⁻²), suggesting adding FeNi@NGC co-catalysts into the PC system can significantly enhance the oxidation activity of the host photocatalysts. As displayed in the linear sweep voltammograms (LSV) under visible light irradiation (Fig. 3f), when the applied potential increases, the photocurrent density goes up as well until reaching a plateau, which indicates that most of the electrons produced by oxidizing water molecules at this applied potential have been transferred to the counter electrode *via* an electronic circuit and no significant increase of the photocurrent density will be obtained when further increasing the applied potential. The highest saturated photocurrent of FeNi@NGC/H-TiO₂ photocatalysts exhibits that its oxidizing activity is better than all as-prepared materials, resulting from the introduction of FeNi@NGC co-catalysts into the PC system. All these experiment results provide evidence that integrating FeNi@NGC co-catalysts into the H-TiO₂ PC system can significantly enhance the light absorption range and separation rate of photogenerated charge carriers.

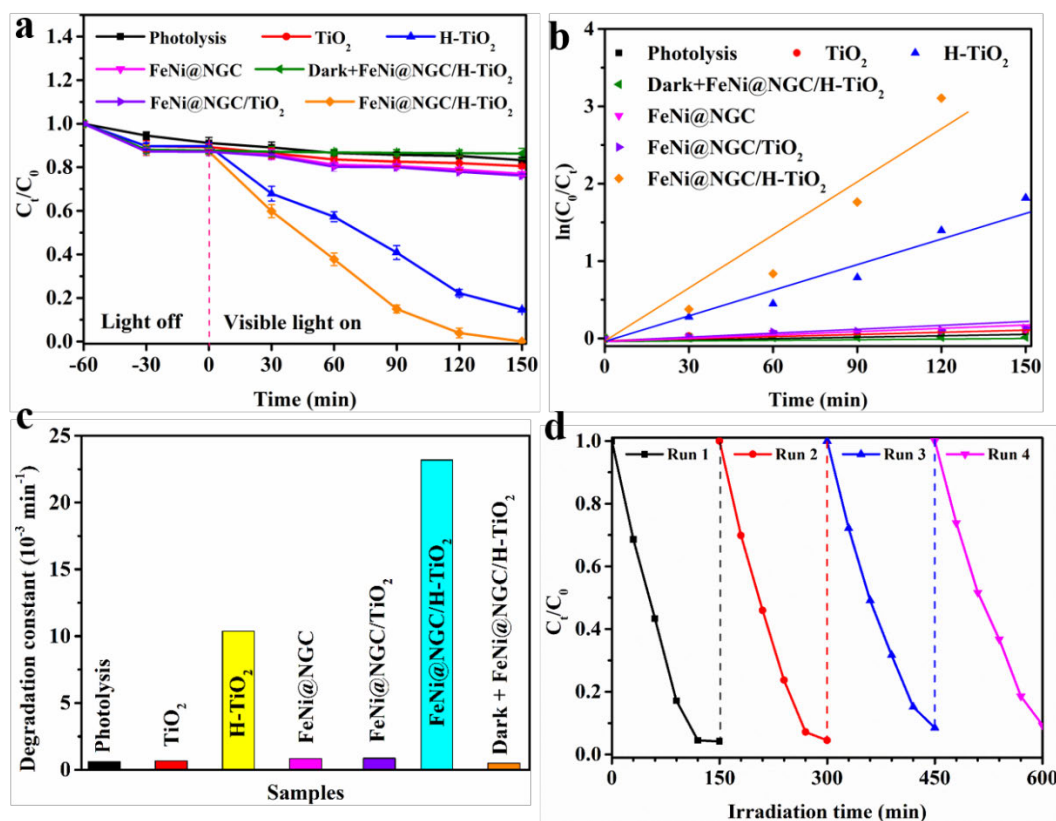## 3.2 TC-HCl degradation performance with FeNi@NGC/H-TiO₂

Figure 4. (a) PC degradation of TC-HCl on the as-prepared photocatalysts in the presence and absence of visible light; (b) Pseudo-first-order kinetics plots for the removal of TC-HCl with the as-prepared samples; (c) the reaction rate constants of TC-HCl degradation for all the samples, (d) recycling runs for the FeNi@NGC/H-TiO$_2$ photocatalyst on the degradation of TC-HCl.

The performance of PC degradation on TC-HCl using as-prepared photocatalysts, with and without the presence of co-catalysts, has been carried out under various conditions (Fig. 5a). As shown in the figure, the degradation rate of TC-HCl in the photolysis process is negligible. The introduction of FeNi@NGC co-catalysts could not enhance the removal rate of TC-HCl, suggesting that solely co-catalysts cannot activating the PC degradation process though FeNi@NGC possesses superior visible light absorption. After adding the TiO$_2$ photocatalysts, the degradation rate on the model antibiotics does not increase significantly as well since the bare TiO$_2$ cannot respond to the visible light irradiation. Based on a similar reason, the FeNi@NGC/TiO$_2$ also exhibits poor degradation performance under visible irradiation. The removal rate of TC-HCl under visible light irradiation significantly improved to 83.7% within 150 min degradation after utilizing H-TiO$_2$ nanorods as the photocatalysts. The enhanced performance can be ascribed to the abundant oxygen vacancies brought by the hydrogenation process, which enlarges the light absorption range of pristine TiO$_2$. After further integrating the FeNi@NGC co-catalysts into the H-TiO$_2$ PC degradation system, the FeNi@NGC/H-TiO$_2$ photocatalysts exhibit the best performance compared to all the other experiments results. A degradation rate of 100% within 150 min under visible light irradiation is achieved (Fig. 5a). The pseudo-first-order kinetic model is applied for the further investigation of antibiotics removal performance *via* Eq. 2:

$$\ln (C_0/C_t) = kt \qquad\qquad (2)$$

where C$_0$ represents the concentration of the initial antibiotic, C$_t$ represents the antibiotics concentration at time t, and k represents the degradation rate constant. All the plots presented in Fig. 5b are obtained based on Eq. 2. The degradation rate constant of each system is calculated from the kinetics plots (Fig. 5b) and displayed in Fig. 5c. The reaction rate constant of FeNi@NGC/H-TiO$_2$ photocatalysts has reached 23.18 × 10^{-3} min^{-1}, which was much higher than that of bare H-TiO$_2$ PC degradation process (10.39 × 10^{-3} min^{-1})

and degradation system integrating FeNi@NGC co-catalysts with unhydrogenated TiO_2 (FeNi@NGC/TiO_2, $0.86 \times 10^{-3}\,min^{-1}$). The results suggest that the superior performance of the FeNi@NGC/H-TiO_2 degradation system results from two aspects. Firstly, the hydrogenation of host photocatalysts will bring in large amounts of oxygen vacancies into the crystal lattice of pristine TiO_2, which considerably improves the visible light absorption of the photocatalysts. Moreover, the introduction of FeNi@NGC can enhance the separation rate of photo-induced electron-hole pairs by the secondary electrons transmission effect in the FeNi intermetallic compounds. Additionally, the N-doped graphitic carbon shell can efficiently trap the irradiation inside the core-shell structure, which further improves the light absorbance of the FeNi@NGC/H-TiO_2 system. The stability test of PC performance for FeNi@NGC/H-TiO_2 was investigated by repeating the degradation experiments toward 20 mg L^{-1} TC-HCl under visible light (Fig. 4d). Photocatalyst is collected and washed several times with distilled water and ethanol after each test. The plots show no significant decrease with only a 5.1% decline in degradation rate after four cycles, which can be ascribed to the photocatalyst loss during the washing process.

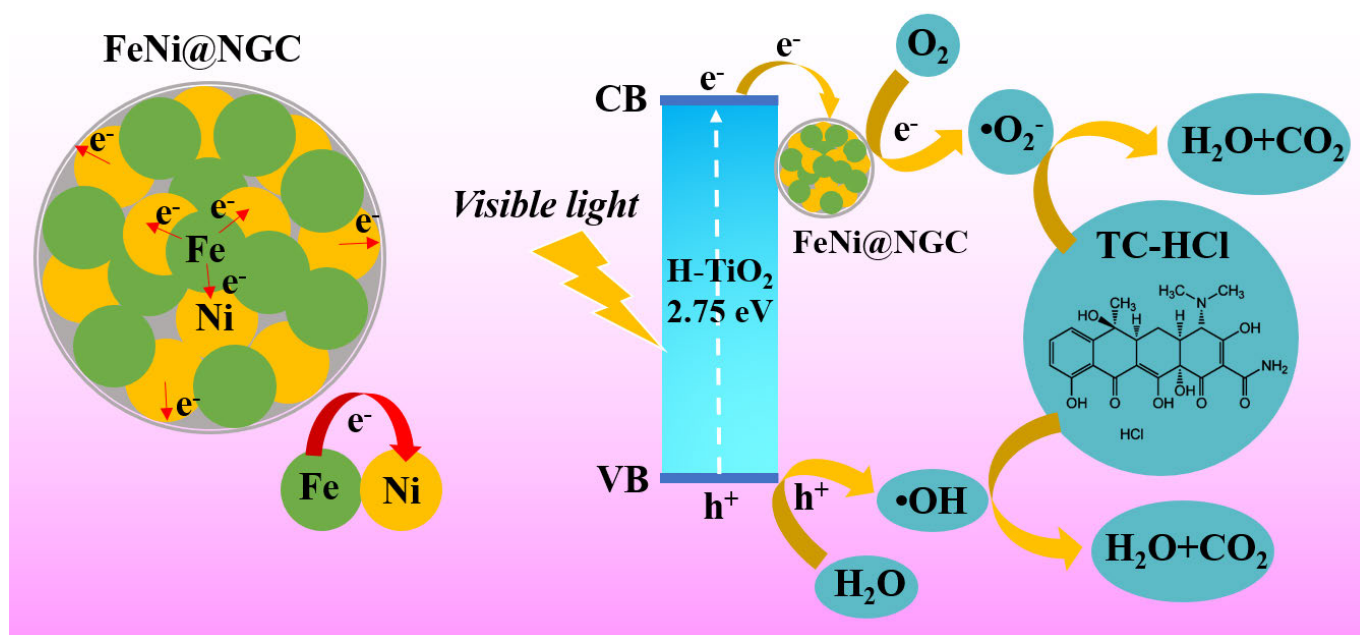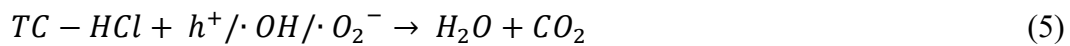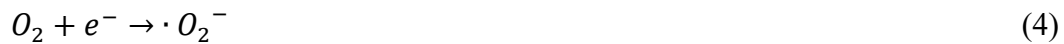**3.3 Mechanism of V-PC/FC-SP degradation of TC-HCl**

Figure 5. Proposed mechanism for FeNi@NGC/H-TiO_2 PC degradation on TC-HCl under visible light.

Based on all the experimental results mentioned above, a proposed mechanism for the FeNi@NGC/H-

TiO₂ system in TC-HCl degradation is provided in Fig. 5. As shown in the SEM images of the FeNi@NGC/H-TiO₂ photocatalysts (Fig. 1c and d), the H-TiO₂ nanorods and FeNi@NGC co-catalysts are in close contact with each other. When the visible light is introduced into the system, the electrons in the valence band (VB) of H-TiO₂ can be stimulated to the conduction band (CB) due to its decreased band-gap energy. As reported in the previous study [12], the CB potential of H-TiO₂ is way higher than that of FeNi@NGC, which favors the photo-induced electrons transferring from the CB of H-TiO₂ nanorods to FeNi@NGC nanoparticles through the contact interface between them. This electron transmission leads to an interfacial electric field at the interface between H-TiO₂ and FeNi@NGC [26]. With the accumulation of photogenerated electrons in the co-catalysts, a secondary electron transmission occurs within the FeNi intermetallic structure, which is a redistribution of electrons [27]. This secondary electron transmission can significantly facilitate the separation rate of photogenerated electron-hole pairs by continuously capture and trap the electrons from the H-TiO₂. Then, part of the photo-induced holes (h^+) left in the VB of H-TiO₂ will react with the water molecules to generate highly oxidizing hydroxyl radicals (•OH, E_0=2.80 V vs. NHE), while the others are going to oxidize the organic compounds in the solution (Eq. 3 and 5). The oxygen dissolved in the water will be reduced by the abundant electrons in the co-catalysts and generated superoxide radicals (•O_2^-) (Eq. 4). In this way, the TC-HCl will be attacked by various active radicals in water and finally be degraded into H₂O and CO₂ (Eq. 5).

$$H_2O + h^+ \rightarrow \cdot OH \tag{3}$$

$$O_2 + e^- \rightarrow \cdot O_2^- \tag{4}$$

$$TC - HCl + h^+/\cdot OH/\cdot O_2^- \rightarrow H_2O + CO_2 \tag{5}$$

4. Conclusion

In conclusion, we designed and synthesized an N-doped carbon-wrapped FeNi intermetallic co-catalyst (FeNi@NGC), which is integrated into the H-TiO₂ PC degradation system to promote its performance on the removal of antibiotics under visible light irradiation. The FeNi@NGC/H-TiO₂ exhibits exceptional PC degradation performance with a degradation rate of 100% in 120 min reaction time and a degradation

constant of 23.18 min^{-1}, which is achieved with simultaneous effects from several aspects. Firstly, incorporating FeNi@NGC co-catalysts into the PC system effectively improves the light absorption capacity of host photocatalysts and promotes the separation of photogenerated electrons and holes. On the one hand, the N-doped graphitic carbon shell will significantly enlarge the visible light absorption of the photocatalysts, and the core-shell structure also benefits the light absorption capacity by trapping irradiation light inside the co-catalysts. On the other hand, the secondary electron transmission process in the FeNi metallic compounds will seize the electrons generated from the host photocatalysts and gathering them on the Ni atoms for further reaction, impeding the recombination of photogenerated electron-hole pairs. Moreover, the hydrogenation on the host photocatalysts improves the visible light absorption considerably *via* introducing plenty of oxygen vacancies into the crystal lattice of TiO_2. With all these advantages, the FeNi@NGC/H-TiO_2 system seems to be a promising solution to the efficient removal of refractory antibiotics in water bodies.

Reference:

1.	Koe, W.S., et al., *An overview of photocatalytic degradation: photocatalysts, mechanisms, and development of photocatalytic membrane.* Environmental Science and Pollution Research, 2020. **27**(3): p. 2522-2565.

2.	Zhang, Q., et al., *Photocatalytic degradation of tetracycline antibiotics using three-dimensional network structure perylene diimide supramolecular organic photocatalyst under visible-light irradiation.* Applied Catalysis B: Environmental, 2020. **277**: p. 119122.

3.	Shi, W., et al., *Construction of CuBi2O4/Bi2MoO6 pn heterojunction with nanosheets-on-microrods structure for improved photocatalytic activity towards broad-spectrum antibiotics degradation.* Chemical Engineering Journal, 2020. **394**: p. 125009.

4.	Yang, Y., et al., *In Situ Grown Single‑Atom Cobalt on Polymeric Carbon Nitride with Bidentate Ligand for Efficient Photocatalytic Degradation of Refractory Antibiotics.* Small, 2020. **16**(29): p. 2001634.

5.	Huang, C., et al., *Unraveling fundamental active units in carbon nitride for photocatalytic oxidation reactions.* Nature communications, 2021. **12**(1): p. 1-8.

6.	Wu, S. and Y.H. Hu, *A comprehensive review on catalysts for electrocatalytic and photoelectrocatalytic degradation of antibiotics.* Chemical Engineering Journal, 2020: p. 127739.

7.	He, Y., et al., *Remarkably enhanced visible-light photocatalytic hydrogen evolution and antibiotic degradation over g-C3N4 nanosheets decorated by using nickel phosphide and gold nanoparticles as co-catalysts.* Applied Surface Science, 2020. **517**: p. 146187.

8.	Chen, D., et al., *Decorating Cu2O photocathode with noble-metal-free Al and NiS co-catalysts for efficient photoelectrochemical water splitting by light harvesting management and charge separation design.* Chemical Engineering Journal, 2020. **381**: p. 122655.

9.	Hu, T., et al., *Noble-metal-free Ni2P modified step-scheme SnNb2O6/CdS-diethylenetriamine for photocatalytic hydrogen production under broadband light irradiation.* Applied Catalysis B: Environmental, 2020. **269**: p. 118844.

10.	Zhao, H., et al., *Photo-assisted separation of noble-metal-free oxidation and reduction co-catalysts for graphitic carbon nitride nanosheets with efficient photocatalytic hydrogen evolution.* Applied Catalysis B: Environmental, 2021. **280**: p. 119456.

11.	Alrafei, B., et al., *Remarkably stable and efficient Ni and Ni-Co catalysts for CO2 methanation.* Catalysis Today, 2020. **346**: p. 23-33.

12.	Chen, S., et al., *FeNi intermetallic compound nanoparticles wrapped with N-doped graphitized carbon: a novel co-catalyst for boosting photocatalytic hydrogen evolution.* Journal of Materials Chemistry A, 2020. **8**(6): p. 3481-3490.

13.	Yang, G., et al., *Cocatalyst Engineering in Piezocatalysis: A Promising Strategy for Boosting Hydrogen Evolution.* ACS Applied Materials & Interfaces, 2021.

14.	Cui, Y., et al., *Mitigating Metal Dissolution and Redeposition of Pt-Co Catalysts in PEM Fuel Cells: Impacts of Structural Ordering and Particle Size.* Journal of The Electrochemical Society, 2020. **167**(6): p. 064520.

15.	Adekoya, D., et al., *Hierarchical Co3O4@ N-doped carbon composite as an advanced anode material for ultrastable potassium storage.* ACS nano, 2020. **14**(4): p. 5027-5035.

16.	Liu, P., et al., *Carbon nanocages with N-doped carbon inner shell and Co/N-doped carbon outer shell as electromagnetic wave absorption materials.* Chemical Engineering Journal, 2020. **381**: p. 122653.

17.	Xiong, Y., et al., *Single-atom Rh/N-doped carbon electrocatalyst for formic acid oxidation.* Nature nanotechnology, 2020. **15**(5): p. 390-397.

18.	Qin, Y., et al., *Nitrogen-doped hydrogenated TiO2 modified with CdS nanorods with enhanced*

optical absorption, charge separation and photocatalytic hydrogen evolution. Chemical Engineering Journal, 2020. **384**: p. 123275.

19. Zhang, L., et al., *Hydrogenated TiO2 membrane with photocatalytically enhanced anti-fouling for ultrafiltration of surface water.* Applied Catalysis B: Environmental, 2020. **264**: p. 118528.

20. Yu, J., et al., *Preparation and photocatalytic activity of mesoporous anatase TiO2 nanofibers by a hydrothermal method.* Journal of Photochemistry and Photobiology A: Chemistry, 2006. **182**(2): p. 121-127.

21. Shen, R., et al., *Enhanced solar fuel H2 generation over g-C3N4 nanosheet photocatalysts by the synergetic effect of noble metal-free Co2P co-catalyst and the environmental phosphorylation strategy.* ACS Sustainable Chemistry & Engineering, 2018. **6**(1): p. 816-826.

22. Khan, H., et al., *Spray dried TiO2/WO3 heterostructure for photocatalytic applications with residual activity in the dark.* Applied Catalysis B: Environmental, 2018. **226**: p. 311-323.

23. Odhiambo, V.O., et al., *Synthesis of tio2/wo3 composite nanofibers by a water-based electrospinning process and their application in photocatalysis.* Nanomaterials, 2020. **10**(5): p. 882.

24. Gao, H., et al., *One-dimensional Z-scheme TiO2/WO3/Pt heterostructures for enhanced hydrogen generation.* Applied Surface Science, 2017. **391**: p. 211-217.

25. Chen, F., et al., *Atomic-Level Charge Separation Strategies in Semiconductor-Based Photocatalysts.* Advanced Materials, 2021. **33**(10): p. 2005256.

26. Zhou, H., et al., *One-step synthesis of self-supported porous NiSe2/Ni hybrid foam: an efficient 3D electrode for hydrogen evolution reaction.* Nano Energy, 2016. **20**: p. 29-36.

27. Chang, J., et al., *Monocrystalline Ni 12 P 5 hollow spheres with ultrahigh specific surface areas as advanced electrocatalysts for the hydrogen evolution reaction.* Journal of Materials Chemistry A, 2016. **4**(25): p. 9755-9759.

CHAPTER 7

CONCLUSIONS AND FUTURE WORK

7.1 GENERAL CONCLUSIONS

To summarize the results presented in this thesis, we have successfully used several rational strategies to synthesize and design a series of TiO_2-based photocatalysts for application in the detection and degradation of organic compounds. This thesis's central theme is to use facile approaches to manipulate the electronic, morphological, and structural properties of TiO_2-based materials to improve their PC and PEC performance. The major findings from the works in this thesis can be concluded as follows:

1. An anatase-branch@hydrogenated rutile-nanorod (AB@H-RTNR) TiO_2 electrode has been designed and successfully prepared via a two-step hydrothermal method combined with a hydrogenation process. The role of hydrogenation in AB@RTNR was investigated. The as-prepared photoanodes successfully achieved sensitive determination of COD with a detection limit of 0.2 ppm (S/N = 3), an RSD% of 1.5%, a wide linear detection range of 1.25−576 ppm, and an average recovery rate fluctuating between 100% ± 4% for artificial wastewater sample analyses. These results show that AB@H-RTNR is a promising photocatalyst for detecting COD in water bodies.

2. A comprehensive study on designing a highly efficient, scalable, portable, and low-cost wastewater treatment and purification device for small-scale textile plants was carried out, and several conclusions are summarized as follows. Firstly, to improve the efficiency of contaminant degradation and reduce the operating device's cost, the H-AB@RTNRs nanocomposites were successfully fabricated via a hydrothermal route. The H-AB@RTNRs were characterized by different methods to prove that the photocatalysts possessed abundant oxygen vacancies and Ti^{3+}, which facilitated the separation rate of electron-hole pairs and enhanced light absorption in the visible region. In this way, clean and low-cost solar energy can be utilized for wastewater

treatment with H-AB@RTNRs. Secondly, the introduction of PS anions into the PC degradation process enables the reactor to degrade refractory organic contaminants that could not be achieved by the PC process alone. Thirdly, the thin-layer cell design could reduce the light loss in the aqueous solution by minimizing the thickness of the water film between the irradiation source and photocatalysts, which maximizes light absorption by the photocatalysts and therefore achieves a better degradation performance compared with the conventional bulk cell. The device design also improves the portability of the reactor and exhibits its potential for up-scaling. This work highlights that the H-AB@RTNRs photocatalysts and PC-PS degradation system in the thin-layer cell have significant potential for practical PC removal of organic dye contaminants in the environment.

3. We designed a visible-light-driven PC/chlorination synergetic degradation system to increase the pseudo-first-order degradation rate constant of a model antibiotic, tetracycline hydrochloride, by 3.66 and 86.57 times more than that in the pure photocatalysis and traditional chlorination processes, respectively. The PC/chlorination synergetic degradation system is feasible and easily implementable by activating the residual chlorine present in tap water and treated reused wastewater to enhance the micropollutant degradation in the chlorination process of the water treatment plant. Although part of the h^+ might be trapped by other organic components in real water bodies, the improvement in the yield of active radicals, such as •OH, is still significant, because those radicals are mainly generated from the activation of chlorine by e^- and •O^{2-}. Another benefit of the PC/chlorination synergetic degradation system is that the process can be integrated to the end of the chlorination tank to achieve simultaneous degradation and chlorination to improve the effluent quality. This work demonstrates that the visible-light-driven PC/chlorination synergetic degradation system is a novel AOP for degrading

antibiotics.

4. We successfully fabricated an efficient co-catalyst of N-doped graphitized carbon wrapped FeNi nanoparticles (FeNi@NGC) to enhance the degradation rate of antibiotics by host photocatalysts (H-TiO$_2$). The FeNi@NGC/H-TiO$_2$ system exhibits outstanding PC degradation performance and stability, resulting in a degradation rate constant of 23.183 min^{-1} under visible-light irradiation, which is 2.23 times higher than that of H-TiO$_2$ without the assistance of co-catalysts. The favorable performance of the co-catalysts can be ascribed to two aspects. Firstly, the N-doped graphitized carbon shell can trap the irradiation inside, which significantly enhances the light absorption of the host photocatalysts. Moreover, the secondary electron transfer in the FeNi intermetallic compounds results in the instantaneous generation of electrons accumulated on Ni atoms, which favors the separation of photogenerated electrons and holes. The work results suggest that the non-precious metal FeNi@NGC co-catalyst is a promising solution for boosting the PC antibiotics degradation performance.

7.2 FUTURE WORKS

This thesis focused on synthesizing and applying TiO$_2$-based photocatalysts to detect and degrade organic compounds in water bodies. Although the aim of this thesis has been achieved, there is still sufficient room for improvement in terms of the scope of TiO$_2$-based PC technology, material characterization, and characterization tools. These details are summarized as follows:

1) When modifying the TiO$_2$-based photocatalysts to increase the light absorption range and reduce the recombination rate of photogenerated charge carriers, many strategies are used. However, most of those modification methods will increase the

instability and cost of synthesizing materials, which is not economically sustainable. Therefore, more economically-friendly, stable, and easily implementable methods should be explored in the future.

2) The PC and PEC reactor design plays a crucial role in the successful application of photocatalysts. The specifications and requirements of reactors vary a lot depending on different photocatalytic application demands, and the scaling up of lab-scaled reactors is urgently needed. At this stage, we are facing several hindrances which impede the scaling up of lab-scaled PC and PEC reactors, such as high cost in building and operating up-scaled devices, due to the simultaneous interaction of several parameters (irradiation, temperature, pressure, and applied potential, etc.). In the future, the focus of the work should concentrate on developing low-cost approaches for up-scaling PC and PEC reactors.

3) The synthesis methods, fabrication techniques, and other modification techniques used in this thesis can be further developed to inspire the synthesis of other crystalline structures of different types of heterostructures.

4) Advanced characterization techniques such as *in-situ* characterization technologies, e.g., *in-situ* FTIR, XPS, and XRD, should be used to investigate the structural changes, functional group transformations, and phase/oxidation state variation during degradation process.

5) Finally, theoretical and computational tools like Density Functional Theory (DFT) calculation have guided the design and application of photocatalyst materials for PC and PEC applications. Consequently, the combination of computational tools with electrochemical techniques should be utilized to design advanced photocatalysts.